Investigating a novel protein-based cofactor: toward elucidating the catalase mechanism of *Mycobacterium tuberculosis* KatG

by

Tarfi Aziz

A dissertation submitted to the Graduate Faculty of
Auburn University
in partial fulfillment of the
requirements for the Degree of
Doctor of Philosophy

Auburn, Alabama
December 10, 2022

Keywords: catalase-peroxidase (KatG), catalase, peroxidase, heme, protein-based cofactor, MYW adduct, heme-reconstitution protocol

Approved by

Douglas C. Goodwin, Professor and Chair of Chemistry and Biochemistry
Eduardus Duin, Professor of Chemistry and Biochemistry
Angela Calderon, Associate Professor of Drug Discovery, and Development
Holly R. Ellis, Professor of Brody School of Medicine at East Carolina University

Abstract

Catalase-peroxidases (KatGs) have been engineered by nature to exhibit dual functionalism, degrading H_2O_2 by catalase and peroxidase mechanisms. This serves to protect the organisms that carry it (primarily bacteria and fungi) against peroxide-dependent oxidative damage. Despite bearing no resemblance to monofunctional (*i.e.*, typical) catalases, KatGs have robust catalase activity due at least in part to a novel covalent linkage between three side chains (by *Mycobacterium tuberculosis* KatG [*Mtb* KatG] numbering, Met 255, Tyr 229, and Trp 107) (MYW). This MYW cofactor redox cycles between its radical ($MYW^{\bullet+}$) and fully covalent states, enabling KatG to leverage heme intermediates for catalatic O_2 production. However, the molecular mechanism by which the adduct is formed and how this unique structure contributes to overall catalytic mechanism of KatG have yet to be fully elucidated. Here, site-directed mutagenesis in combination with optical stopped-flow spectrophotometry and rapid freeze-quench EPR spectroscopy have been used to investigate the mechanism of MYW adduct formation and the catalase activity that emerges from it.

In order to pursue these lines of research, it was essential to develop a robust and reliable protocol for producing KatG which possessed its heme prosthetic group but had not yet engaged in the autocatalytic formation of its MYW cofactor. Historically, it has always been challenging to produce KatG that contains heme, but at the same time, lacks this critical post-translational modification, *and* is capable of forming the adduct on demand and displaying the full range of KatG's catalytic abilities. Due to the large size of the protein (80 kDa), denaturation or unfolding has never been a successful strategy to regain the protein in the native form. Moreover, use of harsh organic compounds for denaturing has also made the protein vulnerable for mechanistic investigation. Throughout the field of KatG biochemistry, heme is incorporated during expression. Exposure to endogenous peroxides or other oxidants during expression ensures that the purified enzyme product invariably contains the fully formed MYW

cofactor, making it impossible to evaluate the steps of its formation. The alternative is to produce KatG such that heme is not incorporated. That is, that apoKatG (*a*KatG) would be expressed and purified. The *a*KatG must then be successfully reconstituted with the heme cofactor *after* isolation from the expression culture to prevent premature peroxide-induced MYW formation. This challenge has thwarted the KatG field for many years.

As described in Chapter 2 of this dissertation, we were able to develop a protocol which solved this problem. Using a standard *E. coli* laboratory expression strain (BL-21 [DE3] pLysS) and withholding heme and heme precursors, we were able to express KatG from which the overwhelming product was the *a*KatG form. We were able to reconstitute *a*KatG with heme in the midst of the purification process to generate the reconstituted form (*r*KatG). Structural consistency and fully functional capacity of *r*KatG were demonstrated by strong and typical UV absorption features and enzymatic activity. The striking yield of *r*KatG (at least 20-fold higher) is one of the most fortuitous aspects of this study and created the possibility of using more sophisticated and material-intensive techniques like rapid freeze-quench electron paramagnetic resonance (RFQ-EPR) spectroscopy and Mössbauer spectroscopy. By all measures employed to date, *r*KatG is indeed a suitable tool for mechanistic investigation.

With separate protocols in hand to generate reconstituted and mature forms of WT KatG (*r*WT and *m*WT KatG, respectively), we evaluated and compared each form for their reactions with peroxides using optical stopped-flow and RFQ-EPR spectroscopy (Chapter 3). Under multiple-turnover conditions using H_2O_2, optical stopped-flow experiments showed an initial appearance of a high-valent ferryl-like (Fe^{IV}=O) intermediate instead of the intermediate typically observed for KatG engaging in catalatic H_2O_2 decomposition under steady-state conditions, a Fe^{III}-$O_2^{\bullet-}$-like species. Nevertheless, in contrast to catalase-negative canonical heme peroxidases, full catalase H_2O_2 decomposition did emerge over the course of the reaction. This was evident in two ways. First, the resting or Fe^{III} form of the enzyme reemerged at the

conclusion of the reaction, indicating that the balance of H_2O_2 present at the start of the reaction had been depleted. Second, the initial Fe^{IV}=O state observed early in the reaction gave way to the Fe^{III}-$O_2^{\bullet-}$-like KatG catalase steady-state species. This latter transition was accompanied by an irreversible increase in absorbance near 315 nm, consistent with the establishment of the MYW cofactor (or precursors thereof). Interestingly, pretreatment of *r*WT KatG with limited molar equivalents of peracetic acid (PAA), a peroxide that supports only heme/enzyme oxidation, produced an enzyme with the properties of the *m*KatG enzyme.

EPR experiments revealed that an admixture of radical species appeared before any evidence of a MYW cofactor radical intermediate, suggestive of the preferred site of crosslink initiation. At the earliest reaction time (6 ms), *r*KatG produced an exchange-broadened radical signal followed by a narrow doublet signal. Such an early appearance of an exchange-coupled radical is not observed with *m*KatG when it is reacted with its natural substrate, H_2O_2. Rather, this type of signal is only detected upon reaction with peroxides incapable of supporting catalatic turnover (i.e., peracetic acid). Reactions of *m*KatG with H_2O_2 invariably produce the narrow doublet radical assigned as the $MYW^{\bullet+}$ species. Thus, we propose that such an exchange-broadened species arises from a radical centered on the distal Trp prior to its incorporation into the MYW cofactor.

Variants of KatG incapable of establishing the MYW adduct (M255I, Y229F and W107F) were also constructed, expressed, purified, and reconstituted with heme. Stopped-flow and UV-vis analyses of these variants showed disrupted catalase activities and incomplete catalatic turnover. Interestingly, partial adduct bearing *r*M255I supported catalatic turnover at a rate greater than other adduct negative variants at low pH (i.e., pH 5.0). As compared to the WT activity, the rate and extent of O_2 was relatively low; however, measurable O_2 production above that of typical peroxidases has not been reported among these adduct negative variants. These observations strongly suggest that the distal side Trp 107 and Tyr 229 are essential

components of the catalase mechanism; limited catalase activity can be accomplished with just those two residues, but the full activity of the enzyme cannot be achieved without the sulfonium linkage provided by Met 255. Our reconstituted KatG proteins may permit investigation of radical transfer reactions leading to formation of KatG's novel MYW cofactor as well as the influence of other protein radical transfer reactions on that process. However, as far as the molecular mechanism is concerned, a main limitation of steady state kinetics is that the nature of the rate-limiting step in the global catalytic process cannot always be established with certainty, so that it is not always clear which step(s) the limits the overall rate. We propose that a technique combining rapid quench with mass spectrometry for detecting and quantitating the covalent intermediates and products of MYW cofactor formation. Used in combination with the kinetics of adduct formation monitored at 315 nm and the transient kinetics of radical species observed by EPR, a thorough elucidation of the mechanism of MYW adduct formation is anticipated.

Another important aspect of this study was the evaluation of protein-based radicals alongside the kinetics of formation and decay of transient heme states. To a significant degree continuous-wave, X-band EPR and optical absorption measurements, respectively, carry with them ambiguity that is addressed by alternative and complementary techniques. Signals that we obtained from conventional EPR measurement creates ambiguity due to resemblance in shape and relaxation behavior of the Tyr or Trp radical. Further confirmation requires isotopic labeling of tyrosine and tryptophan residues, nitric oxide radical trapping techniques, and/or ^{57}Fe-labeling to verify the influence of the heme iron on protein-based radicals in very close proximity to the active site. The latter is also essential for Mössbauer studies which provide more definitive assignment of iron oxidation states, particularly those that are EPR silent. Our protocol for expressing KatG without heme followed by successful reconstitution with the cofactor after purification not only enabled the studies described in this dissertation, but also

make possible these more advanced and material-intensive spectroscopic strategies. A complete understanding of radical transfer processes is the key to unlocking all aspects of KatG catalysis, including but not limited to MYW cofactor generation and utilization, through-protein radical transfer as an enzyme activity fail-safe. These are the central to KatG's role in important physiological processes like host-pathogen interactions and isoniazid activation.

This work was supported by a grant from the National Science Foundation (MCB 1616059)

Acknowledgments

First, I want to attribute this work to the incredible blessings Almighty has bestowed upon me, which are too numerous to count and certainly too extensive to detail here.

I could not have asked for a better mentor Dr. Douglas Goodwin, my graduate research advisor who from the beginning, was incredibly supportive and understanding. You encouraged and challenged me, and it was under your guidance that I realized my potential and discovered my passion for research. Doc, I am thankful for your valuable time, resources, and knowledge, and appreciate everything you have done for me during my thesis work.

Thank you to my committee members, Dr. Evert Duin, Dr. Angela Calderon, Dr, Holly Ellis for your assistance, advice, and commitments during my graduate studies. I am also thankful to the university outside reader Dr. Robert Judd for his wonderful cooperation. To Dr. Duin, thank you for always being so helpful using the EPR instrument and open to discuss for analyzing EPR results. Thank you to Dr. Melissa Boersma for providing guidance and support using Mass-spec facility. Melissa, I really appreciate that you were always willing to sit down and chat, and to help me work through my issues, whatever they were. To the faculty and staff in the Department of Chemistry and Biochemistry, thank you for supporting me during my years in the graduate program. To my teaching lab advisors, thank you for allowing me to learn and grow as an educator.

To my lab mates, Dr. Rene Fuanta, Dr. Hui Xu, Dr. Jessica Krewall, Dr. Jahangir Alam, Dr. Callie Barton, Rejaul Islam, Chidozie Ugochukwu, Patrick Sahrmann, Kirklin McWhorter, Aishah Lee, Laura Minton, and Ryan Mumford, thank you for creating a welcoming laboratory environment and helping me achieve my research goals. To my dear friends and fellow graduate students, Dr. Yixuan Yang, Dr. Shuxin Li, Dr. Shamim Iqbal, Dr. Shahriar Khan, Dr.

Radini Himashini Dissayanka, Dr. Shadi Yavari, Theophila Dusabamahoro, Sana Karbalaei, Asanka Newan, Niharika Dalpati, Humayra Yeasmin, Amanda Kurian thank you all for making the grad life forever memorable. I especially want to thank my friend Jessica and Callie, all the laughs, memories made, and our friendship have had such a positive impact on my time in Goodwin lab.

I cannot thank my family and loved ones enough. To my mom, Shahriar Aziz, I would not be where I am today without your unwavering support, encouragement, and prayers. To my mother-in-law, Shamim Ara Baten, I am forever grateful for your kindness and sacrifice to start my graduate school.

No word will be enough to express my gratitude to my husband Dr. Asif Mahmud, who is the source of wisdom, love, support, strength, and perseverance. This is you Asif, who has grown all my passion for molecular biology and transformed me from a chemistry person to a dedicated scientist of biochemistry. Without your relentless guidance and encouragement, I would not be the person I am today. Last but not the least, I want to dedicate this work to my daughter Areebah Yashfin Mahmud, who sacrificed most during my journey to achieve this degree. Thank you all.

Table of Contents

List of Figures

List of Tables

List of Abbreviations

Å	Angstrom
ABTS	2,2'-azino-bis (3-ethylbenzthiazoline-6-sulfonic acid)
AhpC	Alkyl hydroperoxide reductase subunit C
*a*KatG	apo KatG
APx	Ascorbate peroxidase
Arg, R	Arginine
BSAO	Bovine serum amine oxidase
CAO	Copper-containing amine oxidase
CcO	Cytochrome c oxidase
C*c*P	Cytochrome *c* peroxidase
CDO	Cysteine dioxygenase
CTQ	Cysteine tryptophylquinone
Cys, C	Cysteine
EPR	Electron paramagnetic resonance spectroscopy
Fe	Iron
Gly	Glycine
GO	Galactose oxidase
GSH	Glutathione
H_2O_2	Hydrogen peroxide
His, H	Histidine
HPLC	High-performance liquid chromatograph
HRP	Horseradish peroxidase
HS	High-spin
IN•	Isonicotinoyl radical
INH	Isoniazid, isonicotinic acid hydrazide
InhA	Enoyl acyl-carrier protein reductase
IN-NAD	Isonicotinoyl-nicotinamide adenine dinucleotide adduct
IPTG	Isopropyl β- d-1-thiogalactopyranoside
KatG	Catalase-peroxidase
LB	Luria Broth
LC	Liquid chromatography
LOX	Lysyl oxidase
LTQ	Lysine tyrosylquinone
MADH	Methylamine dehydrogenase
MauG	Methylamine utilization protein
mCPBA	m-Chloroperoxybenzoic acid
MDR	Multi-drug resistant
Met, M	Methionine
*m*KatG	mature KatG
MS	Mass spectrometry
Mtb	Mycobacterium tuberculosis

MYW	Methionine-Tyrosine-Tryptophan adduct/cofactor
NAD	Nicotinamide adenine dinucleotide
Nm	Nanometers
O_2	Molecular oxygen
PAA	Peracetic acid
PC	Peroxidase-catalase (superfamily)
PDC	Protein derived cofactor
Phe, F	Phenylalanine
PMSF	Phenylmethylsulfonyl fluoride
Por	Porphyrin
PpIX	Protoporphyrin IX
PQQ	Pyrroloquinoline quinone
Pro, P	Proline
PTM	Post translational modification
PxED	Peroxidatic electron donor
QHNDH	Quinohemoprotein amine dehydrogenase
RFQ	Rapid freeze-quench
*r*KatG	reconstituted KatG
RNR	Ribonucleotide reductase
RNS	Reactive nitrogen species
ROS	Reactive oxygen species
Rz	Reinheitzahl
TB	Tuberculosis
TCA	Trichloroacetic acid
TPQ	Topa quinone
Trp, W	Tryptophan
TTQ	Tryptophan tryptophylquinone
Tyr, Y	Tyrosine
WT	Wild-type
YW	Tyrosine-Tryptophan adduct
δ-ALA	δ-aminolaevulinic acid

1. CHAPTER ONE

LITERATURE REVIEW

1.1. Functional Role of Post-Translational Modification (PTM) Across Biology

Post-translational modifications (PTM) decorate proteins to provide functional heterogeneity to an existing proteome. The diversification of protein structure and function can be observed at multiple levels. For example, at the transcriptional level, mRNA splicing, including tissue-specific alternate splicing, is observed, and well known. A second route of diversification is the covalent modification that occurs after DNA has been transcribed into RNA, and RNA translated into proteins. Post-translational modification (PTM) of proteins refers to the covalent and (typically) enzymatic modification of proteins following translation. There are more than 400 different types of PTMs based on the type of amino acid side chain modified, the category of the modifying enzyme, and the extent of reversibility.[1] Protein PTMs can be broadly divided into two main groups. The first includes all enzyme-catalyzed covalent additions of functional groups, usually an electrophilic fragment of a substrate, to a nucleophilic amino-acid side chain from a target protein (Scheme 1.1). Some of the most common PTMs of this type include glycosylation, deamidation, phosphorylation, ubiquitination, and acetylation (Table 1.1). Further details of some of these common PTMs are discussed below. In any case, PTMs are key modulators of biological processes by significantly affecting the activity of proteins.

A second category of PTM is covalent cleavage of peptide backbones in proteins either by the action of proteases or, less commonly, by autocatalytic cleavage (Scheme 1.2). The involvement of proteases is ubiquitous, and its role is critical in antigen processing, apoptosis,

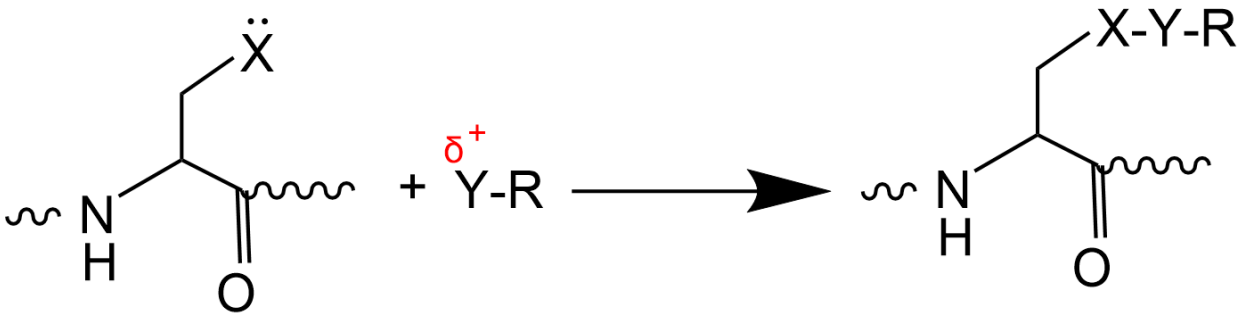

Scheme 1.1. Covalent modification of a nucleophilic amino acid side chain by an electrophilic fragment of a co-substrate. (Adapted from *Christopher T. Walsh et al.*[2])

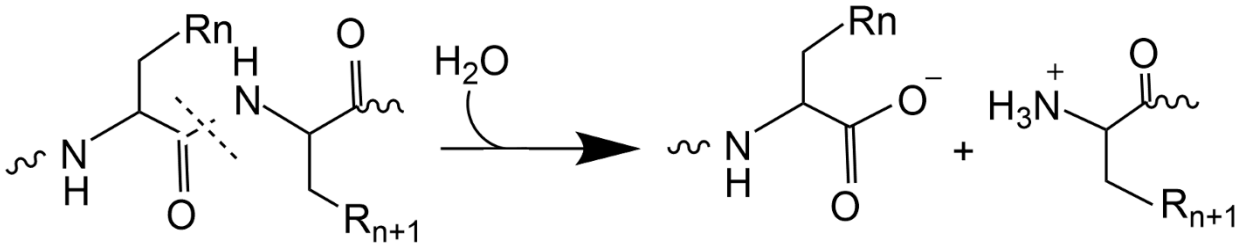

Scheme 1.2. Cleavage of a protein backbone at a specific peptide bond. (Adapted from *Christopher T. Walsh et al.*[2])

Table 1.1. Common types of post-translational modification.

Post-translational modification type	Modified amino acid residues	Mechanism
Phosphorylation	Ser, Tyr or Thr	Addition of a phosphate group to an amino acid residue.
Acetylation	N-terminus	Addition of an acetyl group to an N-terminus of a protein, or at Lys residues.
Methylation	Arg, Lys	Addition of a methyl group, most often at Lys or Arg residues.
Glycosylation	Ser, Thr (O-linked), Asn (N-linked)	Covalent addition of a carbohydrate moiety to an amino acid, forming a glycoprotein.
Sulfation	Tyr	Addition of a sulfate group into a Tyr residue of a protein molecule.
Ubiquitination	Lys	Binding of a ubiquitin protein to a protein via a three-step process.
C-hydroxylation	Pro	Formation of hydroxyproline by hydroxylating the γ-Carbon atom of Pro.
Nitration	Tyr, Trp, Cys, Met	Addition of a nitro group into amino acid residues.

surface protein shedding and cell signaling. For example, the serine protease thrombin is generated by proteolytic cleavage of the zymogen precursor, prothrombin. Thrombin, once generated, is itself a protease which converts fibrinogen into fibrin. Perturbation in the homeostatic level of thrombin can promote pathological states, including thrombosis and fibrinolysis. Other examples include cysteine proteases, metalloproteases, aspartic acid proteases, zinc metalloproteases etc.

1.1.1. Phosphorylation

Phosphorylation is one of the most extensively studied PTMs. It can occur in both a reversible and an irreversible manner. Here, the terms *reversible* and *irreversible* should not be understood as strictly thermodynamic expressions because both protein phosphorylation by a nucleoside triphosphate (catalyzed by kinases) and hydrolysis of phosphoryl groups from amino acid side chains (catalyzed by phosphatases) are highly exergonic. Rather, these terms refer to metabolic reversibility where a given pair of enzymes kinase/phosphatase are available to add/remove phosphoryl groups as cellular signaling dictates. Reversible phosphorylation of proteins involves addition of a nucleoside triphosphate-derived phosphate group to Ser, Thr, or Tyr residues. Several enzymes or signaling proteins are switched 'on' or 'off' by phosphorylation or dephosphorylation. Phosphorylation and dephosphorylation is performed enzymatically by 'kinases' and 'phosphatases' respectively. Addition of a phosphate group can induce conformational changes in the target protein by imparting a concentrated negative charge to an otherwise neutral protein moiety. Phosphorylation/dephosphorylation is a critical regulatory mechanism for several cellular processes, including cell cycle progression, cell growth, apoptosis, and signal transduction pathways.[3] One example is the activation of a tumor suppressor protein p53, a transcription factor capable of integrating distinct environmental signals including DNA damage, viral infection, and cytokine signaling. Phosphorylation of a

key phospho-acceptor site in the p53 transactivation domain is mediated by distinct stress-activated kinases, including ataxia telangiectasia mutated (ATM) kinase, casein kinase 1 (CK1), and AMP-activated protein kinase (AMPK).[4]

1.1.2. Glycosylation

Glycosylation is a very common modification observed for proteins and lipids, and most glycosylation reactions occur in the endoplasmic reticulum (ER) and Golgi apparatus. This modification involves linkage of an oligosaccharide chain to either a nitrogen atom (*N*-linked glycosylation) or an oxygen atom (*O*-linked glycosylation). According to the target residues, glycosylation can be classified into six groups: *N*-glycosylation, *O*-glycosylation, *C*-glycosylation, *S*-glycosylation, phosphoglycosylation and glypiation. Among these, *N*-glycosylation and *O*-glycosylation are two major types of glycosylation and have important roles in the maintenance of protein conformation and activity.[5] *N*-linked glycosylation proceeds with the attachment of an oligosaccharide (glycan) to the amide nitrogen of Asn residues within the motif, Asn-X-Thr (where X cannot be Pro) while the *O*-linked glycosylation proceeds with the attachment with a glycan to the oxygen atom of the hydroxyl groups of Ser or Thr residue.

Glycosylation has critical roles in many important biological processes such as cell adhesion, immune recognition,[6] receptor activation,[7] inflammation, protein intracellular trafficking,[8] and secretion.[9] For example, most cytokines like interleukins are found in their mature state as glycosylated proteins. In the case of an important immune cytokine interleukin 5 (IL5), chemical digestion of either the *N*-linked or *O*-linked sugar residues on recombinant hIL5 had profound effects on the biological activity of the cytokine in terms of its ability to stimulate release of IgM from BCL_1 cells.[10]

1.1.3. Acetylation

N-acetylation is the transfer of an acetyl group (-$COCH_3$) to the amino group of protein residues catalyzed via lysine acetyltransferase (KAT) and histone acetyltransferase (HAT) enzymes. Although Lys acetylation is the most commonly observed protein modification, acetylation on Ser, Thr, Arg, Lys, Met residues of proteins also have been detected at different frequencies.[11,12] Acetyl-CoA is the acetyl donor used by acetyltransferases in this process. Among three known types of acetylation (*N*α-acetylation, *N*ε-acetylation, and *O*-acetylation), *N*ε-acetylation is widely observed across all eukaryotic organisms, occurring in essentially every cellular compartment. Lysine acetylation (*i.e.*, *N*ε-acetylation) is a key regulatory mechanism for critical epigenomic and metabolic processes, in addition to other major cellular functions. [13] Acetylation has an essential role in biological processes such as chromatin stabilization, protein–protein interaction, cell-cycle control, nuclear transport, and actin nucleation. Moreover, acetylated Lys is vital for cell development, and its dysregulation would lead to serious diseases such as cancer, aging, immune disorders, neurological diseases (Huntington's disease and Parkinson's disease) and cardiovascular diseases.[14] For example, *N*-acetylglutamate synthase catalyzes acetylation of L-glutamate, the first step in Arg biosynthesis.[15]

1.1.4. Ubiquitylation

Ubiquitylation is one of the most versatile and important PTM which can occur on all 20 amino acids. However, Lys residues are the most frequently observed. In ubiquitylation, a covalent bond is formed between the C-terminus of an active ubiquitin protein and the *N*ε of a Lys residue. Ubiquitylation is catalyzed by a series of enzymes. These are ubiquitin-activating (E1), ubiquitin-conjugating (E2) and ubiquitin ligase (E3) enzymes.[16]

Ubiquitination plays important roles in stem cell preservation and differentiation by regulation of the pluripotency.[17] Other important activities include proliferation, regulation of transcription, DNA repair, replication, and the control of signal transduction. Dysfunction in the ubiquitin pathway can lead to diverse diseases such as different cancers, metabolic syndromes, inflammatory disorders, type 2 diabetes, and neurodegenerative diseases.[18]

1.1.5. Methylation

Methylation is the addition of a methyl group to Lys or Arg residue of a protein.[19] Methylation takes place inside cell nucleus. Methylation plays an important role in histone modification, which can lead to gene activation or repression based on the residue that is methylated.

Methylation is associated with fine tuning of various biological processes ranging from transcriptional regulation to epigenetic silencing via heterochromatin assembly. Disruption of methyl modification can lead to various diseases such as cancer, mental retardation (Angelman syndrome), diabetes mellitus, and occlusive disease.[20]

1.2. Post-translational oxidation of proteins and enzymes

One of the major classes of posttranslational modification occurs by the oxidative modification of the target protein. Protein oxidation can occur as covalent changes either through direct interaction with reactive oxygen species or indirectly by reaction with secondary by-products of oxidative stress. Carbonyl derivatives of several amino acid residues (e.g., Arg, His, Lys, Pro, Thr and Cys) are well known biomarkers for protein oxidation and oxidative stress in aging and diseases.[21] Metal-catalyzed free-radical-based attack on His and Tyr residues leads to the formation of oxo-histidine[22] and dityrosine[23] respectively. The sulfhydryl moiety of Cys is highly prone to oxidative attack by several mechanisms, leading to the

formation of thiyl radicals, disulfide bonds, and other species.[24,25] Cysteine thiols can also be oxidized through progressively greater levels of oxygenation from the sulfenate ($R\text{-}SO^-$) to the sulfinate ($R\text{-}SO_2^-$) to the sulfonate ($R\text{-}SO_3^-$). As described further below, less extensively oxygenated Cys derivatives often have catalytic roles (*e.g.*, AhpC-catalyzed peroxide reduction).[26] Numerous other oxidative pathways lead to the oxidation of Met residues, leading to the formation of methionine sulfoxide.[27] Reaction of myeloperoxidase-derived HOCl with Tyr, Trp, Lys, and Met residues leads to the formation of chlorotyrosine[28], chloramines, in addition to methionine sulfoxide.[29–31]

Proteins have various, specific, and essential biological functions; their oxidation can result in structural changes, and consequently, positive or negative alteration in those functions.[32,33] For example, sulfur containing amino acids (Met and Cys) often undergo reversible redox modifications by ROS or RNS, leading to *S*-sulfenation (-S-OH), *S*-nitrosylation ((-S-NO),), S-glutathionylation ((protein-SSG),), and disulfide formation ((R-S-S-R),). These Cys-oxidation products have been demonstrated in the redox-based regulation of protein function[34] and, therefore, these modifications could serve as a means to protect critical Cys residues against irreversible oxidative inactivation under elevated oxidative stress.[35] Such changes in Cys oxidation/oxygenation state also form essential steps in enzyme catalytic cycles. The peroxidase activity of AhpC which relies on two active site Cys residues is an example of this. Indeed, Cys-SH/CysSH, Cys-S-S-Cys, and Cys-SOH/Cys-SH are all known intermediates of the AhpC catalytic cycle.[36] Irreversible mechanisms of protein oxidation are also frequently observed in enzymes containing Trp and Tyr residues which are each highly susceptible to oxidation by multiple mechanisms. The abundance of Tyr/Trp chain is observed in almost all enzyme classes and occurs with the greatest frequency in oxidoreductases and hydrolases.

The enrichment or greater abundance of Tyr and Trp residues in amino-acid compositions is observed with greatest frequency in oxidoreductases and hydrolases. It is proposed that these residues protect the protein from oxidative damage by serving as endogenous antioxidants.[37]

However, protein oxidation can be remarkably deleterious if the accumulation of oxidized products results in a free-radical reaction leading to diverse functional consequences, such as inhibition of ligand binding and enzyme catalytic activities, increased susceptibility to aggregation and proteolysis, increased or decreased uptake by cells, and altered immunogenicity. For example, oxidative damage of tyrosine often leads to generation of tyrosyl radicals. These radicals may dimerize, generating dityrosine, a process involved in cross linkage and protein aggregation.[38]

1.3. Preponderance of Oxidizable Residues: A Radical Approach for Protein-based Cofactor Biogenesis

As noted by Gray and Winkler,[39] oxidoreductase enzymes tend to have amino acid compositions that are enriched for the side chains that are oxidizable under biologically relevant conditions (*i.e.*, Cys, Met, Trp, and Tyr). In light of this, it is not surprising to find residues in these enzymes which undergo post-translational oxidative modification which target these residues. As alluded to above, such events have historically been interpreted as, at best, inconsequential or incidental, or far more likely, deleterious to enzyme function. Increasingly, however, it is understood that these residues and the modifications they endure are indispensable to sustained enzyme function. There are many proteins which capitalize on oxidative susceptibility of several amino acid residues.[40–42] The side chains of selected amino acids such as Cys, Met, Trp, and Tyr participate in a systematic electron (or electron-hole) transfer reactions.[43] Many redox enzymes[44–46] containing clusters of Tyr and Trp residues

generate high-potential reactive intermediates (*i.e.*, formal reduction potentials in the 1.0–1.25 V range). These residue clusters serve to transfer electron-holes through an enzyme's protein matrix. Thus, clusters of Tyr and Trp residues can acts as conduits for the migration of high-potential electron-holes in proteins, providing an antioxidant protection of enzyme widely followed in biological redox processes. For example, human SOD2, contains an above-average number of Tyr/Trp residues (9 Tyr, 6 Trp in each of four 199-residue polypeptides) and generally found in O_2-processing compartment of the cell, a vulnerable location for the exposure to ROS and RNS.

Moreover, numerous studies have suggested that the side chains of Tyr, and Trp perform a protective role by transporting oxidizing equivalents (or electron holes) away from the active site to the protein's surface, where they can be scavenged by the reductants generated/maintained by the cell. One prominent example of this class of enzyme is KatG which has Trp content of 4.1%, Tyr content of 3.7%, and Met content of 3.2%.[47] These values are substantially higher than those observed for typical proteins. This disproportionate representation of oxidizable residues helps achieve unique function of KatG by sacrificially oxidizing residues for relief from oxidative stress.

A preponderance of oxidizable amino acids residues is a common phenomenon among oxidoreductases where they can act as branched or linear electron transfer pathaways.[37] For example, yeast cytochrome *c* peroxidase (C*c*P) has unusually high Trp (2.38%) and Tyr (4.76%) content forming an extensive network connected to the heme. This feature bestows on the enzyme a high capacity for electron-hole hopping within its polypeptide, enables the oxidation of its large protein-based substrate, cytochrome *c*, despite the buried location of the ultimate electron donor (cytochrome *c*'s heme) and the ultimate electron acceptor (C*c*P's ferryl heme). More recently, it has been shown that in the absence of cytochrome *c* as an exogenous

electron donor, the C*c*P scaffold itself can act as a sacrificial antioxidant, delivering reducing equivalents from its own oxidizable amino acids, thus preserving critical active site components for future function.[48] Glutathione (GSH) also performs a protective function by inhibiting oxidation at most of these residues, consistent with the presence of protective chains that direct holes away from the heme toward surface residues for scavenging by GSH.[49]

1.4. Biogenesis of Protein Derived Cofactors

A protein-derived cofactor refers to a catalytic or redox-active site in a protein that is formed by irreversible, covalent, post-translational modification of one or more amino acid residues.[50] In some cases, protein-derived cofactors, once generated, work in concert with more typical extra-protein small-molecule/ion cofactors (*e.g.*, FMN, heme, etc.), in other cases a protein-derived cofactor circumvents the need for an exogenous cofactor. In all cases, as the name "cofactor" implies, the presence of a protein-derived version imparts catalytic function absent from the unmodified protein. The biogenesis of protein-derived cofactors can be autocatalytic or can be carried out by accessory proteins. The former is assisted only by the proper fold of the target protein to ensure that the participating components react and generate the correct products. It is not unusual for the autocatalytic process to proceed with the assistance of a metal-based cofactor. Requirement of an accessory protein is evidenced in pyruvoyl-dependent decarboxylases where the pyruvoyl cofactor is formed by the post-translational modification of an internal amino acid residue that occurs during cleavage of an inactive precursor protein. Enzymes such as aspartate decarboxylase[51], phosphatidylserine decarboxylases[52,53], *S*-adenosylmethionine decarboxyl-ase[54], and histidine decarboxylase[55] all follow a well-established reaction mechanism where the hydroxyl group of a specific Ser residue donates oxygen and part of it is transformed into the pyruvoyl group.[56]

Protein-derived cofactors are more commonly observed in metalloenzymes. As a class of enzymes, oxidoreductases are already well known to be heavily dependent on cofactors to carry out redox transformations which are beyond the scope of the 20+ standard amino acid side chains. There are very few examples of oxidoreductases that do not rely on one or more redox-active cofactors (*e.g.*, flavins, pyridine nucleotides, transition metal ions, multinuclear transition metal clusters, etc.) to accomplish their catalytic activity. The convergence these kinds of cofactors (especially transition-metal-based species) along with amino-acid compositions enriched with oxidizable amino acids (*i.e.*, Trp, Tyr, Cys, and Met) has given rise to the contribution of these kinds of residues to redox activity, frequently cycling between multiple oxidation states. Many well-characterized protein-derived cofactors are devised from post-translational modification of Tyr and Trp residues, mostly in the presence of a metal ion, usually copper or iron. There is an expanding list of metalloenzymes which contain covalently modified aromatic amino acids in their active sites. The His-Tyr cross link in cytochrome *c* oxidase, the His–Tyr crosslink in catalase HPII, a Tyr-Cys crosslink in galactose oxidase and cysteine dioxygenase are a few examples of this class of protein-derived cofactors. In addition, quinones are a major class of cofactors found in oxidases and dehydrogenases. Quinones are a class of organic compounds which undergo two, reversible, one-electron reductions to form the corresponding diphenol. Because of their redox abilities, quinones are associated with the enzymes that catalyze oxidations. Pyrroloquinoline quinone (PQQ), topa quinone (TPQ), tryptophan tryptophylquinone (TTQ), and lysine tyrosylquinone (LTQ) are some well-studied quinocofactors.

1.4.1. Quinone Cofactors

The first protein-derived cofactor to be identified was 2,4,5-trihydroxyphenylalanine quinone (TPQ) in 1990 from bovine serum amine oxidase (BSAO), which was initially

believed to be a covalently attached pyrroloquinoline quinone (PQQ) cofactor. Since then, three additional quinone cofactors have been reported, including both Tyr- and Trp-derived quinone species (Figure 1.1). The examples of Tyr-derived quinone cofactors are TPQ from copper-containing amine oxidase (CAO) and lysine tyrosylquinone (LTQ) of lysyl oxidase (LOX). [57] PQQ was first isolated from bacterial dehydrogenase[58] that catalyze the oxidation of alcohols and aldose sugars and are likely to influence mitochondriogenesis, reproduction, growth and aging.[59]It is an well appreciated part of quinone cofactors family and serves as a dehydrogenase cofactor, a free radical scavenger, and an amine oxidase catalyst[60,61] One interesting feature of the TPQ-dependent enzymes is the dual requirement of copper ion and molecular oxygen during its biosynthesis from a precursor Tyr.[62] While participating in the catalysis, copper also remains bound at the active site. The catalysis is mainly the stabilization of transient intermediates in the oxidative half-reaction.[63] Members of the CAO protein family contribute to the regulation of a myriad of complex processes in mammals due to the diversity in their substrates, their wide distribution throughout mammalian tissues (including the brain, blood plasma, kidneys, placenta, and throughout the cardiovascular and gastrointestinal systems), and changes in expression and activity during disease and throughout pregnancy.[64]

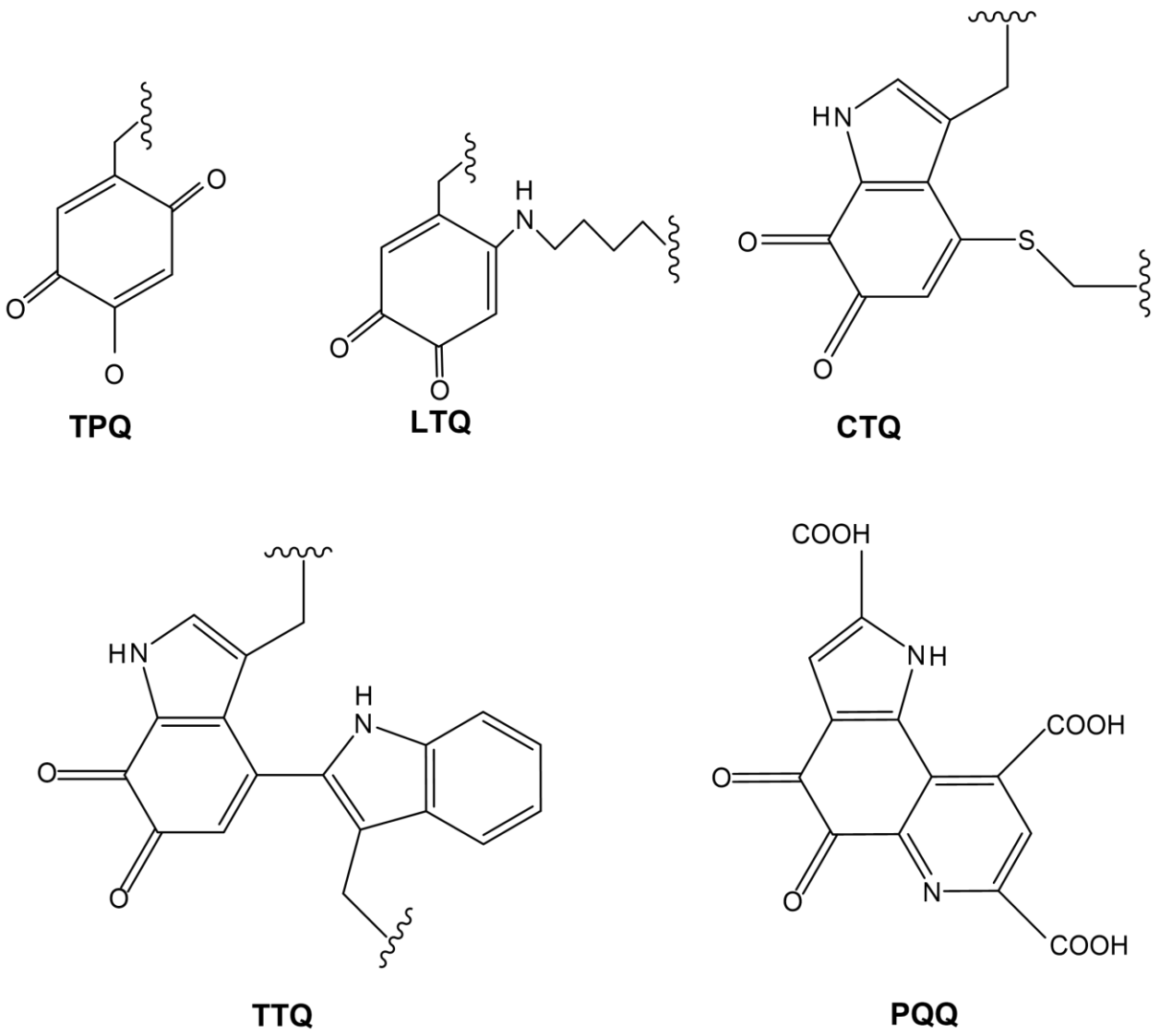

Figure 1.1. Structures of the established quinone cofactors, TPQ, LTQ, TTQ, CTQ, and PQQ.

The examples of some common Trp derived cofactors are tryptophan tryptophylquinone (TTQ) of methylamine dehydrogenase (MADH) and cysteine tryptophylquinone (CTQ) of quinohemoprotein amine dehydrogenase (QHNDH). In each of these, oxygen atoms have been inserted into the indole ring of a Trp side-chain that is cross-linked to the side-chain of another amino acid residue.[65] All TTQ-bearing enzymes are dehydrogenases. CTQ has been found in both dehydrogenases and oxidases.

While the biogenesis of the Tyr-derived cofactors occurs through an autocatalytic process requiring only Cu^{2+} and O_2,[66,67] the biogenesis of TTQ requires the action of four gene products, *mauD*, mau*E*, *mauF* and *mauG*, in addition to the two that encode for the alpha and beta subunits, *mauA* and *mauB*, of the MADH protein.[68,69] Among these, the MauG protein is a critical regulator of this biosynthesis mechanism and mediates the long-range electron transfer.[70] The role of TTQ is critical for maintaining both the catalytic and redox properties of MADH as it physically bridges active-site chemistry, the oxidative deamination of methylamine, and surface mediated electron transfer to amicyanin (a blue copper protein).

1.4.2. Cross-linked Amino Acids in Metalloproteins

1.4.2.1. Tyr-His Crosslink

Cytochrome *c* oxidase (C*c*O) is in the respiratory electron transport chain of the cell membrane (many prokaryotes) or mitochondrial inner membrane (eukaryotes) and catalyzes the transfer of four electrons, one each from four equivalents cytochrome *c* to molecular oxygen. Coupled to this redox activity, C*c*O also translocates four protons across the membrane in which it resides, typically *against* the H^+ concentration gradient.[71] One of the unique features of C*c*O is the presence of a covalent crosslink between a Tyr and one of the three His ligands which coordinate the Cu_B ion of the mononuclear Cu_B metal center. This Tyr-His crosslink is commonly observed in all three distinct families of heme-copper oxygen reductases.[72] The

integrity of the dinuclear center seemed to be essential for catalytic activity[73] until subsequent investigations prompted a revised mechanism from Pinakoulak, *et al*.[74] Site-directed mutagenesis studies showed that, C*c*O unable to establish the crosslink still retained the correct coordination of catalytic site (heme a_3-Cu_B) that allows O_2 binding to heme a_3. However, a slight perturbation was caused by the mutation, that ultimately affected the properties of the bound ligands to heme a_3.[74]

1.4.2.2. Tyr-Cys Crosslink

The presence of Tyr-His crosslink is an increasingly common post-translational modification observed in several kinds of proteins, such as copper-dependent galactose oxidase[75] and glyoxal oxidase[76], eukaryotic iron-dependent Cys dioxygenases[77], heme-containing sulfite reductase from *Mycobacterium tuberculosis*[78], and cytochrome *c* nitrite reductase from *Thioalkalivibrio nitratireducens*.[79] This crosslink is autocatalytically formed by covalent attachment of the Cε atom of Tyr and the Sγ atom of a nearby Cys. This modification has been shown to be important for the catalytic functions of the above mentioned enzymes.[78,80–82]

1.4.2.3. His–Cys Crosslink

The x-ray crystal structure of octopus hemocyanin,[83] plant catechol oxidase[84], and mushroom (*Agaricus bisporus*) tyrosinase[85] revealed that one of the His ligands coordinating the coppers of the di-nuclear Cu_A-Cu_B metal site is covalently cross-linked to a Cys *via* a thioether bond. The His-Cys cross-link plays significant roles in catalytic properties, where thioether substituent seems to perturb the electron-donating character of the Cu-coordinating imidazole of the His ligand. Site-directed mutagenesis of replacing Cys with Ala in tyrosinase caused its inactivation.[86]

1.4.2.4. Met-Tyr-Trp Crosslink

The heme-dependent bifunctional enzyme KatG contains a protein-based cofactor that has not been observed in any other enzyme. It is essential for imparting catalase activity to the type of active site that is otherwise only able to catalyze a peroxidase reaction. The cofactor consists of a Met and Trp residue covalently crosslinked through the aromatic ring of an intervening Tyr. All three residues of the adduct are strictly conserved across all KatGs, and the structure has been observed in crystal structures of KatG enzymes from multiple species, including *M. tuberculosis*,[87] *Haloarcula marismortui*,[88] *Burkholderia pseudomallei*,[89] and *Magnaporthe grisea*.[90] KatG is the only catalase-active member of the peroxidase-catalase superfamily.[91] Aside from the Met-Tyr-Trp crosslink, the identity and position of key residues of the KatG active site are indistinguishable from its fellow members of class I of the super family. Site-directed mutagenesis studies demonstrated that the cross-link is essential for the catalatic activity, but peroxidase activity remains unchanged in its absence.[92–96]

1.5. Reactive Oxygen Species (ROS) in the Interface of Host-Pathogen Interaction

The partial reduction of molecular oxygen (*i.e.*, falling short of the complete [four-electron] reduction to H_2O) (Scheme 1.3) forms the core of compounds known as reactive oxygen species (ROS). Subsequent reactions involving this core group of ROS can generate others. ROS can either be generated exogenously or intracellularly during a wide range of biochemical and physiological processes and involves many enzymatic and non-enzymatic reactions (Figure 1.2). The category, ROS, includes both radical (*e.g.*, superoxide anion [$O_2^{\bullet-}$], hydroxyl radical [$^{\bullet}OH$], and nitric oxide [NO]) and non-radical (hydrogen peroxide [H_2O_2], hypochlorous acid [HOCl], and peroxynitrite [$ONOO^-$]) species. Several different enzymes have been implicated in the generation of ROS.

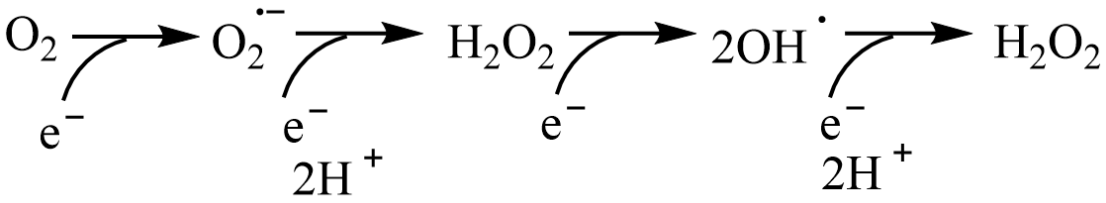

Scheme 1.3. Partial reduction of molecular oxygen.

The core ROS shown in Scheme 1.3 are often the unintended and deleterious byproducts of oxidative metabolism (*e.g.*, aerobic ATP production). However, they are also critical components of biological defensive strategies. ROS can cause extensive damage to biological molecules including lipids, protein, DNA and RNA. This obvious ROS toxicity is certainly beneficial in oxidative killing of engulfed microbial pathogens in specialized immune cells, such as neutrophils[97] or macrophages[98]. The classic example is the destruction by of phagocytized microorganisms when superoxide, produced by NADPH oxidase 2 (NOX2) is converted first to H_2O_2 which is then used by myeloperoxidase to oxidize Cl- into the potent cytotoxic molecule hypochlorous acid.[99] In addition to the ability of ROS to serve as an antimicrobial repertoire of macrophages, they can also trigger pathogen defense of phagocytes by various non-oxidative means, such as autophagy, receptor signaling, extracellular traps formation and instructing lymphocyte responses.[100] There is also extensive evidence to suggest that ROS serve as critical signaling molecules in regulation of biological and physiological processes such as cell growth, vasoconstriction, signal transduction, proliferation, and survival.[101–103] ROS play important roles in synaptic plasticity, immune responses and immunometabolism, cardiac muscle function and oxygen sensing. Hydrogen peroxide is an important regulator of several kinase-mediated signaling pathways.[104]

However, ROS production must be tightly regulated in a spatial and temporal manner if it is to be applied to the benefit of host physiology, and of course, in all other circumstances,

ROS production must be limited to the greatest extent possible. The uncontrolled production of ROS can result in oxidative damage to biomolecules such as lipids, proteins, and DNA. This process can provoke damage to multiple cellular organelles and processes, which can ultimately disrupt normal physiology. DNA, when exposed to ROS, can be oxidized to 8-oxoguanine and establish a bond with cystine and adenine. This mutation can occur in both nuclear and mitochondrial DNA and can give rise to double stranded breaks (DSBs) in the DNA, leading to mutations and neoplastic transformation in many organisms.[105] Proteins are also vulnerable target for ROS. Amino acid side chains and backbones and particularly thiol-containing Cys and Met residues are susceptible to oxidation by ROS. This can result in structural changes to the protein that may lead to loss of protein function and of protease inhibitor activity, protein aggregation, or be used for ROS mediated signaling.[106] Additionally, the exposure of lipids to ROS results in lipid peroxidation which gives rise to cell membrane damage and generates reactive by-products which can further damage the cell.[107] Figure 1.3 represents the potential damage caused by ROS. Biomolecular damage of the type caused by ROS has been implicated in aging as well as the development and progression of debilitating chronic (even terminal) diseases, including cancer, emphysema, diabetes, coronary disease, Parkinson's disease, Alzheimer's disease, and other neurodegenerative disorders.[108–111]

Therefore, it is well understood that a delicate balance between ROS production and ROS elimination is essential. Maintaining a homeostatic levels of ROS as a result of this balance is important both for preventing oxidative damage as well as maintaining an appropriate redox environment for normal signaling pathways within the cell. There are many enzymatic and nonenzymatic antioxidant systems in cells that regulate the concentration of ROS. One of the landmark discoveries of such enzymatic antioxidant is superoxide dismutase (SOD). Over the years, new examples of enzymatic antioxidant systems have emerged, including catalase, NADH peroxidase, ascorbate peroxidase (APX), guaiacol peroxidase

(GPX), glutathione reductase (GR), etc. Examples of nonenzymatic antioxidants include ascorbic acid (AA), reduced glutathione (GSH), α-tocopherol, carotenoids, flavonoids, and the osmolyte Pro. Together, these components work hand in hand to scavenge ROS. For example, superoxide dismutase converts superoxide into hydrogen peroxide which is in turn degraded by catalase or by glutathione peroxidase.

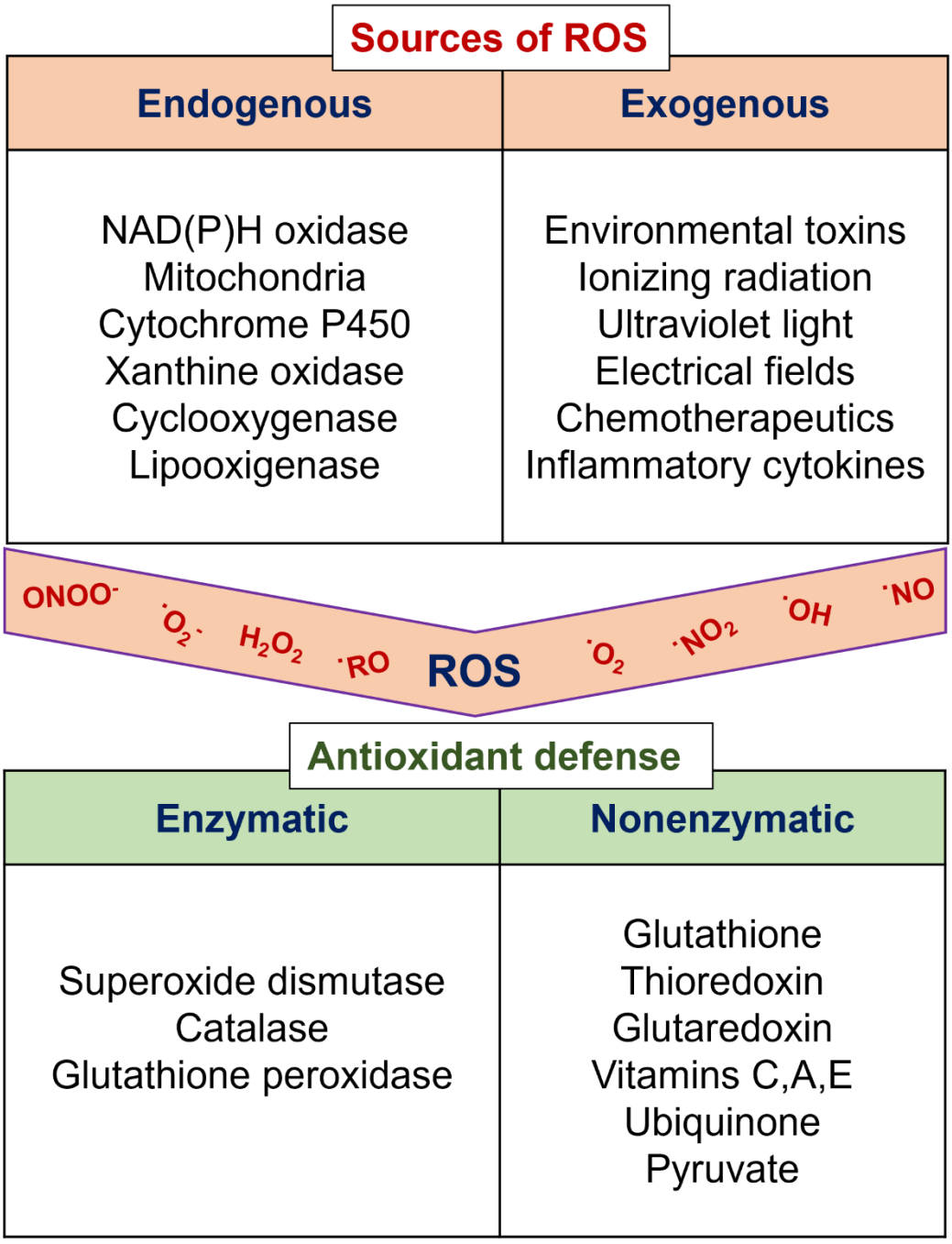

Figure 1.2. Sources of ROS and the intracellular antioxidative defense system.

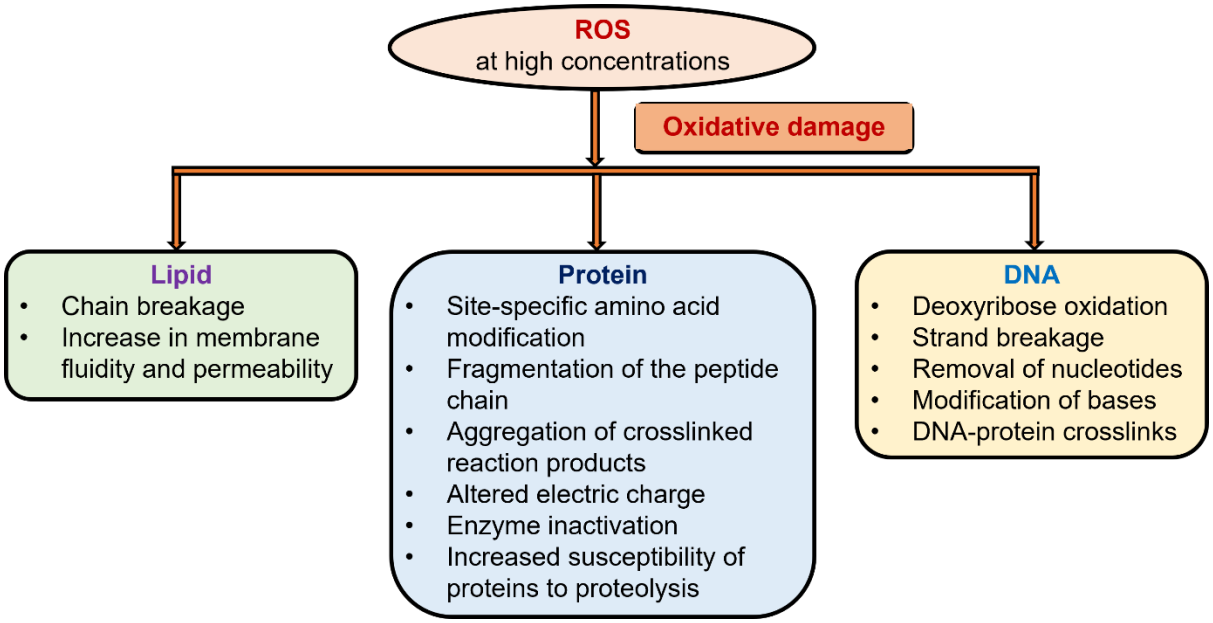

Figure 1.3. Reactive oxygen species (ROS) induced oxidative damage to lipids, proteins, and DNA.

1.6. Microbial Defense against ROS

All organisms that survive in an aerobic environment must have multiple lines of defense against the uncontrolled production and accumulation of ROS. As a result, mechanisms for the enzymatic disposal of ROS are universally distributed organisms that come in contact with and or use O_2 metabolically. However, it should also be noted that a typical response of higher eukaryotes (from plants to mammals) to combat pathogenic invasion is to produce high concentrations of hydrogen peroxide (H_2O_2) and other highly destructive oxidants as a central component of their defense against these pathogens. Correspondingly, a common pattern observed among a wide variety of bacterial and fungal pathogens is that they have evolved a diverse suite of enzymes to mitigate cellular damage from reactive oxygen species (ROS) that are distinct and/or exceed in capacity those deployed by their nonpathogenic counterparts.

A varying distribution of ROS defense mechanisms is observed across the bacterial and fungal domains. The universality of ROS defenses across the bacterial domain was recently assessed by using available genomic data, which substantiated the distribution of 26 known ROS defense enzymes across a wide range of bacterial phyla.[112] Among these, there are some opportunistic "potential pathogens" which capitalize on host derived ROS in order to enhance survival and colonization in their target host cells.[113] One of the prominent example of this class of pathogen is *Mycobacterium tuberculosis (Mtb),* a facultative intracellular bacterium which has evolved sophisticated defense mechanisms to allow it to survive inside the highly oxidative environment of phagocytic cells.[114,115] Examples of such defense systems include *katG* (encoding a catalase-peroxidase), and *ahpC* (encoding a homolog of alkyl hydroperoxide reductase). The products of these two genes are important in protection against oxidative stress, specifically peroxides, and their importance and essentiality are amplified in macrophage parasitism context of pathogenic *Mycobacteria*.[116–120] Catalase-peroxidase (KatG) is prominent

among the H_2O_2 defensive enzymes and is a single catalase-peroxidase, encoded by the *katG* gene in *Mtb.*[121] In addition to KatG, *Mtb* also uses SOD[122], thioredoxin and peroxiredoxin as antioxidant enzymes. Intracellular redox homeostasis is maintained by mycobacterial redox buffers mycothiol and ergothioneine which provide a barrier of protection against oxidative stress.[123,124] As an intracellular pathogen, *Mtb* combats up to millimolar concentration of H_2O_2 using a highly delicate defense system.[125,126] Moreover, KatG is one of the two prominent catalase active enzyme of *Mtb* and well recognized for conferring protection against H_2O_2-mediated damage even in the absence of adequate catalase and peroxidase activities, thus promoting survival of the organism in the environment of the phagocyte oxidative burst.[127]

Another common source of ROS is NADPH oxidase complexes typically associated with rapid respiratory burst mechanisms of professional phagocytic cells and carry out the electron transferring reaction from NADPH to molecular oxygen (O_2) in the membranes of phagosomes, endosomes, and the cell membrane.[128] Due to its protective role as an innate immunity component, it is a logical target for microbial intervention. Many bacteria can interfere with the accumulation of ROS molecules by preventing NADPH oxidase assembly. *Francisella tularensis, Anaplasma phagocytophilum, A. phagocytophilum* are few examples of bacteria which can escape neutrophil phagosomes and directly prevent NADPH oxidase assembly during intracellular infection.[129] There are other pathogens like *Legionella pneumophila* and *Coxiella burnetii*, which can inhibit the recruitment of NADPH oxidase subunits, and thus, can limit respiratory burst within infected neutrophils.[130,131]

Extracellular microorganism, *Burkholderia cenocepacia,* known for causing Cystic Fibrosis, contributes to the persistence of infection by altering intracellular ROS production. These bacteria have been demonstrated to inhibit ROS production in infected neutrophils, primarily through exopolysaccharide formation.[132] *Neisseria gonorrhoeae* is known to

suppress oxidative bursts in neutrophils.[133] Opportunistic fungal pathogen, *Candida albicans, Aspergillus fumigatus* have the ability to suppress ROS production in host immune cells, and thereby limit the ROS production in neutrophils.[134,135]

Overall, a large amount of evidence suggests that a numerous pathogens have adapted complex yet converging molecular strategies to limit or exacerbate ROS formation in order to subvert immune defenses and support self-survival and long-term carriage in their target host cells.

1.7. Physiological Importance of Catalase-peroxidase (KatG): Host-pathogen Interactions and Antibiotic Activation

KatG plays an integral role in the pathogenesis of the disease tuberculosis by facilitating the bacterial survival. Because of this, KatG protein has long been implicated as virulence factor that detoxifies antibacterial reactive oxygen compounds generated by host macrophages to prevent pathogenic invasion.[136]

In addition to being a virulence determinant, KatG also plays an important role in antitubercular therapy by activating the prodrug isoniazid (*i.e.*, isonicotinic acid hydrazide, or INH), the primary first-line antibiotic used against *M. tuberculosis* infections.[137,138] INH activation is largely impacted by mutation in *katG* gene, causing elimination or reduction of its catalase-peroxidase activity, promoting INH resistance in the organism.

A better understanding of the mechanisms of activation and action of the drugs prescribed to treat tuberculosis could lead to better drug design and elimination of drug resistant TB strains. The pro-drug isoniazid enters *Mycobacterium tuberculosis* (*Mtb*) via passive diffusion and is activated by KatG via oxidation to the isonicotinoyl acyl radical (Figure 1.4).[139] That radical then combines with NADH to form an IN-NADH adduct. This adduct then binds

and obstructs the active site of another enzyme, enoyl acyl carrier protein (ACP) reductase (InhA), which normally uses NADH as the reductant for the *trans*$^{\Delta 2}$ double bond of enoyl-ACP to generate the fully saturated derivative. [140] The IN-NADH adduct produces conformational changes in InhA which render it inactive. InhA is essential for mycolic acid synthesis (Figure 1.5). Mycolic acids are the part of cell walls in *Mycobacteria* which render them less susceptible to attack and cause the bacteria to be classified as "acid fast" (Figure 1.6). When those mycolic acids are no longer able to be produced, the bacteria cannot survive.

The majority of the isoniazid-resistant strains of *Mtb* (~70%)[141,142] have a mutation that selectively eliminates isoniazid activation activity or more extensively disrupts the KatG structure or a deletion of the *katG* gene which eliminates its expression entirely.[143] Decreased activation of isoniazid results in decreased bactericidal activity due to attenuated IN-NADH adduct formation. A strain that is not resistant to INH usually has a minimum inhibitory concentration (MIC) of less than 0.02 to 0.05 μg/mL INH,[143] whereas "highly resistant" *Mtb* strains exceed this range by at least 20-fold (1μg/mL MIC). Remarkably, a substantial portion of INH resistance in *Mtb* arises from the addition of a single methyl group to the >80 kD structure of the KatG monomer. In fact, over 40% of all clinical INH resistant strains[144] and 61.7% of "highly resistant" strains[145] contain a mutation in the S315 codon of the *katG* gene, replacing a serine with a threonine. This is widely considered to be the most common resistance mutation.[144]

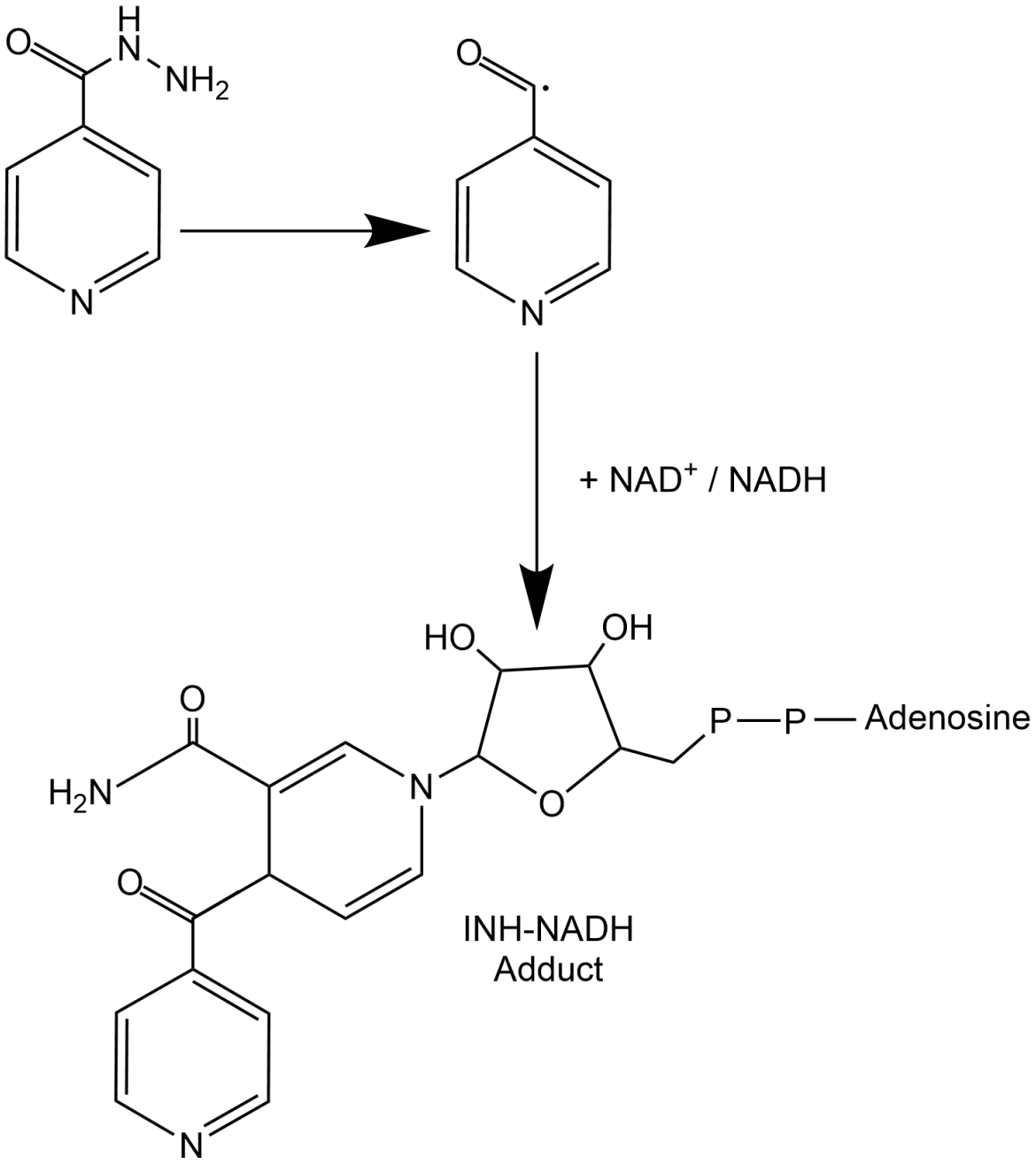

Figure 1.4. Schematic representation of INH-NAD adduct formation as catalyzed by KatG via a putative isonicotinoyl radical.

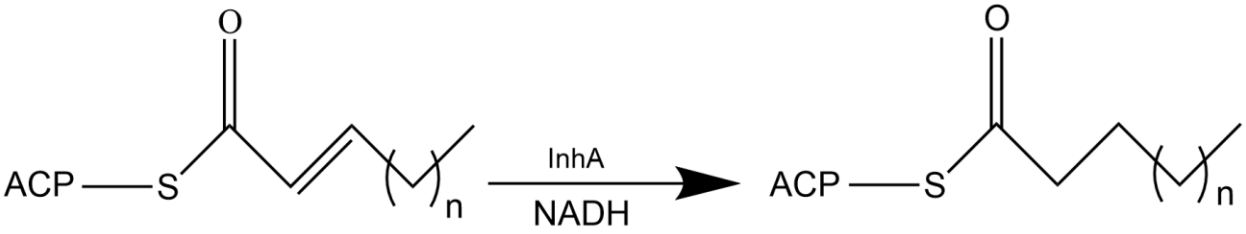

Figure 1.5. InhA reduction of the *trans*$^{\Delta 2}$ double bond of an enoyl-ACP substrate. NADH is the hydride donor.

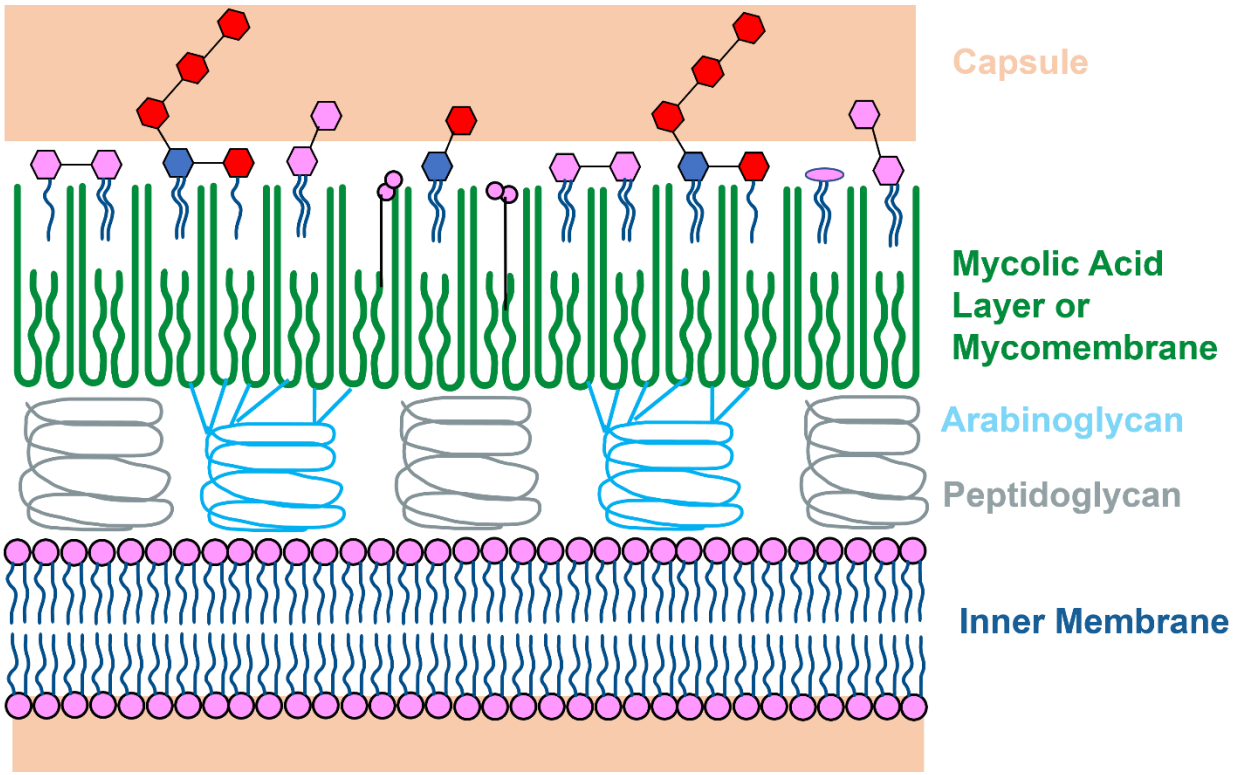

Figure 1.6. Schematic representation of mycobacterial cellular assembly.

1.8. KatG Structure and Mechanism

All aerobic organisms, require protection against the damaging effects of reactive oxygen species. *Mtb* KatG is a component of the oxidative defense system of the bacteria and functions primarily as a catalase to remove hydrogen peroxide. Such catalase activity is regarded as one of the virulence factors for *M. tuberculosis*[146], because this reaction detoxifies reactive oxygen species generated by macrophages and facilitates bacterium survival. On the other hand, KatG functions as a peroxidase, oxidizing INH to its active form. KatG is thought to be the only enzyme in *Mtb* that is capable of generating isoniazid susceptibility.[95] It has been shown that most INH resistance in clinical isolates results from blocking prodrug activation through mutation of the *katG* gene that alters or diminishes KatG activity, most often exclusively INH activation rather than catalase or peroxidase activities.[143]

Based on amino acid sequence similarity, KatGs have been classified as members of class I of the peroxidase-catalase superfamily.[147] Formerly known as the plant peroxidase superfamily, peroxidase-catalases include peroxidases of prokaryotic origin, secreted fungal and secreted plant peroxidases. The superfamily is subdivided into three families, Class I, Class II, and Class III,[148] and all members of the three classes catalyze the reduction of H_2O_2. The enzymes which occupy class I include peroxidases of prokaryotic origin (primarily KatGs) as well as ascorbate peroxidases and cytochrome *c* peroxidase. Class II peroxidases include the secretory fungal peroxidases such as lignin peroxidase and manganese peroxidase. Class III peroxidases are the plant peroxidases that are targeted for the secretory pathways. These include horseradish peroxidase (HRP), soybean, and guaiacol peroxidases.

Despite sharing substantial sequence identity with the other class I members, there are several structural features which set KatG apart from the other enzymes in the group. First, there are three additional insertions in the N-terminal domain of KatG which other class I

peroxidases do not possess.[149] The first, named large loop 1 (LL1) is highly variable in length (39 – 70 residues).[150] In *Mtb* KatG, LL1 covers from Trp36 to Ala60. Elimination of LL1 from KatG by deletion mutagenesis produces an enzyme with no catalase activity and peroxidase activity enhanced by nearly 10-fold.[92] The interhelical insertion known as large loop 2 (LL2) is nearly invariant in its length (34 – 35 amino acids). In *Mtb* KatG covers from Pro194 to Asn231. This structure appears to form an essential interaction with the C-terminal domain of a second KatG subunit. Without this interaction, active site structure is subtly altered diminishing reactivity of the Fe^{III} state with H_2O_2.[150] Interestingly, together both LL1 and LL2 contribute to an active site access channel that is substantially more constricted than the other members of the peroxidase-catalase superfamily.[151] A third insertion known as large loop 3 (LL3). In *Mtb* KatG this loop spans from Pro280 to Ile313.[150] To date, the function of LL3 is unexplored and unknown.

KatGs are homodimeric proteins; this is not particularly unique among class I enzymes. However, in KatG the inter-subunit interface involves a substantially greater surface area because the KatG monomer is composed of two comparably-sized domains, making it roughly twice as large as a typical class I peroxidase (*e.g.*, C*c*P or APX). Interestingly, the two domains of KatG each bear the canonical 10-helix structure of a "plant peroxidase". Accordingly, this feature has been ascribed to a gene-duplication event.[151] The KatG N-terminal domain contains the active site where heme binds.[152] The C-terminal domain has lost its heme and has a much lower homology to cytochrome *c* peroxidase. Nevertheless, the C-terminal domain has been shown to be essential for KatG to maintain the proper coordination environment for the heme cofactor in the active site some 30 Å away in the N-terminal domain.[153,154]

In contrast to all other members of the peroxidase-catalase superfamily, KatGs exhibit a robust catalase activity whose kinetic parameters match well those displayed by

monofunctional catalases. Interestingly, KatG has essentially no sequence or structural similarity to typical monofunctional catalases.[155]Although the large-loop structures and C-terminal domain of KatG impact its catalase function, to understand the origin of its unique catalytic capabilities, one must examine the active site more closely.

1.8.1. The KatG Active Site

The KatG active site uses heme *b* as its prosthetic group (Figure 1.7).[156] The two distinct amino acid triads Arg104/Trp107/His108* and His270/Trp321/Asp381 occupy the active site pockets on the distal and proximal sides of the heme, respectively. All six residues are strictly conserved in class I enzymes, and four of the six (excluding the tryptophans) are strictly conserved across the entire peroxidase-catalase superfamily.[148]

On the proximal side, the His (His270) is coordinated to the heme cofactor as the protein-supplied fifth ligand; it is an H-bond donor to the carboxylate side chain of the nearby Asp381. This H-bond imparts a substantial imidazolate character to the ligand. Across the peroxidase-catalase superfamily, this lowers the reduction potential of the heme iron which serves to stabilize the higher oxidation states (*e.g.*, Fe^{IV}=O) associated with catalysis. Asp381 is also an H-bond acceptor for the indole (NH) of the proximal Trp residue (Trp 321).

On the distal side, the His (His108) serves as a general base to facilitate the deprotonation of H_2O_2 and assist in the formation of the compound I intermediate, the first step in the enzyme's catalytic cycles.[157] The distal Arg (Arg104) is critical for polarizing the breaking O-O bond of H_2O_2 ensuring its heterolytic cleavage, a feature essential for forming the compound I intermediate. Specifically, electrostatic interactions between the positive charge of its side chain and the developing negative charge on the distal oxygen of the bound

* Unless otherwise indicated, amino acid numbering corresponds to KatG from *M. tuberculosis*.

H_2O_2 favors heterolytic bond scission as opposed to a homolytic scission mechanism .[157] Two conserved residues, Asp137 and Ser315, help regulate access to the heme's distal side. It has been proposed that these residues orient water dipoles in the active site and active-site access channel.[158,159] Notably, Asp137 is required for catalase activity but not peroxidase activity. In addition, the location Asp137 is in favorable interaction between the carboxylic acid side chain and the pyridinyl moiety of INH, thereby considered as a key residue in INH binding.[158]

In addition to these peroxidase-typical structural features, active site of KatG possess some unusual structural features not seen in peroxidases. The most striking of these features is the covalent cross-linking of the side chains of Met255, Tyr229 and Trp107 (Figure 1.7) to form the so-called MYW adduct. In addition to these three residues, Arg418, which reversibly forms an ion-pairing association with the phenolate oxygen of Tyr229, acts as a molecular switch to modulate catalase activity. The MYW adduct and the arginine switch are discussed further below.

There is no question that KatG is built on a peroxidase scaffold and bears a peroxidase active site. Despite these overarching components to its structure, KatG exhibits a catalase activity that none of the other members of its superfamily possess. How this occurs has been a question of considerable debate over many years; it remains unresolved. Catalases are universally poor peroxidases. Likewise, with this one exception in KatG, peroxidases are universally poor catalases. Unification of these two segregated properties is seen nowhere else in nature, but KatG.[160,161] In this study, this question has been addressed from a unique structural point of view which is a key contributor to the unique catalase mechanism of KatG.

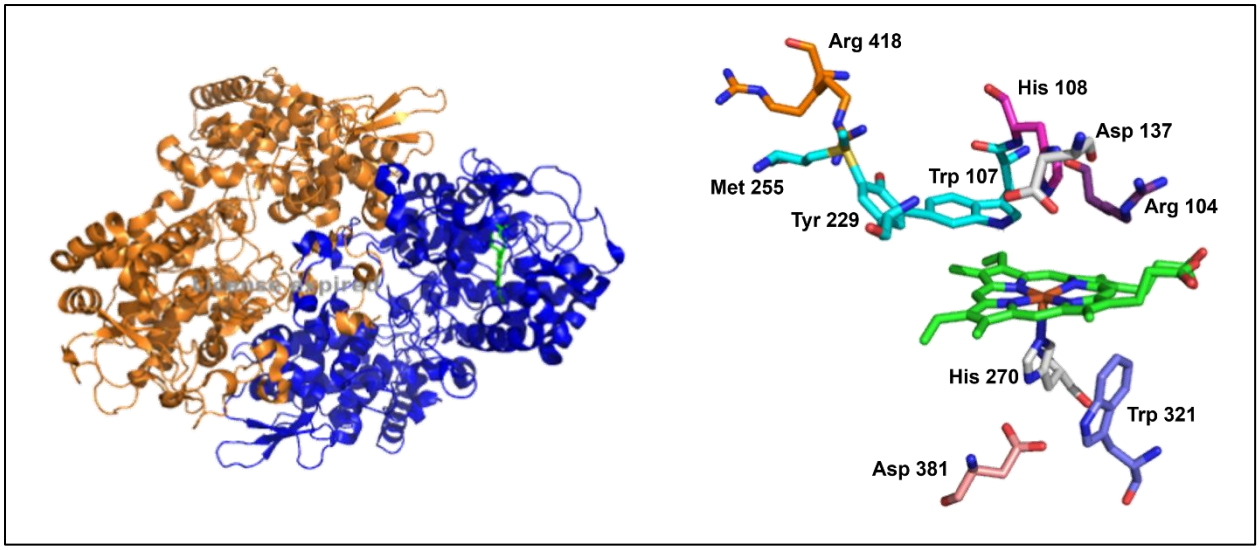

Figure 1.7. Detailed view of active site residues of catalase-peroxidase from *Mycobacterium tuberculosis.* The distal active residues Met255, Tyr229 and Trp107 are covalently linked to form the MYW adduct. Two conserved amino acid triad (His108, Arg104 and Asp137) and His270, Trp321, and Asp381 are depicted. The Figure was constructed using the coordinates deposited in the Protein Data Bank (accession code 2CCA).

1.8.2. The Covalent Met255-Tyr229-Trp107 (MYW) Crosslink

The first crystal structure solved for a KatG was for the enzyme from *Haloarcula marismortui* (1ITK). It revealed the presence of a novel covalent crosslink between the side chains of three amino acids in the distal cavity of the active site (a Met, a Tyr, and a Trp). Structures solved for KatG from *M. tuberculosis* (1SJ2)[156] [88], *Burkholderia pseudomallei* (1MWV)[162] and *Synechococcus* PCC 7942 (1UB2)[163] have since all showed the same structure.[156] Mass spectrometric analyses of trypsinized KatGs from several species revealed that the adduct is present in KatG in solution and not simply an artifact of X-ray radiation.[89,91,164] The covalent adduct joins Met255 to Tyr229 and Tyr229 to Trp107. Replacement of either Trp107 or Tyr229 by site-directed mutagenesis prevents formation of the crosslink, whereas exchange of Met255 still allows autocatalytic covalent bond formation between Trp107 and Tyr229.[165] Nevertheless, KatG variants targeting any of the three residues possess little if any catalase activity. Without exception, these same variants either retain peroxidase activity comparable to the wild-type enzyme, or in numerous cases, exhibit peroxidase activity that substantially exceeds the unmodified enzyme.[94,95,149,157] Moreover, a similar cross-link has not been reported and the distal Tyr and Met are not conserved in monofunctional peroxidases. This suggests that the full three-amino acid crosslinked structure is required for catalatic activity but not for peroxidatic activity, providing a clear explanation for why the apparently closely related plant peroxidases have little or no catalase activity.

1.8.3. Conformationally Dynamic Arg418 Residue

A strictly conserved arginine residue (R418 by *Mtb* KatG numbering) is a critical contributor to KatG function despite its substantial distance from the heme (~20Å). The function of this arginine is not fully understood. The side chain of Arg418 can adopt two conformations.[166] At pH values above an apparent pK_a of 6.5, the guanidinium moiety of the

Arg418 residue forms a close association with tyrosyl phenoxide anion of Tyr229 of the MYW adduct. This is the so-called "in" or "Y" conformation.[167] At pH values below the apparent pK_a of 6.5, the guanidium moiety is oriented away from the adduct to a region containing two other Arg residues and making contact with a solvent-accessible groove between the KatG N- and C-terminal domains. Critically, in the so-called "out" or "R" conformation, Arg418 has no association with Tyr229 or any other part of the MYW adduct. The conformationally dynamic Arg418 side-chain equilibrium can be demonstrated as a function of its sensitivity to pH. At a pH, equal to pK_a of the phenolate oxygen of $_{MYW}$Tyr, "*out"* and "*in"* conformations become equally distributed; This coincides with and is purported to be a condition producing optimum catalase activity of KatG with respect to the value of k_{cat}. The pH dependence of the Arg418 side-chain conformation coupled with its key role in catalase activity suggested that it can act as a molecular switch reversibly interacting with the MYW adduct to inductively alter heme reactivity.[168] Therefore, striking conclusion is that the conformation of the side-chain of Arg 418 influence the electronic interaction and must be modulated through MYW adduct.[167]

1.9. KatG Catalytic Mechanisms

1.9.1. The Unique Catalase Mechanism of KatG

KatG catalatic mechanism does not truly follow conventional catalase and peroxidase mechanism. They are unique in modulating substantial catalase and peroxidase activity from a single enzyme. Moreover, KatG unique MYW cofactor is not found in monofunctional catalases or peroxidases. Both the heme and the MYW cofactors are mutually dependent on one another to support efficient H_2O_2 dismutation. However, the MYW cofactor is an essential component only for catalase reaction but not for peroxidase reaction, evidenced by site-directed mutagenesis, spectroscopic and kinetic studies.[96,169] The proposed catalatic mechanism states that the covalent adduct redox cycles between a fully covalent (reduced) and a free-radical

(oxidized) state. Despite the lack of similarity in the sequence and structure between catalase-peroxidases and monofunctional catalases, KatG share a common catalatic reaction for the compound I formation. At this point, KatG behaves antithetical to canonical, monofunctional catalases and peroxidases and undergoes an internal electron transfer process to form an oxo-iron (IV) and the adduct radical ($MYW^{\bullet+}$) by rapidly quenching the porphyryl radical formed in compound I.[170,171] This Fe^{IV}=O ($MYW^{\bullet+}$) intermediate is basically compound II associated with a protein radical, and hence the name given compound I^{*}. Further, compound I^{*} reacts with the second equivalent of H_2O_2 in a non-scrambling mechanism to directly form compound III^{*}, a di-oxy heme intermediate [Fe^{II}-O_2], which is isoelectronic with superoxide bound to the ferric heme [Fe^{III}-$O_2^{\bullet-}$].[172] Monofunctional peroxidases have negligible catalase activity and are trapped in this compound III state in the presence of H_2O_2 only.[172] However, in KatG, the MYW adduct radical initiates the superoxyferric complex (*i.e.*, compound III*) and thereby keeping an oxidation equivalent very close to superoxide in the [Fe^{III}-$O_2^{\bullet-}$] complex[171,173,174], which is the dominating electronic structure during KatG turnover.[175] Following this, compound III* rapidly returns to the ferric resting state, releasing triplet oxygen (Figure 1.8).[170]

Previous studies have unequivocally assigned the MYW adduct radical (narrow-doublet) as the tyrosyl radical located on the MYW covalent adduct by applying the techniques such as site-directed mutagenesis of all 21 Tyr residues of KatG, deuterium labeling of the β-methylene hydrogen and 3,5-ring hydrogens of the adduct Tyr, in combination with rapid freeze-quench and manual quench EPR.[171,176] The narrow doublet is considered as a signature signal that appears within milliseconds when KatG reacts with steady-state concentrations of H_2O_2. The presence of narrow-doublet was observed in all Tyr mutants except the one located on the MYW adduct (Tyr229). Further, deuterium labeling of the β-methylene protons collapsed the narrow-doublet to a singlet radical. Interestingly, deuteration of the 3,5-ring protons still produced the narrow-doublet radical like wild-type KatG. The collapse of MYW

narrow-doublet radical upon β-methylene hydrogen deuteration and the retention of narrow-doublet radical upon 3,5-ring hydrogen deuteration supports that the radical was tyrosyl based.[171] KatG variants targeting the covalent adduct lack the ability to produce the unique MYW adduct radical which give rise to the narrow-doublet signal, consequently losing catalytic activity and transformed to a typical peroxidase.

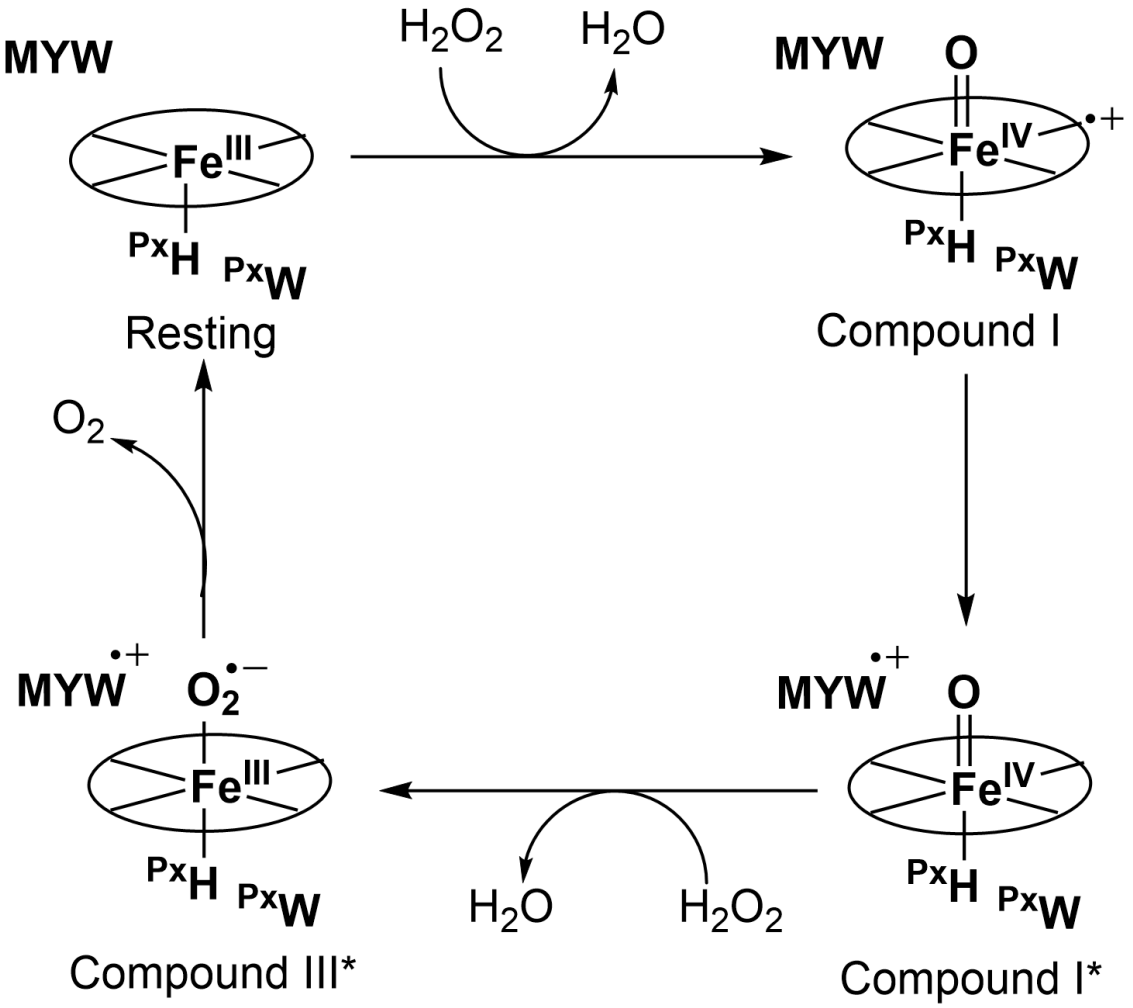

Figure 1.8. Proposed mechanism of KatG catalatic turnover. The superscripted *Px* designates residues that are on the heme's *proximal* side. By convention, the proximal side of the heme is the same as that occupied by a protein-supplied fifth ligand to the heme, a histidine (^{Px}H) in the case of KatG.

1.9.2. The Through-protein Radical Mechanism of KatG Peroxidase Activity

KatG has a long narrow access channel produced by LL1 and LL2 which restricts the entry of large molecules like most aromatic peroxidatic electron donors (*e.g.*, ABTS). Due to the restricted access, only small peroxidase substrates (H_2O_2, I^- and peracetic acid) can enter the main entrance channel. This structural restriction is well aligned with the monofunctional catalases which are basically all poor peroxidases in nature. However, KatG is a strong peroxidase. Indeed, it operates in a mechanism that can defeat the barrier imposed by the narrow access channel. KatG, being enriched in the oxidizable amino acids (high percentage of Met/Tyr/Trp content) is capable of moving oxidizing equivalents from the heme site to the protein surface where the donors can be oxidized. This is how the peroxidase activity is retained by through protein electron transfer which allow oxidizing equivalents to be directed toward oxidation of H_2O_2 to O_2.

Although naturally occurring peroxidase substrate for KatG is unknown, this enzyme can still oxidize typical artificial peroxidase substrates like *o*-dianisidine, guaiacol or ABTS. The pH profile of the peroxidase activity of KatG has its maximum around pH 5.5 independent of the nature of most donors. The peroxidatic reaction of KatG undergo series of redox reactions after forming compound I (Fe^{IV}=O [porphyrin]$^{\bullet+}$) as the first reaction intermediate. After that, it returns to its ferric state by two one-electron reduction steps, first forming compound II, a ferryl-oxo (Fe^{IV}=O) complex where the porphyrin cation radical has been reduced. Subsequent reduction of compound II returns the enzyme to its ferric form. In both steps, one equivalent of an exogenous electron donor is oxidized to its corresponding free-radical state (Figure 1.9). The peroxidase activity of bifunctional KatG is not as robust as observed for some representatives of its superfamily (*e.g.*, HRP). Nevertheless, it corresponds to what is observed for other superfamily members (*e.g.*, lignin peroxidase). Interestingly, it

has been shown that lignin peroxidase also relies on the radical transfer between the enzyme's active site and a distant Trp residue for peroxidase activity. This may well account for slower peroxidase reaction rates for these enzymes.

In physiological conditions it is well-known that KatG from *Mycobacterium tuberculosis* can activate the anti-tuberculosis drug isoniazid[159] but otherwise, the physiological function of these enzymes remain unknown. Due to the restricted access, only small peroxidase substrates can enter the main entrance channel. A second access route, found in monofunctional peroxidases, approximately in the plane of the heme, is blocked by the KatG-typical large loop structural features.

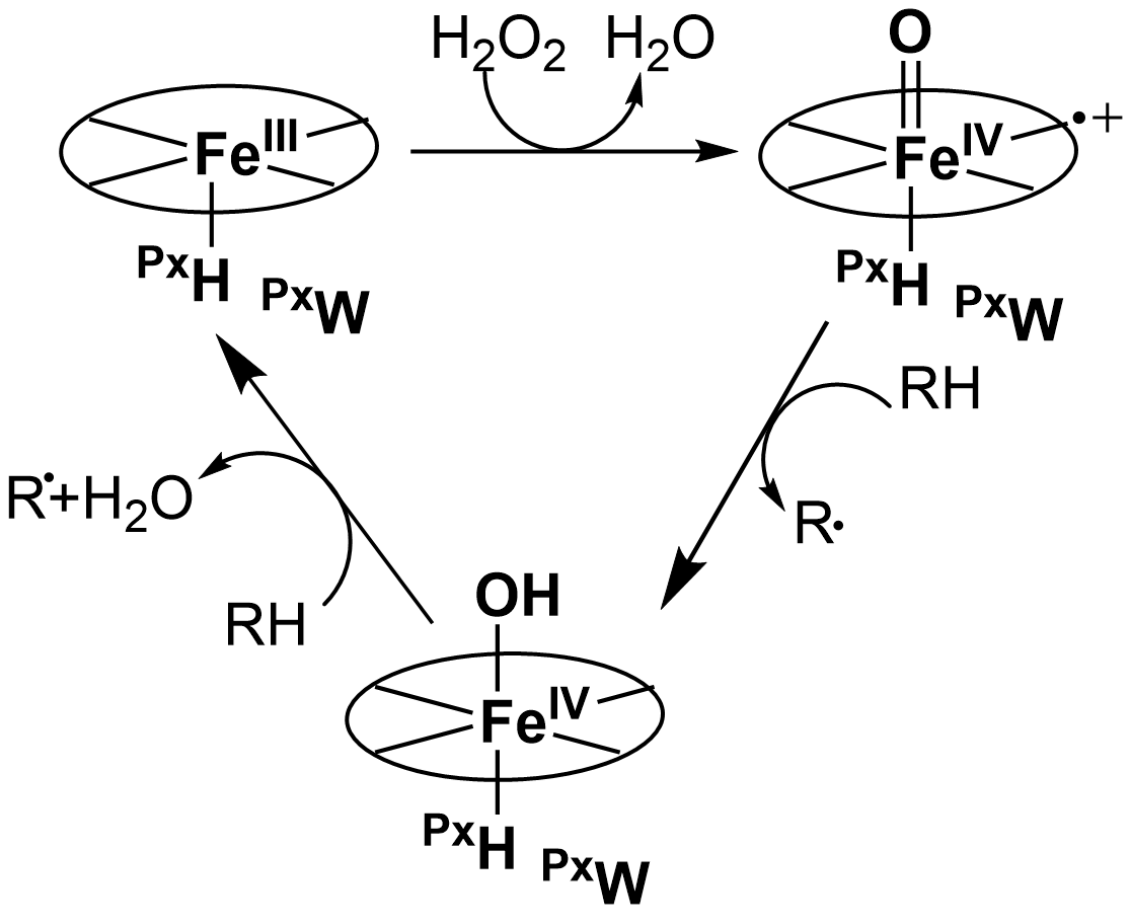

Figure 1.9. Peroxidase mechanism of KatG. The superscripted *Px* designates residues that are on the heme's *proximal* side. By convention, the proximal side of the heme is the same as that occupied by a protein-supplied fifth ligand to the heme, a histidine (^{Px}H) in the case of KatG. A generic exogenous peroxidatic electron donor (RH) is oxidized to its corresponding free-radical product (R$^{\bullet}$)

1.10. Overview of Spectroscopic Techniques

Spectroscopy is the study of the interaction between light and matter. These techniques may be classified by the wavelength of radiation applied in the experiment and produce a spectrum consisting of a plot of light intensity as a function of frequency or wavelength. The absorption or emission spectrum is associated with a transition between two allowed discrete energy levels of an atom or molecule. The frequency at which energy is absorbed or emitted is related to the energy levels involved in the transitions by

$$h\nu = |E_2\text{-}E_1|$$

The fact that atoms and molecules possess a set of discrete energy levels is an essential component of spectroscopy. The energy levels are characteristic and structurally unique to a particular atom or molecule, and the spectra provides important structural and electronic information about the system.

1.10.1. UV-vis Absorption Spectroscopy

UV-vis spectroscopy is used to determine the absorption of the samples at different wavelengths. The absorbance, A, of the sample is a factor of the extinction coefficient, ε, at a specific wavelength, the concentration of the species in the sample, c, and the path length of the light, b. Absorbance is a measure of the light that does not pass through the sample and corresponds to the base ten logarithm of incident light, I_0, divided by light registered by the detector, I. This is known as Beer-Lambert law which is written as:

$$A = log_{10}\frac{I}{I_0} = \varepsilon cb$$

The peptide groups of the protein main chain have a characteristic electronic absorption profile that give rise to a specific feature in the 'far-UV' range (180–230 nm). The most distinctive absorption features of the spectra occurring in 'near-UV' or the 'aromatic' region (240–300nm) are the hallmarks of the chromophores present in the side chain of aromatic amino acids (Figure 1.10). From the absorbance properties of the aromatic amino acids (Table 1.2.), it is clear that Tyr and Trp have much higher molar absorptivity than Phe. Therefore, the typical protein absorption spectrum in the 240-300 nm range, will be dominated by the contributions from Tyr and Trp. The fluorescence capacity of Phe is relatively weak, and its absorption features are only visible at 250-260 nm in the absence of both Tyr and Trp. In this study, we observed a very specific absorption at 280 nm for our protein KatG because of the abundances of Tyr and Trp content in the overall protein matrix. This specific absorption peak at 280 nm allowed us to measure the protein concentration directly using the spectrophotometer.

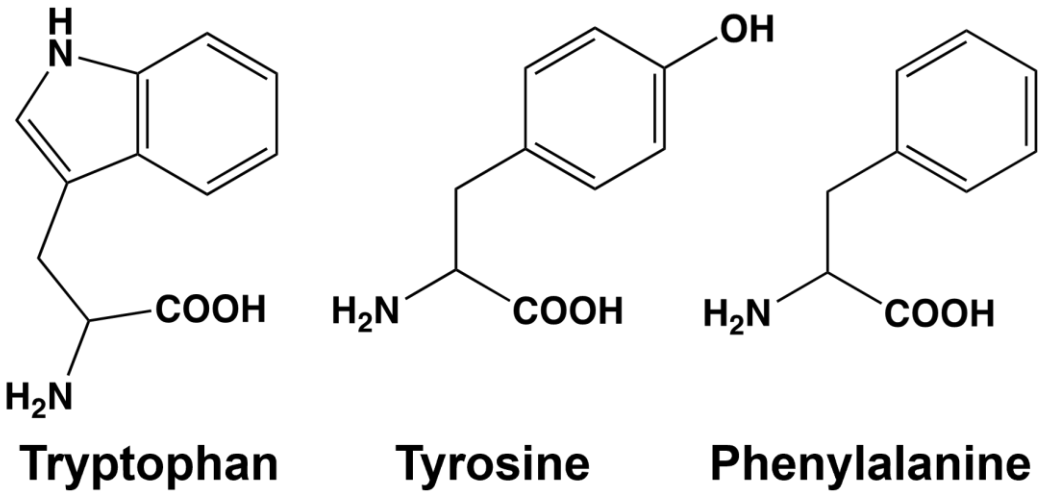

Figure 1.10. Chemical structure of the aromatic amino acids.

Table 1.2. Absorbance characteristics of the aromatic amino acids.

Amino Acid	**λ (nm)**	**ε (M^{-1} cm^{-1})**
Trp	280	5600
Tyr	274	1400
Phe	257	200

1.10.1.1. Evaluation of Heme Structure by UV-vis Absorption Spectroscopy

Strictly speaking, heme is a porphyrin ring complexed with ferrous iron and protoporphyrin IX. Of course, iron protoporphyin IX complexes also accommodate the ferric and other iron oxidation states. Ferric protophorpyrin IX is formally referred to as hemin, and when in complex with Cl^- as a ligand, hemin chloride. The term "hematin" refers to Fe^{III} protophorphyrin IX in complex with a hydroxide ligand. Nevertheless, in the vernacular of most research fields, "heme" is a term that refers loosely to any of these species, and the oxidation state is typically explicitly included in the description (*e.g.*, ferric heme). Hemoproteins such as catalase, peroxidase, hemoglobin, myoglobin, cytochrome *c* oxidase, cytochrome P450 all contains heme, which is a complex form of porphyrin ring bound with ferrous iron and protoporphyrin IX. This porphyrin is a strong chromophore that typically shows strong absorption features in the visible region of the electromagnetic spectrum. The porphyrin ligand can undergo several transitions due to their characteristic ring structure of conjugated double bonds. The electronic absorption spectrum of a typical porphyrin ring is characterized by an intense band due to a strong transition from ground state (S_0) to the second excited state (S_2). This usually occurs within 400-436 nm and given the name Soret or B band region. The transition from ground state (S_0) to the first excited state is relatively weaker but still displayed with considerable intensity. This occurs within 490-650 nm and generally termed as Q-band. Both of this B and Q band transition are the outcome of π–π^* transitions and known for years from the Gouterman four orbital model (HOMO and LUMO orbitals). The Q-band is further classified in β and α band and their relative intensity is a criterion to describe the proximity of the orbitals (a_{2u} and a_{1u}) for energy transfer. The transition of electrons from ground state to the higher vibrational levels in the S1 state is characterized as β band whereas transition to a vibrationless S1 state is the α band.

In this study, we have used UV-visible spectroscopy to determine oxidation state and coordination information for the heme in the KatG active site. The details of this in terms of experimental results comparing various enzyme preparation methodologies will be addressed in Chapter Two. According to our observations, the absorption spectra from our KatG preparations is characterized by a Soret band at 406.5 nm and additional lower-intensity bands at 505 nm, 545 nm and 633 nm (Figure 1.11).[177] The band at 633 nm is a ligand to metal charge-transfer band which is typical of high-spin Fe^{III} hemes. Its position can provide information regarding the presence or absence of a sixth axial ligand. The bands near 505 and 545 nm represent a mixture of Q bands and another charge-transfer band. In ferric hemes, these are difficult to differentiate and interpret. KatG is somewhat unusual in the near universal observation of a mixture of coordination states, with substantial contributions from 5- and 6-coordinate high-spin Fe^{III} heme.

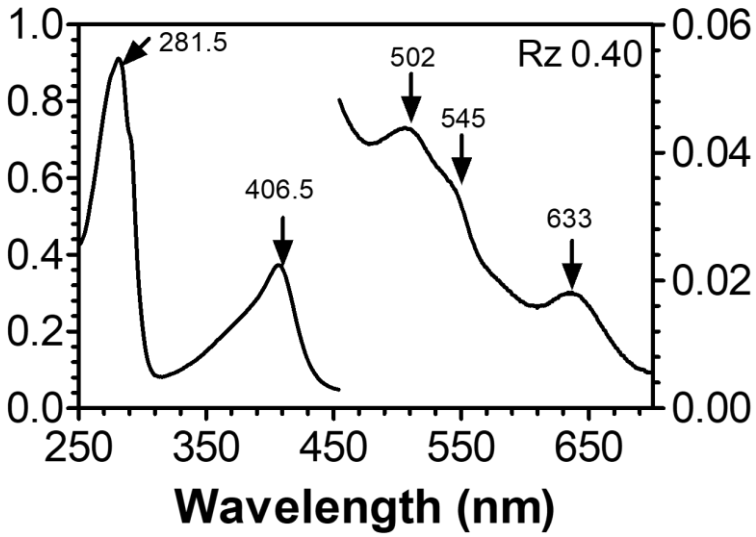

Figure 1.11. Electronic absorption spectra of freshly purified reconstituted KatG. Position of the Soret band (406.5) and the low-intensity Q and charge-transfer bands (502, 545, and 633) provides information about heme coordination, spin states, and the nature of exogenous sixth ligands.

The optical purity ratio (Reinheitzahl or *Rz*) is another parameter determined by UV-vis spectroscopy by comparing the A_{Soret}/A_{280} ratio. This ratio provide insight into the occupancy of a target heme protein with its heme cofactor.[177] The value of *Rz* depends heavily on the heme protein in question. For HRP, this value is >3.0 for pure HRP with a 1:1 occupancy of heme in the active site. In this study, we have observed *Rz* value ranging from 0.53-0.65 for holo proteins (reconstituted and mature) indicating that the protein being fully loaded with heme. Importantly, the low value compared to HRP is not an indication of a poor heme occupancy or impure enzyme. Rather, KatG is extraordinarily rich an Trp and Tyr residues. Thus, *Rz* values are low because of the outsized contribution of the denominator.

In addition to evaluating the ferric state of purified KatG and its variants, UV-vis absorption can also be used to determine steady-state kinetic parameters by monitoring the change in absorbance at a specific wavelength over time. In this case, the molar extinction coefficient of enzymes, different substrates, and oxidized PxEDs are also determined by monitoring their unique absorption features. For example, H_2O_2 degradation can be monitored at 240 nm ($\varepsilon = 39.4\ \mu M^{-1}cm^{-1}$), a widely accepted technique for determining catalase activity of enzymes, including KatG.

1.10.2. Monitoring Transient Intermediates by Optical Stopped-flow Spectroscopy

Stopped-flow is a technique which has been used widely for monitoring the kinetics of very rapid chemical and biochemical reactions.[164,165] Many traditional kinetic methods[178] fall short of detecting the change in concentration of a reactants, intermediate and products due to the limitation of time that is required for reagent mixing and instrument activation.[179] In this context, stopped-flow provides a beneficial approach where time requirement for the process of interest has been minimized to seconds (s) or milliseconds (ms) range. This technique has a

diverse range of application that involves biological interactions; such as protein folding,[180,181] inhibition mechanism,[182] binding kinetics of drugs, or small molecules[183,184] etc.

Standard stopped-flow instruments are equipped with two syringes for single mixing of enzyme and substrate (Figure 1.12). The reaction is initiated by depressing the reactant syringes and delivering the reactants into the connecting "mixing chamber." The volume injected is limited by the action of stop-syringe which provides the "stopped-flow" as soon as a steady-state flow is achieved. As the solution fills the stopping syringe, the plunger hits a block, causing the flow to be stopped instantaneously. In the optical cell, the kinetics of the reaction is measured as a function of time. There is a very short delay time in the stopped-flow system that is unavoidable during the mixing of the reagents and the beginning of signal observation which is known as "dead time."[178,185] Dead time is also an indication of the age of the reaction at the time when data collection becomes possible (*i.e.*, when the solution comes to rest). For most present-day instrumentation, the dead time is between 1 and 2 ms. For the Applied Photophysics instrument applied in these studies, the dead time is 1.2 ms.

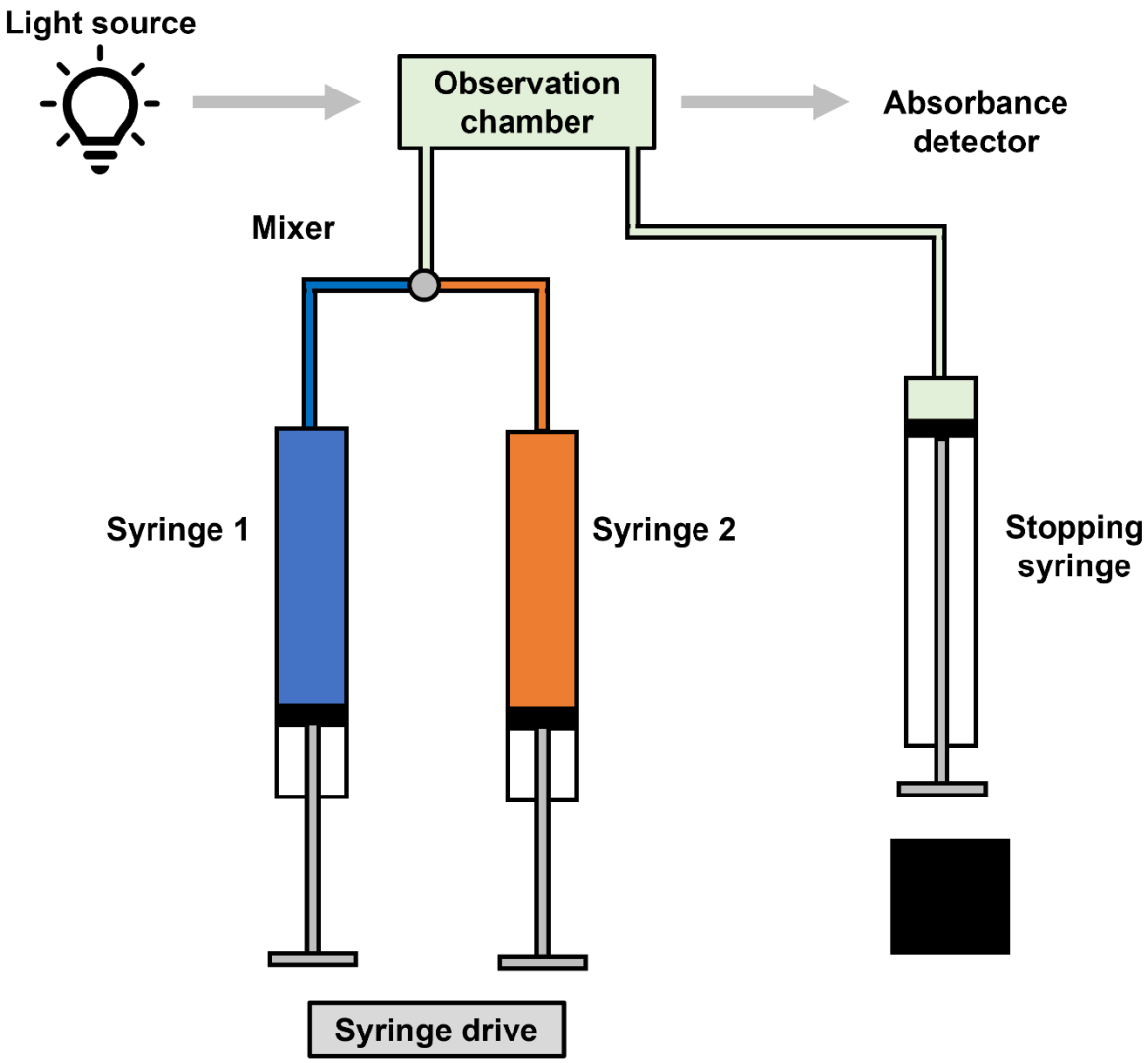

Figure 1.12. A schematic representation of stopped-flow spectrophotometer. The instrument is equipped with photodiode array for absorbance detection.

1.10.2.1. Evaluation of Heme-based Intermediates of KatG

In this study, optical stopped-flow experiments have been employed to detect the high-valent iron intermediates formed during the reaction of KatG with peroxides (Figure 1.13). Heme-dependent catalases, peroxidases and KatG all utilize heme *b* as cofactor, and compound I is a common occurrence across this board. Formally, compound I is oxidized by two electrons above the Fe^{III} oxidation state. Conventionally, this is accounted for by the oxidation of the heme iron (Figure 1.13 A) to a ferryl-oxo state (Figure 1.13 B) along with the oxidation of the porphyrin macrocycle to yield a π cation radical (*i.e.*, Fe^{IV}=O[porphyrin]$^{\bullet+}$). As more heme-dependent enzymes have been investigated, the designation "compound I" has become more convoluted. Strictly speaking, compound I refers to the oxidation level relative to the resting (*i.e.*, Fe^{III} state). That is, it is always oxidized by two electrons above resting. This then includes states where the porphyrin radical has been reduced at the expense of a protein-based moiety (*e.g.*, the proximal Trp or the MYW adduct). Thus, investigators have taken to calling a Fe^{IV}=O[MYW]$^{\bullet+}$ state of KatG, "compound I*."

The quintessential peroxidase, HRP, upon reaction with a single equivalent of H_2O_2 forms an intermediate designated by Britton Chance as "compound I." Subsequent studies have demonstrated that this is the classical compound I (*i.e.*, Fe^{IV}=O[porphyrin]$^{\bullet+}$) (Figure 1.13B). This species is characterized by a Soret band whose λ_{max} does not appreciably shift but whose intensity diminishes by about a factor of two (Figure 1.14). However, in *Mtb* KatG, compound I is significantly less stable than that formed in HRP.[186] A canonical compound I state can be observed in many catalase-negative KatG variants, and strikingly, in the W321F KatG variant. However, with the WT enzyme it appears that any porphyrin$^{\bullet+}$ is only transiently formed and is rapidly reduced by adjacent oxidizable protein components.

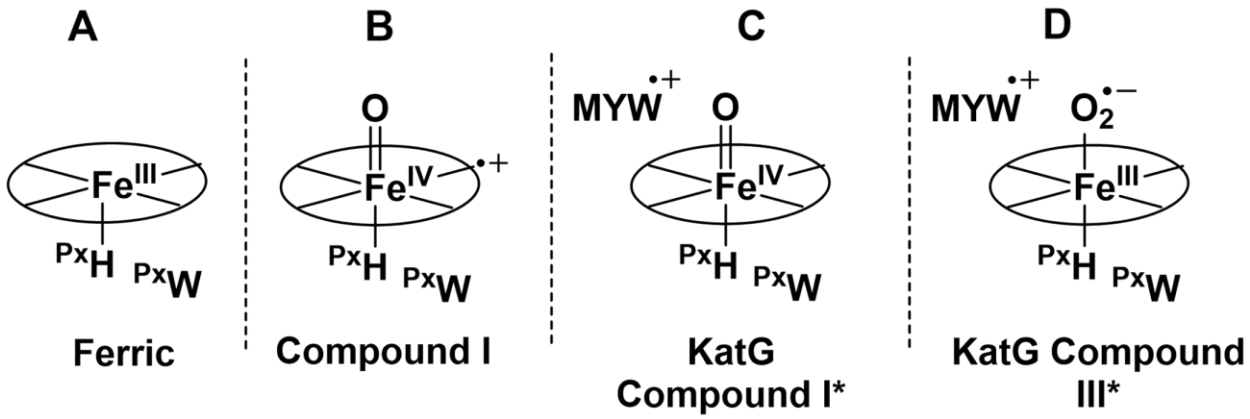

Figure 1.13. Heme intermediates pertinent to KatG.

Thus, in KatG transient-state kinetic studies, compound I is much more typically observed as some Fe^{IV}=O[protein]$^{\bullet}$ state. Importantly, because protein-based-radical contributions to visible absorption spectra cannot be easily accounted for, compounds I of the formulation Fe^{IV}=O[protein]$^{\bullet}$ often have features in optical stopped-flow experiments that are reminiscent of compound II (see below).

Compound I (in its many possible forms) can be reduced by a single electron to yield a second intermediate referred to as compound II. Formally, compound II is oxidized by one electron over the resting state and is designated as a Fe^{IV}=O or ferryl-oxo intermediate (Figure 1.13 C). It is characterized by a Soret band red-shifted relative to the Fe^{III} state to ~ 416 nm as well as by β and α transitions at ~ 530 and ~ 560 nm, respectively.[91,170,187]

The heme state known as compound III is complex and has been a subject of controversy in various corners of the field of heme-dependent enzymes. Indeed, compound III has raised its own controversies among KatG investigators. Formally, compound III is designated as a Fe^{II}-O_2 complex or its isoelectronic equivalent, Fe^{III}-$O_2^{\bullet-}$ (*i.e.*, ferri-superoxo). The former is how the O_2 complexes of the O_2 transport/storage proteins hemoglobin and myoglobin (*i.e.*, oxyhemoglobin and oxymyoglobin, respectively) are often presented. Thus, in the KatG and peroxidase literature, compound III is sometimes referred to as "oxyperoxidase." In any case, compounds III across all heme proteins are probably most accurately represented by some resonance mixture of these isoelectronic states, with the active-site environment around the heme exerting a substantial influence on the form which dominates. For example, the presence of an appropriately placed H-bond donor in the active site adjacent to the bound O_2 would serve to stabilize the Fe^{III}-$O_2^{\bullet-}$ form relative to Fe^{II}-O_2.

The formulations of compound III give an indication as to different routes by which it can be generated: 1) reaction of the Fe^{II} state with O_2, 2) reaction of the Fe^{III} state with $O_2^{\bullet-}$,

and not as obviously, 3) reaction of the Fe^{III} state with excess peroxide. The latter is the most explored in peroxidase mechanistic investigations. Among typical peroxidases like HRP, the actual step to generate compound III is the reaction of H_2O_2 with compound II (*i.e.*, the Fe^{IV}=O state). Spectroscopic features of compound III were characterized by a very slight (if any) red shift in the Soret band (~ 418 nm) and the much more obvious shift in β and α transitions from ~530 and ~560 nm to ~540 and ~580 nm, respectively (Figure 1.13 D).[91,187]

Within peroxidase and KatG studies, the transition from compound II to compound III is very important but for completely different (almost opposite) reasons. For typical peroxidases like HRP, compound III represents an inactive form of the enzyme. The enzyme, in the absence of an adequate electron-donor substrate, reacts with excess peroxide to form inactive compound III. This has been posited as a mechanism to protect the enzyme from peroxide-dependent irreversible inactivation. Notably, catalase-negative variants of KatG appear to follow the same profile as their peroxidase relatives, forming compound III as a response to excess H_2O_2 in the absence of an adequate PxED.

In stark contrast to this, the compound III-like state of WT KatG is ***only*** observed when the enzyme is actively degrading H_2O_2 through its catalase activity. Consequently, the return of the Fe^{III} state after accumulation of compound III is fully expected. This is easily observed by the return of Soret absorbance at 406 nm along with the reemergence of the signature charge-transfer band at ~640 nm. For typical peroxidases, the return of the Fe^{III} form from compound III is not typically observed or expected. Rather, if anything, evidence of the irreversible inactivation of the enzyme is observed, including heme bleaching and protein aggregation. As illustrated below (Figure 1.15), we are easily able to form and distinguish between compound II and compound III intermediates for wild-type KatG. Consistent with the experience of our colleagues, we do not detect the canonical compound I state with the wild-type enzyme.

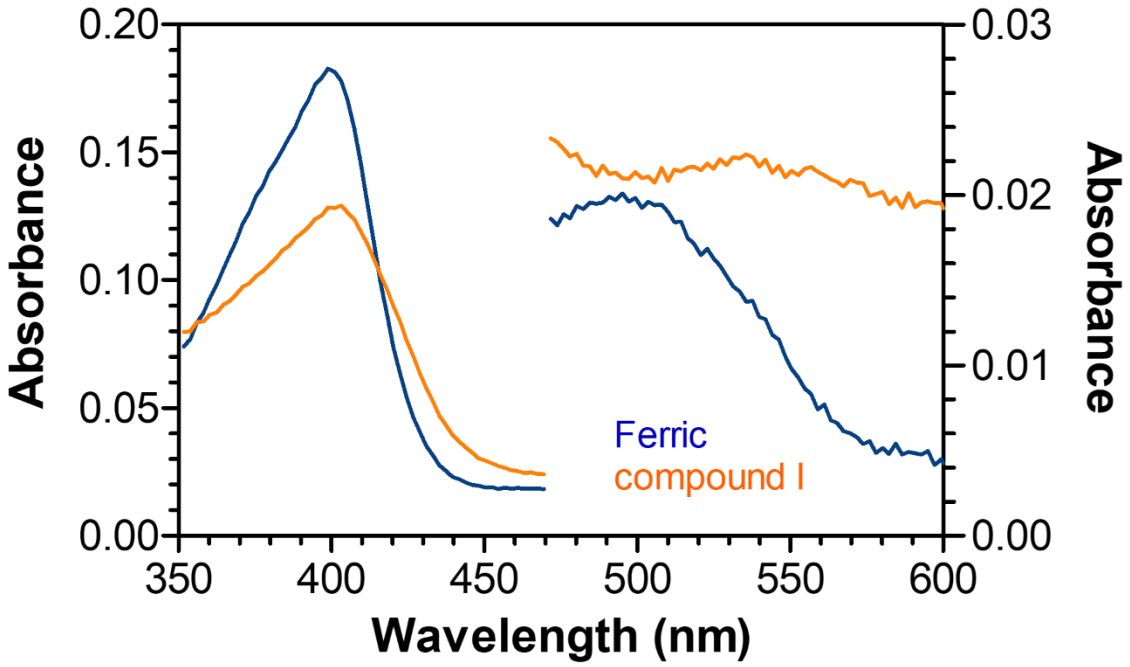

Figure 1.14. Visible absorption spectra obtained for horseradish peroxidase (HRP) by optical stopped-flow methods. The spectrum for compound I (Fe^{IV}=O[por]$^{\cdot+}$) (orange line) was obtained 100 ms after mixing resting HRP with 0.9 molar equivalents H_2O_2. Compound I generated as above was also reacted with 10 µM capsaicin/50 µM ascorbate for 9.6 s to produce Fe^{III} HRP (blue line). All reactions were carried out at 25 °C in 50 mM phosphate, pH 7.0. Additional experimental details on the reactions of HRP with capsaicinoid compounds can be found in Goodwin and Hertwig, 2003.[188]

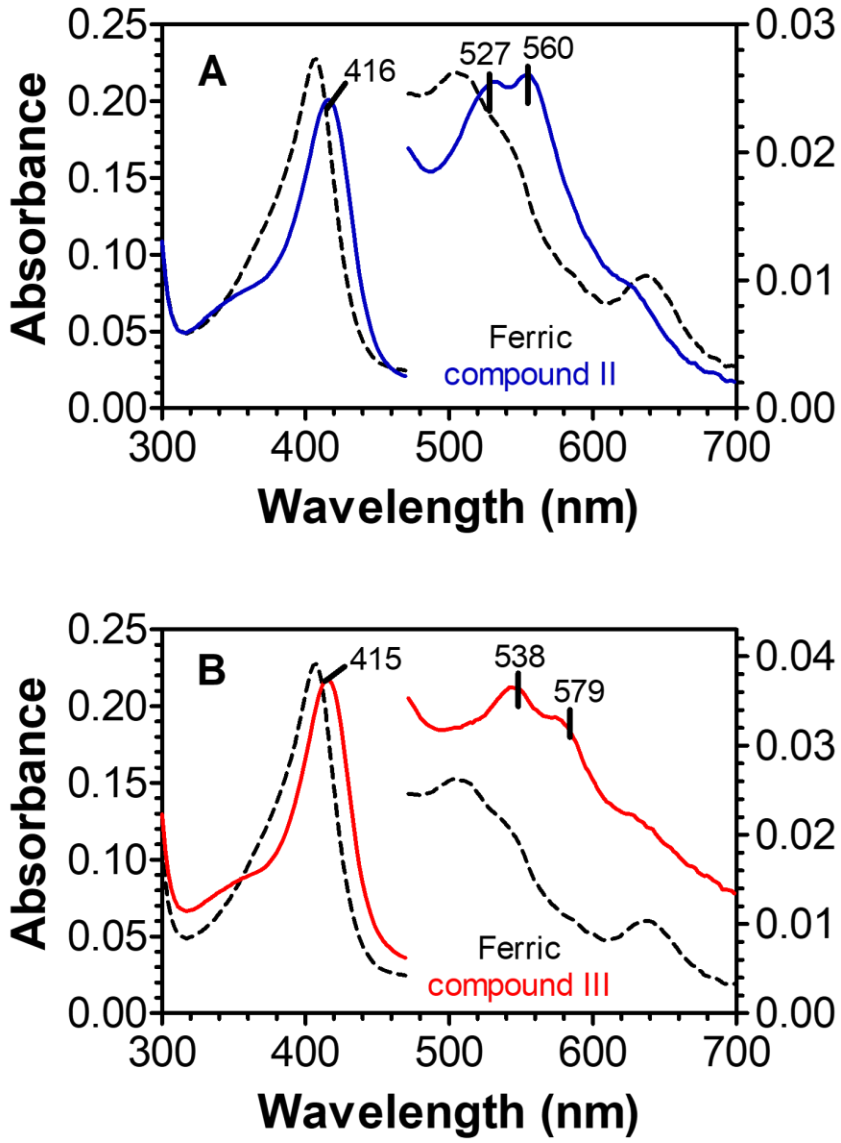

Figure 1.15. Typical absorption spectra of KatG compound II (A, blue) and compound III (B, red) in the Soret and charge-transfer/Q-band regions.

1.10.3. Electron Paramagnetic Resonance (EPR) Spectroscopy

EPR is a spectroscopic technique in which an oscillating magnetic field induces magnetic dipole transitions between the energy levels of a system of paramagnetic species. This technique is very sensitive to the electronic environment of the paramagnetic system (*e.g.*, transition metal center or free radical). The technique is versatile, enabling the investigator to evaluate paramagnetic species in solid (*i.e.*, frozen) or liquid states. In this study, EPR has been extensively used to evaluate aspects of KatG structure and catalysis which are difficult or impossible to access by UV-visible absorption (steady-state or transient-state). These include clear distinctions of Fe^{III} coordination and spin states for KatG at rest, as well as transient, protein-based radicals formed during its reaction with H_2O_2.

As an elementary particle, electrons possess intrinsic, quantized angular momentum (*i.e.*, spin) and behave like tiny bar magnets, or magnetic dipole, with a magnetic moment $\bar{\mu}$. However, the electron spin magnetism cancels if electrons are all paired. Therefore, EPR can only be applied if unpaired electrons are present, and those atoms, ions, molecules, and radicals possessing at least one unpaired electron are commonly referred to as "paramagnetic centers." The absorption of electromagnetic radiation varies within a molecule or atom, representing discrete (or separate) states, each with a corresponding energy. The energy differences due to the interaction of unpaired electrons with the external magnetic field is basically measured in the EPR spectroscopy. This effect is called the Zeeman Effect.

In the presence of an external magnetic field B, the spin magnetic moment of a single free electron (spin quantum number S = 1/2) can orient one of the two positions depending on the direction of the magnetic field. The state of lowest energy is represented by the parallel placement of the electron magnetic moment along the magnetic field whereas, placement of electron moment against the magnetic field represents the state of highest energy. The two

states are labeled by the projection of the electron spin, m_s. Because the electron is a spin ½ particle, the parallel state is designated as m_s = -½ and the antiparallel state is m_s = +½. The energies of these two directions are proportional to the strength of the external magnetic field B and represented by the equation,

$$E=g\beta B_0 m_s$$

Where *g* (= 2.0023193) is the *g* factor of a free electron and β is the electronic Bohr magneton (9.274 x 10^{-24} J^{-1}). Therefore, electrons in the lower energy state, $m_s = -1/2$, can be excited to the upper level (m_s = +1/2), by electromagnetic radiation of appropriate frequency to satisfy the resonance condition and is represented as following

$$\Delta E = \frac{1}{2} g\beta B_0 m_s - (-\frac{1}{2} g\beta B) = g\beta B_0 m_s = h\nu$$

Where *h* is Planck's constant (6.62 x 10^{34} Js^{-1}) and ν is the frequency of the applied radiation. Since *h* and β are constant, the g-factor depends predominantly on the direction of the molecule in the external magnetic field, hence called g-tensor. When this condition of resonance is satisfied, absorption occurs in the form of electromagnetic radiation and is detected by EPR experiments. The EPR spectrum of a free electron consists of a single absorption line, which is usually shown in the first-derivative due to the very broad absorption spectrum (Figure 1.16). EPR spectrometers usually run at constant frequency (*e.g.*, X-band ~ 9.5 GHz), and a sweep of the applied magnetic field is applied.

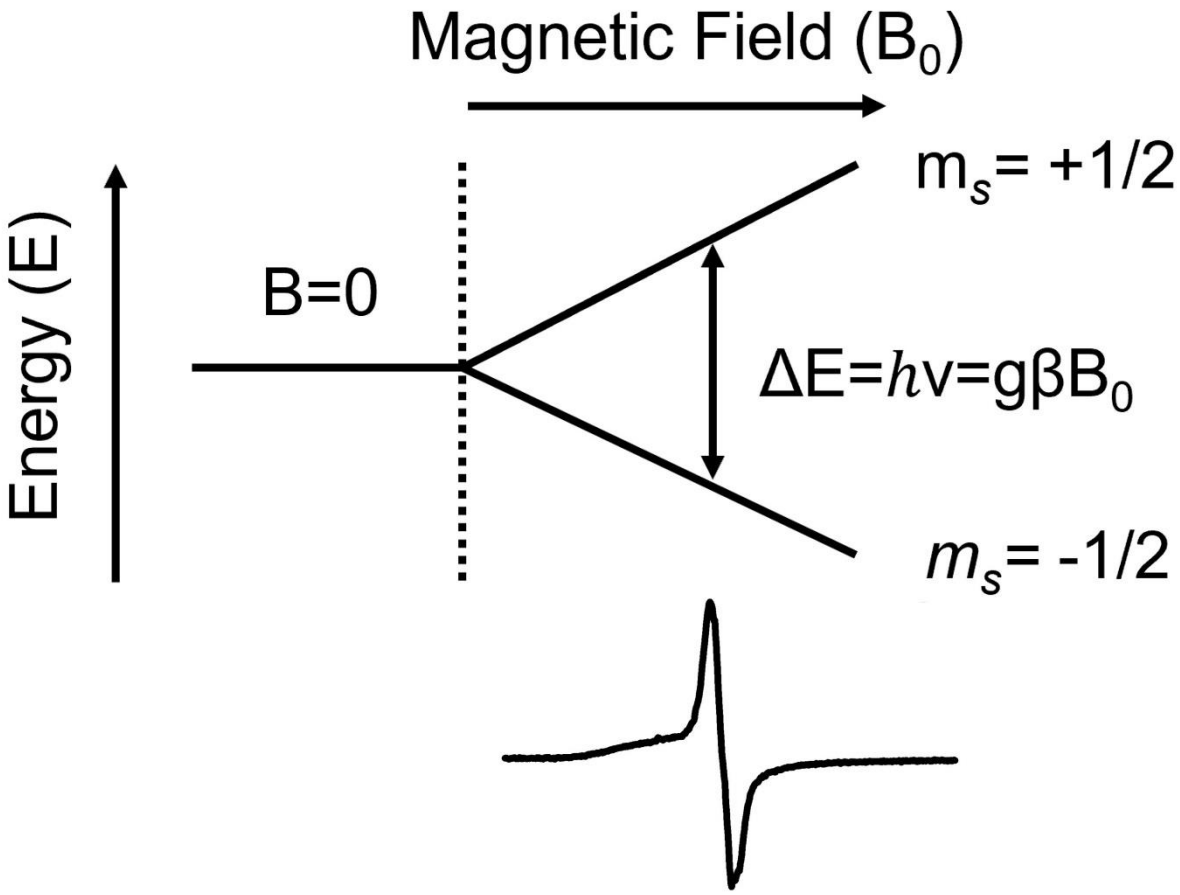

Figure 1.16. The splitting of energy levels of free electron S = 1/2 in a magnetic field B_0. The resulting EPR spectrum is shown in both the absorption (dashed line) and first-derivative (solid line) form.

The g-factor is anisotropic, meaning that an unpaired electron, in a molecule or radical, has its spin oriented by the magnetic field which it experiences. Depending on the orientation of the magnetic field along the *x*, *y* and *z* axes, the *g*-factor for an anisotropic species breaks down generally into three values following a Cartesian coordinate system which is symmetric along the diagonal: g_x, g_y, and g_z (Isotropic, rhombic, and axial) (Figure 1.17). Isotropic spectrum is observed when $g_x = g_y = g_z$ and is independent of orientation in the magnetic field. The spectrum is said to be axial, when two of the g values are equal but one singular value is different than other two. The two equal g-values are perpendicular to the x and y directions ($g_\perp$) while the unique g-value is elongated along the z-axis ($g_\parallel$). Axial signal can also be obtained when the spectrum appears at $g_x = g_y < g_z$ and is shortened in the XY plane. Finally, the rhombic signal appears when none of the g-factors are equal, such as $g_x \neq g_y \neq g_z$.

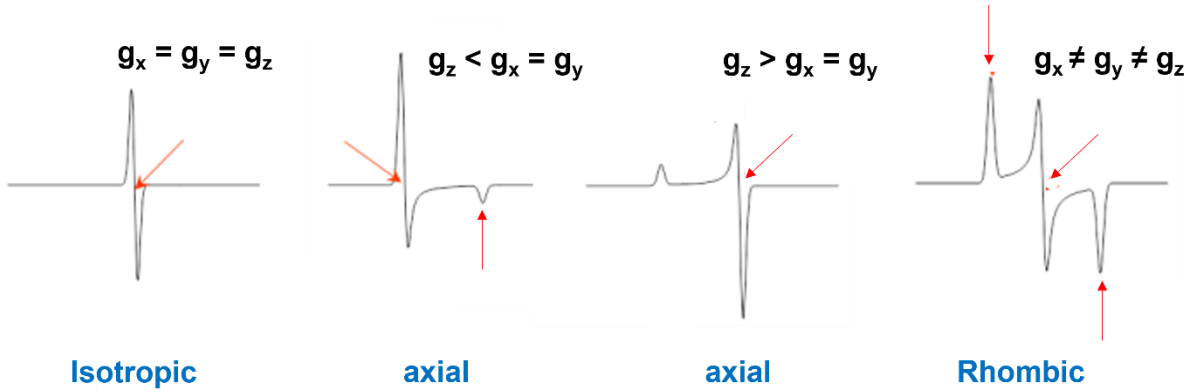

Figure 1.17. Three different classes of anisotropy representing isotropic, axial and rhombic symmetry.[189]

1.10.3.1 Evaluation of heme states by EPR

While The metal center of the heme proteins usually exists in an octahedral coordination mode where the fifth position is occupied by a protein residue as proximal axial ligand, typically a histidine, cysteine or tyrosine. The sixth axial position can either be occupied by another endogenous ligand, an external molecule (such as water), or even left free (uncoordinated) to promote substrate binding. Depending on the axial ligand of the porphyrin complex, as well as their orientation, iron d-orbitals are placed in an intermediate ligand field, affording the 'low-spin to high-spin' transition.[190]

Due to the paramagnetic nature of elemental iron and iron (III), EPR spectroscopy is one of the most suitable techniques for the investigation of heme-based systems. This technique is still beneficial, even if protein is large (i.e., KatG), because it can focus specifically on the paramagnetic active site, where the unpaired electrons reside. In metalloproteins, iron centers can possess multiple unpaired electrons (S>1/2), defined primarily as low-spin state (S=1/2) and high-spin state (S=5/2). Heterogeneity is frequently observed in many heme enzymes distinguished by the g-tensor anisotropy. Previous studies identified the contribution of a broad rhombic (g_x ~ 6.6 and g_y ~ 5.1, g_z ~ 1.95) and a narrow rhombic (g_x ~ 6.0, g_y ~ 5.6 and g_z ~ 1.99) and an intermediate species (gx ~ 6.3, gy ~ 5.3 and gz ~ 1.97).[150,161,177] The specific line shape of the high spin Fe^{3+} for a heme-based system is illustrated in Figure 1.18 depicting both the axial and rhombic cases. Low-spin Fe^{3+} (S=1/2) is also occur in heme structures possessing strong axial ligands and can be easily interpreted EPR spectrum (Figure 1.19).

In this study, we also used EPR spectroscopy for investigating the resting state of ferric KatG (Figure 1.20) which depicts a very typical example of heme-structure heterogeneity and g-tensor anisotropy that goes with this enzyme. We have detected a greater contribution of the

6-coordinate axial state relative to species with substantial rhombic distortion which is typical of the 5-coordinate state.

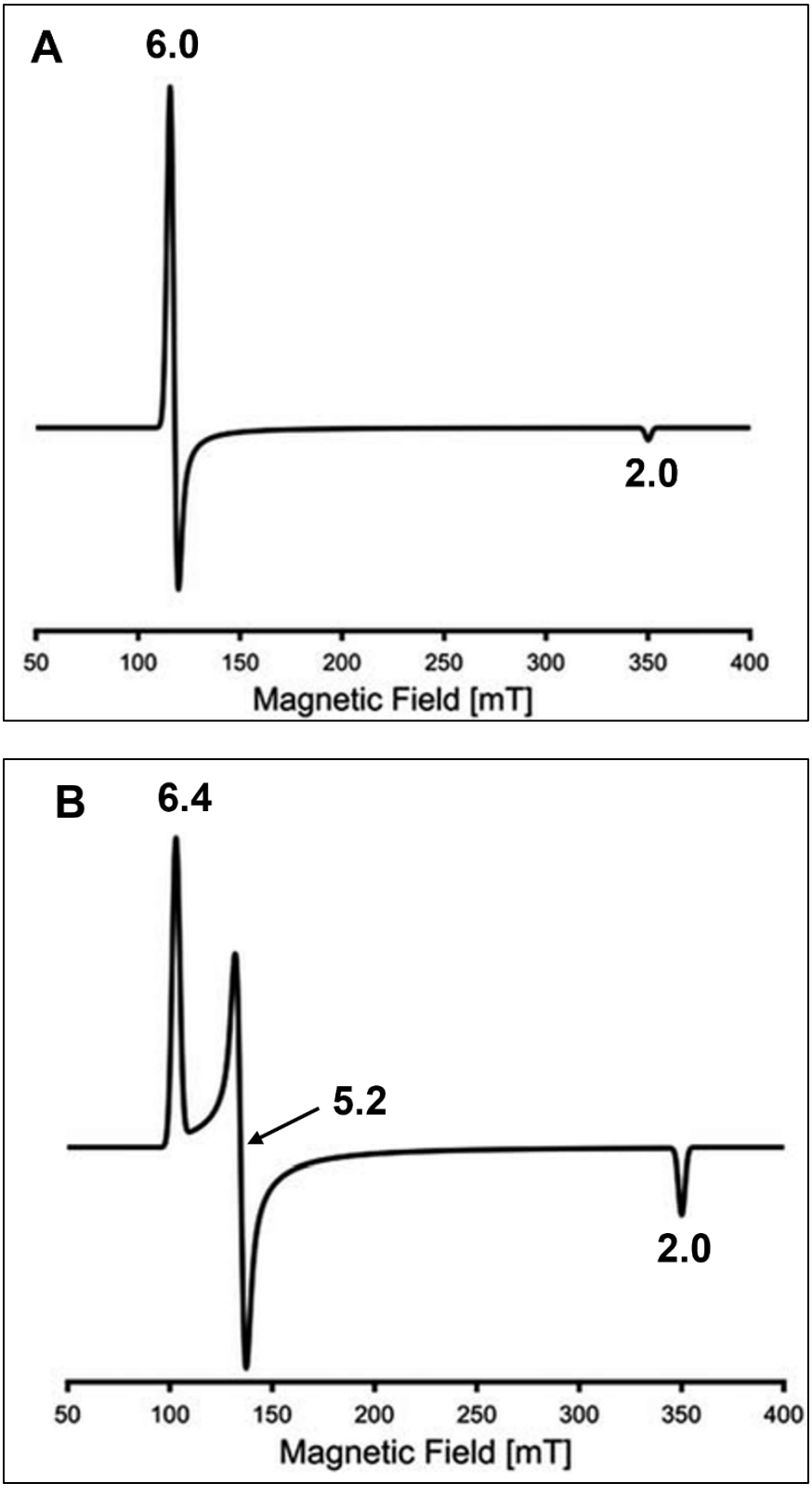

Figure 1.18. Illustration of EPR spectra representing high-spin Fe^{3+} (S=5/2). The axial case is shown in A and rhombic case is shown in B. Figure is adapted from Maruan Bracci *et al.*[190]

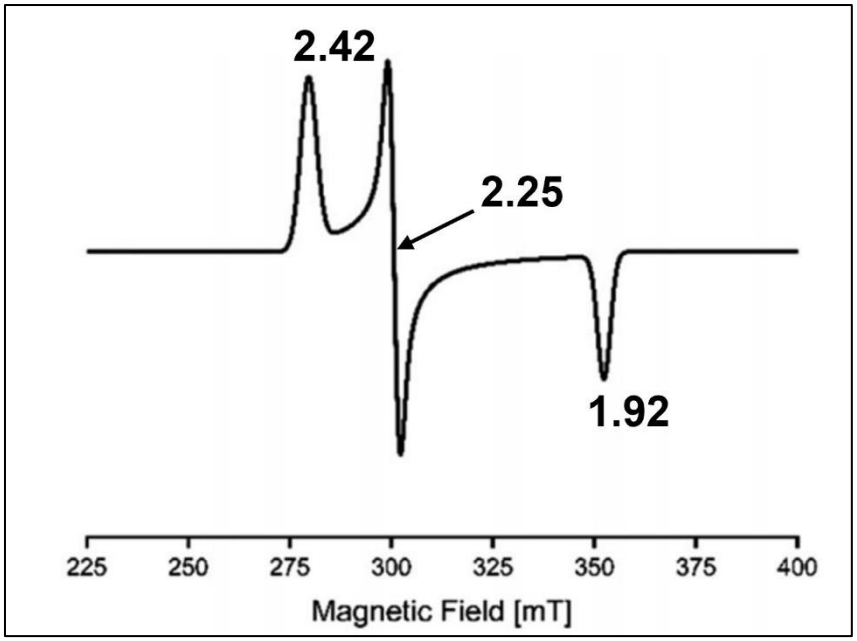

Figure 1.19. Illustration of EPR spectra of a low-spin Fe^{3+} (S=1/2). Figure is adopted from Maruan Bracci *et al.*[190]

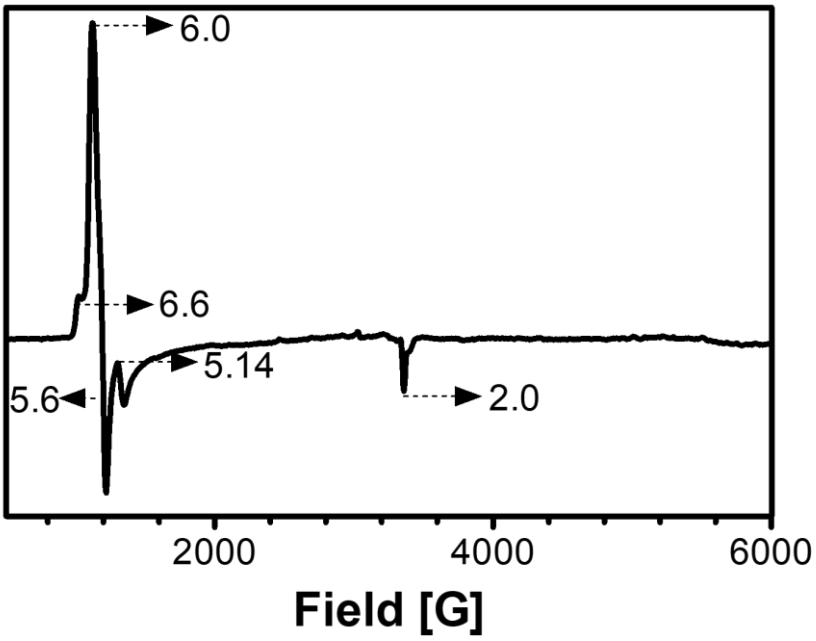

Figure 1.20. Depiction of g-factor anisotropy in the EPR spectrum of reconstituted KatG. The presence of multiple states is evident, but the spectrum is dominated by an axial species.

1.10.3.2 Evaluation of protein-based radical by EPR

Enzymatically catalyzed reactions involving one-electron oxidation or reaction steps often produces a paramagnetic transient state, which can be detectable by EPR spectroscopy. The unpaired electron, thus produced in this manner can be located in the center of a transition metal specially in the metalloenzymes. However, for several cases, radicals derived from a native or post-translationally modified amino acid or from a cofactor can serve as a paramagnetic center. Generation of tyrosyl or tryptophanyl radicals are the most commonly occurring protein-based radicals formed in this mechanism. These types of radicals have been assigned using a combination of mutagenesis, selective deuteration of Trp and/or Tyr residues, rapid freeze quench EPR, and ENDOR spectroscopies. For example, cytochrome *c* peroxidase contains one organic radical which took a long time to discover due to the ambiguity of the broad EPR signal. However, through mutagenesis it was discovered that

Trp191 is the site of radical formation[191] and that the shape of the signal was due to an exchange interaction between the unpaired electrons in the heme and in $Trp^{\bullet+}$. In contrast to this, other peroxidases, like HRP forms a stable porphyrin radical, which does not decay into an amino acid radical.[192] Previous study with *Mtb* KatG identified two Trp radicals as well as a Tyr radical upon the reaction of KatG with peroxyacetic acid (PAA) using multifrequency EPR spectroscopy, selective deuterium labeling, and mutagenesis.[193] One of the Trp radicals was assigned to Trp321 and believed to be in an exchange interaction with the heme center. Our group has also investigated the protein-based radicals formed upon reaction of *Mtb* KatG with H_2O_2 to provide more insight to the appearance of the methionine-tyrosine-tryptophan (MYW) cofactor narrow doublet radical and proximal tryptophan (Trp321) signal.[47] Appearance of $MYW^{\bullet+}$ narrow doublet radical was evident as early as 10 ms, and assigned as Tyr229. However, at H_2O_2 depletion (6s), a broad singlet species consistent with a proximal

tryptophanyl radical (W321$^{\bullet+}$) was observed. A greater time resolved EPR spectra of freeze-quenched samples from reaction of *Mtb* KatG with H_2O_2 were shown in figure 1.21.

The most commonly used EPR frequency (i.e., 9 GHz) can be used to assign *g*-values. However, resolving the *g*-tensor anisotropies for different protein-based radicals are critical because its sensitivity and hyperfine tensor depends on the polarity of the environment and the neighboring hydrogen bonding network.[194] Therefore, deuterium labeling is sometimes necessary in combination with multifrequency EPR spectroscopy to unequivocally identify the chemical nature of the radical(s) formed.[195] The key aspect is that the 9 GHz EPR spectrum of a protein-based radical is dominated by the proton's hyperfine couplings (given by the interactions of the protons with the electron spin of the radical). The nuclear hyperfine interaction causes a measurable change in the 9 GHz EPR spectrum of the Tyr$^{\bullet}$ (or Trp$^{\bullet}$) if the enzyme contains fully-deuterated Tyr (or Trp) residues instead of the normal (protonated) amino acids. formed.[195] The g-values reported for tyrosyl radicals are moderately higher (g_x = 2.009, g_y = 2.0034, and g_z = 2.0018) than tryptophanyl radicals (g_x = 2.0033, g_y = 2.0024, and g_z = 2.0021).[194] In contrast to that, isotopically substituted or electronically modified tyrosyl radical has been noted to have a lower g_x component of about 2.006.[176] Precise measurements of g-shifts using model systems[196] or DFT calculations[197] can provide valuable insight that goes beyond the fingerprint information of the g tensor for unequivocal assignment of the radical identification. In this study, we used X-band and multi-frequency EPR to identify and distinguish between different KatG protein-based radicals that were detected in freeze-quenched samples of KatG or its variants reacted with H_2O_2 or peracetic acid (PAA).

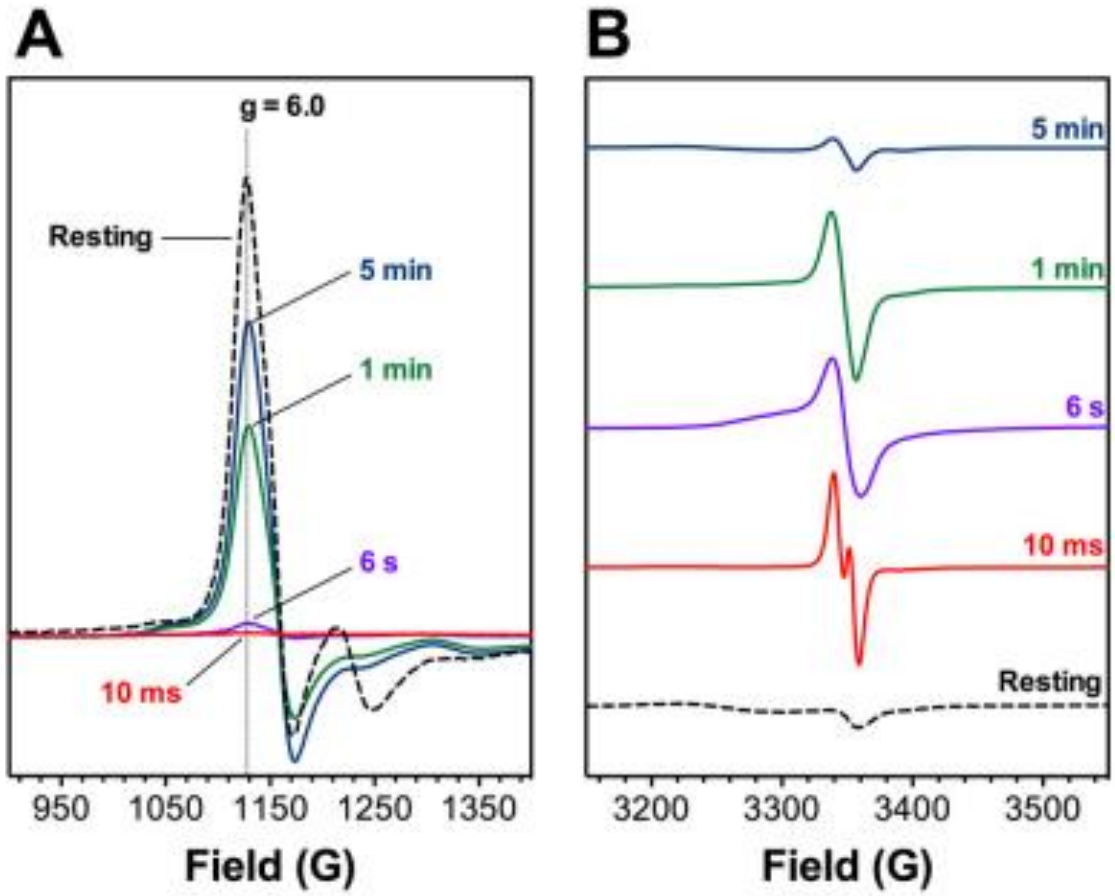

Figure 1.21. High-spin ferric species typical of the WT KatG resting state (g~6) are shown in A, and the $g_{\|}$ component of the resting state as well as protein-based radicals (g~2) are shown in B. Ferric enzyme (150 µM after mixing) was reacted with H_2O_2 (100 mM after mixing) for the time indicated prior to freeze-quenching. Reactions were carried out at 25 °C in 100 mM acetate, pH 5.0. All spectra were recorded at 4.5 K. All the experimental details will be found in Njuma *et al*. 2017.[47]

2. CHAPTER TWO

A NOVEL, HIGH YIELD PROTOCOL FOR HEME INCORPORATION INTO KatG: AN ESSENTIAL TOOL FOR EVALUATING PROTEIN-BASED COFACTOR FORMATION

2.1. Introduction

Cofactors are nonpeptidic molecular moieties that are required for the catalytic function of a given enzyme. Accordingly, cofactors are typically bound in the active sites of their requisite proteins. If a cofactor is covalently associated with its enzyme or so noncovalently bound so tightly that it can only be released upon enzyme denaturation, it is referred to as a prosthetic group. Cofactors can range from simple mononuclear metal ions to complex organic or metalloorganic compounds.[56] Covalently bound porphyrins or flavins are prominent examples of non-diffusible cofactor; these are often involved in the electron- and/or energy-transfer processes.[198]

One of the prominent class of enzymes that are involved in the electron transfer reactions are oxidoreductases and metalloproteins and represents more than one third of all known proteins.[199–204] These enzymes intervene in a number of biological processes and nearly every single one of the enzymes which catalyze them requires one or more cofactors which manage energy reorganization, directional specificity and electron transfers between donor and acceptor substrates.[205] The underlying process that is essential for these reactions is electron transfer in the form of single-electron, hydrogen-atom, or two-electron (*i.e.*, hydride) reactions. These redox enzymes greatly rely on catalytic sites connected by redox chains. Redox-active amino acids such as tyrosine (Tyr) or tryptophan (Trp) can form chain elements, but usually a chain contains non-amino acid cofactors, such as a planar heme or a cubic iron–sulfur (FeS) center. Such transition metals, by their nature of achieving multiple oxidation

states can act as a source/ sink of electrons, and abundantly found in the active sites of a great number of proteins and, thus, play essential roles in redox applications.

Hydroperoxidases (catalases and peroxidases), as well as KatGs are ubiquitous "housekeeping" oxidoreductases which utilize heme *b* (porphyrin derivative) as a prosthetic group (Figure 2.1) for heterolytic cleavage of the peroxidic bond predominantly in hydrogen peroxide (H-O-O-H) but also in some small organic peroxides (R-O-O-H. *e.g.*, ethyl hydroperoxide or acetyl hydroperoxide).[206–208] The biochemical utility of FAD (flavin–adenine dinucleotide) and FMN (Flavin mononucleotide (FMN) are widely distributed in flavoproteins as cofactors (Figure 2.2), which catalyze an astonishing diversity of biological reactions, encompassing dehydrogenation[209], oxidation[210,211], monooxygenation[212], halogenation[213–215] and many more. In addition to these, there is a very limited number of flavoproteins which contain both flavin and heme as cofactors and, are generally termed as flavocytochromes.[216] For example, NADPH–cytochrome P450 oxidoreductase is a membrane bound flavoprotein containing FAD (flavin adenine dinucleotide) and FMN (flavin mononucleotide) as prosthetic groups.[217] This endoplasmic reticulum bound[218] enzyme is responsible for transferring NADPH-derived reducing equivalents to the heme center of cytochrome P450.[219,220] The same is observed with other microsomal enzyme systems including heme oxygenases[221] and the fatty acid desaturation and elongation systems.[222] In addition to these, there is a special class of cofactors termed as protein-derived cofactors, the emergence of which is asserted to circumvent the need of an external cofactors. The construction site of these protein derived cofactors is catalytic or redox-active location modified by one or more amino acid residues.[56] These post-translational modifications are irreversible and endow the modified residues with new functional properties. For example, Cys-Tyr and Met-Tyr-Trp crosslinked species are found in galactose oxidase[75] (Figure 2.3) and catalase peroxidase[156] (Figure 2.4) respectively. In both

cases, these covalent modifications are post-translationally generated and influence the reactivity of redox active metal centers of the protein.

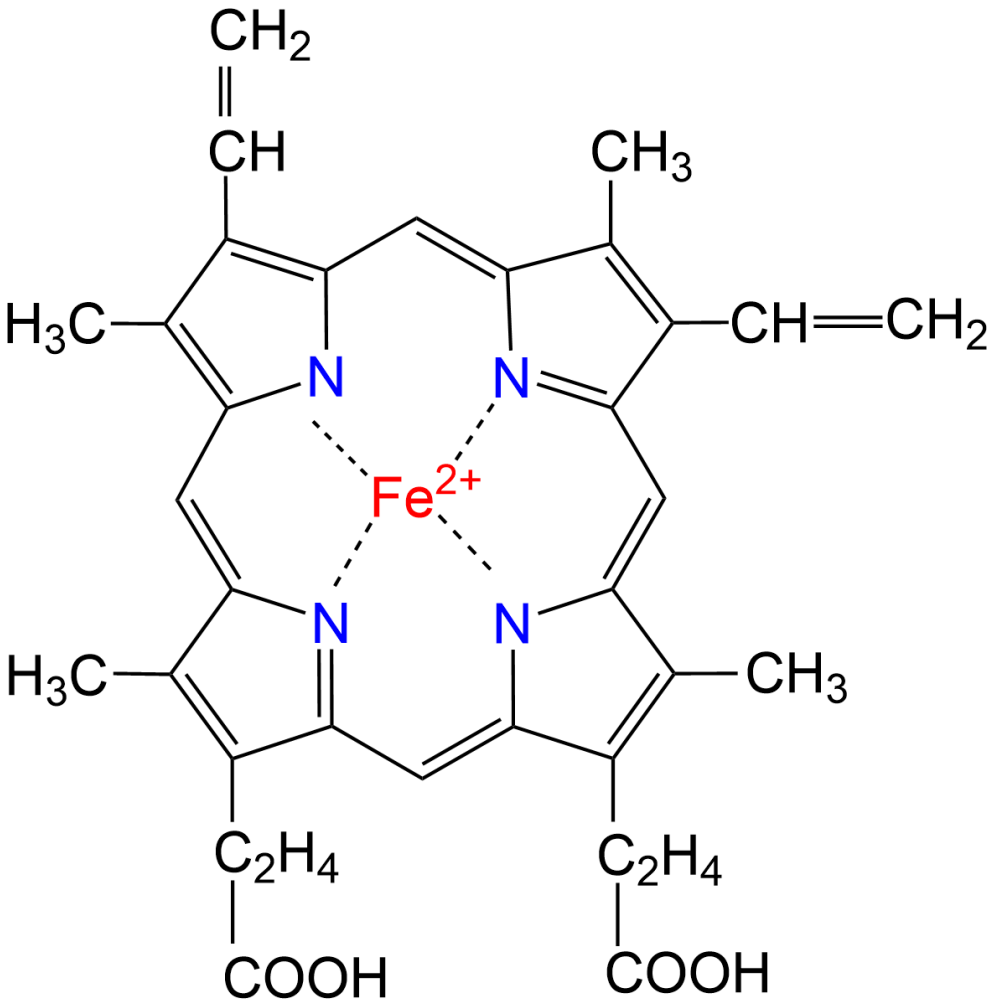

Figure 2.1. Structures of heme *b*. Common examples of heme-bound proteins are hemoglobin, myoglobin, KatG and cytochromes P450.

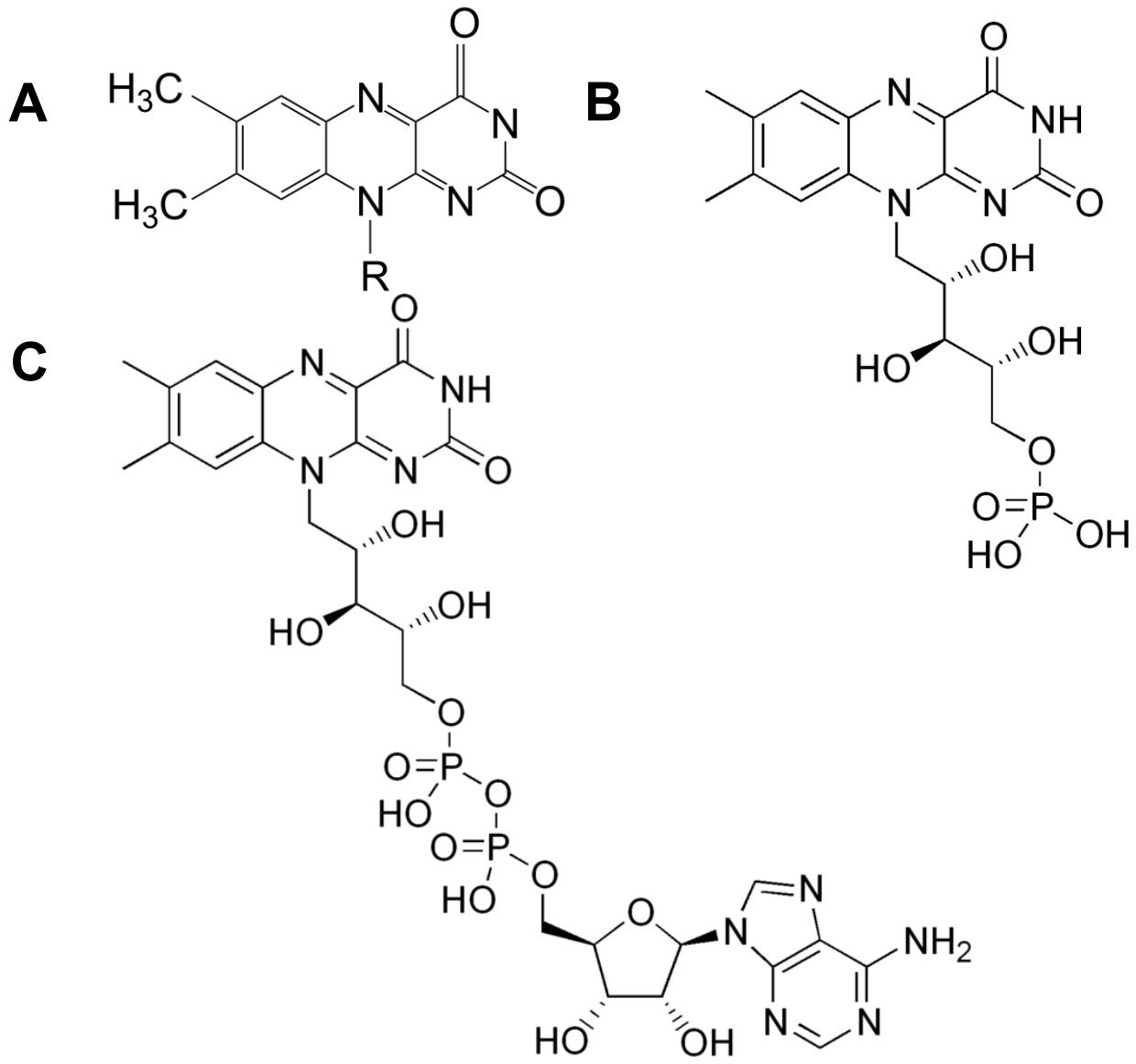

Figure 2.2. (A) Structure of Isoalloxazine, common prosthetic group found in flavoproteins. The R-group varies and differentiates various flavins. For example, (B) Flavin mononucleotide (or FMN) is a phosphorylated form of riboflavin. It is in one or the other of these forms that flavin is present as a prosthetic group in flavoproteins. (C) the flavin moiety, attached to an adenosine diphosphate is known as flavin adenine dinucleotide (FAD).

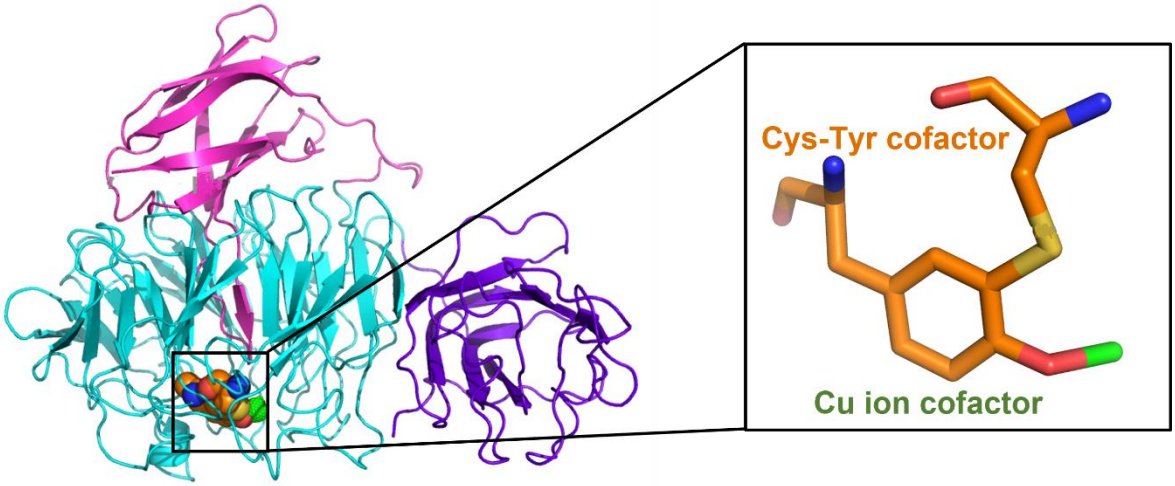

Figure 2.3. Galactose oxidase contains a mononuclear copper ion (light green) coordinated to a post translationally modified, cross-linked cysteine-tyrosine radical cofactor (orange). (PDB ID 1GOG)

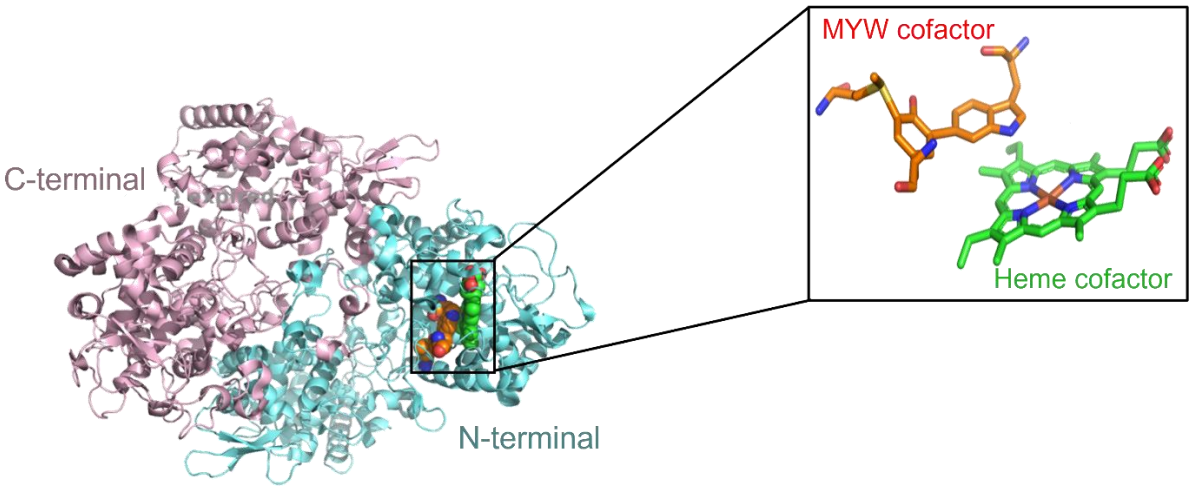

Figure 2.4. X-ray crystal structure of KatG revealed the presence of three covalently cross-linked amino acid residues Met-Tyr-Trp (orange), located on the distal side of the active-site heme (green). (PDB ID 2CCA).

Although prosthetic groups are integral component of the enzymes, these can often be removed from the enzyme by chemical methods or withheld from target enzymes through biological manipulation. Cofactors can be reinserted (modified or otherwise) to obtain enzymes with different or delayed catalytic properties. This process is termed as enzyme reconstitution. Reconstitution allows the reinsertion of naturally occurring or synthetic cofactors with the aim of investigating the reaction mechanism or developing synthetic proteins with new catalytic functions.[223,224]

One of the most common method of reconstitutions is the extraction of the tightly bound cofactor from protein to yield the respective apoenzyme which can subsequently be reconstituted with the natural or artificial analogue of the native cofactor.[225] For example, heme was first extracted from horse heart myoglobin using organic solvents such as butan-2-one and acetone under acidic conditions (pH 2.0 – 4.0) to prepare apo forms of that protein.[226] Later, this method was applied for producing apo versions of other heme proteins such as horseradish peroxidase (HRP) and some variants of cytochromes.[227] .[228] However, stability of the apoprotein is a concern during the treatment of harsh organic chemicals and acidic conditions. Moreover, this technique was further complicated by the unavailability of suitable metal complexes possessing a protoporphyrin IX framework. [228] Another widely used hemoprotein expression method is the addition of hemin or hemin precursor δ-aminolaevulinic acid to the growth medium prior during expression.[229,230] This method has resulted in sufficient production of the holoprotein in ascorbate peroxidase,[229] but complicated by the fact of incorporating heme into completely folded protein, and thus, causing increased risk of nonnative heme coordination and biological interference.[231,232] Another technique for increasing heme incorporation into recombinant proteins involves supplying the bacteria with hemin in the growth media. One downside of this method is the lack of an efficient heme transport system in laboratory *Escherichia coli* strain, causing a reliance on diffusion through

the cell membrane of the bacterial system. Iron-transport systems are important because access to this essential element is severely limited in the host. In addition to that, using a high expression plasmid with a strong promoter (*e.g.*, T7) enhances the rate of protein synthesis but not the rate of heme biosynthesis.[233] As a result, a significant population of protein expresses without the heme prosthetic group.[234–236] Therefore, efficiency of the method requires a co-expression of several heme transport proteins, which could limit yields, and/or require addition of the heme cofactor.

To circumvent this problem, a heme protein expression system (HPEX) was developed, which is particularly advantageous for pathogenic bacteria due to their ability to use heme and/ or hemoglobin. The system is based on a series of plasmids (pHPEX) that contain the gene (*chuA*) from *E. coli* 0157:H7. The gene *chuA* encodes a 69-kDa outer membrane protein responsible for heme uptake.[237] These engineered plasmids are capable to yield target hemoproteins without limiting the rate of protein expression.[232] Numerous techniques have been developed over the years to circumvent the drawbacks of previously reported methods to increase the efficiency of the reconstitution protocol, because this is an excellent tool for elucidating structure–activity relationships of enzymes and also to analyze new functionality in the protein.

In this study, we report a simple and effective protocol for reconstitution in our recombinant *Mycobacterium tuberculosis* KatG with its heme *b* cofactor. KatG is novel among H_2O_2-degrading enzymes in that it can utilize a single active-site to perform both catalase ***and*** peroxidase activity for the degradation of H_2O_2. Despite the active center similarities between KatG and typical peroxidases, there are a few features that are specific to KatG. The most conspicuous among these is an adduct formed by the covalent linkage of methionine, tyrosine,

and tryptophan (MYW) side chains. Every structure that has been solved for KatG from different organisms[156,162,238–241] shows the presence of this covalent adduct. Substitution of any of the residues of the MYW adduct by site-directed mutagenesis consistently produce KatG variants that have negligible catalase activity[93,94,157,242,243] but uncompromised peroxidase activity. Our work and that of others has established that MYW adduct formation is a heme-dependent, autocatalytic process that occurs upon reaction with the first few equivalents of peroxide.[244] KatG, despite being built using a peroxidase scaffold as its core, utilizes this unique adduct to perform remarkable catalase activity which is at least three magnitude higher than any other member of its entire superfamily. Elucidation of the biosynthetic mechanism of this unprecedented MYW adduct and how it is utilized within the active site to impact the overall protein's function are the fundamental questions that remain to be answered. A long-standing obstacle to investigate the mechanism of formation of the MYW adduct has been an inability to consistently produce sufficient quantities of KatG where these post-translational steps have not yet occurred. An effective protocol was due from all previous studies which can unambiguously be applied to yield a high amount of protein with consistent activity. Here, we report a reconstitution protocol, which consistently yields catalytically active protein commensurate with the mature protein (*m*KatG). Typically, *m*KatG is produced either by the addition of exogenous heme to expression culture media or from sufficient *de novo* heme biosynthesis by cells during expression. The presence of heme in the KatG active site along with endogenously generated peroxides enables the autocatalytic formation of the MYW adduct during expression, and isolation of the *m*KatG during purification.[47,245]. Such protocols are well established and have been used for many years to yield highly active protein for a broad range of investigations of KatG structure and mechanism. However, *m*KatG cannot support studies evaluating the biosynthesis of the MYW cofactor because it is already

established before KatG can be purified for further study. Our protocol for producing reconstituted KatG (*r*KatG) begins with the expression and partial purification of apo KatG (*a*KatG). This *a*KatG is incubated with hemin followed by completion of the purification procedure, and *r*KatG is the result. Our data show that *a*KatG lacks heme, the MYW adduct, as well as catalytic activity. Upon reconstitution, *r*KatG contains the full complement of the heme cofactor and shows catalytic activity in steady-state kinetic assays. Nevertheless, evaluation of *r*KatG by LC-MS shows that the MYW cofactor has yet to be established. Importantly, treatment of *r*KatG with peroxide results in the establishment of the MYW adduct (*i.e.*, *m*KatG).

2.2. Materials and Methods

*2.2.1. Expression of a*KatG

Expression of *a*KatG was carried out in *E. coli* (BL21 [DE3] pLysS) transformed with the pMRLB11 plasmid, a pET23b-based construct containing *M. tuberculosis katG* such that the expressed KatG protein would contain a C-terminal 6× His-tag. The pMRLB11 plasmid was originally obtained from the TB Vaccine Testing and Research Materials Contract at Colorado State University. Miller LB broth cultures supplemented with ampicillin (100 mg/L) and chloramphenicol (100 mg/L) were inoculated pMRLB11 transformants identified above and incubated at 37 °C until an OD_{600} of 0.48-0.68 could be obtained at which time expression was induced by inclusion of 1 mM isopropyl-b-D-1-thiogalactopyranoside (IPTG). Following induction, culture temperatures were reduced and maintained at 20 °C for 12 hours. Samples were periodically withdrawn from the growing culture for analysis of protein expression levels. At 12 hours post-induction, cells were harvested by centrifugation at 5000 rpm. The resulting pellet was stored at -80 °C until purification. Successful expression of KatG was verified by trichloroacetic acid (TCA) precipitation and SDS-PAGE gel analysis.

2.2.2. *Purification of a*KatG

For purification cell pellets were resuspended in 50 mM potassium phosphate, 200 mM NaCl, pH 7, supplemented with the serine protease inhibitor phenylmethylsulfonyl fluoride (PMSF) (50 mM PMSF, 200 μL/expression L). Resuspended cells were then homogenized to a smooth slurry using a Dounce glass tissue grinder. Cell lysis was performed by sonication (Branson 250 sonifier, Danbury, CT) using 8 cycles (42 seconds on/42 seconds off) at 30% duty. To the cell lysate, benzonase nuclease (2 μL/expression L) was added to hydrolyze all types of nucleic acid contaminants to individual or oligonucleotides. The solution was then incubated at 4 °C with gentle agitation for 4 to 6 hours. The lysate was then centrifuged at

10,000 × *g* for 30 minutes at 4 °C to precipitate cellular debris. The supernatant was retained and mixed with Ni-NTA resin (5 mL/ liter of expression culture) previously equilibrated with 50 mM Tris, pH 8. The supernatant-resin mixture was incubated at 4 °C with constant, gentle agitation for 12 hours. The supernatant-resin slurry was then poured into a glass column for target protein elution through competitive interaction of imidazole-containing elution buffers. To achieve a higher protein concentration, the protein was eluted in a step gradient of imidazole wash solutions (20, 40, 60, 75, 100, 200, and 500 mM imidazole in 50 mM phosphate, 200 mM NaCl, pH 7.0). Subsequent washes were carried out using 50 mM Tris, pH 8.0; 50 mM phosphate, 200 mM NaCl, pH 7.0, and imidazole wash solutions afterwards. The bulk of the target KatG protein was observed to elute with the 40, 60, and 75 mM imidazole wash fractions. SDS-PAGE gel analysis was performed to evaluate the purification. Fractions containing KatG were combined and concentrated using centrifugal filters (Pall Laboratory, Port Washington, NY) with 30 kDa molecular weight cutoff. Centrifugation was carried out at 3800 × *g* to reach a final retained volume of ~3 mL. The retentate was then introduced onto an Econo-Pac 10G desalting column (BioRad, Hercules, CA) equilibrated with 5 mM phosphate, pH 7.0. The resulting purified protein was kept at -80 °C for at least 12 hours before reconstitution.

*2.2.3. Reconstitution of a*KatG *to Produce r*KatG

A frozen aliquot of purified *a*KatG was diluted to produce a working stock solution of 100 μM enzyme in 5 mM phosphate, pH 7. A hemin (M.W. 651.94 g/mol) stock solution of 175 μM was prepared in 10 mM NaOH solution immediately prior to use. A buffer solution of 0.1 mM potassium phosphate, pH 6.2, was also prepared according to the Table 2.1. The KatG to heme molar ratio desired in this mixture was 1:0.875. To prepare *x* mL of reconstitution solution, *x*/4 mL of 175 μM hemin stock solution was added slowly to *x*/2 mL of 100 μM *a*KatG stock solution. After a 10-min. incubation on ice, *x*/4 mL of potassium phosphate, pH

6.2, was added to the protein-heme mixture. The mixture was then incubated for 4-6 hours at 4 °C with occasional gentle agitation. Centrifugal filters (30 kDa MW cutoff) were used to concentrate the protein before loading onto an Econo-Pac 10G desalting column. This size exclusion column efficiently retains unbound and adventitiously bound hemin while the protein with active site-bound heme emerges in at volume close to the column void volume. The enzyme was further purified through anion exchange chromatography, which achieves efficient separation of any remaining heme-deficient *a*KatG from heme-containing *r*KatG. Purity of the protein was confirmed by SDS-PAGE gel analysis, in combination with spectrally observed optical purity (or Reinheitzahl) ratio ($Rz = A_{406}/A_{281}$). Fractions with the higher *Rz* values (> 0.45) were combined and concentrated in 5 mM phosphate, pH 7.0. Reconstituted enzyme concentration was evaluated using the pyridine hemochromagen assay as previously described.[246] Activity of *r*KatG preparations were checked prior to storing at -80 °C. The schematic representation of reconstitution method was illustrated in Figure 2.5.

Table 2.1. Preparation of 0.1 M potassium phosphate buffer at 25 °C.

pH	**Volume of 1M K_2HPO_4**	**Volume of 1M KH_2PO_4**
5.8	8.5	91.5
6.0	13.2	86.8
6.2	19.2	80.8
6.4	27.8	72.2
6.6	38.1	61.9
6.8	49.7	50.3
7.0	61.5	38.5
7.2	71.7	28.3
7.4	80.2	19.8
7.6	86.6	13.4
7.8	90.8	9.2
8.0	94.0	6.0

0.5 L of 1 M K_2HPO_4 at 174.18 g mol^{-1} = 87.09 g
0.5 L of 1 M KH_2PO_4 at 136.09 g mol^{-1} = 68.045 g

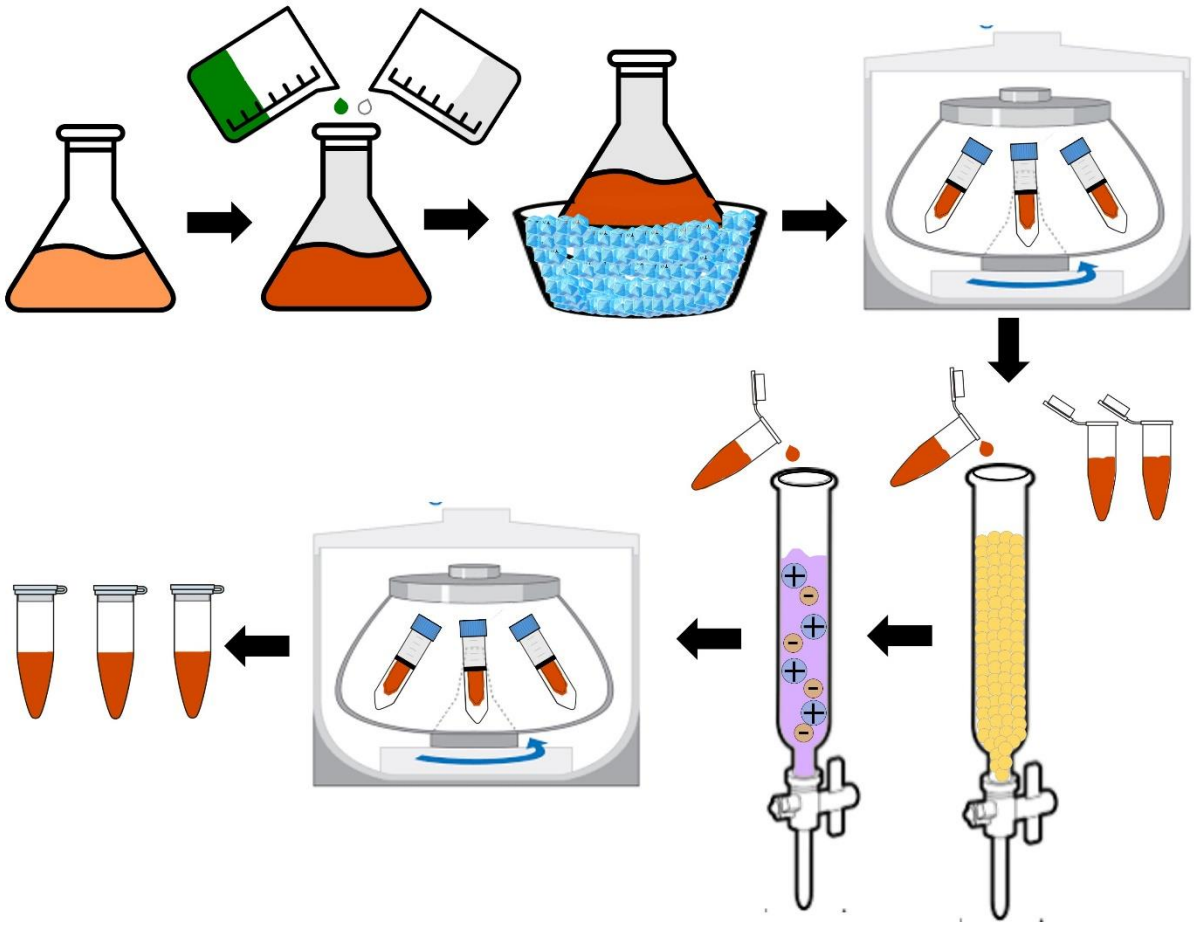

Figure 2.5. Schematic representation of the reconstitution method. Major steps involved here are dilution of *a*KatG, quantitative mixing of hemin and potassium phosphate buffer, ice incubation, centrifugation, size exclusion chromatography, anion-exchange chromatography, centrifugation for desalting/ buffer exchange and finally storage in -80 ℃ freezer.

*2.2.4. Expression and Purification of m*KatG

Chemically competent *E. coli* C41(DE3) cells were transformed using the *h*eme *p*rotein *ex*pression plasmid pHPEX3 to express the *m*KatG and variants[232] and transformants were selected on the basis of tetracycline/ampicillin resistance. Expression and purification of *m*KatG and all variants was carried out according to previously published procedures.[150]

2.2.5. UV-vis Spectroscopy

Following purification, the heme content of *r*KatG and *m*KatG was estimated by UV-visible absorption spectra using a Shimadzu UV 1601 PC spectrophotometer (Columbia, MD). Spectra (250 - 800 nm) were recorded using x KatG concentration in 100 mM phosphate, pH 7.0. All spectra were recorded at room temperature (23 °C). Spectra were adjusted based on equivalent absorption at 280 nm to normalize for protein concentration. The optical Purity ratio (Reinheitzahl or *Rz*, defined as A_{Soret}/A_{280}) was calculated for all three forms of protein (*a*KatG, *r*KatG, and *m*KatG).

2.2.6. Electron Paramagnetic Resonance Measurements

Electron paramagnetic resonance (EPR) spectroscopy was utilized to evaluate the resting (*i.e.*, ferric) states of *r*KatG and *m*KatG. Each protein was concentrated to 300 µM in 5 mM phosphate, pH 7.0, using centrifugal filters with 30 kDa MW cutoff. Each sample was then loaded into precision bore EPR tube and immediately immersed in liquid nitrogen until spectral data could be recorded. Low temperature EPR spectra were collected at 4.5 K using Bruker EMX X-band EPR spectrometer. Unless otherwise indicated, instrument parameters were as follows: microwave frequency, 9.393 GHz; modulation amplitude, 10 G; modulation frequency, 100 kHz; microwave power, 1 mW; time constant 163.84 ms; sweep time 167.772

s; number of scans, 1; conversion, 163.84 ms; resolution, 1024 point; receiver gain, 1.0×10^4; and phase, 0 degrees.

2.2.7. Enzyme Assays

Following purification, *m*KatG and *r*KatG were evaluated for their catalase and peroxidase activities. Catalase activity was evaluated spectrophotometrically by monitoring the decrease in H_2O_2 concentration over time at 240 nm ($e = 39.4\ M^{-1}cm^{-1}$).[247] Assays contained 20 nM KatG and H_2O_2 concentrations ranging from 0.05 - 50 mM. All assays were conducted over a 60 s time window, and initial rates were calculated by linear least-squares analyses of the early reaction times. Catalase activity was also evaluated by monitoring O_2 production over time using Clark-type O_2-sensitive electrode (Hansatech, Pentney, Norfolk, UK) as described previously.[248] These assays employed 5 nM KatG and were carried out at room temperature (23° C) in either 50 mM acetate and/or 100 mM phosphate buffer at the corresponding pH of the reaction. Peroxidase activity was determined by monitoring the formation of $ABTS^{\bullet+}$ at 417 nm upon reacting the 20 nM enzyme with 0.1 mM ABTS, and a range of H_2O_2 concentration (0.01 - 5 mM) in 50 mM acetate, pH 5. Kinetic parameters (k_{cat}, k_{on}) were obtained from nonlinear regression (nonlinear least-squares fitting) of KatG activity dependence on H_2O_2 concentration. In order to ensure that the two desired parameters were the result of direct fitting rather than the result of an operation that depended on two parameters whose accuracy requires saturation, we used a rearranged Michaelis-Menten model to fit the data (Equation **1**) and kinetic constants reported here for catalase activity are "apparent" values. Here, $[E]_T$ is the total concentration of enzyme present in the assay reactions (see above), k_{cat} is the asymptotic $v_o/[E]_T$

$$\frac{v_o}{[E]_T} = \frac{k_{cat}[H_2O_2]}{\frac{k_{cat}}{k_{on}} + [H_2O_2]} \quad \textbf{[1]}$$

approached as [H_2O_2] approaches saturation and is the maximum catalytic output of the enzyme. The parameter k_{on} is the catalytic efficiency of the enzyme and is observed at concentrations of [H_2O_2] well below that which yields half the enzyme's maximum rate (i.e., well below the K_M for H_2O_2). The k_{on} is also given by the k_{cat}/K_M with respect to [H_2O_2]. Under some conditions, KatG displays a multicomponent response to H_2O_2, where the first component is a high-sensitivity Michaelis-Menten rectangular hyperbola governed by a relatively low K_M. The second is a low-sensitivity component whose K_M is too large to be observed within the H_2O_2 concentration range that can be utilized. Accordingly, only an apparent second-order rate constant (k_{app}) for this component is estimated in data fitting (equation **2**).[245]

$$\frac{v_0}{[E]_T} = \frac{k_{cat}[H_2O_2]}{\frac{k_{cat}}{k_{on}} + [H_2O_2]} + k_{app}[H_2O_2] \qquad [\mathbf{2}]$$

2.2.8. Tryptic digests and LC-MS detection

Formation of MYW adduct in *r*KatG was initiated by reacting the protein with peroxides (5 equivalents of peracetic acid) and compared against *a*KatG and *m*KatG and untreated *r*KatG. 250 µL of 50 µM solution of KatG (~ 1 mg of KatG) was diluted in 50 mM

NH_4HCO_3. Reaction mixture was incubated for 3 h at 37 °C for proteolytic digestion in presence of Promega Sequencing-grade modified trypsin (200:1 protein to protease ratio) at pH 8.0. 20 µL of glacial acetic acid has been added at the end of 3 hours to quench the reaction. Molecular masses were determined on an ultra-performance LC system (ACQUITY with TUV Detector, Waters Corp., USA) coupled with a quadrupole time-of-flight mass spectrometer (Q-Tof Premier, Waters) with electrospray ionization (ESI) in positive mode using Masslynx software (V4.1). LC was performed by injecting 10 µL of the sample onto a C18 column (Waters UPLC BEH C18 2.1x50 mm, 1.7 µm) with a 300 µL/min flow rate of mobile phase solution A (water with 0.1% formic acid) and solution B (95% acetonitrile:5% water and 0.1%

formic acid). The UV absorbance at 330 nm was collected at 40 points/second. The capillary voltage was set at 3.1 kV, the sample cone voltage was 30 V, and the extraction cone was 4.3 V. The MS scan was 1.0 s long from 100 to 4000 *m/z* with a 0.02 s inter-scan delay using the centroid data format. MS/MS scans were 0.5 to 1.0 s long with a 0.02 s inter-scan delay with a collision energy ramp from 20 V to 40 V.

2.3. Results and Discussion

2.3.1. *Expression of a*KatG *in the BL21(DE3) pLysS System*

To verify the expression of KatG by *E. coli* BL21(DE3) pLysS cells and compare it with to enzyme expressed by our strain for production of *m*KatG, we withdrew aliquots from active expression cultures of pMRLB11-transformed *E. coli* C41 (DE3) pHPEX3 and pMRLB11-transformed *E. coli* BL21(DE3) pLysS cells prior to and following induction with IPTG. Aliquots were subjected to trichoroacetic acid precipitation, pellets were suspended in SDS-PAGE loading buffer, and separated by SDS-PAGE. Post-induction expression of *a*KatG in heme-deficient media continued for 12 hours at 20 ℃ whereas post-induction expression of *m*KatG in hemin supplemented media continued for 4 hours at 37 ℃. With aliquots of both types of cells, we observed an intense protein band which migrated with an apparent molecular weight of 80 kDa (Figure 2.6 A and B). This corresponds to the monomer molecular weight of KatG. A gradual increase in the intensity of this band was observed for at least 10 hours in BL-21 (DE3) pLysS cell cultures whereas expression by C41 pHPEX3 cells tended to remain constant or even decrease after the third hour of incubation after IPTG induction. Our results indicated that, *E. coli* BL21 (DE3) pLysS supports the substantial expression of recombinant KatG even in the absence of hemin- supplemented media. The pLysS plasmid containing the T7 lysozyme gene (LysS), regulates the T7 RNA polymerase-based pET system by causing the inhibition until the IPTG induction. A low-temperature expression system (20 ℃) has shown

to be advantageous for the production of toxic proteins whose activities are harmful to the host cells, such as proteases that degrade the essential components of the host by suppressing the enzyme activity. This low temperature is also favorable to the overproduction of proteins that tend to form inclusion bodies.[247] The level of expression in the heme-deficient medium by BL-21 (DE3) pLysS cells is more robust than that observed with hemin-supplemented cultures of *E. coli* C41 pHPEX3 (Figure 2.6). Previous study on other hemoproteins from *E.coli* also observed low heme incorporation in BL21 (DE3)-pLysS cell line.[232]

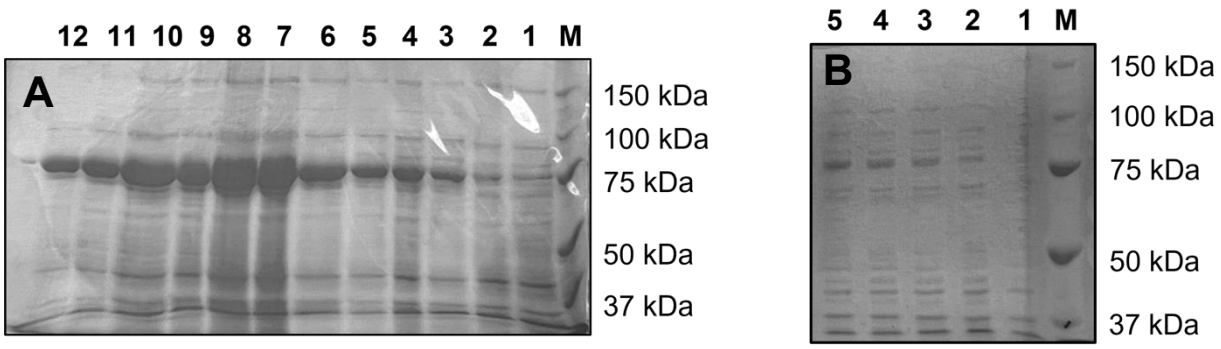

Figure 2.6. SDS-PAGE gel analyses of IPTG-induced expression products from *E. coli* BL-21 (DE3) pLys (A) and C41 pHPEX3 (B). In each panel, Lane 1 corresponds to cells withdrawn just prior to IPTG induction. An aliquot was drawn from each hour thereafter for 11 hours (A) or 4 hours (B). Each aliquot of cells was subjected to trichoroacetic acid precipitation and resuspended in SDS-PAGE loading buffer prior to gel loading.

2.3.2. *UV-visible absorption features of a*KatG, *r*KatG *and m*KatG

Because we observed that large amounts of *a*KatG were produced by *E. coli* BL21 (DE3)-pLysS cells in hemin-deficient media, we then evaluated the efficiency of heme incorporation into this protein upon reconstitution with the cofactor (*r*KatG). The results were compared to protein produced using the C41 (DE3) pHPEX3 cell line in hemin-supplemented media (*m*KatG). Heme occupancy was estimated by calculating the Reinheitszahl ratio (*Rz* = A_{407}/A_{280}). We consistently observed a ten-fold increase in *Rz* value from *a*KatG (0.05) to *r*KatG (0.48 – 0.56). This confirmed the very low heme occupancy for *a*KatG preparation of enzyme prior to reconstitution. Our purified *r*KatG showed *Rz* values consistent with the conventionally expressed mature protein being fully loaded with heme (*Rz* 0.6-0.7).[47,89,165] Although additional heme reconstitution resulted in an even higher *RZ* value of 0.65 (data not shown), we refrained from this additional heme incorporation as it resulted in contributions from adventitiously bound heme, interfering with the homogeneity of the sample. Successful incorporation of heme into the active site of *a*KatG by our reconstitution protocol was confirmed by the comparative absorption features of *a*KatG, *r*KatG and *m*KatG (Figure 2.7 A). The substantial increase in the Soret intensity (406 nm) from *a*KatG to *r*KatG is mentioned above. It should be noted that the λ_{max} and line shape of the Soret band are consistent with enzyme-bound heme and in stark contrast with heme free in solution which has a λ_{max} near 385 nm and much diminished molar absorptivity. In addition, charge-transfer bands (504 and 630.5 nm) observed for reconstituted proteins agree with the values obtained for the mature protein, thereby confirming the electronic structures of the heme is not perturbed upon its exogenous addition (Table 2.2).

Our *m*KatG preparations show a broader Soret band with a λ_{max} near 407 nm and a characteristic shoulder at 370 nm. These features are indicative of a mixture of

hexacoordinate and pentacoordinate high-spin ferric heme states. By comparison, Fe^{III} horseradish peroxidase (HRP) is almost entirely in the pentacoordinate high-spin state. It has a broader Soret band with a l_{max} at 403 nm and more prominent contributions at 370 nm. In contrast, our *r*KatG demonstrates a narrower Soret band with a lesser contribution to absorption below 400 nm (Figure 2.7 A), suggesting a greater contribution from hexacoordinate high-spin heme (6c-HS) than is observed with the *m*KatG preparation of our enzyme. Indeed, *m*KatG bears the features of greater contributions of 5c-HS heme evidenced by a shoulder at 370 nm along with Soret at 406 nm and a CT1 band at or above 640 nm.[249] As was initially evident from SDS-PAGE analyses of protein expression (see Figure 2.6), an additional benefit of preparing the enzyme in its *r*KatG form was the striking increase in yield (~800 nmol/L), which is 6 - 8 fold greater than that obtained from typical purifications of *m*KatG.

Of course, one of the anticipated distinctions between *r*KatG and *m*KatG would be the presence of the MYW covalent adduct in the former and its absence from the latter. At this point then, exposure of *r*KatG to peroxide should be sufficient to drive the autocatalytic formation of the adduct in *r*KatG. We reacted our *r*KatG enzyme with 100 molar equivalents H_2O_2. Spectra recorded following a ten-minute reaction time showed an increase in absorption from 300 – 350 nm, with the largest increase observed at 330 nm (Figure 2.7 B). There is some evidence of a shift in heme coordination toward a greater contribution of the 6c-HS state. However, the increase in absorption near 330 nm would be consistent with the formation of the MYW adduct.[177]

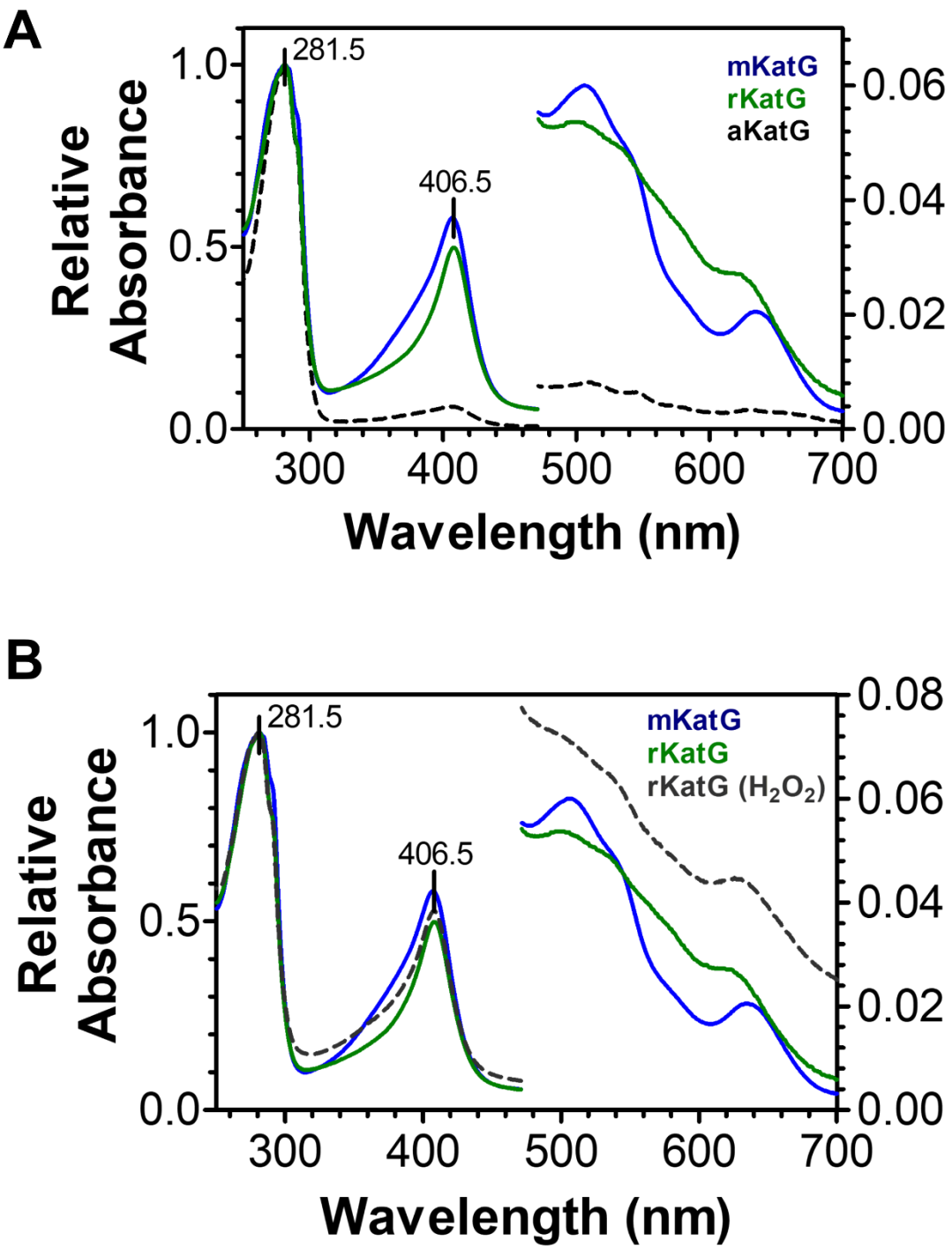

Figure 2.7. Comparison of UV-visible absorption spectra for KatG preparation products. Spectra for *a*KatG (dashed black), *r*KatG (green), and *m*KatG (blue) products are compared (A) as are spectra for peroxide-treated *r*KatG (dashed black), *r*KatG (green), and *m*KatG (blue) (B). Peroxide-treated *r*KatG was reacted with 100 molar equivalents H_2O_2. All spectra were recorded at 25° C using 100 mM phosphate, pH 7

Table 2.2. UV-vis absorption features of *a*KatG, *r*KatG, *m*KatG and peroxide treated *r*KatG.

KatG	***Rz* Value[a]**	**Soret (nm)**	**CT (nm)**	**Yield[b]**
*a*KatG	0.05	406	635.5	800
*r*KatG	0.51	406.5	504, 540, 630.5	300
*m*KatG	0.53	406.5	509, 543, 639	40
Peroxide-treated *r*KatG[c]	0.52	406	502, 543, 630	N/A

[a]*Rz* (Reinheitazhl) value is an optical purity ratio given by A_{407} nm/A_{281} nm. Typical ratios for KatG are 0.5-0.7.
[b]Yield refers to purified protein in terms of nmols KatG protein isolated per L of expression culture.
[c]Prior to recording of spectra, *r*KatG was prereacted with five molar equivalents of peracetic acid (PAA).

*2.3.3. EPR Spectroscopic Comparison of r*KatG *and m*KatG

UV-visible absorption features provided a general sense of the distribution of spin and coordination states of ferric forms of *r*KatG and *m*KatG. However, further insight on relative contributions of spin and coordination states can be discerned by EPR. As isolated, ferric KatG is dominated by high-spin ferric species with a mixed population of hexacoordinate and pentacoordinate states.[150,248,250] The X-band EPR spectra of both *m*KatG and *r*KatG clearly demonstrate the contribution of multiple high-spin ferric species (see the $g \sim 6$ region of each spectrum). This is typical of the KatG resting state. The g_z component which is observed at $g \sim 2$ for high-spin ferric heme enzymes can be helpful for discerning the relative contributions of axial and rhombic signals to KatG spectra. Both *r*KatG and *m*KatG were analyzed further based on their *g*-tensor anisotropy to determine the rhombic and axial characteristics of the heme structure. Although both KatG preparations showed a mixture of rhombic and axial signals which was well within the range observations across the field, the *r*KatG heme spectrum appeared to have a greater contribution from an axial signal. These distinctions are most clear in the $g \sim 2$ region where *r*KatG exhibits relatively small contribution from a g=1.96 feature (Figure 2.8). Importantly, hexacoordinate low-spin species (observed g_x, g_y, g_z of ~2.9, ~2.3, and ~1.5, respectively) which are known to be inactive forms of KatG[195,251] were not observed in any of our mature or reconstituted enzymes. This is consistent with the abundance of high-spin species observed in our UV-visible spectra. The prevalence of 6-coordinate high-spin complexes other than the low-spin species are assigned to enzyme containing water as a sixth ligand to heme iron.[252]

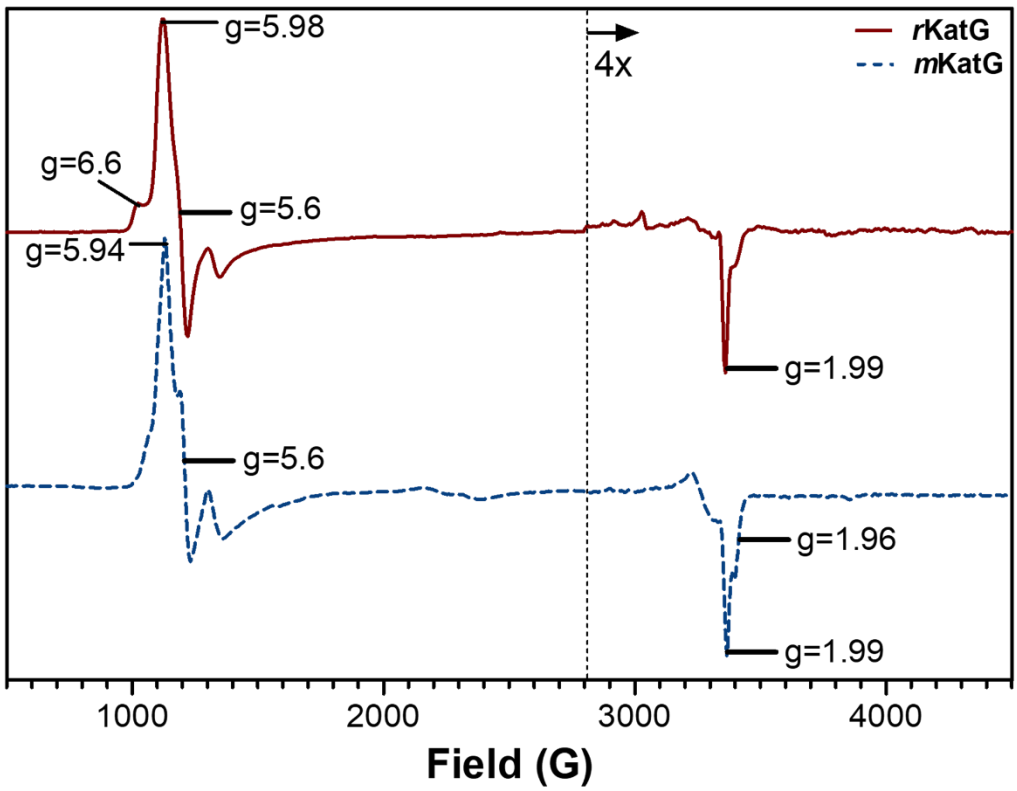

Figure 2.8. EPR spectra recorded for the ferric forms of *m*KatG (blue) and *r*KatG (red) preparations of the wild-type enzyme. All spectra were recorded at 4.5 K. Important EPR spectrometer parameters are reported in section 2.2.6.

2.3.4. LC Separation and MS Characterization of the MYW Adduct

We investigated *r*KatG generated by our protocol to determine the presence or absence of the MYW adduct in comparison to our *m*KatG purification product which should contain its fully formed MYW cofactor. To do this, tryptic peptides of apo, reconstituted, and mature forms of KatG were analyzed by LC-MS/MS to investigate the efficacy of our reconstitution protocol to generate heme-containing but MYW-deficient KatG. Eluting KatG tryptic peptides monitored at 330 nm revealed differences in heme content and the extent of MYW cofactor formation (Figure 2.9). Because heme incorporation occurred for *m*KatG during its expression in the *E. coli* cell where peroxides and other oxidants are also endogenously generated, its MYW adduct was formed prior to purification as confirmed by two peaks detected in the LC elution profile. One corresponded to the heme (~45 min) and the other corresponding to the covalent adduct (~32 min). The *r*KatG digest showed an equivalent signal to *m*KatG at a 45 min-retention time, consistent with the presence of heme. A much less intense feature at 32 min indicated that the MYW adduct had not yet been established for a large majority of the enzyme in the *r*KatG preparation. For *a*KatG minimal signal was detected at either retention time consistent with the absence of heme, and therefore, the inability to carry out the chemical steps to form the covalent adduct. The data from 330 nm elution profiles indicated that a negligible portion of MYW cofactor was present in *a*KatG and *r*KatG. The limited amount detected may be due to the presence of low heme content resulted from the expression host's own basal heme-biosynthetic activity.[253]. These data support the hypothesis that endogenous peroxides or other oxidants are necessary to advance formation of the MYW adduct following heme incorporation into the KatG scaffold. Thus, KatG receiving heme after purification (*i.e.*, *r*KatG) produces MYW-based signals (*i.e.*, 32-min elution features) more consistent with *a*KatG than *m*KatG. In support of this idea, reaction of *r*KatG with five molar equivalents of PAA (peracetic acid) prior to trypsinization produced LC chromatograms (monitored at 330

nm) highly similar to *m*KatG (Figure 2.9). Further inspection of MS ions corresponding those retention times (~45 min and ~32 min) also confirms their identity as the heme cofactor and MYW adduct respectively. Such LC chromatograms of the digested KatG (Figure 2.10) demonstrates that the reconstitution protocol indeed facilitates proper heme cofactor without promoting MYW adduct generation.

The presence of MYW cofactor in *m*KatG and PAA-treated *r*KatG was confirmed by analyzing trypsin-generated samples by mass spectrometry. Previous studies have shown that the fully covalent adduct including each participant's (i.e., Met 255, Tyr 229, and Trp 107) associated tryptic peptide generates a monoisotopic mass of 6880.0 Da. Specifically, this includes the tryptic fragments ^{255}**M**AMNDVETAALIVGGHTFGK^{274}, ^{215}DLENPLAAVQ-MGLI**Y**VNPEGPNGNPDPMAAAVDIR^{249}, and ^{105}MA**W**HAAGTYR^{114}. Several multiply-charged ions correspond to this species and are detectable in our LC/ESI-MS analyses.[89,165,254] The 1377.8 (+5), 1148.4 (+6), and 984.5 (+7) *m/z* ions detected with the 330 nm-positive peak eluting ~32 min were all observed (Figure 2.10) and matched with previously published MS analyses of the fully formed MYW cofactor of *M. tuberculosis* KatG[165]. In some instances, other ions are detected around this retention time these correspond to fragments of the MYW adduct observed at 1216.3 (+4) and 672.3 (+3). Both of these ions are the result of in-source fragmentation between the γ-carbon and the sulfur atom of the Met side chain of the MYW cofactor. The former (i.e., 1216.3 *m/z*) corresponds to the addition of a thiomethyl group to the YW portion of the adduct.[165] The latter (i.e., 672.3 *m/z*) corresponds to the 255-274 tryptic peptide where Met 255 has been deprived of its sulfur and ε-methyl group. . These in-source fragment ions 672.3 (3+) *m/z* and the 1216.3 (4+) *m/z* were also detected in our tandem MS analysis, resulted from a predominant ion. To further test our hypothesis that the reconstituted enzyme lacks the complete MYW cofactor but has the ability to properly form it upon treatment with peroxides, *r*KatG was treated with peroxides and the resulting contribution from MYW

derived peptide products was evaluated. PAA is a strongly oxidizing peroxide that can bind to the active-site heme of KatG and generate ferryl heme states without serving as a reducing substrate for those states (in contrast to H_2O_2 reactions involving *m*KatG). That is, PAA is not a physiological substate of KatG and hence, does not support catalase turnover. Accordingly, PAA has been used to facilitate formation of the MYW adduct. The elution profiles and ions detected for tryptic peptides eluting at 32 minutes are identical for both *m*KatG and 5 molar equivalents of PAA treated *r*KatG (Figure 2.10 A and B). The fragmentation pattern, indicating the cleavage at the sulfur atom are also identical for both *m*KatG and 5 molar equivalents of H_2O_2 treated *r*KatG (Figure 2.11 A and B). These results support our expectation that KatG protein prepared using reconstitution protocol has all the necessary attributes to further investigate the steps of autocatalytic MYW cofactor formation in KatG.

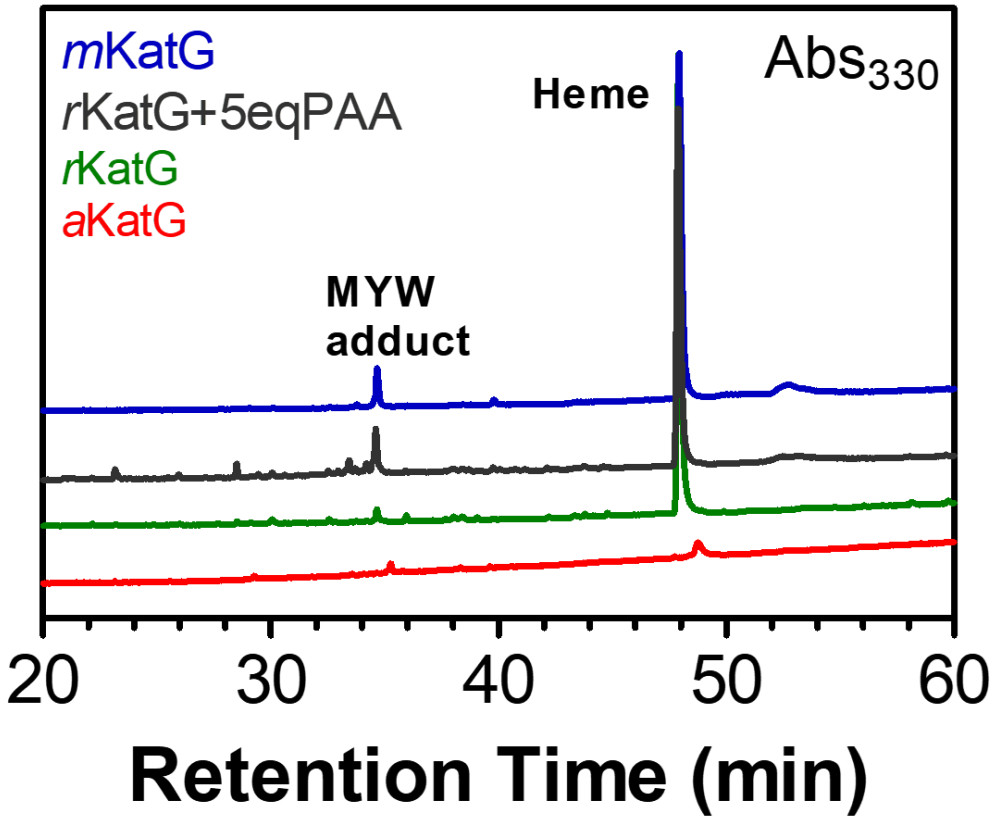

Figure 2.9. The LC elution profiles (330 nm) for trypsinized *a*KatG (red), *r*KatG (green), *m*KatG (blue), and *r*KatG pretreated with five molar equivalents peracetic acid (PAA) (black).

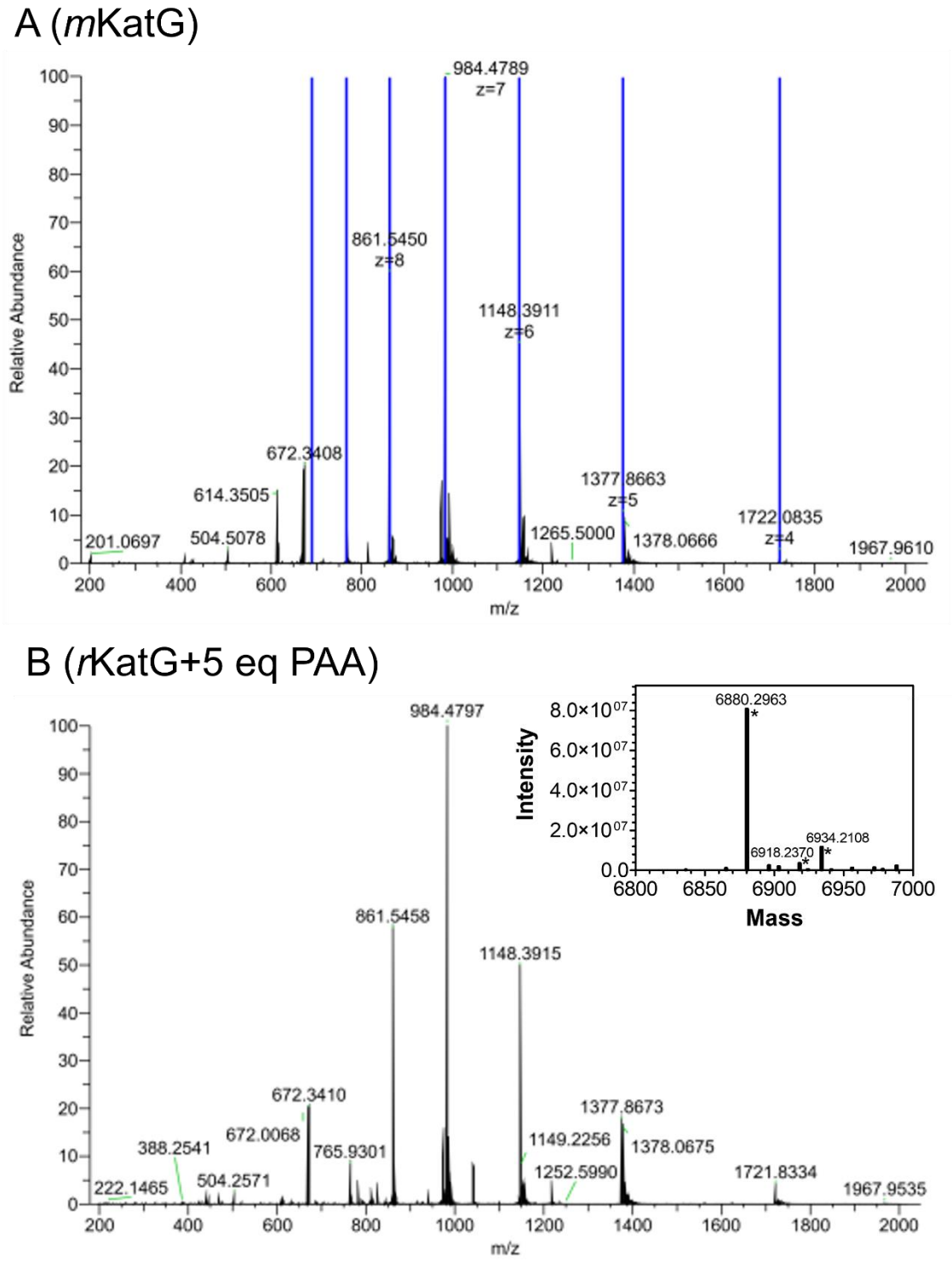

Figure 2.10. Mass spectra corresponding to the KatG tryptic peptide eluting at 32 min for *m*KatG (A) and *r*KatG following its treatment with 5 molar equivalents of PAA (B). The inset shows the mass spectrum of the calculated neutral (zwitterionic) mass of the fully covalently linked MYW and each residue's associated tryptic peptides.

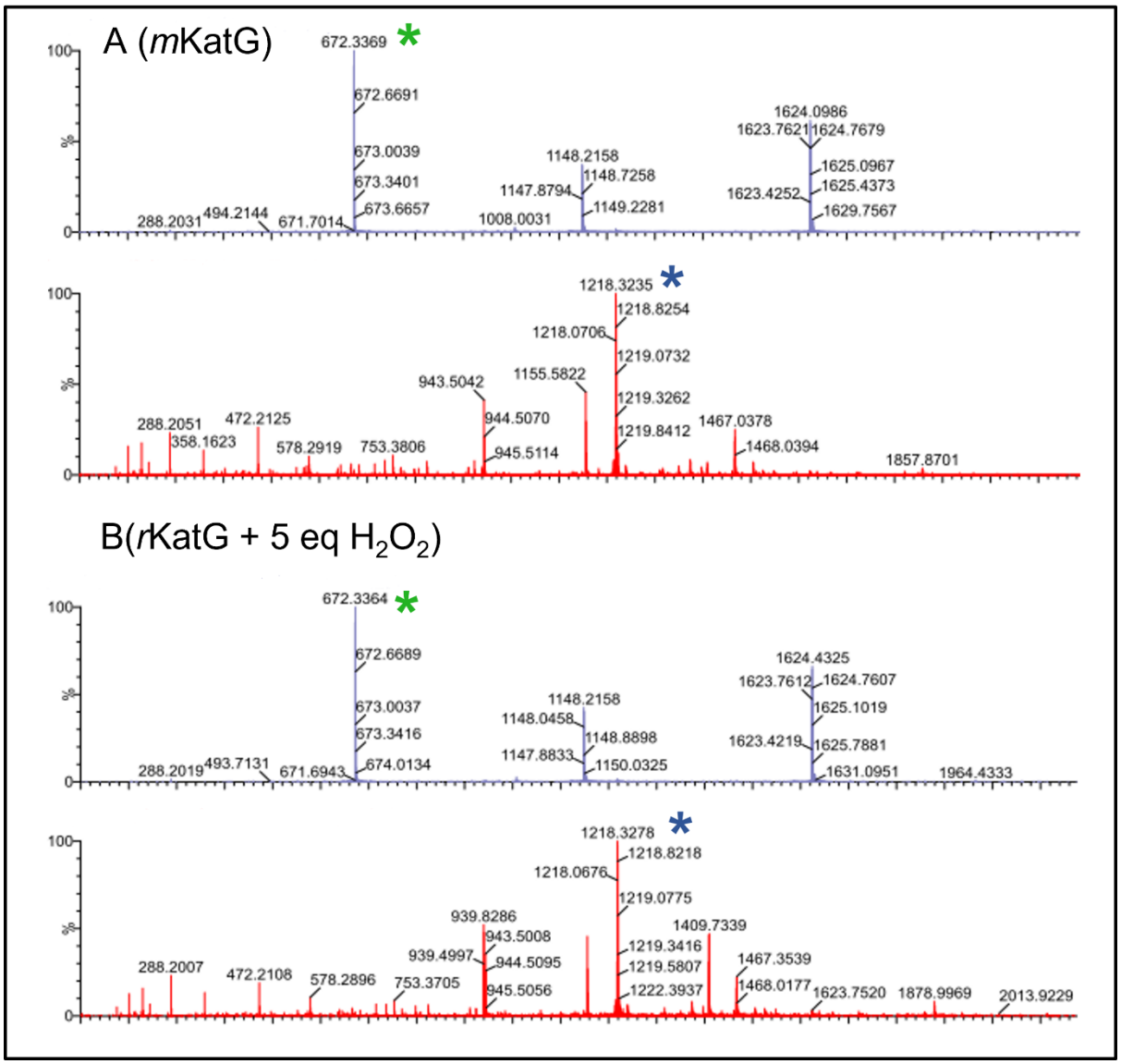

Figure 2.11. Mass spectra corresponding to the fragment assignment from a predominant ion. The tryptic peptides of *m*KatG (A) and *r*KatG following its treatment with 5 molar equivalents of H_2O_2 (B) show the presence of fragment ions 672.2 (+3) and 1218.3 (+4) resulting from the cleavage of full MYW adduct.

2.3.5. Catalase and Peroxidase Activities of KatG (apo, reconstituted and mature)

The efficiency of the heme reconstitution protocol was demonstrated by the catalase and peroxidase activities in *a*KatG, *r*KatG and *m*KatG. The steady-state kinetic investigations (k_{cat} and catalytic efficiency k_{cat}/K_m) were summarized in Table 2.3. The *a*KatG protein, lacking the MYW adduct, showed poor catalase activity with a turnover number (k_{cat}) of 1360 s^{-1}. Upon reconstitution, an overwhelming catalase activity was observed for *r*WT KatG with a turnover number (k_{cat}) of 4630 s^{-1} at the pH optimum (pH 7.0) consistent with the previously reported values[47] obtained for *m*WT KatG. At pH 5, catalase activity is compromised yet determinable for both forms of KatG, demonstrating that the integrity of MYW adduct is preserved successfully in *r*KatG. Peroxidase activity was measured by monitoring a H_2O_2-dependent oxidation of an organic electron-rich substrate, ABTS, thus showing peroxidatic activity. Titration with increasing concentrations of H_2O_2 and constant ABTS concentration (0.1 mM), showed a non-saturable kinetics comparable with *m*WT KatG hence accounted for apparent values.[250,252]

Table 2.3. Activity parameters for *r*KatG and *m*KatG

Activity	**KatG form**	**Kinetic Parameters**	
		k_{cat} (s^{-1})	k_{cat}/K_M ($M^{-1}s^{-1}$)
Catalase (pH 7.0) [a]	*r*KatG	4630 ± 19	$(1.1 \pm 0.1) \times 10^6$
	*m*KatG	4780 ± 36	$(1.0 \pm 0.2) \times 10^6$
Peroxidase (H_2O_2) [b, c]	*r*KatG	2.4 ± 0.1	$(3.2 \pm 0.4) \times 10^4$
	*m*KatG	1.7 ± 0.1	$(2.5 \pm 0.2) \times 10^4$
Catalase (pH 5.0) [d]	*r*KatG	830 ± 60.0	$(8.2 \pm 1.1) \times 10^4$
	*m*KatG	160 ± 30.0	$(3.1 \pm 2.6) \times 10^5$

[a] Activity by H_2O_2 consumption (240 nm) 23 °C in 100 mM phosphate, pH 7.0.
[b] All peroxidase activity evaluated at 23 °C in 50 mM acetate, pH 5.0.
[c] Peroxidase parameters with respect to H_2O_2 were determined using 0.1 mM ABTS.
[d] Activity was determined by O_2 production at 23 °C in 50 mM acetate, pH 5.0.

2.4. Conclusions

The unique catalatic mechanism of KatG is conferred by its novel features and evidence is continuing to accumulate that KatG uses a peroxidase scaffold, a one-of-a-kind Met-Tyr-Trp covalent adduct, and even assistance from peroxidatic electron donors (PxEDs) to perform its dominant catalase activity. It is also established that the MYW cofactor cannot be generated without the heme, and the heme is incapable of supporting KatG catalatic turnover on its own. To better understand the complex interplay between these two cofactors, it is essential to elucidate the mechanism of MYW cofactor formation. A well understood mechanism is anticipated to shed long-absent light on the unique catalatic mechanism of KatG. The major roadblock to achieving this goal has been the lack of a procedure to express and purify the enzyme in a form where the MYW adduct has yet to form. In this study, the protocol explained above for *a*KatG expression followed by heme reconstitution to generate our *r*KatG form of the enzyme has overcome the difficulties impeding the observation of cross-link formation. Moreover, this protocol is effective for generating very high yields of the active protein, creating the possibility of using more sophisticated and material-intensive techniques like EPR and Mössbauer spectroscopy to monitor MYW adduct formation events. This protocol is expected to enable monitoring the kinetics and appearance of catalytically competent intermediates that lead to the formation of the MYW adduct. Based on the data collected with the reconstituted protein, our **central hypothesis** is that the generation of the MYW adduct results from a series of properly directed intraprotein radical transfer reactions. Spectral evidence has been collected based on this hypothesis and discussed in the following chapters.

3. CHAPTER THREE

SPECTRAL EVIDENCE FOR THE HEME-DEPENDENT BIOSYNTHESIS OF THE KatG MYW PROTEIN-BASED COFACTOR

3.1. Introduction

Catalase-peroxidase (KatG) is an important virulence determinant in *Mycobacterium tuberculosis (Mtb)* due to its role in optimizing defense against high concentrations of H_2O_2, a compound generated by the deliberate action of higher eukaryotes to defend themselves against microbial pathogens.[116,118] This class I heme peroxidase has been specially engineered by nature to exhibit robust catalase activity like monofunctional catalases despite possessing low structural resemblance with such enzymes.[147,160] Aerobic metabolism as a matter of course produces toxic levels of H_2O_2, and its detoxification is carried out by a suite of enzymes that, for many bacteria and fungi, includes KatG, As alluded to above, for intracellular pathogens like *M. tuberculosis* the stakes are raised considerably, and the ability of KatG to efficiently dismutate H_2O_2 prevents the damaging consequences of highly destructive compounds that can be generated using H_2O_2 (*e.g.*, HOCl). It is the product derived from downstream reactions of H_2O_2 which typically act as a mediators of the cell death.[255] Thus, KatG ensures the persistence of pathogens within host immune cells[256] by actively mitigating the substantial cellular oxidative stress that comes at the host-pathogen interface.

Remarkably, KatG has all the marks of its membership in the peroxidase-catalase superfamily. Indeed, the enzyme shows substantial peroxidase activity, especially at acidic pH, and this is supported by all the active-site residues of a typical peroxidase that are shared by the fellow superfamily members like yeast cytochrome *c* peroxidase (C*c*P), ascorbate peroxidase (APX) etc.[257,258] Indeed, the active sites of C*c*P (2CYP)[259] and KatG (2CCA)[260] are virtually superimposable (Figure 3.1).

In addition to the peroxidase-typical residues, the KatG active site also hosts a unique, post-translationally generated structure resulting from a novel covalent linkage between Trp107 (Cη2) and an adjacent Tyr229 (Cε1) which further linked to the sulfur of a Met255 side chain (Figure 3.2). This MYW adduct is in close proximity to the active site heme cofactor and forms autocatalytically with the inclusion of peroxides. Site-directed mutagenesis on KatGs from several species has shown that the MYW adduct is essential for catalase activity. Accordingly, it is appropriately referred to as a protein-based cofactor. Notably, the MYW adduct is not required for peroxidase activity.[254,260]

Historically, all heme-dependent catalases and peroxidases undergo two-electron oxidation of the resting (i.e., Fe^{III}) enzyme by H_2O_2 (or alternative peroxides like peracetic acid) to generate an oxo-ferryl moiety (Fe^{IV}=O) with the concomitant formation of a porphyrin π-cation radical ($por^{\bullet+}$). This is known as compound I. At this point, KatG compound I undergoes an intramolecular electron transfer to generate a protein-based radical in place of the $por^{\bullet+}$. This is not unheard of among KatG's peroxidase relatives. Indeed, cytochrome *c* peroxidase oxidizes an active-site Trp to produce a Fe^{IV}=O[W191]$^{\bullet+}$ intermediate. However, KatG deviates from all known monofunctional catalases and peroxidases by using the MYW cofactor to rapidly quench the porphyrin radical, generating the KatG-unique compound I* (i.e,. Fe^{IV}=O[MYW]$^{\bullet+}$). Compound I* then reacts with second equivalent of H_2O_2. The identity of the intermediate formed has not been unequivocally identified. Its absorption spectrum is very similar to a species known as compound III.[47,170,244] Compound III is a Fe^{III}-$O_2^{\bullet-}$ state which is isoelectronic with the Fe^{II}-O_2 state known in oxygen storage/transport proteins as oxymyoglobin or oxyhemoglobin. In peroxidases, this intermediate, sometimes referred to as oxyperoxidase, readily forms in the presence of excess H_2O_2.[261] The contrast is that in typical peroxidase catalysis the Fe^{III}-$O_2^{\bullet-}$ (i.e., compound III) is inactive.[262] Thus, it is not without controversy that compound I* is proposed to react with H_2O_2 to form compound III* (Fe^{III}-$O_2^{\bullet-}$

[MYW]$^{\bullet+}$).[161,172,244] Regardless of the electronic structure of the intermediate, its spectrum is easily identifiable in optical stopped-flow experiments, and this is the species which dominates during stead-state consumption of H_2O_2 by KatG's catalase activity. The Fe^{III}-$O_2^{\bullet-}$[MYW]$^{\bullet+}$ is then proposed to undergo a second intramolecular electron transfer, returning the heme to the ferric state, restoring the MYW cofactor to its fully covalent form, and releasing molecular oxygen as a product (Figure 3.3). The asterisk (*) connected with compounds I and III in this context indicates the participation of the MYW-based radical in the errand of catalatic dismutation of H_2O_2.[244,173,171] This redox recycling of any covalent adduct (let alone an MYW species) and a Fe^{III}-$O_2^{\bullet-}$ intermediate in the presence of excess H_2O_2 is totally unique to KatG. As mentioned above, the (Fe^{III}-$O_2^{\bullet-}$) state of typical heme-dependent peroxidases is inactive, and these enzymes are unable to perform catalase activity. Meanwhile, typical (i.e., monofunctional) catalases are purported to only utilize the Fe^{III} and Fe^{IV}=O[por]$^{\bullet+}$ states to achieve the *catalatic* dismutation of H_2O_2.[263]

The novel protein-derived MYW cofactor solidifies KatG's place within a growing list of metalloenzymes that involve the covalent crosslinking of amino acid residues in or near their active sites. This intraprotein crosslinking strategy invariably produces modified properties (e.g., alternative redox intermediates, altered metallocentre reduction potential, increase in thermostability, etc.). A common theme is the fortuitous placement of oxidatively modifiable amino acids in close proximity to a metal center required for catalysis. Prominent examples include cytochrome *c* oxidase (His240–Tyr244; $heme_{a3}$-Cu_B)[264,265] and galactose oxidase (Tyr272–Cys228; copper).[75,266]

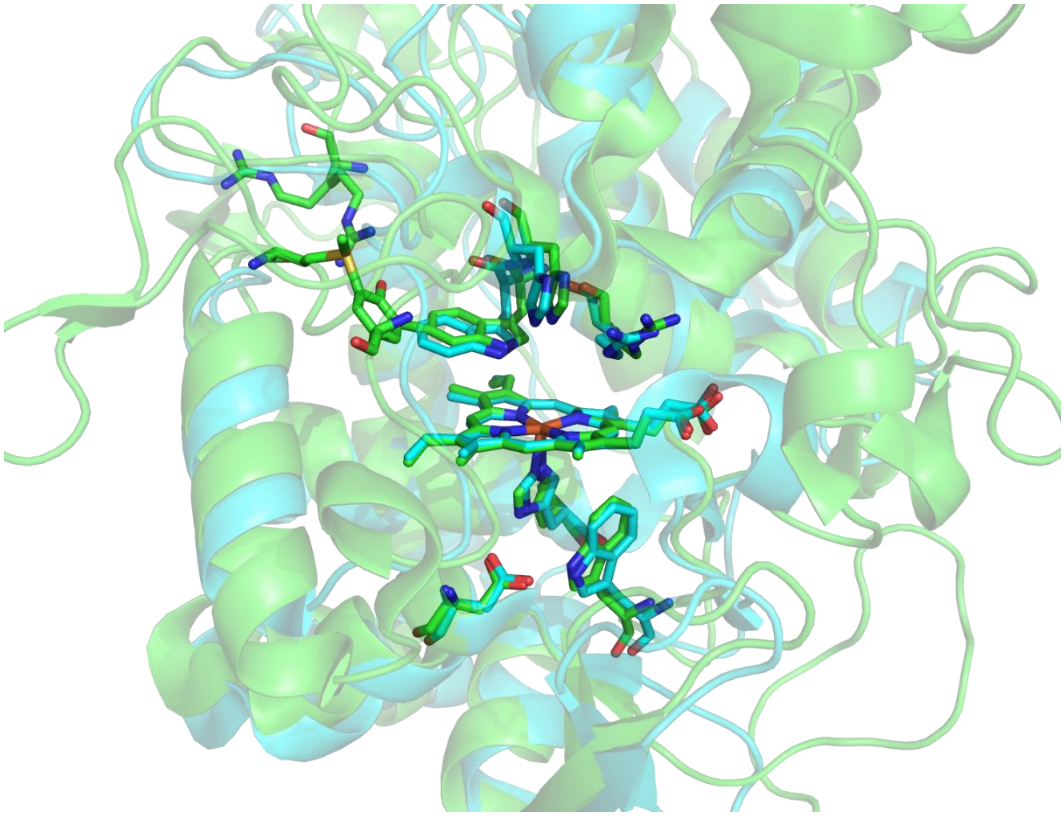

Figure 3.1. Overlay of the active sites of KatG and C*c*P. Residues common to both KatG and C*c*P are shown and annotated in green and teal, respectively. This image was generated using PyMOL 2.3.0.0 using coordinates from PDB accession code 2CCA (*Mtb* KatG)[159] and 2CYP (yeast C*c*P).[259]

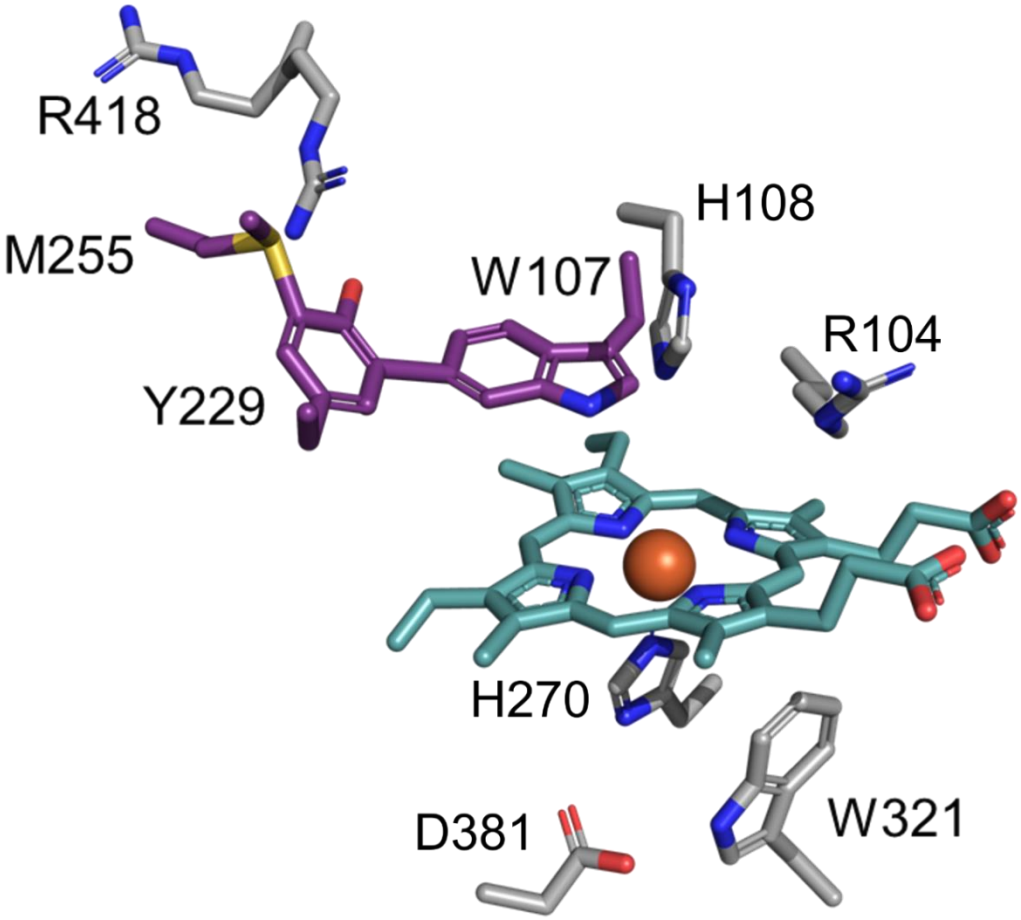

Figure 3.2. Cofactors within active site of KatG. The main active-site residues of KatG are presented in light gray, the MYW cofactor is presented in purple, and the heme cofactor is presented in teal. This image was generated using PyMOL v2.3.0.0 using coordinates from PDB accession 2CCA. [159]

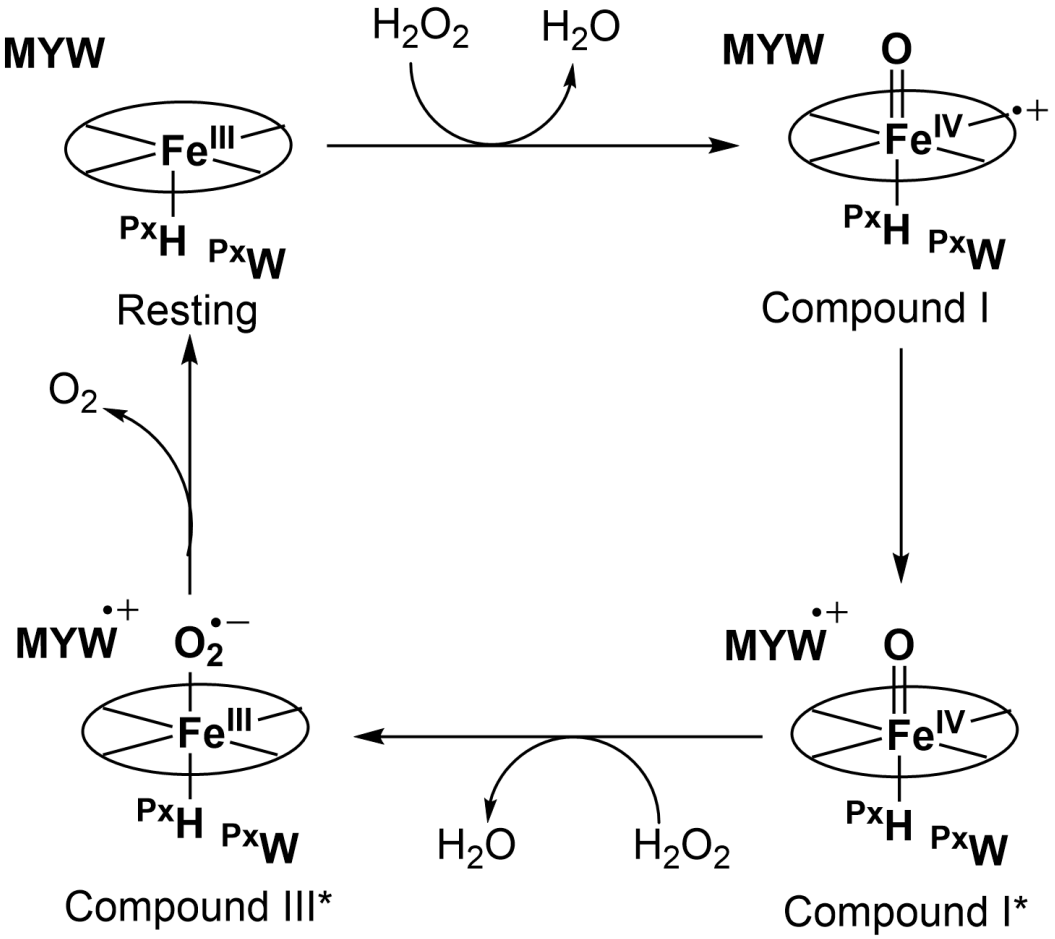

Figure 3.3. A proposed catalytic cycle for KatG catalase activity with putative reaction intermediates. The MYW cofactor cycles between its fully covalent (MYW) one-electron oxidized radical ($MYW^{\bullet+}$) states. As stated above, the asterisk (*) designation for compounds I and III denotes the participation of MYW adduct radical. The relative position of the enzyme's proximal tryptophan residue (W321 in *Mtb* KatG is designated by ^{Px}W. By convention, the heme's protein-based fifth ligand designates its "proximal" side. Thus, KatG's proximal histidine ligand to the heme is designated by ^{Px}H. By this same convention, the MYW adduct would be found on the heme's distal side.

Although KatG catalase activity operates by a novel mechanism, a full understanding of its mechanistic pathway has been a source substantial controversy within the KatG field for many years.[156,169,267] Perhaps the most difficult questions to address center on the mechanism of MYW cofactor formation. Since its initial discovery over twenty years ago,[88] this protein-based cofactor has presented numerous significant challenges to investigators seeking to understand its participation in KatG catalysis. Indeed, a full understanding of its participation in KatG's catalase activity has remained elusive due to its unresolved intermediates involved at different stages. A prominent roadblock to progress has been the great difficulty in separating the incorporation of heme during expression from the heme-dependent oxidiative chemistry that generates the adduct. On one hand, expression of KatG such that its heme cofactor is incorporated during expression invariably results in the full autocatalytic formation of the MYW cofactor prior to enzyme purification. On the other hand, KatG expressed without its heme cofactor has proven to be resistant to successful reconstitution.

The generation of MYW from its component side chains is proposed to arise from intramolecular electron transfers and protein-based radical mechanism. This idea brought forth the basis of this research with purpose of evaluating important reaction intermediates (heme-based and protein-based) that could lead us to follow the MYW formation in real time. Formation of MYW adduct appeared to be preceded first by heme and peroxide dependent generation of a Fe^{IV}=O[porphyrin]$^{\bullet+}$ intermediate. This heme dependency has been exploited as an effective tool in our study to observe the stages involving the mechanism of MYW cofactor formation and further insight on catalytic mechanism.

In this study, we employed a simple and useful method developed in our laboratory for the production of hemin-reconstituted KatG (*r*KatG). The enzyme was expressed predominantly in its apo (*i.e.*, *a*KatG) form using the laboratory *E. coli* strain BL21(DE3) *pLysS* cells transformed only with the pMRLB11 plasmid, a pET23b-derived vector bearing the *Mtb*

KatG gene. This is in contrast to our typical expression protocol using *E. coli* C41(DE3) pHPEX3[268] which is equipped with pMRLB11 ***and*** a plasmid to support uptake of heme from supplemented media. This approach produces the mature (*m*KatG) enzyme, meaning that it contains the heme cofactor and the full MYW protein-based cofactor. Details of our new methodology for KatG expression (*a*KatG, *r*KatG, *m*KatG *etc.*) are covered in Chapter Two. The *r*KatG we prepared exhibited catalytic properties and kinetic parameters equivalent to *m*KatG. To evaluate steps in MYW cofactor formation in *r*KatG, we also prepared and investigated the M255I, Y229F and W107F KatG variants. Both the *m*KatG and *r*KatG preparations of these variants were evaluated by steady-state kinetic methods, UV-vis spectroscopy, and mass spectrometry. Stopped-flow spectroscopic investigations identified a distinct heme electronic state generated by *r*WT KatG in response to H_2O_2, prior to the most dominant steady-state catalase (Fe^{III}-$O_2^{\bullet-}$-like) intermediate typically observed with *m*KatG. Rapid freeze-quench electron paramagnetic resonance (RFQ-EPR) spectroscopy was also employed for the WT and MYW-negative variants for detecting the protein-based radicals. Data obtained in this study identified heme and protein-based precursor radical intermediates presumed to be involved in the mechanism for MYW cross-link formation.

3.2. Materials and Methods

3.2.1. Reagents

Ampicillin and isopropyl β-D-thiogalactopyranoside (IPTG) were from Gold Biotechnology, Inc. (St. Louis, MO). H_2O_2 (30%), peracetic acid (PAA), hemin, imidazole, calcium chloride hydrate and phenylmethylsufonyl fluoride (PMSF) from Sigma Aldrich (St. Louis, MO). Miller Luria Broth (LB) powder, benzonase nuclease and diammonium 2,2'-azino-bis-[3-ethylbenzothiazoline-6-sulfonate] (ABTS) from VWR life science. Chloramphenicol, mono- and dibasic sodium phosphate, sodium chloride, potassium chloride, magnesium sulfate, magnesium chloride, tetracycline hydrochloride from Fisher Scientific (Pittsburg, PA). Centrifugal filters (30 kDa cutoff) from Pall Laboratories (Port Washington, NY). We obtained Ni-NTA resin from GBiosciences (St. Louis, MO). Macro-Prep High Q resin and 10DG buffer-exchange columns were purchased from Bio-Rad (Hercules, CA). T4 DNA ligase, *Pfu* polymerase, *E. coli* BL21(DE3) pLysS and (XL-1 Blue) cells were obtained from Agilent (La Jolla, CA). Sequencing grade modified trypsin was obtained from Promega (Madison, Wisconsin). All buffers and media were prepared using water purified through a Barnstead (Barnstead, NH) GenPure pro UV-UF water system (18.2 MOhm/cm resistivity).

3.2.2. Site-directed Mutagenesis

Site-directed mutagenesis was performed using the "Round-the-Horn"[269] approach to generate plasmid for expressing W107F, M255I, and Y229F KatG variants. The template used for all three of these variants was pMRLB11, a pET23b-derived plasmid carrying the *M. tuberculosis katG* gene. The enzyme is expressed such that a six-histidine tag is expressed on the enzyme's C-terminus. This template was obtained from the tuberculosis vaccine Testing and Research Materials Contract at Colorado State University. The forward primer design for generating the W107F KatG expression plasmid was 5'-CG**TTT**CACGCTGCAGGCACCT-

ACCGCATCC-3' and contained the Trp to Phe codon substitution (bold) as well as a silent Ala codon substitution to include a new *Pst*I restriction site for diagnostic restriction screening of candidate mutant plasmids (underline). The reverse primer sequence was 5'-CCAT-CCGGATAAACAGCGGCCCGTAGTGGC-3' and required no substitutions. The forward primer for generating the Y229F KatG expression plasmid was 5'-GGCTGATC-**TTT**GTGAACCCGGAGGCG-3'. Here, the Tyr to Phe codon substitution also accomplished the removal of a *Bsa*AI restriction site and was valuable for diagnostic restriction screening. The reverse primer was 5'-CCCATCTGCACGCGGCCAGCG-3' and required no substitutions. Finally, the forward primer design for generating the plasmid for M255I KatG expression was 5'-CGC**ATC**GCAATGAACGACGTCGAAACAGCGGC-3' where the Met to Ile codon substitution (bold) and a silent Ala codon substitution (underline) were included. The latter removes an *Msc*I restriction site from the pMRLB11 plasmid. The reverse primer for M255I *katG* mutagenesis was 5'-CCGAAACGTCTCGCGAATGTCGACCGCC-3' and required no substitutions. All of the primers were modified to include 5' phosphoryl groups to allow for blunt end ligation after PCR. All PCR reactions were carried using Phusion High-Fidelity polymerase in GC-rich buffer-containing Master Mix and 3% DMSO. After PCR, the reaction mixtures were immediately mixed with *Dpn*I (New England Biolabs, Ispwich, MA), a restriction enzyme used to degrade the template; this was followed by ligation using T4 DNA ligase. Ligated products were then used to transform *E. coli* XL-I Blue cells by a standard heat shock procedure and transformants were selected based on antibiotic resistance from the agar plates. In this case, all plasmids provided ampicillin resistance. The success of the transformation was confirmed by the appropriate restriction enzyme digest as evaluated by agarose gel electrophoresis. Once the plasmids passed initial restriction screening, they were sent for full DNA sequence analyses (Laragen Sequencing, Culver City, Ca) to verify that the

correct substitutions had been completed without any unintended mutations to the expression plasmid.

*3.2.3. Overexpression of a*KatG

E. coli (BL21[DE3] pLysS) was used to express WT KatG and its variants in their corresponding apoenzyme or *a*KatG states. This cell line was transformed with pMRLB11 (or corresponding mutagenized plasmids for expression of KatG variants). The details of the expression protocol can be found in Chapter Two. KatG expression was verified by TCA precipitation and SDS-PAGE analysis.

*3.2.4. Reconstitution of a*KatG

Frozen aliquots of purified *a*KatG were diluted to 100 μM in 5 mM phosphate, pH 7.0, which was further mixed with hemin in a stoichiometric molar ratio. The details of this procedure are presented in Chapter Two. The enzyme was further purified through anion exchange chromatography, which enabled effective separation of heme-deficient (*i.e.*, apo or *a*KatG) KatG from *r*KatG with heme cofactor in place. The purified *r*KatG was stored in 5 mM phosphate buffer (pH 7) at -80 °C. Reconstituted enzyme concentration was determined using the pyridine hemochromagen assay as previously described.[270]

*3.2.5. Overexpression and Purification of m*KatG

Competent *E. coli* C41(DE3) cells generated by the $CaCl_2$ protocol[271] were transformed using the heme protein expression plasmid pHPEX3[232] to generate our C41 (DE3) pHPEX3 expression strain. These cells, never frozen, were made competent ($CaCl_2$ protocol) again for transformation by pMRLB11 (or mutants thereof) to express the mature form of WT KatG and the corresponding variants, respectively.[232] Transformants were selected on the basis of

tetracycline (pHPEX 3) and ampicillin (pMRLB11) resistance. Expression and purification of WT KatG and all variants were carried out according to previously published procedures.[47]

3.2.6. UV-visible Absorption Spectra

Following purification, UV-visible spectra for the *r*KatG and *m*KatG forms of WT KatG and the MYW-targeting variants (M255I, Y229F and W107F KatG) were collected as previously described.[245] The absorption features evaluated included 1) the Soret band lineshape, λ_{max}, and intensity, 2) the Reinheitzahl (*Rz*) or optical purity ratio (i.e., A_{408}/A_{280}), and 3) the λ_{max} values for two charge-transfer bands (CT1 and CT2) commonly observed for Fe^{III} high-spin heme enzymes. These data provide information about the occupancy of the KatG active site with heme as well as the oxidation, coordination, and spin state of the active-site heme iron.

3.2.7. Catalase and Peroxidase Activity Assays

After purification, *m*- and *r*KatGs were evaluated for their catalase and peroxidase activities using UV-visible absorption methods. Catalase activity was measured by monitoring the decrease in H_2O_2 concentration at 240 nm (ε = 39.4 $M^{-1}cm^{-1}$). All assays were carried out over 60 s of reaction time at ambient temperature using 100 mM phosphate, pH 7.0. Each assay contained 20 nM enzyme. Initial rates of H_2O_2 consumption were estimated for reactions containing H_2O_2 concentrations ranging from 0.05 – 50 mM. Peroxidase activity was determined based on the oxidation of 2,2'-azino-bis(3-ethylbenzthiazoline-6-sulfonate) (ABTS) by monitoring the formation of $ABTS^{\bullet+}$ at 417 nm (ε = 34.7 $mM^{-1}cm^{-1}$). All reactions contained 20 nM enzyme and 0.1 mM ABTS and were conducted using 50 mM acetate, pH 5.0, at room temperature. Initial rates of $ABTS^{\bullet+}$ production was determined for reactions initiated with H_2O_2 concentrations ranging from 0.01 – 5 mM.

Catalase activity was also evaluated by monitoring O_2 production using a Clark-type O_2-sensitive electrode (Hansatech, Pentney, Norfolk, UK) as previously described.[245] All reactions contained 5 nM KatG and were carried out at room temperature in either 50 mM acetate, pH 5.0, or 100 mM phosphate, pH 7.0. Analyses of steady-state kinetic data were carried out as described previously[245] to obtain kinetic parameters k_{cat} and k_{on} (i.e., k_{cat}/K_M). In all situations where these terms are applied, k_{cat} is the maximum rate approached asymptotically with increasing concentrations of substrate divided by the total concentration of enzyme as estimated by heme concentration. The catalytic efficiency (k_{on} or k_{cat}/K_M) was utilized as the main value of comparison across enzyme preparations. The mechanistic and physical meaning of observed apparent K_M values varies substantially across these assays and resists meaningful interpretation. As such, it is not intended to refer to anything more than the concentration of substrate necessary to produce half of the maximum rate of enzyme-catalyzed reaction.

3.2.8. *Mass Spectrometry*

Roughly 1 mg KatG (i.e., 250 µL of 50 µM enzyme) or its variants (M255I, Y229F, or W107F) was diluted in 50 mM NH_4HCO_3. KatG reactions with peroxide were initiated by the addition of 50 molar equivalents of H_2O_2 to the protein and allowed to incubate for at least 10 minutes to ensure reaction completion before the addition of trypsin. Following the addition of sequencing grade trypsin (200:1 KatG to protease ratio) samples were incubated for three h at 37 °C to achieve proteolytic digestion of the enzyme. After three hours of reaction time, reactions were quenched by the addition of 20 µL of glacial acetic acid.

Molecular masses were determined on an ultra-performance LC system (ACQUITY with TUV Detector, Waters Corp., Beverly, MA) coupled with a quadrupole time-of-flight mass spectrometer (Q-TOF Premier, Waters Corp.) with electrospray ionization (ESI) in positive mode using Masslynx software (V4.1). Liquid chromatographic separations were

performed by injecting 10 µL of the sample onto a C18 column (Waters UPLC BEH C18 2.1 × 50 mm, 1.7 µm) with a 300 µL/min flow rate of mobile phase solution A (water with 0.1% formic acid) and solution B (95% acetonitrile 5% water and 0.1% formic acid). Initially B was held for 2 minutes at 3%, followed by linear ramp to 50% in next 58 minutes. Finally, 100% of solution B was set to a linear ramp at 62 minutes, with hold for 5 minutes and return to 3% B in 3 minutes with 10 minutes of reequilibration. The elution of peptides from the column was monitored at 330 nm at a density of 40 points/second. The capillary voltage was set at 3.1 kV, the sample cone voltage was 30 V, and the extraction cone was 4.3 V. The MS scan was 1.0 s long from 100 to 4000 *m/z* with a 0.02 s inter-scan delay using the centroid data format. MS/MS scans were 0.5 to 1.0 s long with a 0.02 s inter-scan delay with a collision energy ramp from 20 V to 40 V.

3.2.9. Stopped-flow Optical Spectroscopy

The heme intermediates observed upon reaction of peroxide with *r*KatG and *m*KatG preparations of WT enzyme and its variants were monitored by optical stopped-flow methods. Reactions were carried out using a PC-upgraded SX18.MV rapid reaction analyzer from Applied Photophysics (Leatherhead, UK). Enzyme solution was prepared in 5.0 mM potassium phosphate buffer at pH 7.0 and substrate solution (H_2O_2 or PAA) was prepared in 100 mM acetate buffer at pH 5.0. Single-mixing experiments were conducted by loading 6 µM enzyme in syringe A and varying concentrations of H_2O_2 or PAA in syringe B. The temperature of the reaction cell was constantly maintained at 4.0° C by circulating water bath.

3.2.10. Rapid Freeze-Quench (RFQ) Preparation of EPR Samples

KatGs (WT and variants) were concentrated using Amicon Ultra-4 centrifuge filters (MW cutoff of 30 kD) to obtain a final concentration of ~300 µM. For rapid mixing, two

syringes were required: One contained ~300 μM enzyme in 5 mM phosphate, pH 7.0, and the other syringe contained varying concentrations of H_2O_2 in 100 mM acetate, pH 5.0. Reactions were also carried out using varying concentrations of peracetic acid (PAA) instead of H_2O_2.

EPR samples were prepared by mixing equal volumes of solution from each syringe. Each reaction was quenched by freezing after the appropriate time following mixing. Samples frozen less than 1 s after mixing were quenched by spraying the reaction mixture directly into liquid ethane (-150 °C) by a standard rapid quench procedure using a KinTek RFQ-3 Quench-Flow Instrument (KinTek Corporation, SnowShoe, PA). The sample age was determined by the length of the ageing loop and velocity of the motor driving the syringes. For reactions between 1 and 30 s, the samples were still quenched with liquid ethane. For reaction times longer than 30 s, reactions were initiated by hand mixing. The samples were centrifuged to remove excess bubbles, transferred to quartz EPR tubes, and quenched manually in cold isopentane (-130 °C). Samples were packed into EPR tubes and stored in liquid N_2 until EPR spectra could be recorded.

3.2.11. EPR Measurements

Low temperature EPR spectra were collected at 4.5 K using Bruker EMX X-band spectrometer operating in perpendicular mode. Unless otherwise indicated, instrument parameters were as follows: microwave frequency, 9.393 GHz; modulation amplitude, 10 G; modulation frequency, 100 kHz; microwave power, 1 milliwatt; time constant 163.84 ms; sweep time 167.772 s; number of scans, 1; conversion, 163.84 ms; resolution, 1024 point; receiver gain, 1.0×10^4; and phase, 0 degrees. Power saturation for select species was examinedby fitting normalized signal intensities using equation **3**, where $P_{½}$ is the microwave power at half saturation and *b* describes the contribution from inhomogeneous broadening.[272]

$$\frac{\left(1/\sqrt{P}\right)}{\left(1/\sqrt{P}\right)_0} = \frac{1}{1\Big/\left(1+P/P_{1/2}\right)^{b/2}} \qquad \textbf{[3]}$$

3.3. Results and Discussion

3.3.1. Spectral Properties of KatG (WT, M255I, Y229F and W107F)

The WT KatG and variants (M255I, Y229F and W107F KatG) were produced in their *r*KatG and *m*KatG forms using a protocol newly developed in our lab (see Chapter 2) or by an *E. coli*-based heme protein expression (pHPEX) system developed previously by the Goodwin Laboratory,[268] respectively. The electronic absorption spectra and relevant spectral features of the Fe^{III} (i.e., resting) forms *r*KatG and *m*KatGs are shown in Table 3.1. Generally, spectra for heme enzymes have three features or groups of features which can be compared to one another: The so-called Soret (γ) band, the β and α bands (Q_{01} and Q_{00} transitions, respectively), and charge-transfer (CT) bands. Without exception, the resting states of the *r*- and *m*KatG proteins characterized in this research contained high-spin Fe^{III} heme. Accordingly, prominent features to evaluate were the Soret and CT bands. The wavelength maxima for the Soret band observed for WT KatG and most of the variants were very close to those reported elsewhere for heterologously expressed and purified *Mtb* KatG.[123,273,274] The optical purity ratio, *Rz* (A_{407}/ A_{280}), of the large majority of purified variants was ≥ 0.45, consistent with the protein being fully loaded with heme. Interestingly, despite the same growth conditions as the *m*KatG preparations of the other variants, *m*M255I produced an *Rz* value of only 0.22, indicating a lower heme occupancy. However, the Soret and charge-transfer band maxima of this variant were nearly identical to those of the WT enzyme, suggesting that despite the lower heme content, the electronic structure and environment of the heme in the active site of *m*M255I KatG was very similar to those of *m*WT KatG.

Table 3.1. UV-visible absorption characteristics of WT KatG and variants.

Protein	**Absorption Features**			**Heme Occupancy**
	Soret (λ_{max})	**CT[a] 1**	**CT 2**	***Rz*[b] value**
***r*WT KatG**	407.5	504	633	0.58
***m*WT KatG**	407.5	504	629	0.56
***r*M255I KatG**	408	502.5	642	0.46
***m*M255I KatG**	409	502	641.5	0.22
***r*Y229F KatG**	408.5	504	640.5	0.49
***m*Y229F KatG**	408.5	504	633	0.42
***r*W107F KatG**	409	504	639	0.59
***m*W107F KatG**	409.5	504	638.5	0.47

CT[a] = charge transfer transition. CT1 is usually near 640 nm, and CT 2 is usually near 500 nm.
Rz[b] = Reinheitzahl ratio: Ratio of absorbance at the Soret λ_{max} divided by absorbance at 280 nm.

The position of the Soret and CT1 bands provide a general sense of the spin distribution and coordination states of the ferric enzyme. As isolated, ferric KatG is dominated by high-spin (HS) states with a mixed population 6-coordinate (6c) and 5-coordinate (5c) forms.[150,161,275] When compared to 6c HS hemes, a 5c HS heme generally exhibits a slightly blue shifted and hypochromic Soret band with a shoulder at 380 nm and a CT1 feature at ~640 nm (or higher). In our observation, all reconstituted proteins have narrow Soret feature with a λ_{max} near 406 nm, suggesting a greater proportion of 6c HS state. Appearance of the hypsochromic shoulder on the Soret band is predominantly observed with the *m*KatG preparation of enzymes, and this indicates a greater contribution from 5c HS heme states (Figure 3.4.A).

For *r*M255I KatG, the CT2 band showed a nearly identical λ_{max} as compared to *r*WT KatG but, but the CT1 band was blue-shifted from 644 to 629 nm (Figure 3.4.B). Such a shift in CT1 has previously been observed for *m*WT *Mtb* KatG, but only upon aging of the enzyme, and this was ascribed to an increased contribution from 6c in place of 5c heme.[177] The optical spectrum of *r*W107F KatG showed a Soret peak at 407 and sharp CT2 and CT1 bands around 504 and 637 nm respectively (Figure 3.4.C), typical of 6c HS heme.[260] A nearly identical Soret band and a slight red shift in the CT1 band is observed for *r*Y229F (Figure 3.4.D).

Upon storage of the variant enzymes for a longer time at -80 °C, a prominent red shift (~412 nm) in the soret region was frequently observed, especially in the mature form of the proteins. This bathochromic shift is common for the KatG variants where an active site structural shift allows the distal His to coordinate to the heme iron.[153,154] This effect was also observed, when a strong field ligand like CN^- or $N3^-$ was exogenously added, producing a substantial red shift in the Soret band to ~ 418 nm, the loss of the CT bands, and increased prominence of the β and α transition at ~ 535 nm and ~ 570 nm, respectively.[153] The commonality observed in all reconstituted proteins is essentially the absence of a characteristic

shoulder around ~310-320 nm typically observed with mature KatG. Narrowing of the soret peak is more prominent in reconstituted proteins, indicating the presence of greater population of 6-C heme. To justify this argument about 6-C species, *r*WT KatG was treated with H_2O_2, which gave rise to the shoulder near soret region and a hyperchromic shift of 406 peak (Figure from chapter 2). This distinct but subtle spectral feature is clear indication of forming MYW adduct upon peroxide treatment. In contrast to that, none of these variants (M255I, Y229F and W107F) showed any change in spectral features upon peroxide treatment (data not shown) due to the loss of inherent absorptivity imparted by Tyr229 and/or Trp107 during the formation MYW cofactor.

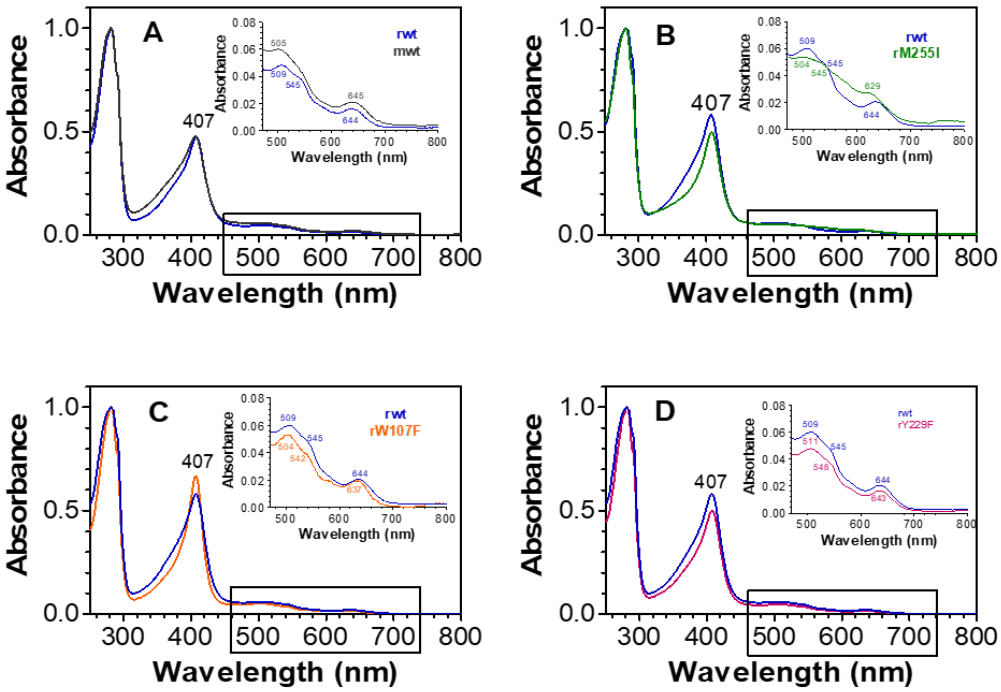

Figure 3.4. Comparison of UV-visible spectral features of WT KatG and variants. Soret and charge transfer bands of *r*WT and *m*WT KatG were shown in A. Similarly, reconstituted variants (*r*M255I, *r*W107F, and *r*Y229F) were compared with reconstituted WT and shown in panels B, C, D, respectively.

3.3.2. Catalase and Peroxidase Activities WT KatG and Its MYW-targeting Variants

We scrutinized the impact of MYW residue substitution on KatG catalytic function by evaluating the catalase and peroxidase activities of each enzyme (WT, M255I, Y229F, and W107F) prepared in its *r*- and *m*KatG forms (Table 3.2). Where catalytic activity was observable, two kinetic parameters were obtained and are reported: 1) The maximum catalytic output under ideal conditions (*i.e.*, saturating concentration of substrate) k_{cat}, and 2) the catalytic efficiency (k_{on} or k_{cat}/K_M). summarizes the data of these steady-state kinetic investigations (k_{cat} and catalytic efficiency k_{cat}/K_m). Upon reconstitution, the catalase activity for *r*WT KatG (k_{cat} = 4630 s^{-1}) was in close agreement with that reported previously for *m*WT KatG.[47] Similarly, k_{cat}/K_M values, within error, were identical for *m*- and *r*WT KatG. KatG is well known to have diminished but measurable catalase activity at acidic pH (*e.g.*, 5.0).[208,245] Interestingly, at this pH *r*WT KatG showed a substantially greater k_{cat} for catalase activity than the *m*WT enzyme. The k_{cat}/K_M values for the two preparations were highly similar. These data are consistent with our recent finding that *m*KatG preparations of enzyme show greater vulnerability to H_2O_2-dependent catalase inactivation at low pH than their *r*KatG counterparts.

Disruption of the MYW covalent adduct by site directed mutagenesis drastically reduced the catalase activity observed in all three reconstituted variants (*r*M255I, *r*Y229F and *r*W107F) consistent with previous investigations.[94,157,276] Among these, M255I variant, capable of forming partial adduct (YW), exhibited slightly elevated catalase activity at both pH 5.0 and 7.0 determined by monitoring the release of dioxygen with a Clark-type electrode, but not with the UV-vis spectrum. However, severely disrupted adduct in Y229F and W107F completely abolished the catalase activity, hence used the notation ND (not determined) in Table 3.2. In contrast, all these variants were able to catalyze the H_2O_2-dependent oxidation of an organic electron-rich substrate, ABTS, thus showing peroxidatic activity. Titration with increasing

concentrations of H_2O_2 and constant ABTS concentration (0.1 mM), showed a non-saturable kinetics comparable with WT KatG, hence accounted for apparent values.[250,252] Negligible catalase activity and comparable peroxidase activity observed in the variants indicate that the loss of integrity of the covalent adduct converts bifunctional KatG to the monofunctional peroxidase.

Table 3.2. Activity parameters for WT KatG and the MYW-targeting variants.

Activity	KatG	Kinetic Parameters	
		k_{cat} (s^{-1})	k_{cat}/K_m ($M^{-1}s^{-1}$)
Catalase (pH 7.0) [a]	*r*WT	4630 ± 19	(1.1 ± 0.10) × 10^6
	*m*WT	4780 ± 36	(1.0 ± 0.20) × 10^6
	*r*M255I, *r*W107F, *r*Y229F	ND	ND
	*m*M255I, *m*W107F, *m*Y229F	ND	ND
Peroxidase (H_2O_2) [b, c]	*r*WT	2.44 ± 0.1	(3.2 ± 0.4) × 10^4
	*m*WT	1.66 ± 0.1	(2.5 ± 0.2) × 10^4
	*r*M255I	10.90 ±0.16	(2.95 ± 0.12) × 10^6
	*m*M255I	1.41 ± 0.05	(8.7 ± 0.10) × 10^5
	*r*W107F	2.7 ± 0.2	(3.7 ± 0.09) × 10^3
	*m*W107F	5.6 ±0.1	(1.04 ± 0.09) × 10^4
	*r*Y229F	1.5 ± 0.07	(9.2 ± 0.02) × 10^3
	*m*Y229F	2.3 ± 0.09	(5.43 ±0.08) × 10^3
Catalase (pH 5.0) [d]	*r*WT	830 ± 0.6	(8 ± 1) × 10^4
	*m*WT	163 ± 0.3	(3.1 ± 0.03) × 10^5
	*r*M255I	192 ± 0.23	(2.2 ± 0.02) × 10^4
	*m*M255I	99 ± 0.15	(1.4 ± 0.05) × 10^4
	*r*W107F, *r*Y229F	ND	ND
	*m*W107F, *m*Y229F	ND	ND

[a] Activity by H_2O_2 consumption (240 nm) 23 °C in 100 mM phosphate, pH 7.0.
[b] All peroxidase activity evaluated at 23 °C in 50 mM acetate, pH 5.0.
[c] Peroxidase parameters with respect to H_2O_2 were determined using 0.1 mM ABTS.
[d] Activity was determined by O_2 production at 23 °C in 50 mM acetate, pH 5.0.

3.3.3. *Evaluation of MYW Adduct Formation: WT KatG and MYW-targeting Variants*

In Chapter Two, we demonstrated the gradual formation of MYW adduct upon peroxidatic treatment of *r*KatG employing the tryptic digestion of the protein in combination with liquid chromatography (LC) and tandem mass spectrometry (MS/MS). Here again, we compared the LC-MS data of the *r*WT KatG against the reconstituted MYW-negative variants to provide evidence that adduct formation is solely dependent on the presence of Met255, Y229 and W107 residues. Employing the similar techniques, previous studies also identified the presence of crosslinked-peptide-fragment (CLPF) in *Mycobacterium tuberculosis*[254], *Bulkholderia pseudomonas*[169] and *Synechocystis* PCC 6803[164] KatG and its absence in the adduct negative variants. One notable difference between their studies and our attempts is analyzing the reconstituted protein for the first time and targeting the adduct formation using H_2O_2. It is noteworthy to mention that higher amount of H_2O_2 is the enzyme's natural substrate and can be used for catalytic turnover after formation of the MYW adduct. Previous study with PAA showed significant decrease of the MYW-related ions, most likely due to oxidative damage caused by the reaction with PAA.[165] Each of the key residues in the MYW structure is located on a separate tryptic peptide fragment, and the absence of those fragments combined with the presence of larger fragments of calculated neutral (zwitterionic) mass would confirm the presence of the adduct. A list of specific MS ions and their corresponding peptide structures are provided in Table 3.3.

In this study, all proteins (*r*WT, *r*M255I, *r*Y229F and *r*W107F) were treated with 50 equivalents of H_2O_2 before digestion with trypsin to ensure the formation of adduct. These clusters of ions resulted from the tryptic fragments ^{255}**M**AMNDVETAALIVGGHTFGK^{274}, ^{215}DLENPLAAVQMGLI**Y**VNPEGPNGNPDPMA-AAVDIR^{249}, and ^{105}MA**W**HAAGTYR^{114} were detectable by LC/ESI-MS analysis. For our treated *r*WT KatG, one of the digested components showed a molecular mass of 1377.6 (+5) (Figure 3.5 A). This monoisotropic

neutral mass is very close to the sizes predicted for combined peptides in the MYW adduct observed for other KatG as well.[88,156] In chapter two, we showed the fragmentation of the MYW adduct between the γ-carbon and the sulfur atom of the Met residue. This was evidenced by the 672.3 (3+) *m/z* ion and the 1216.3 (4+) *m/z* ion as in-source fragments resulted from 1147.6 (6+) *m/z* ion. These two ion sources are the representative of tryptic peptides fragmented at the thiomethyl position. Theoretical calculation of parent ion 4861. 2 *m/z* and 2013.9 *m/z* indicates the YW adduct attached with the thiomethyl group and M255-bearing tryptic peptide detached from the thiomethyl group, respectively.[165] In contrast to that, peroxide treated *r*M255I variant showed the presence of YW adduct represented by ions at *m*/*z* 1206.32 (4+) and 965.26 (5+) (Figure 3.5 B). The combined monoisotopic value (4822.4 Da) is in good agreement with the calculated value of the YW adduct.[165] Tandem MS analysis of same tryptic fragment also showed *m/z* 1205.82 (4+) and 964.86 (5+) which is a mass 2 Da lower than that calculated for the Tyr-Trp adduct. The 2 Da lower value of the tryptic fragment is well agreed to the mass of quinone-like intermediate, resulted from the 2*e*- oxidation of the YW adduct.[165] Complete absence of partially- or fully-formed, adduct-containing tryptic peptides were not observed in the treated *r*Y229F and *r*W107F variants (Figure 3.6 A and B).

Table 3.3. Tryptic peptides detected by mass spectrometry

Parent ion *m/z*	Observed ion *m/z*	Structure of the molecule	Condition observed	Identity
6880.0	1377.8 (+5) 1148.4 (+6) 984.4 (+7)	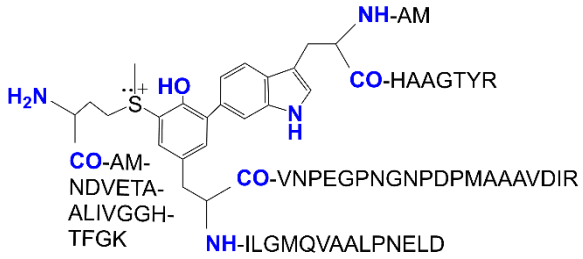	*m*WT and 50 eq H_2O_2 treated *r*WT	Full MYW adduct
2013.9	672.3 (3+)	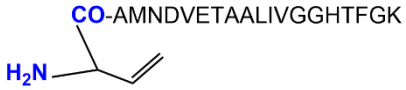	*m*WT and 50 eq H_2O_2 treated *r*WT	M255 peptide without thiomethyl group
4861.2	1216.3 (4+)	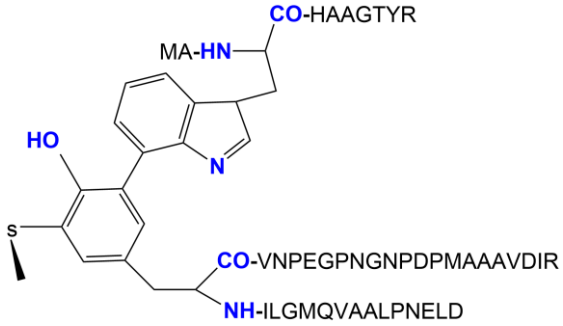	*m*WT and 50 eq H_2O_2 treated *r*WT	YW adduct with thiomethyl group
4822.4	1206.35 (4+) 965.26 (5+)	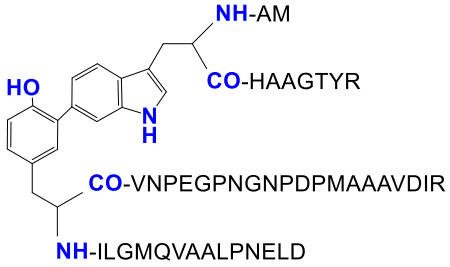	50 eq H_2O_2 treated rM255I	Partial adduct YW
4820.32	1205.83 (4+) 964.86 (5+)	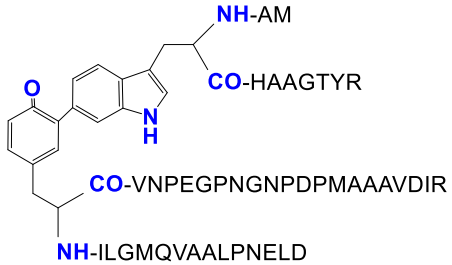	50 eq H_2O_2 treated rM255I	YW quinoid

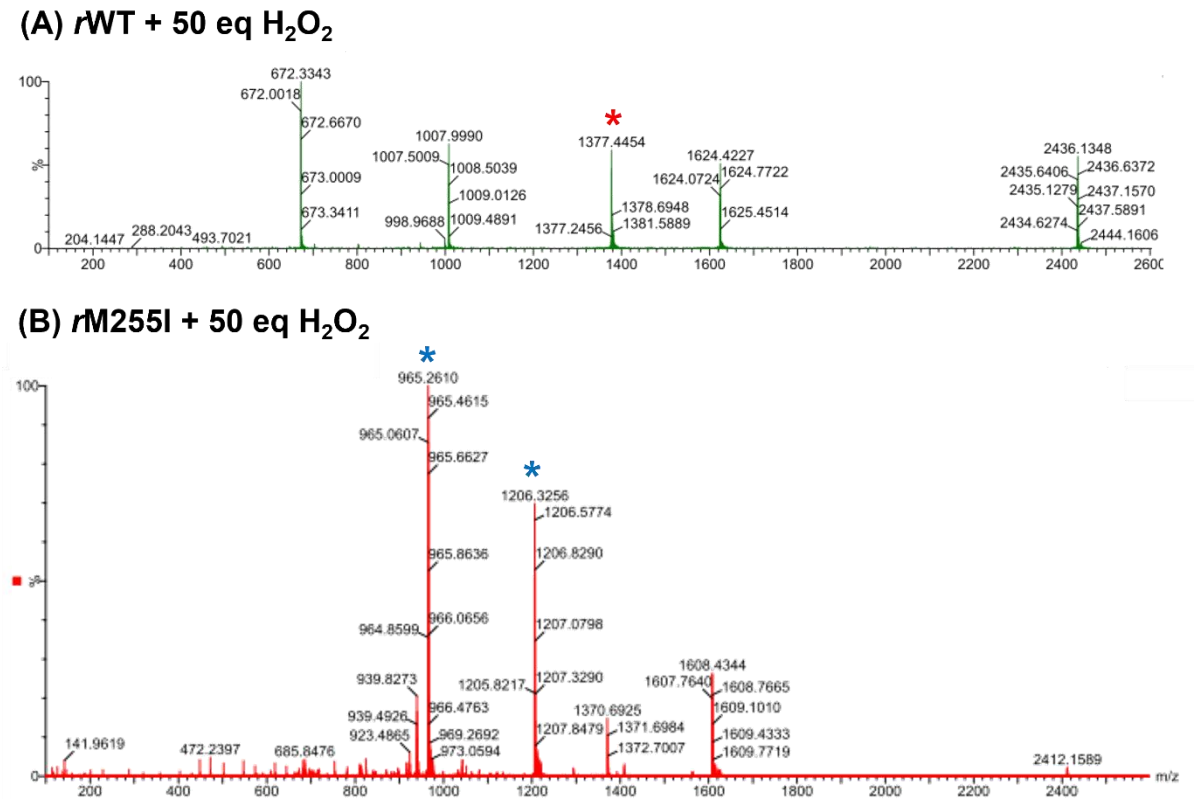

Figure 3.5. LC-MS detection of fully formed MYW adduct and partially formed YW adduct revealed by *r*WT and *r*M255I upon treatment with 50 equivalents of H_2O_2. Tandem MS analysis of the 1377.6 *m/z* ion confirms the presence covalently bonded MYW cofactor whereas 1206.3 *m/z* and 965.26 *m/z* confirm the presence partially formed YW adduct.

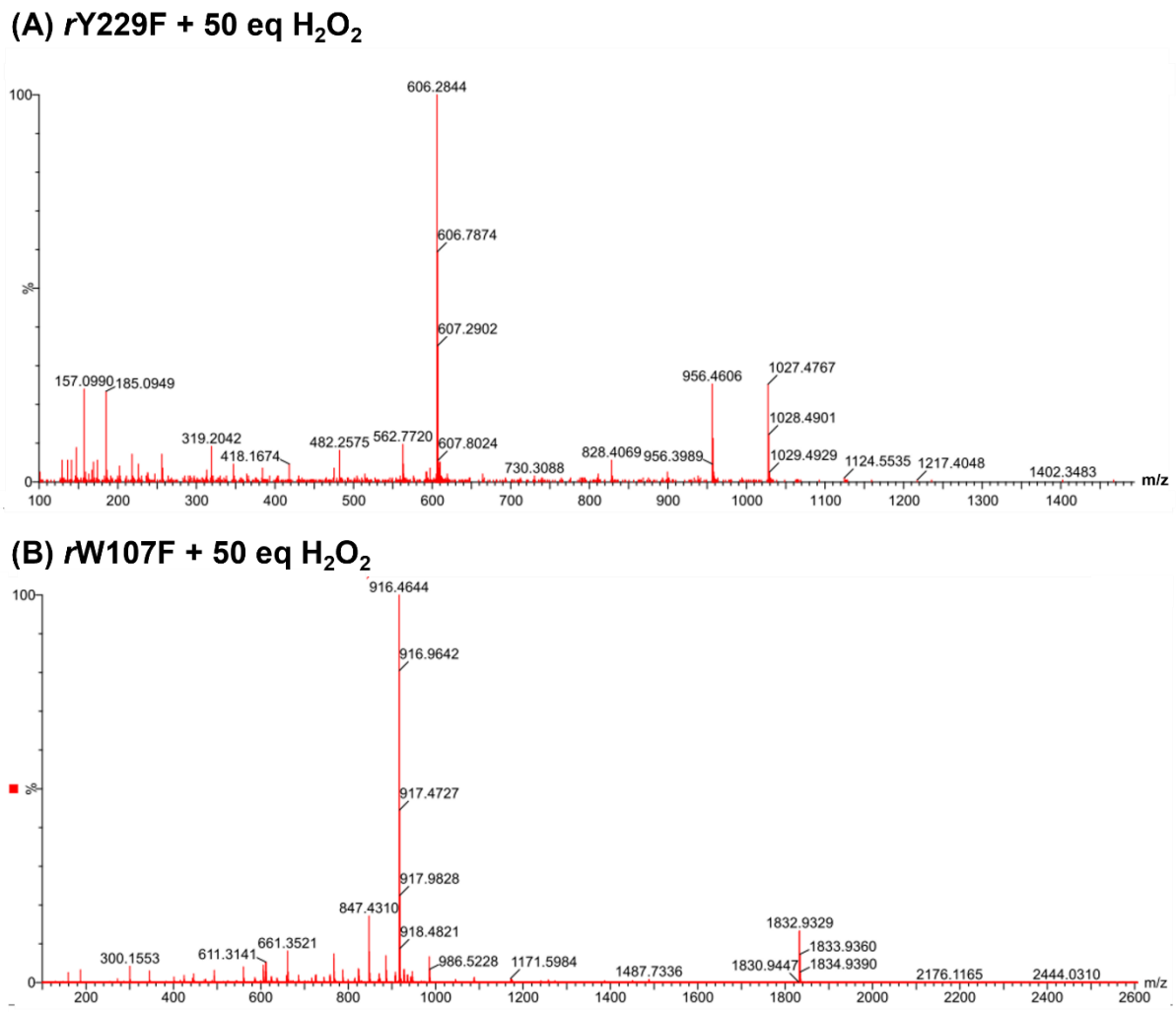

Figure 3.6. LC-MS detection of non-MYW related ions in *r*Y229F and *r*W107F variants upon treatment with 50 equivalents of H_2O_2.

*3.3.4. Heme Intermediates Observed on Peroxide Reaction with r*WT *and m*WT KatG

Optical stopped-flow reactions of 3 µM KatG with 1mM H_2O_2 at pH 5 showed subsequent changes in the heme oxidation states and returned back to the resting state after depletion of H_2O_2. Although both *r*KatG and *m*KatG are capable of catalatic turnover, substantial differences in heme states between *m*WT KatG and *r*WT KatG were observed during reactions with H_2O_2 under sustained turnover conditions (Figure 3.7). The first spectrum recorded (2.5 ms) after mixing of *m*KatG with 1 mM H_2O_2 (*i.e.*, 333 molar equivalents) showed absorption features at 414, 540, and 579 nm, observed by steady-state kinetics (Figure 3.7 A). This was followed over the next 265 ms by a shift in the Soret band to 418 nm along with a broad non-descript increase in absorbance above 520 nm with a slight red-shift in absorption bands to 546 and 586 nm (Figure 3.7 B). This heme state persisted for ~ 4 s (Figure 3.7 B) before H_2O_2 was depleted and the ferric state reemerged (Figure 3.7 C). This is typical for WT KatG with a fully formed MYW cofactor reacting with H_2O_2 under multiple-turnover or steady-state conditions.[244,170,47] The intermediate which dominates during the consumption of the H_2O_2 substrate has been referred to as compound III- or oxyperoxidase-like owing to absorption features which bear a resemblance to the Fe^{III}-$O_2^{\bullet-}$ state observed in canonical peroxidase systems. In contrast, the first heme state observed (2.5 ms) after mixing of *r*KatG with 1 mM H_2O_2 (λ_{max} at 414, 529, and 559 nm) (Figure 3.7 E) was typical of a ferryl (*i.e.*, Fe^{IV}=O) state known as Compound II in canonical peroxidases.[91,170,187] For *r*KatG this state persisted for 270 ms of reaction time, followed by a slow transition to a Fe^{III}-$O_2^{\bullet-}$-like intermediate (λ_{max} at 416, 546, and 576 nm) (Figure 3.7 F). Notably, a concomitant increase in absorbance around 315 nm was observed at this stage of the reaction (Figure 3.7 H). Following nearly 18 s of reaction time, H_2O_2 was depleted, and the return of the ferric state was observed (Figure 3.7 G). Accordingly, an extended delay in the return of the ferric state was observed for *r*KatG that

was absent in reactions with *m*KatG (Figure 3.7 D). To confirm whether formation of compound II was the early intermediate resultant from the reaction of H_2O_2, a double mixing protocol was used. Here, *r*WT KatG was premixed with 3-molar equivalents of peracetic acid (PAA) and allowed to form the adduct in the first mixing phase (resting enzyme plus PAA incubated for 30 s), followed by the addition of H_2O_2. Interestingly, we have observed nearly identical responses to H_2O_2 as observed for *m*KatG (Figure 3.8). Specifically, the initial phase of the reaction dominated by the Fe^{IV}=O-like state was absent, and H_2O_2 was rapidly depleted (within 2 s) as signified by the subsequent return of the Fe^{III} state (Figure 3.9 A). Finally, absorption increases near 315 nm were substantially diminished and only observed along with the initial loss and eventual reemergence of the ferric form of the enzyme (Figure 3.9 B).

The response of *r*KatG to H_2O_2 is striking in that it exhibits two features that have not, to this point, been observed together in KatG catalysis. On the one hand, reaction with excess H_2O_2 produces an initial appearance of a compound II-like (Fe^{IV}=O) state which is followed by a compound III-like (Fe^{III}-$O_2^{\bullet-}$) intermediate. This is typical of KatG variants that are unable to establish the MYW cofactor (*e.g.*, Y229F *Mtb* KatG and analogous substitutions in other KatGs).[96,174,207] Because of the lack of catalase activity imposed by the absence of the MYW cofactor, these KatG variants revert to the typical behavior of monofunctional peroxidases in which they are inactivated in the presence of excess H_2O_2, particularly if an exogenous electron-donor substrate is absent.[96] Although this same progression is observed for *r*KatG, the ferric state reemerges soon thereafter demonstrating that the enzyme is capable of catalatic H_2O_2 degradation independent of an exogenous electron-donor substrate. These data are consistent with an initial H_2O_2-dependent *in situ* establishment of the MYW cofactor in *r*KatG imparting the catalase activity necessary to consume the balance of H_2O_2 present. A heme state with the absorption features of a classical Fe^{IV}=O (compound II) state dominates during this phase of the reaction. Simultaneously, there is an increase in absorbance around 315 nm which

entirely precedes the return of the ferric state (Figure 3.7 H). Neither of these features is observed with *m*KatG. The increase in absorption near 300 nm is noteworthy given the previous observation of absorption features in this wavelength range assignable to the MYW adduct and precursors thereof.[91,165]

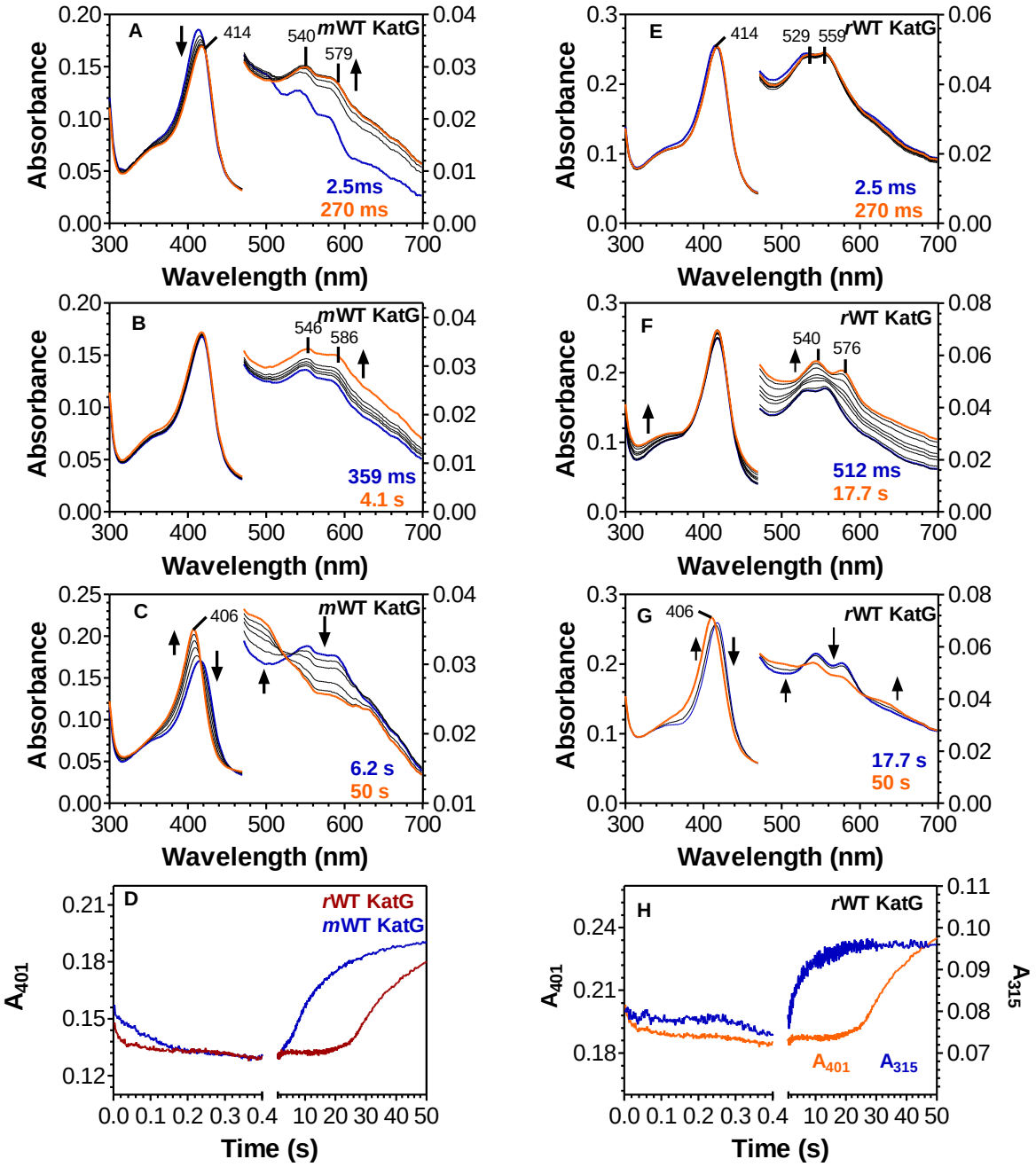

Figure 3.7. Heme states of mature and reconstituted preparations of KatG (*m*WT KatG and *r*WT KatG, respectively) upon reaction with H_2O_2 under sustained turnover conditions. Both *m*KatG (A, B, C) and *r*KatG (E, F, G) were reacted with 1 mM H_2O_2 by stopped-flow and visible absorption were recorded over the time frames indicated in each panel. Arrows indicate the direction of absorption changes over each time span. Absorption at 401 nm (indicative of the Fe^{III} state) was monitored for *m*KatG and *r*KatG (D). The time course of absorption changes at 315 and 401 nm for *r*KatG are also compared (H). All reactions contained 3 μM enzyme and were carried out using 50 mM acetate, pH 5.0, at 4.0 ºC.

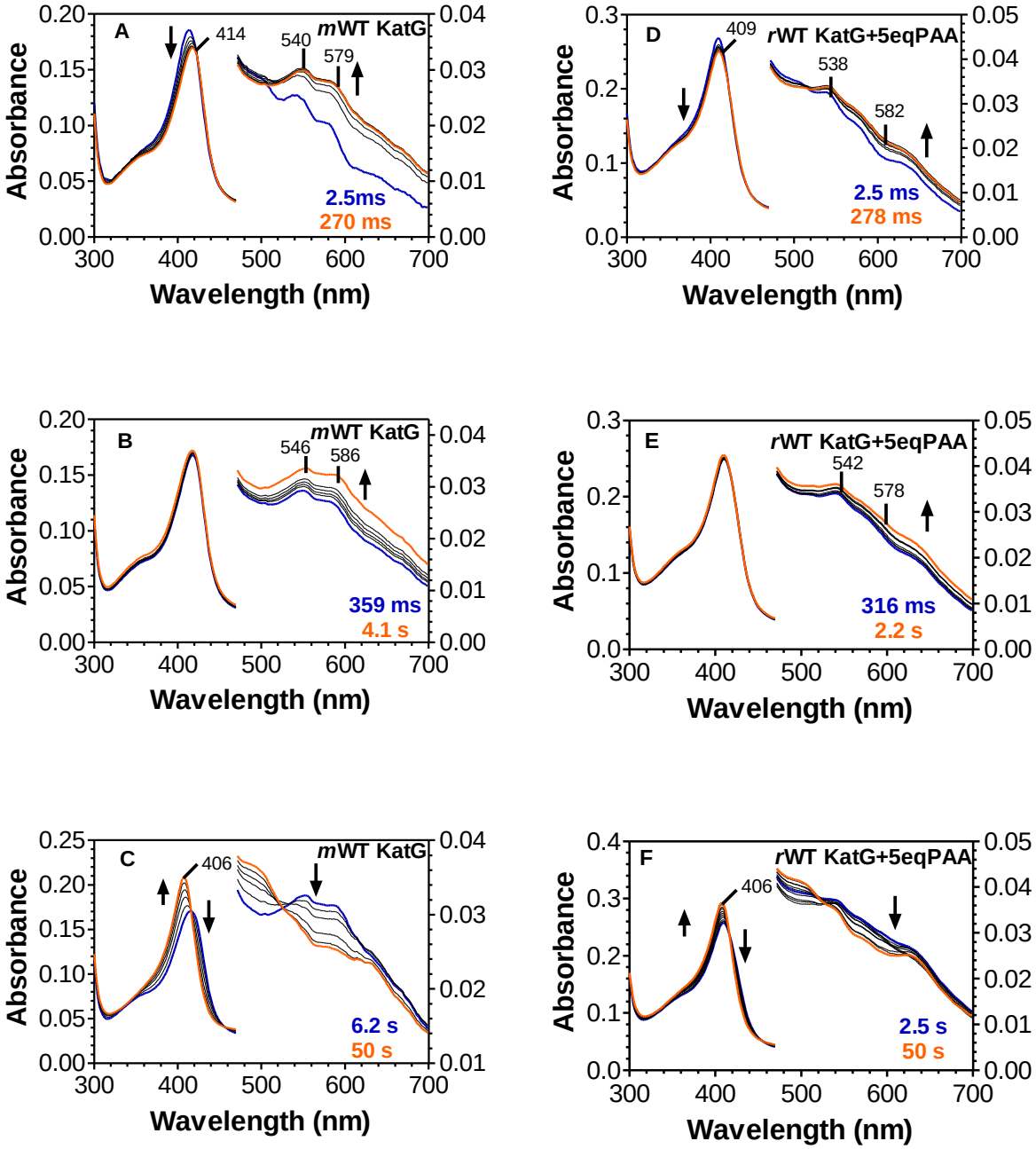

Figure 3.8. Heme states of mature and PAA pre-treated reconstituted preparations of KatG upon reaction with H_2O_2 under sustained turnover conditions. Both *m*KatG (A, B, C) and 5equivalents PAA pretreated *r*KatG (D, E, F) were reacted with 1 mM H_2O_2 by stopped flow and visible absorption were recorded over the time frames indicated in each panel. Arrows indicate the direction of absorption changes over each time span. All reactions contained 3 mM enzyme and were carried out using 50 mM acetate, pH 5.0, at 4.0 ºC.

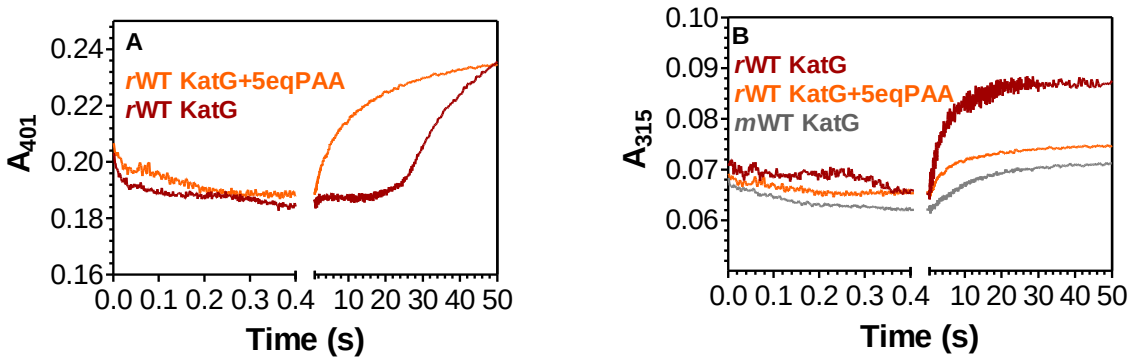

Figure 3.9. Effect of pretreatment of *r*KatG with peracetic acid (PAA) on enzyme absorption features during consumption of H_2O_2 under multiple-turnover/steady-state conditions. Five molar equivalents of PAA were reacted with *r*KatG. This preparation was then reacted with 1 mM H_2O_2 by stopped flow. The contributions of the Fe^{III} state were monitored at 401 nm (A), and the putative formation of the MYW covalent adduct was monitored at 315 nm (B)

3.3.5. Rapid Freeze-Quench Electron Paramagnetic Resonance (RFQ-EPR) Spectroscopy

In chapter two, the detail of ferric heme states of both *r*KatG and *m*KatG have been discussed based on heme environment and coordination state. In this section, RFQ-EPR results will be discussed to gain insight on possible site of protein oxidation. A hydrogen-bonding network maintains the reduction potentials of redox-active residues, which is an important factor in the formation of protein-based radicals. These protein-based radicals act as catalytic intermediates and were previously characterized by using multi-frequency EPR, selective deuterium labeling, and mutagenesis.[277] In a previous study, *m*WT KatG produced a narrow doublet signal or $MYW^{\bullet+}$ radical as early as 10 ms and an exchange-coupled signal or $Trp321^{\bullet+}$ radical at 6s upon reaction with 667 equivalents of H_2O_2.[47] Since, optical stopped-flow data showed the generation of Fe^{III}-$O_2^{\bullet-}$ species as the very first reaction intermediate for *m*WT KatG, therefore, narrow doublet radical signal obtained from EPR study is reminiscent of that dominant steady-state intermediate[171,173,244] In this study, using 9 GHz EPR spectroscopy, our *r*WT KatG, produced radical signals, bearing distinct line shape than those appeared with *m*WT KatG. Our stopped-flow data suggested that *r*WT KatG is capable of producing Fe^{IV}=O-like species as the first reaction intermediate and persisted for 2.6 ms to 270 ms (Figure 3.7 E). In RFQ-EPR, we have been able to quench the reaction as early as 6 ms and obtained a narrow doublet signal with exchange-broadening (Figure 3.10, black trace). This multifarious feature may be due to the generation of two or more organic radicals at different population during catalatic turnover. Power saturation characteristics have been analyzed for *r*WT KatG 6 ms sample by collecting spectra from 0.2 μW to 20 mW (Figure 3.11 A). The radical signal obtained from exchange coupling is very pronounced at 20 milliwatt (Figure 3.11 A, blue dashed line) but loses intensity with the power attenuation. However, the persistence of doublet signal is still visible at power as low as 0.2 microwatt (Figure 3.11 A, red line). Temperature resistance of the radical species were also characterized by analyzing the same *r*WT KatG 6

ms sample at 4.5 K and 77 K (Figure 3.11 B). The observed decay of the broad shoulder at higher temperature, may be due to the loss of exchange interaction between the unpaired electrons in the heme and the $Trp^{\cdot+}$. Therefore, considering both power and temperature data, it can be assumed that exchange-coupled radical is more sensitive to power and temperature than the doublet producing radical. The duplexity of this 6 ms sample arises the question of precedence in terms of radical formation. To better understand the individual nature of mixed signal, we reacted our *r*WT KatG protein with 40 equivalents of H_2O_2, knowing that this low equivalent of peroxides would only permit Fe^{IV}=O or Compound II like heme state (Figure 3.12 A), before returning the enzyme to the resting state. To capture a radical species, corresponding to this Compound II-like state, we have freeze quenched our sample at 1.5 s. The radical signal (Figure 3.12 B) observed at this time point is basically a singlet with a broad feature (~300 G), consistent with previously observed $Trp321^{\bullet+}$ generated during H_2O_2 depletion at 6 s.[47] The same exchange-broadened singlet feature was observed when reacting *r*WT KatG with 5 molar equivalents of peracetic acid (PAA). Based on the timepoint insight obtained from stopped-flow spectroscopy, EPR spectra were also collected, quenching the reaction at 10 ms and 33s. Compound-II and Compound III-like heme spectra were observed at 10 ms and 33 s respectively (Figure 3.13 A). The inactive nature of these intermediates was reflected in the EPR spectra (Figure 3.13 B) also, where narrow doublet collapsed to a singlet. However, the intense broad signal was clearly present at 10 ms. Absence of narrow doublet clearly indicates that PAA does not give rise to the heme or protein based radical state but plays a beneficial role to capture catalase inactive intermediates.

As the reaction progress towards H_2O_2 depletion (18 s) the exchange coupling signal was diminishing and only the doublet feature was remaining (Figure 3.10, red line). It is noteworthy to mention that narrow doublet signal with g=2.0034 with a principal hyperfine splitting of ~11

G is only associated with catalase activity of KatG. This radical signal was previously assigned for the $MYW^{\bullet+}$ radical of *m*WT KatG and more reminiscent to the Fe^{III}-$O_2^{\bullet-}$ like state.[47]

At the end of the reaction (50 s), a signal corresponding to the ferric state was clearly present (Figure 3.10, blue line). The ferric state was represented by a singlet protein-based radical but with diminished intensity as compared with the resting state (Figure 3.14 A). The progression of radical signals from the resting state to the intermediate states (6 ms, 0.7 s, 10 s, 18 s) and finally, the reemergence of the ferric state (60 s) is shown in Figure 3.14 A and B. Together these data present greater time resolution of the of the protein-based radicals generated during active catalatic turnover. The power saturation profiles for the 6 ms, 10 s and 18 s samples are shown in Figure 3.15.

In our observation, peroxide reaction with *r*WT KatG produced at least two different radical species during active catalatic turnover. The EPR spectra recorded at 6 ms unambiguously represents the mixture of multiple radicals evidenced by broad shoulder and doublet feature. Previously, similar spectral pattern was observed upon applying high-frequency EPR (285 GHz/ 10 T) on *Mtb* KatG[277] and *Sy*KatG[195], where contribution of two protein-based radicals ($Trp^{\bullet}$ and $Tyr^{\bullet}$) were confirmed, as expected from the deuteration results. The broad signal (>300 G) resulted from magnetic interaction with heme is a common phenomenon among KatGs and assigned as a proximal Trp through extensive studies.[47,195,277,278] In *m*WT KatG, this Fe^{IV}=O[$Trp321^{\bullet+}$] intermediate was formed during the time of H_2O_2 depletion and spectral features were corresponding to the Compound II-like state (Figure 3.7 B).

Our *r*WT KatG permits monitoring the preceding steps before the occurrence of most dominant catalatic species. This preceding step or compound-II like state was never observed with *m*WT *Mtb* KatG. Therefore, it is convenient to propose that exchange broadening

corresponding with this compound II-like state is the contribution of a Trp residue other than proximal Trp321. Closer inspection of the distance mapping (Figure 3.16) from the active site heme to the numerous Trp residue reveals that the Trp107 is the closest to the heme iron (4.2 Å) and in H-bonding interaction through a water molecule.[277] On this basis, it can be proposed that Trp107 is the site of intramolecular electron transfer and consequently shifts the radical to other oxidative residues. Previous study with *Mtb* KatG excluded the possibility of this distal Trp107 and Trp91 residue, due to the identical signal (400G broad signal) obtained after site-directed mutagenesis as the WT enzyme at 4K.[277] Our proposed site of radical formation is at odds with others mainly because of the use of an enzyme (reconstituted type), which showed distinguished characteristics than mature type. Moreover, we used H_2O_2 instead of PAA. H_2O_2 is a natural substrate for the enzyme and a crucial factor for generating radical intermediates during active catalatic turnover.

Formation of narrow doublet is due to the contribution of both Tyr$^{\bullet}$ and Trp$^{\bullet}$ radicals and previous study with deuteration unequivocally assigned the Tyr229 residue as the MYW cofactor precursor radical species.[171] Consistent with the literature, our 9 GHz EPR spectra of *r*WT KatG also obtained narrow doublet feature at 6 ms with the features . Although this doublet feature persisted for 18 s or more, a subtle distinction in the line shape is fairly observed may be due to the migration of radical to other oxidative residues. The collapsing of the signal from a doublet to a singlet during the time of H_2O_2 depletion was observed with *m*WT but not with *r*WT. Therefore, it can be hypothesized that in *r*WT, after first intramolecular electron transfer from Trp107, the radical migrates to the Tyr229 residues. After that, MYW adduct redox cycles between a fully covalent (reduced) state and free-radical (oxidized) state, until the consumption of all H_2O_2 is ensured. Further migration to the radical to another oxidizable residue leads to the closed shell MYW and the ferric state is resumed. Thus, freeze-quench

EPR data were in good agreement with our stopped-flow results where the re-emergence of the ferric state was observed only after catalatic consumption of >300 equivalents of H_2O_2.

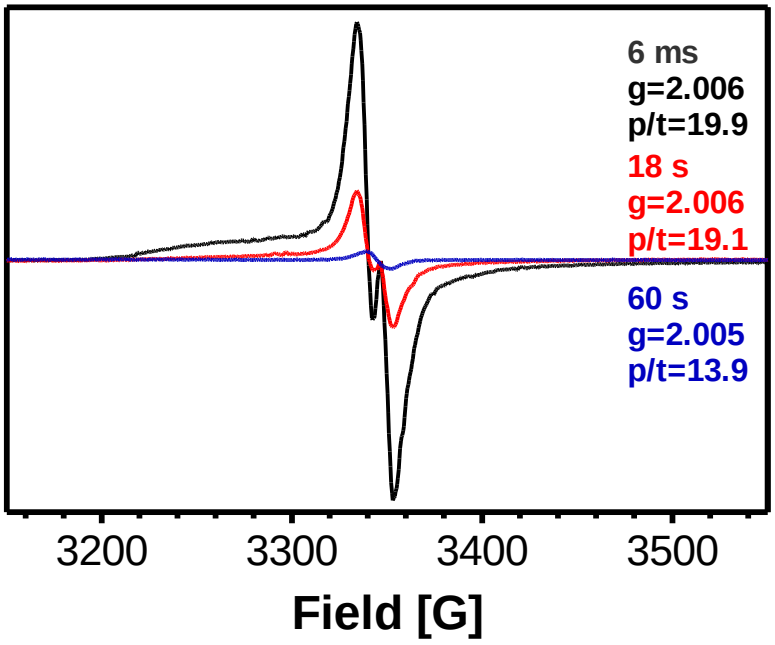

Figure 3.10. Evaluation of protein-based radicals formed upon reaction of *r*WT KatG and H_2O_2. The narrow doublet radical with a broadened shoulder observed at 6 ms after mixing with H_2O_2 (black line). The doublet signal without shoulder observed 18 s after mixing with H_2O_2 (red). The singlet radical corresponding to the ferric state observed 60 s after mixing with H_2O_2 (blue). Reactions were carried out at 25 °C in 100 mM acetate, pH 5.0. All spectra were recorded at 4.5 K. Spectrometer settings were as described in experimental procedures.

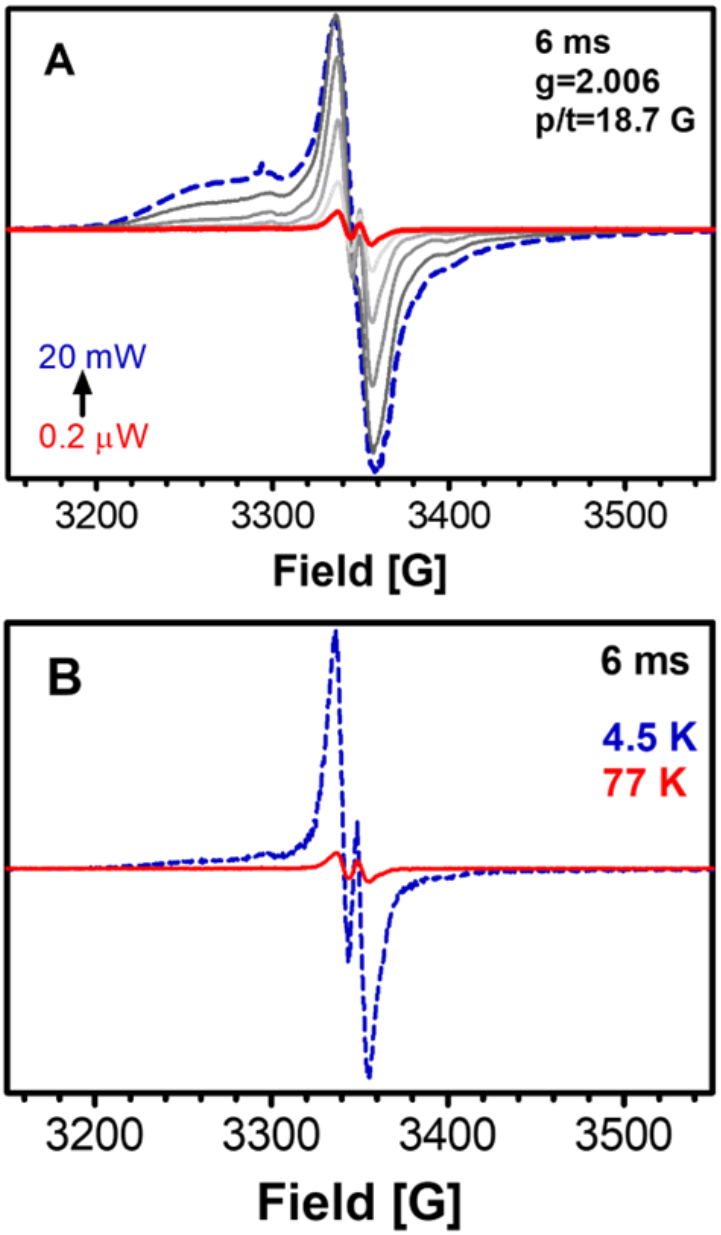

Figure 3.11. The effect of microwave power (0.2 μW (red line) to 20 milliwatt (blue dashed line) on the spectrum recorded for the sample quenched 6 ms after *r*WT KatG reaction with H_2O_2 is shown (A). The effect of temperature on EPR spectra for *r*WT KatG at the earliest timepoints (6ms) of its reaction with H_2O_2 (B). Spectra recorded at 4.5 K (blue dashed line) and 77 K (red line) are scaled for comparison.

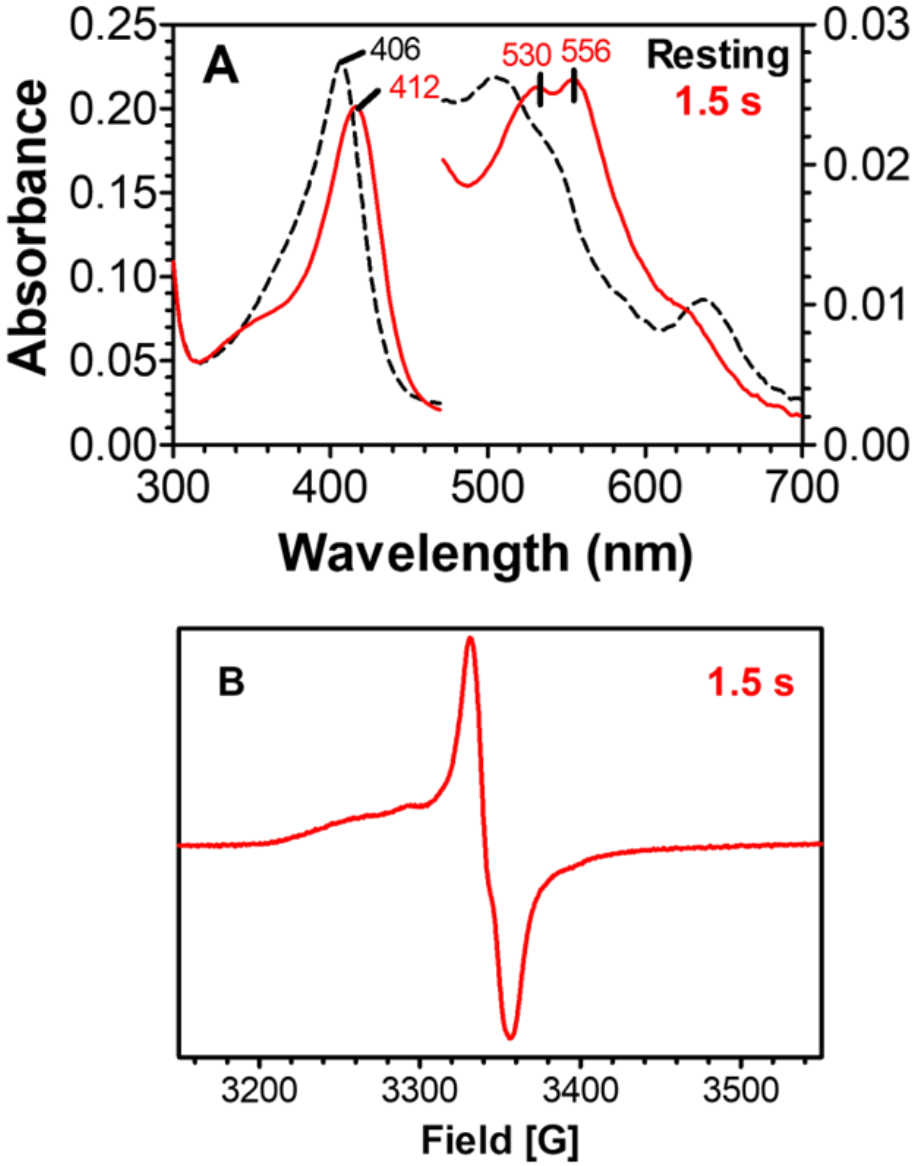

Figure 3.12. Monitoring the heme state and corresponding free radical state of *r*KatG upon reacting with 40 molar equivalents of H_2O_2 at pH 5 in stopped-flow spectroscopy (A) and EPR spectroscopy (B), respectively. The state observed at 1.5 s is corresponding to Fe^{IV}=O $[protein]^{\cdot+}$ intermediate.

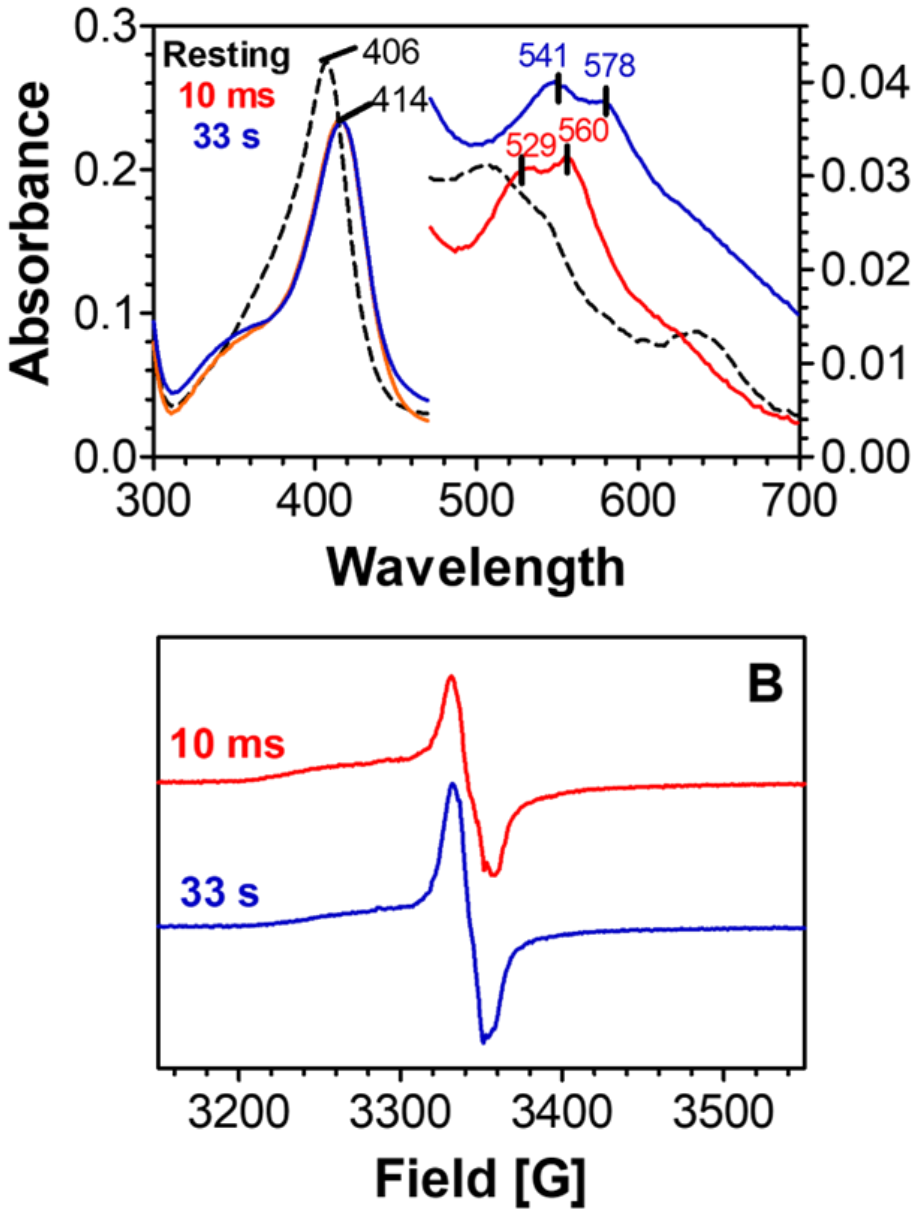

Figure 3.13. Monitoring the heme state and corresponding free radical state of *r*KatG upon reacting with 5 molar equivalents of PAA at pH 5 in stopped-flow spectroscopy (A) and EPR spectroscopy (B), respectively. The states observed at 10 ms and 33 s are corresponding to Fe^{IV}=O [protein]$^{\bullet+}$ and Fe^{III}-$O_2^{\bullet-}$ [protein]$^{\bullet+}$ intermediates, respectively.

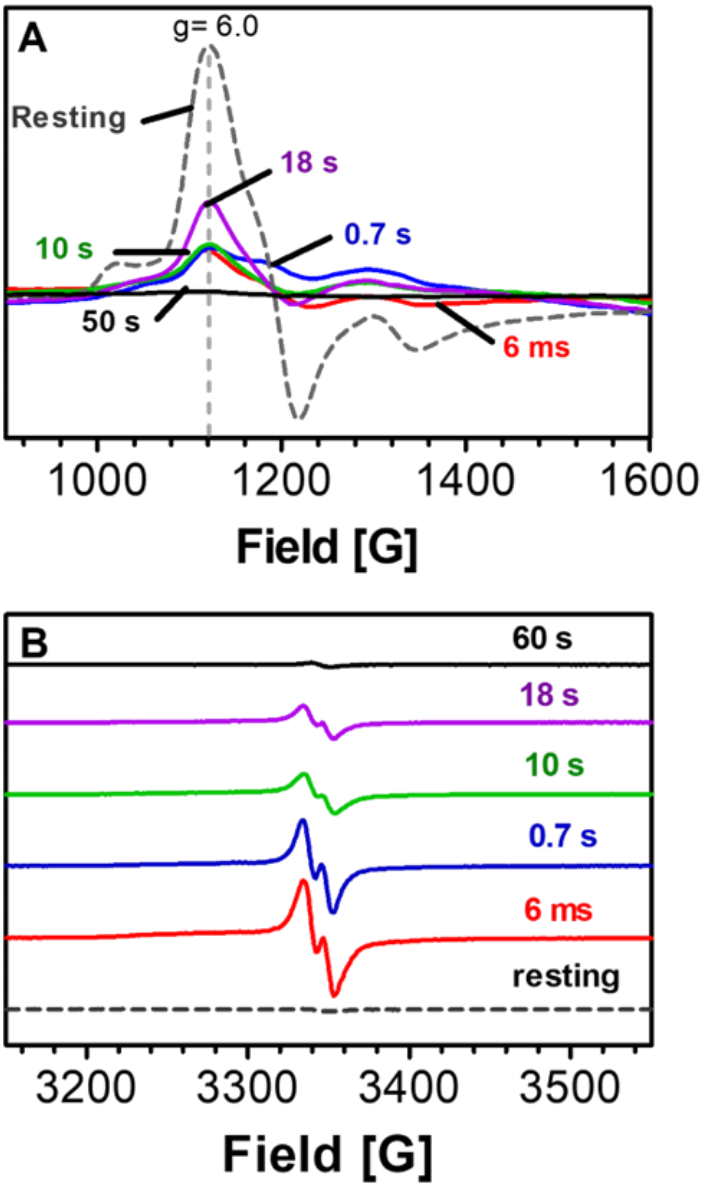

Figure 3.14. EPR spectra recorded for freeze-quenched samples from reaction of *r*WT KatG with H_2O_2. The contribution of high-spin ferric species typical of the KatG resting state are shown in the g~6 region (center field 3250 G and sweep width 5500 G) (A), and the g_z component of the resting state as well as protein-based radicals are shown in the g~2 region of the spectrum (center field 3350 G and sweep width 400 G) (B). The molar proportions of enzyme to H_2O_2 used for stopped-flow experiments (1:333) were maintained for these experiments. Consequently, ferric KatG (150 μM after mixing) was reacted with H_2O_2 (50 mM after mixing) for the time indicated prior to freeze-quenching. Reactions were carried out at 25°C in 100 mM acetate, pH 5.0. All spectra were recorded at 4.5 K. Spectrometer settings were as described in Experimental Procedures.

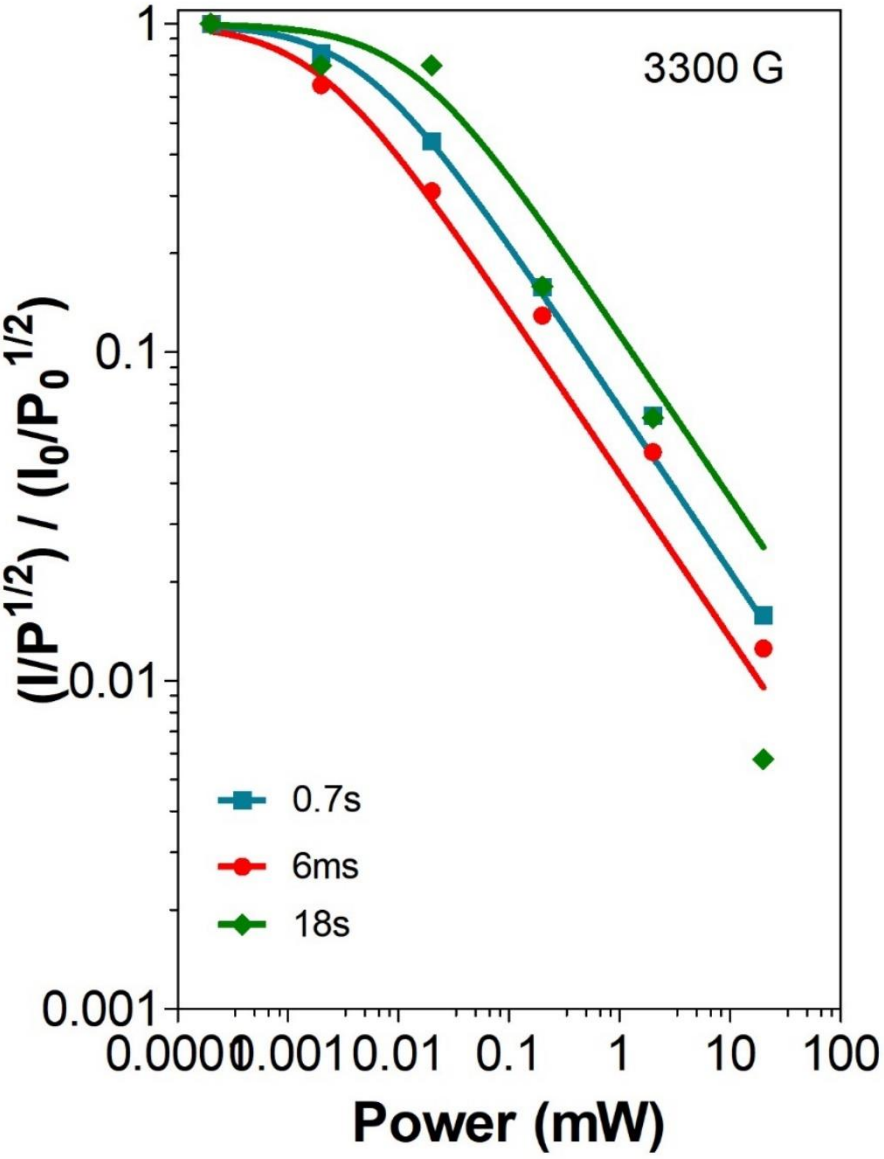

Figure 3.15. Effect of power on the radicals observed for *r*WT KatG after its reactions with 333 equivalents of H_2O_2 at 6 ms (red line), 0.7 s (blue line) and 18 s (green line).

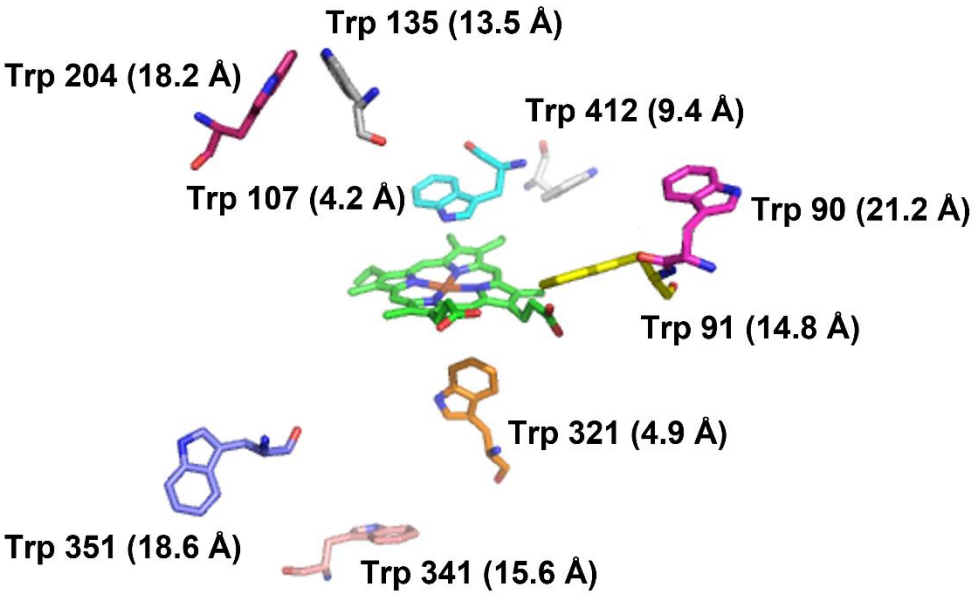

Figure 3.16. Tryptophan residues located near the active site heme. Position of Trp107 is suitably located for through-protein radical migration. Approximate distances between two closest atoms have been calculated using The PyMOL molecular graphics system, version 2.3.0.

3.4. Conclusion

In this work, we have investigated the spectral changes arising from reconstitution procedure and it is obvious that *r*KatG is mechanistically very different than *m*KatG. The efficiency and applicability of *r*KatG was confirmed by determining the spectral features and activity consistent with *m*KatG. The purpose of producing protein in reconstituted form was primarily to investigate the mechanism of novel MYW cofactor. Successfully producing *r*KatG, lacking the MYW cofactor, allowed us to monitor steps corresponding to *in vivo* biosynthesis of MYW cofactor preceding to the catalase turnover. We have studied cross-link formation using KatG's natural substrate H_2O_2, which permits catalatic turnover upon successful formation of the MYW adduct. Our kinetic studies reported early observation of Compound-II formation that led to the *de novo* MYW cofactor synthesis, a rare observation among WT KatGs. All observed intermediates formed by the reaction of KatG with H_2O_2 were also investigated with alternative peroxide, PAA. Prior treatment with PAA followed by H_2O_2 reaction obtained spectral features consistent with *m*KatG, indicating that the early intermediates observed by H_2O_2 reaction are not the artifacts of reconstituted proteins. Our EPR analysis also provided insight on intramolecular electron transfer pathway and identified at least two different types of protein radicals associated with Compound-II and Compound-III-like intermediates. The origin of intramolecular electron transfer and their migration to other oxidative residues requires further research and rigorous analysis due to the distinct radical signal observed at the earliest time points (6 ms).

In this study, we investigated *r*KatG using LC-MS/MS, stopped-flow and RFQ-EPR spectroscopy, and gathered spectral evidence that the autocatalytic formation of MYW adduct, indeed, can be followed during steady-state reaction condition in the presence of H_2O_2. Presence of high-valent ferryl-oxo intermediates, concomitant with the radical formation

supports our hypothesis that MYW adduct formation, as well as KatG catalatic mechanism proceeds with free radical-based propagation. Our proposed mechanism (Figure 3.17) complies with previous studies that MYW adduct formation is a sequential autocatalytic process. The very first reaction of *r*KatG with H_2O_2 generates Compound I, which act as an oxidizing intermediate. Due to very rapid quenching of the porphyrin radical, we were not able to detect Compound I in *r*WT KatG. However, its oxidizing capacity leads to the oxidation of Tyr 229 and Trp 107 to their corresponding free radical state confirmed by EPR spectroscopy. Both radicals are in close proximity to the heme (Trp107~3.7 Å and Tyr229~5.4 Å) and positioned within the threshold for long range electron transfer, facilitating the Tyr229-Trp107 (YW) covalent bond. Further oxidation of YW adduct by second equivalents of H_2O_2 results in a quinoid state, furnishing an electrophilic center for attack by M255 to form the Y-M sulfonium structure and complete the entire MYW covalent adduct. Successful formation of MYW adduct shapes the reconstituted enzyme mechanistically consistent with mature enzyme evidenced by spectroscopic and enzymatic properties.

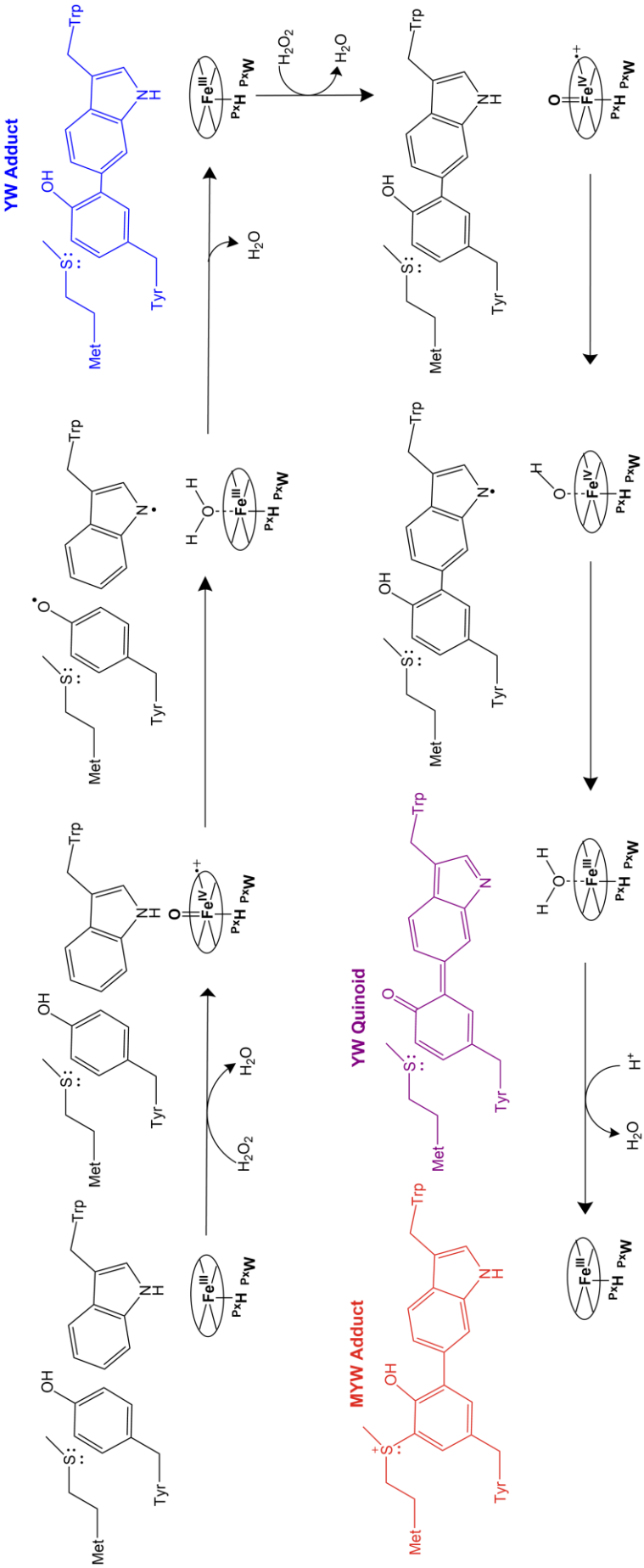

Figure 3.17. Scheme representing the proposed mechanism of MYW cofactor biosynthesis.

4. CHAPTER FOUR

PARTIAL FORMATION OF A PROTEIN-BASED COFACTOR IN *M. tuberculosis* KatG AND ITS IMPACT ON CATALYSIS

4.1. Introduction

The heme-dependent enzymes catalase-peroxidases (KatGs) constitute a very abundant peroxidase–catalase superfamily[156], broadly distributed among prokaryotic and eukaryotic systems. KatG can dismutate H_2O_2 using both catalase and peroxidase activity[279], a stand-alone property in its entire superfamily. The rapid rate of catalatic turnover (*i.e.*, catalase activity) surpasses the peroxidatic turnover (*i.e.*, peroxidase activity), albeit the physiological substrate of the peroxidatic reaction remained unidentified. Thus, KatG fulfils the role of efficient H_2O_2 removal, protecting the organisms which utilize KatG to detoxify the threat posed by H_2O_2. In the context of protection against host defenses, another *Mycobacterium tuberculosis* (*Mtb*) non-heme di-iron catalase Rv2633c play important role in the adaptation to host-derived antimicrobial mechanisms such as phagosomal acidification and reactive oxygen species.[280]

Although KatG's primary function is catalase activity, all its active site residues are typical of heme peroxidases with low resemblances with heme catalases, establishing the proposition that the KatG is a structure-function anomaly that supports catalatic turnover despite built in a peroxidase scaffold. One of the most conspicuous of its structural oddity is the presence of a protein-based cofactor which has been discussed in detail in previous chapters. Site-directed mutagenesis studies by our group and others[89,243,281] showed that mutation on Tyr229 or Trp107 prevents the crosslink whereas exchange of Met255 (*Mtb* KatG numbering) allows the covalent bond formation between Tryr229 and Trp 107.[165] The partial crosslink (Tyr229-Trp107 or YW) not only bears important ramification in elucidating the sequential biosynthetic mechanism of the MYW cofactor, but also expected to be one of the most common causes for increasing sensitivity to INH.[282] Substitution for M255I induced the

significant alteration in the active-site access channel which has been shown to diminish catalase activity and a high enhancement of peroxidase activity.

Previous studies reported a negligible catalase activity (k_{cat} 1.1 ± 0.1 s^{-1}) for $_{MYW}$Met substituted enzymes (bearing partial adduct) almost similar to $_{MYW}$Tyr or $_{MYW}$Trp substituted enzymes (no adduct) indicating that the mature state of partial adduct cannot support catalase activity at all.[96,164,243,283] Although Ghiladi and group provided valuable insight into the enzymatic and spectroscopic properties of the partial adduct, all the dominant reaction intermediates that they observed, required the incubation with peracetic acid (PAA), a two-electron oxidant, or 2-methyl-1-phenyl-2-propyl hydroperoxide (MPPH) which is susceptible homolytic cleavage.[165] However, monitoring the formation of the partial adduct in real time and the intermediates involved in the MYW biosynthetic process is only possible with its natural substrate H_2O_2, which we extensively used in this study. Additionally, the catalase activity that has been reported for reconstituted M255I KatG (*r*M255I) is not distinct from mature M255I KatG (*m*M255I) which excludes the differential capacity between the impromptu formation of YW adduct (*r*M255I) and the naturally forming YW adduct (*m*M255I).[165] In this study, we have prepared the *r*M255I variant by site directed mutagenesis and expressed the protein according to our established reconstitution protocol. The detail of mutagenesis and expression detail will be found in Chapter Three, section 3.2.2 to 3.2.4. The catalase activity of *r*KatG (k_{cat} 61.54 ± 0.06 s^{-1}) appeared a bit higher than *m*KatG (k_{cat} 12.88 ± 0.89 s^{-1}).

Further investigation on the partial adduct has been employed by UV-visible, stopped-flow spectroscopy, and mass spectrometric analyses to characterize the variant in contrast with wild-type and completely adduct lacking variants (Y229F and W107F) both in their reconstituted and mature forms. In our observation, correlations can be made within the rates

of O_2 production, catalase activity and generation of compound II and III formation. This variant, despite lacking the complete MYW cofactor, supports O_2 production at rates greater than are observed for other MYW cofactor variants (*e.g.*, Y229F and W107F KatG). Interestingly, reconstituted M255I can be accounted for higher O_2 production as compared to its mature form (*i.e.*, *r*M255I > *m*M255I). Catalase activity observed in our study can be expressed as *r*Y229F < *r*M255I < *r*WT whereas all mature form of variants behaved the same (negligible catalase activity). Therefore, we conclude that YW crosslink in M255I variant forms in the early stages of MYW adduct formation. Its presence in reconstituted and mature form distinctly alters the spectral features of heme intermediate. Consistent with all previous studies, none of the variants returned to their resting state.

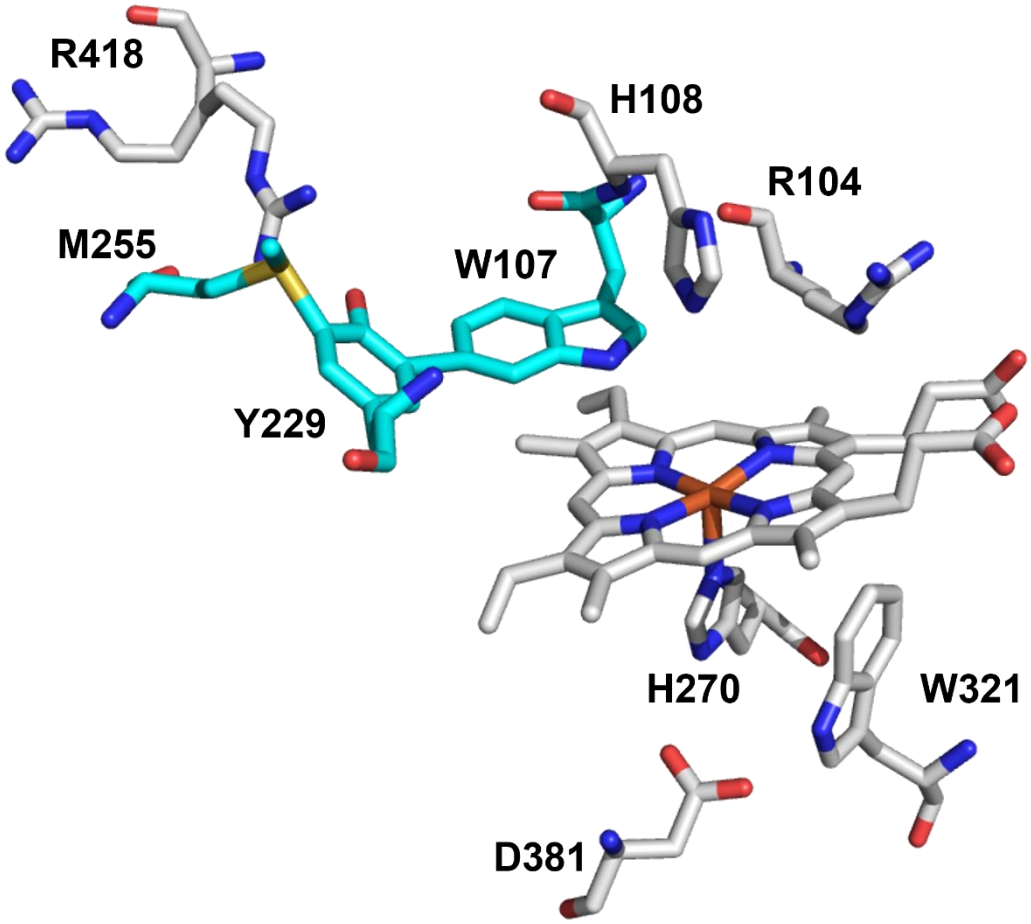

Figure 4.1. Active site of KatG. Location of mutations are highlighted in teal. Coordinates were obtained from the protein data bank (PDB ID 2CCA).

4.2. Materials and Methods

All the materials and reagents used in this study are already listed in Chapter 3. Variants construction details are also elaborated in Chapter 3. Expression and purification techniques for apo, reconstituted and mature forms are followed as described in Chapter 2.

4.2.1. Enzyme Assays

All measurements were performed with minor modification from published procedure.[47] Assays were carried out in Shimadzu UV-vis Spectrophotometer. Catalase activity was also evaluated by monitoring O_2 production over time at pH 5.0 and 7.0 using Clark-type O_2-sensitive electrode (Hansatech, Norfolk, UK) as described previously.[245] Kinetic parameters (k_{cat} and k_{on}) were obtained from nonlinear regression (least-squares fitting) of Michaelis-Menten plots using the GraphPad Prism kinetics software package.

4.2.2. Extent of Oxygen Production

The extent of O_2 production was evaluated at pH 5.0 with 50 mM acetate in the presence and absence of 0.01 mM ABTS as well as at pH 7 with 100 mM phosphate using a Clark-type O_2-sensitive electrode (Hansatech, Pentney, Norfolk, UK). In this reaction, 5 nM enzyme was reacted with 0.5 mM H_2O_2 at room temperature after the electrode had been calibrated.

4.2.3. Stopped-Flow Optical Spectroscopy

Kinetic measurements of the direct reaction between the ferric KatG with hydrogen peroxide, and peroxyacetic acid were performed using a PC-upgraded SX18.MV rapid reaction analyzer from Applied Photophysics (Leatherhead, UK). Peroxide solutions were prepared freshly and diluted in appropriate 50 mM acetate buffer (pH 5.0) or 100 mM phosphate buffer (pH 7.0).

4.3. Results and Discussion

4.3.1. UV-visible Spectroscopic Analysis of KatG (M255I)

The electronic absorption spectrum of *r*M255I KatG and *m*M255I KatG showed all bands typical of a heme *b*-containing peroxidase in the high-spin ferric state (Figure 4.2). The relative population of 6-coordinate heme tends to be higher in *r*M255I KatG revealed by CT-1 feature at ~630 nm. No visible feature of low-spin heme (red-shifted Soret and charge transfer bands at 565 and 580 nm) was observed with any of *r*M255I and *m*M255I KatG. The optical purity ratio (*i.e.*, Reinheitzahl or *Rz* value, defined as (A_{406}/A_{280}) for *r*M255I was found to be much higher (0.56) than the *m*M255I (0.2), indicating the better efficacy of protein to incorporate heme in the active site. The overall yield of the purified enzyme is also found to be higher for *r*M255I (500 nmol/L) than for *m*M255I (50 nmol/L) which encouraged implementation of this method for more sophisticated techniques. Figure 4.3 compares representative low-temperature EPR spectra of *r*M255I and *m*M255I KatG which predominantly shows the contribution of high-spin species. In our observation, obtained EPR spectra indicate very similar heme geometry with low rhombicity as observed with WT. For better comparison, EPR spectra of *r*Y229F and *r*W107F was also presented.

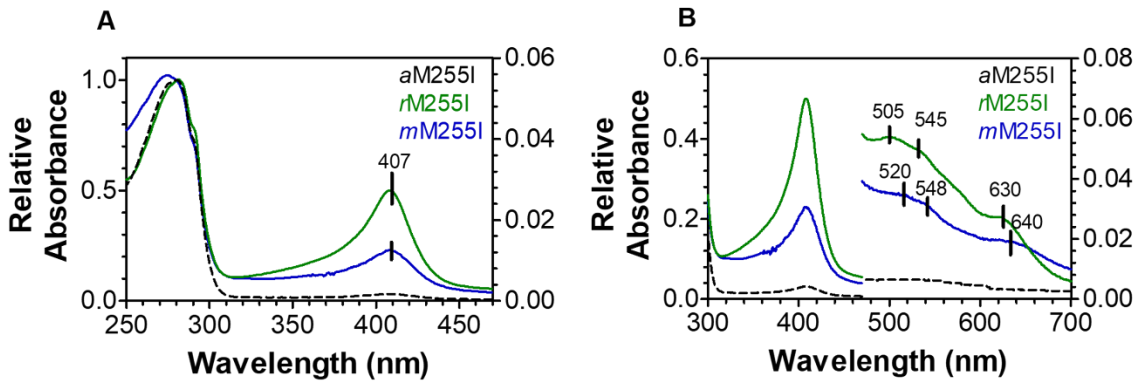

Figure 4.2. UV-visible spectra of apo (black), *r*M255I KatG (green) and *m*M255I KatG (blue). Panel A shows the protein peak at ~280 nm and heme peak ~407 nm. Panel B shows the features in soret and charge transfer regions of M255I KatG in apo, reconstituted and mature form.

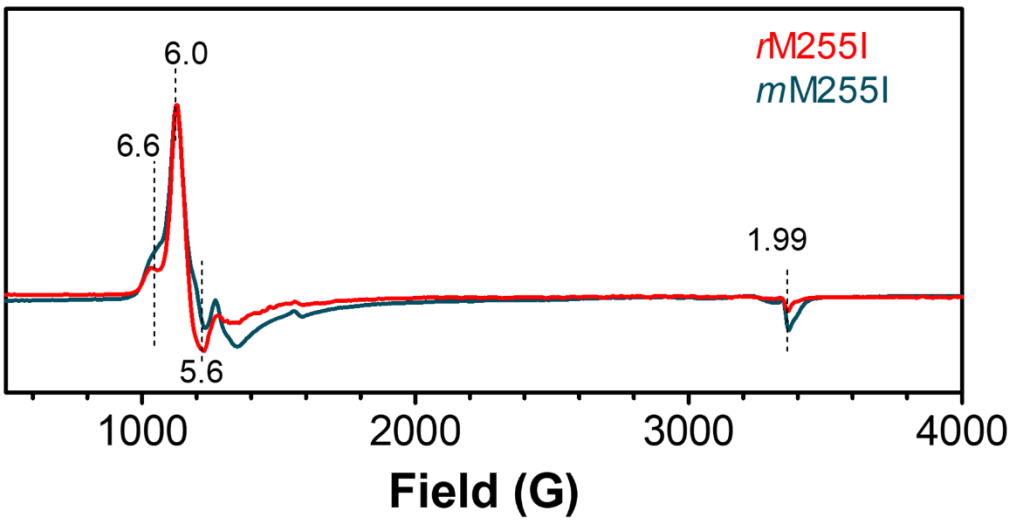

Figure 4.3. Low-temperature EPR spectra of *r*M255I (red) and *m*M255I (blue) KatG.

4.3.2. Catalase and Peroxidase Activities of M255I KatG

Steady-state kinetic analyses were performed to determine the kinetic parameters (*k*cat and catalytic efficiency, *k*cat/*K*m) for the catalase and peroxidase activities of M255I KatG and further compared with WT and other adduct-negative variants. As conventional catalases do not follow typical Michaelis-Menten kinetics due to their lack of a detectable enzyme-substrate complex and inability to reach saturation with H_2O_2 before inactivation, kinetic constants reported here for catalase activity are 'apparent' values. Our UV-visible spectroscopic analysis did not measure any detectable catalatic activity for M255I (reconstituted and mature) KatG under the conditions employed for this kinetic study, and hence are not presented here. However, catalase activity was detectable by monitoring the O_2 production using a Clark-type, O_2-sensitive electrode (oxygraph). Reconstituted M255I showed marginally better catalase activity than *m*M255I (Table 4.1) but are significantly poorer than that observed for WT KatG. For Y229F and W107F variant, no catalase activity could be recorded using the oxygraph.

Peroxidase activities were also measured for M255I KatG and compared with WT and Y229F variant. Maximum increase in peroxidase activity was observed for *r*M255I KatG (*i.e.*, ~100-fold more than WT KatG and ~10-fold greater than *m*M255I KatG). In the absence of the crosslink, the enzyme converts to monofunctional peroxidase and the increase in peroxidase activity (concomitant with the loss of catalase activity) is due to enhanced formation and/or increased stabilization of compound II (Fe^{IV}=O) intermediates. In this aspect, it was expected that the crosslink-disrupted variants (Y229F and W107F) would also exhibit higher peroxidase activity. However, we have seen a slight decrease in peroxidase activity than WT KatG, probably due to the instability of the enzyme.

Table 4.1. Kinetic parameters for catalase and peroxidase activities of M255I in the reconstituted and mature forms. For comparison, the values for WT, Y229F and W107F are provided.

	Catalase activity observed in oxygraph instrument			Peroxidase activity observed in UV-vis instrument		
KatG	k_{cat}, s^{-1}	K_m, mM	k_{cat}/K_m, $(M^{-1}s^{-1})$	k_{cat}, s^{-1}	K_m, mM	k_{cat}/K_m, $(M^{-1}s^{-1})$
***r*WT**	3092 ± 0.10	3.84 ± 0.20	$(8.05 \pm 0.05) \times 10^5$	2.44 ± 0.1	0.07 ± 0.75	$(3.2 \pm 0.4) \times 10^4$
***m*WT**	2312 ± 0.04	6.19 ± 0.02	$(3.73 \pm 0.02) \times 10^5$	1.66 ± 0.1	0.06 ± 0.03	$(2.5 \pm 0.2) \times 10^4$
***r*M255I**	61.54 ± 0.06	2.46 ± 0.19	$(2.52 \pm 0.31) \times 10^3$	10.90 ± 0.16	0.003 ± 0.03	$(2.95 \pm 0.12) \times 10^6$
***m*M255I**	12.88 ± 0.89	1.43 ± 0.90	$(8.96 \pm 0.09) \times 10^2$	1.41 ± 0.05	0.016 ± 0.05	$(8.7 \pm 0.10) \times 10^5$
***r*Y229F**	ND	ND	ND	1.5 ± 0.07	0.16 ± 0.04	$(9.2 \pm 0.02) \times 10^3$
***m*Y229F**	ND	ND	ND	2.3 ± 0.09	0.42 ±0.05	$(5.43 \pm 0.08) \times 10^3$
***r*W107F**	ND	ND	ND	2.68 ± 0.19	0.72 ±0.07	$(3.7 \pm 0.09) \times 10^3$
***m*W107F**	ND	ND	ND	5.625 ±0.14	0.54 ± 0.06	$(1.04 \pm 0.09) \times 10^4$

4.3.3. Monitoring of O_2 Production using O_2-sensitive Electrode

It is well accepted that both KatG catalase and peroxidase reaction cycles begin with H_2O_2 reduction to achieve higher KatG oxidation states. The completion of each catalytic cycle requires oxidation of another substrate; either H_2O_2 for catalatic turnover or an exogenous electron donor for peroxidatic turnover. Since, KatG catalase activity exclusively depends on the fully formed MYW cofactor, it was not surprising that catalatic O_2 production was not imparted to any of these variants (M255I, Y229F and W107F).[96,243,284] Additionally, the stimulatory effects afforded to catalase activity in the presence of peroxidatic electron donors observed in WT KatG are only applicable other adduct possessing KatG variants, and hence not observed in the MYW-lacking variants W107, Y229, and M255I (data not shown). In this context, it is surprising that *r*M255I KatG generates O_2 production (Figure 4.4 A), let alone at a rate greater than the other MYW-negative variants (*i.e.*, Y229F and W107F). However, aligning with the previous studies[165] *m*M255I KatG does not support O_2 production (Figure 4.4 B) and behaves similar like Y229F and W107F KatG (reconstituted and mature). Although the amount of O_2 production by *r*M255I KatG is significantly lower than WT KatG, this non-zero rate is surely intriguing to explore the contribution of partial adduct.

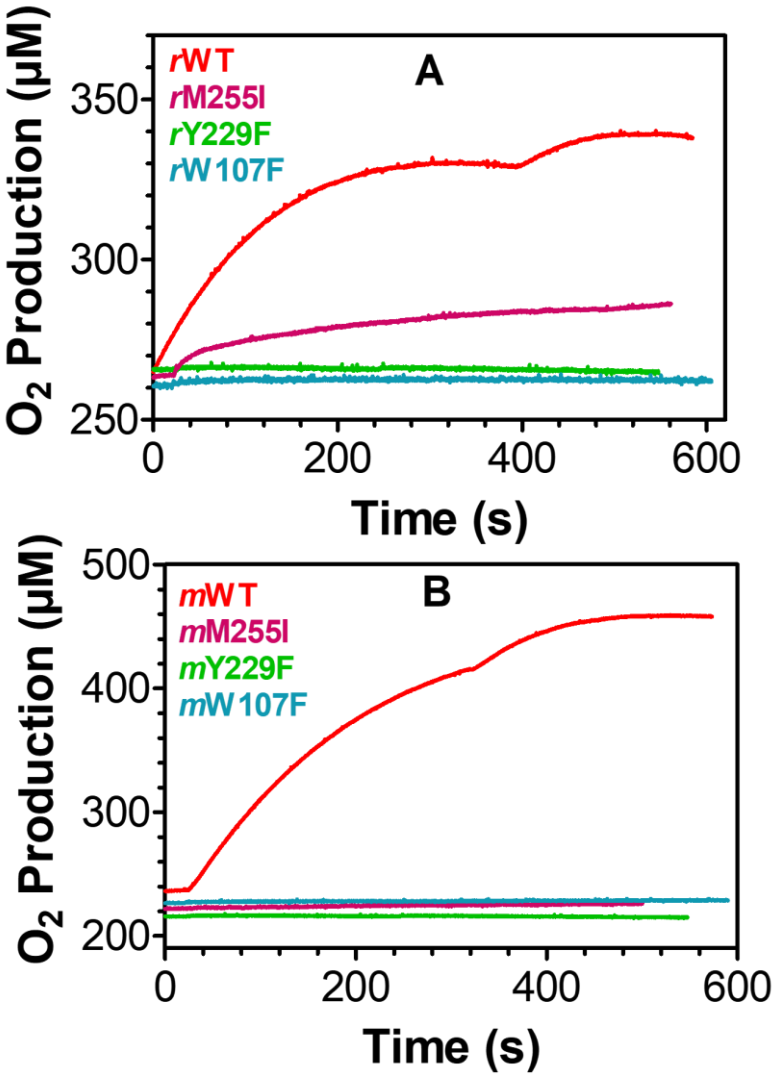

Figure 4.4. The amount of catalatic O_2 produced by reconstituted (A) and mature form (B) of WT, M255I, Y229F and W107F variants.

4.3.4. Monitoring Catalytic Heme Transitions of M255I KatG

Stopped-flow optical spectroscopic experiments were employed to examine the formation of high-valent iron intermediates of M255I KatG in both the reconstituted and mature form and to provide insights into the alterations observed in the steady-state measurements. Neither low or higher equivalents of H_2O_2 allowed us to observe compound I under the conditions known to generate compound II and III because of their less stable nature as compared to plant peroxidase. Rapid formation of compound I within the mixing time of the stopped-flow apparatus is due to the absence of sulfonium ion that obstructs the formation of second positive charge in the form of the porphyrin π-cation radical.

Previous studies suggested that, in the presence of H_2O_2, *Mtb* KatG compound I transforms to compound II by producing a tyrosyl radical at the expense of an electron transfer process.[285] Further formation of compound III indicates that KatG enzymes must cycle through compound II, because the reaction mechanism of oxyferrous enzyme is through an initial single-electron reaction of compound II with hydrogen peroxide.[286] In this study, the change in heme intermediates were observed upon mutation of the crosslink constituents, M255, Y229 and W107 KatG, by stopped-flow spectroscopy.

Upon mixing the *r*M255I enzyme with very low equivalents of H_2O_2 (1-5 equivalents), we have observed only classical oxo-ferryl, compound II (Fe^{IV}=O) intermediate [UV-visible spectrum: 415 (Soret), 528, 560 nm] (data not shown). The spectral feature of this *r*M255I KatG compound II also matches well with the previously characterized Y229F KatG compound II [91,284] or *Synechocystis* PCC 6803 Y249F KatG compound II[96] or that observed in HRP and other peroxidases.[207] Upon increasing the H_2O_2 concentration up to 333 equivalents or higher we have observed the same compound II as the earliest intermediate (Figure 4.5 A), which further converted to oxyferrous compound III intermediate at ~16.5 s, [UV-visible

spectrum: 415 (Soret), 538, 578 nm] (Figure 4.5 B). Persistence of compound III at the end of the reaction (50 s or higher) indicates the inactivation of the species, converting the enzyme to a monofunctional peroxidase. Applying the same reaction conditions to *m*M255I KatG, we have observed a spectral progression slightly distinct than the *r*M2555I KatG. As early as 2.5 ms, *m*M255I KatG produced a radical intermediate with features as [412 (Soret), 531, 582 nm] (Figure 4.5 C). The absorption features don't match very well with compound II-like state but seems like transitioning towards compound III-like state. A clear formation of compound III [412 (Soret), 535, 573 nm] became obvious at 1.0 s and following. (Figure 4.5 D). Neither of the ferric state was observed with any of the *r*M255I or *m*M255I KatG. In general, it can be speculated that presence of compound II is associated with the partial adduct forming stage (*r*M255I), however, its detection is limited in an enzyme where the partial adduct has been already formed (*m*M255I). Formation of compound II becomes progressively less favored in an enzyme that lack a fully intact (YW adduct), as well as its lack of formation in the *m*WT enzyme when the MYW adduct is fully intact. Further, analysis was carried out using PAA as an alternate substrate to validate the data observed with H_2O_2. Both *r*M255I and *m*M255I enzymes were allowed to react with 5 equivalents of PAA, to ensure generation of the crosslink (Figure 4.6). In this case both *r*M255I and *m*M255I KatG showed the formation, however *m*M255I KatG formed it at a rate slower than *r*M255I KatG.

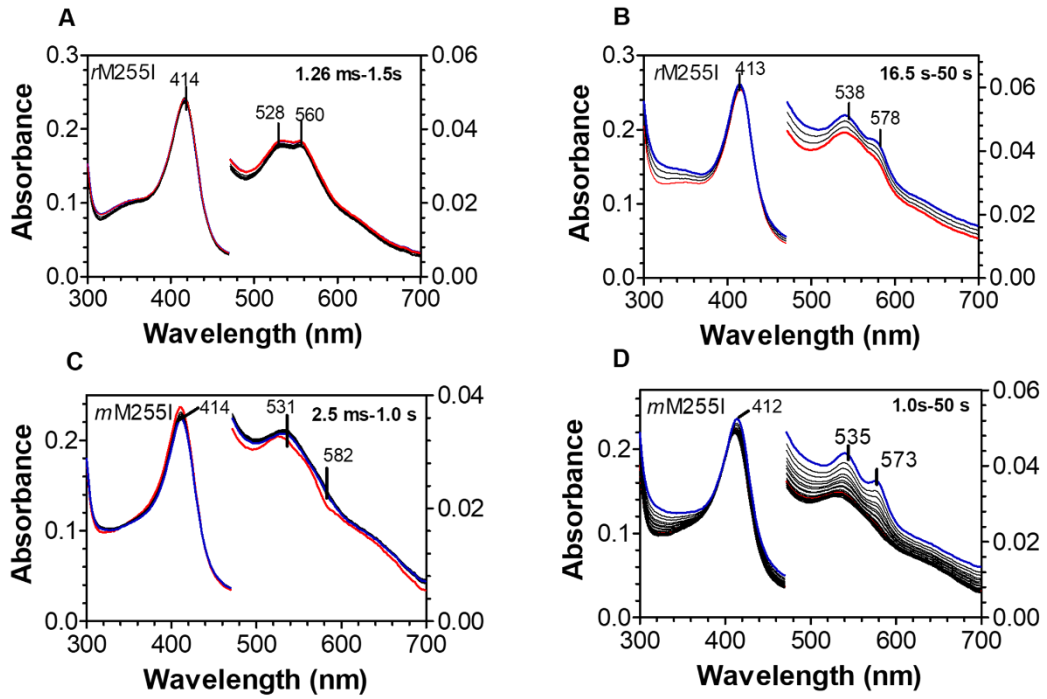

Figure 4.5. Stopped-flow UV-visible spectroscopic monitoring of the reaction between M255I KatG (3 μM) and a 333-fold excess of H_2O_2. Clear formation of compound II is being observed for *r*M255I KatG (Figure 4.5 A, 2.5 ms to 1.0 s) which further converted to compound III (Figure 4.5 B, 16.5 s to 50 s). Similar progression of compound II to compound III was also observed for *m*M255I (Figure 4.5 C and D).

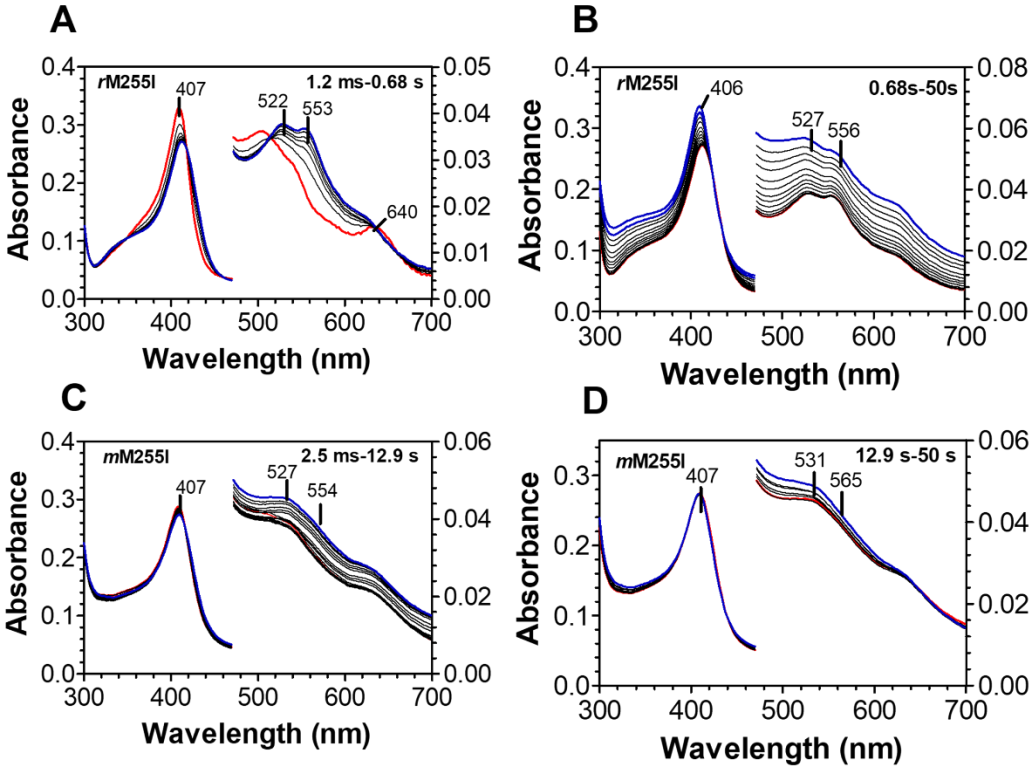

Figure 4.6. Stopped-flow UV-visible spectroscopic monitoring of the reaction between M255I KatG (3 μM) and 5-molar equivalents of PAA. Clear formation of compound II is being observed for *r*M255I KatG (Figure 4.6 A, 1.5 ms to 0.68 s) and its persistence is observed until the end of the reaction. Progression of compound of compound II to was also observed for *m*M255I (Figure 4.6 C and D). Although not clear at the beginning of the reaction but pronounced during the later phase of the reaction.

Heme intermediates formed by M255I KatG was further evaluated by comparing the results with Y229F and W107F variants. For *r*Y229F KatG, we have observed rapid turnover of compound I (not detected) to compound II and slow formation of compound III (Figure 4.7 A and B). The initial spectrum right after mixing the enzyme with H_2O_2 (~2.5 ms-1.5 s), is a red-shifted soret peak (414 nm) and the features near 530 and 560 nm. The features in the final spectrum are common to those found in horseradish peroxidase compound II or C*c*P compound I, both of which contain oxyferryl heme but not the porphyrin-π-cation radical.[207] Heme spectral features across the time courses from 2.6 s to 50 s, yielded a Soret peak at 414 nm and CT bands at 540 and 578 nm also resembling to those of compound III of other oxyperoxidases.[186,287] Interestingly, *r*Y229F KatG yielded compound II by reacting with H_2O_2 as low as 1 equivalents whereas, *m*Y229F KatG generated compound II only in the presence of excess amount of H_2O_2 (333 equivalents or higher) (Figure 4.7 C). Formation of compound III was observed for both *r*Y229F and *m*Y229F variant in both lower or higher equivalents of H_2O_2 (Figure 4.7 D). compound I was not observed for any of the Y229F variants because of its rapid conversion to compounds II and III. This spectroscopic characterization demonstrates that without the Tyr229 residue, the catalytic cycle is unable to be completed. Formation of compound II indicates the absence of adduct the state similar to the *r*WT in the pre-steady state. Mutation to the adduct Trp was also investigated in this study in both reconstituted and mature form. Previous study demonstrated that W107F KatG encounters faulty binding of second molecule of H_2O_2, resulting in an incompetent formation of compound I, resulting .[94,157] Our stopped-flow analysis showed that both *r*W107F and *m*W107F produced stable compound III as the very first reaction intermediate indicating a very fast formation and decay of compound I and compound II.

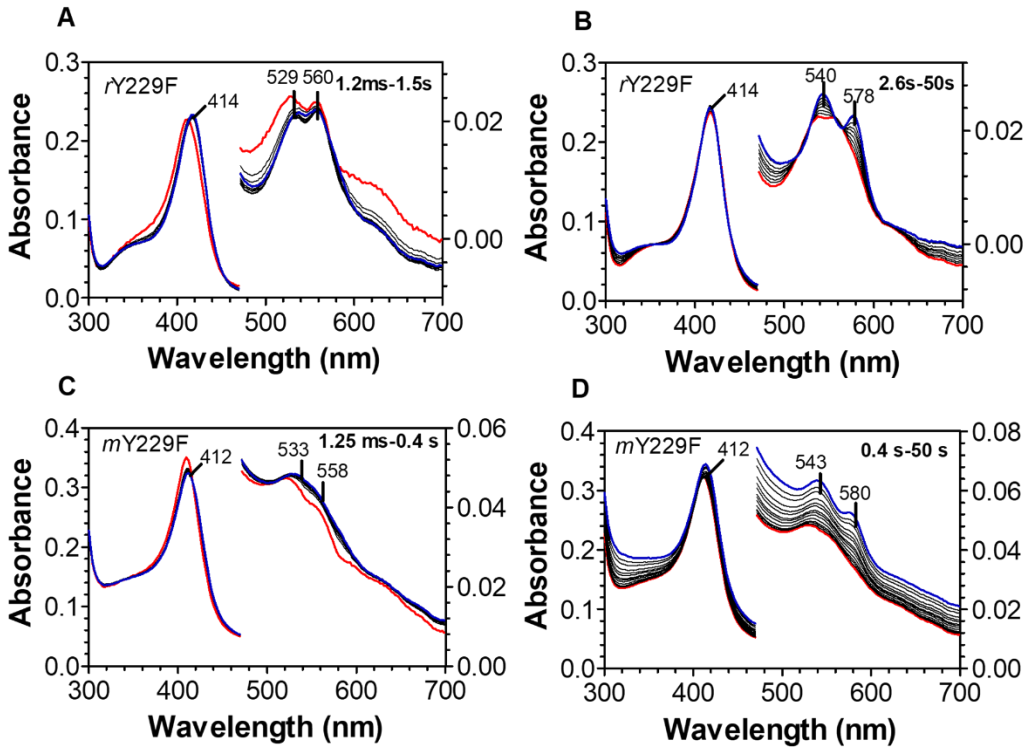

Figure 4.7. Stopped-flow UV-visible spectroscopic monitoring of the reaction between Y229F KatG (3 μM) and a 333-fold excess of H_2O_2. Similar progression from the resting state to the compound II formation and finally catalytically inactive compound III formation is observed for both *r*Y229F (A and B) and *m*Y229F KatG (C and D).

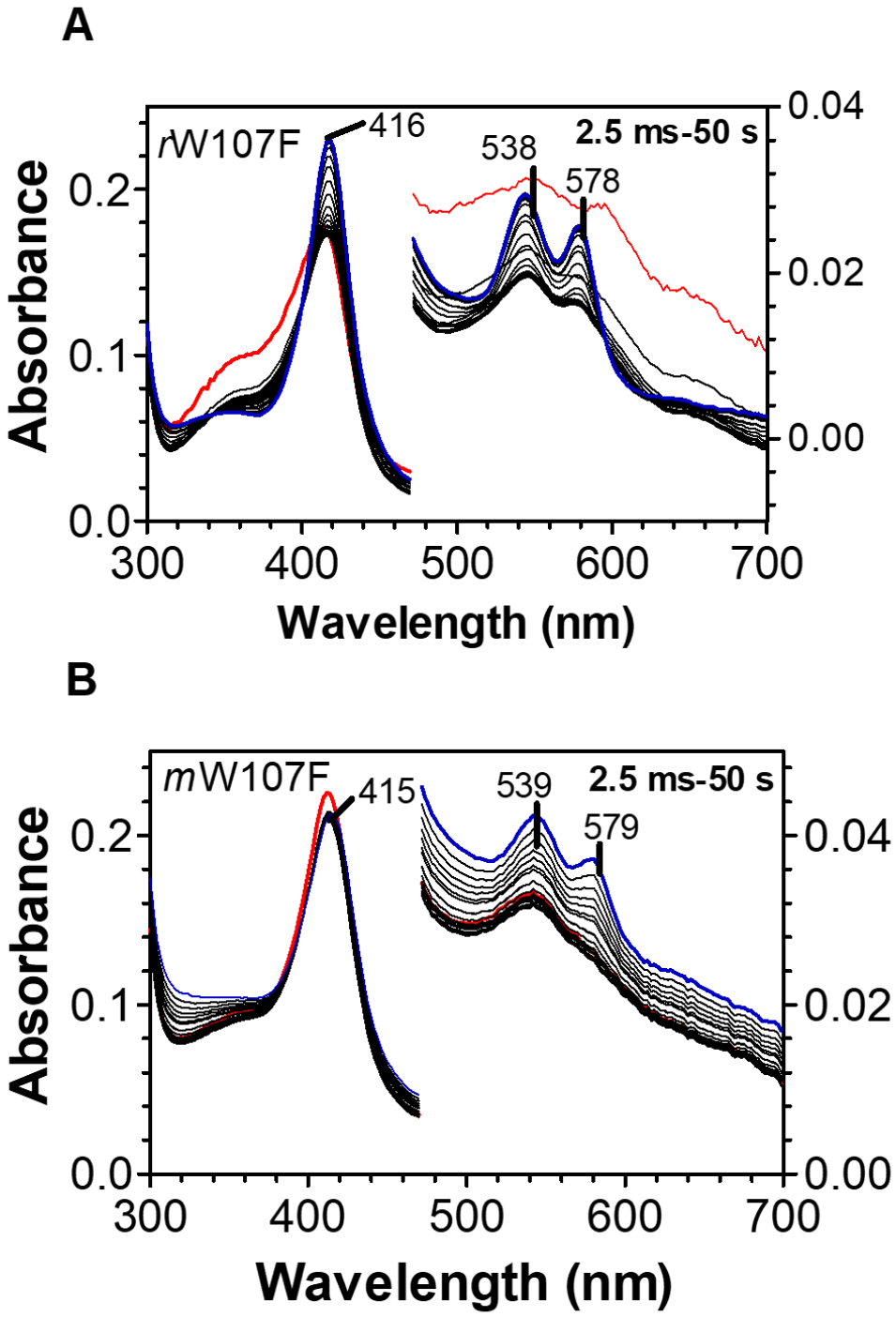

Figure 4.8. Stopped-flow UV-visible spectroscopic monitoring of the reaction between W107F KatG (3 μM) and a 333-fold excess of H_2O_2. The first observed intermediate is compound III for both *r*W107F (A) and *m*W107F (B). The persistence of compound III is observed from the beginning to the end of the reaction (2.5 ms-50 s).

4.4. Conclusion

In this study we investigated the partial adduct containing variant (*r*M255I and *m*M255I), where *r*M255I being lacked the partial adduct initially. The results were evaluated in comparison with WT and other adduct negative variants and demonstrated that perturbations of the MYW adduct affected the variants in different degree. The covalent linkage between Tyr229 and Trp107 plays important part of the hydrogen-bonding network on the distal side of the heme. The mutations on these MYW targeting residues and the expression of the variants in reconstituted and mature form provided insight on the oxo moiety of the ferryl intermediate and change its UV-visible features due to the perturbations in the heme active site and the distal pocket. It is well understood that the distinct functionality, which observed between *r*WT and *m*WT, were not observed in any MYW lacking variants. This makes good sense because covalent adduct is required for establishing the proper geometry of residues that contribute to formation of catalatic site. In the absence of the adduct no such differences were observed between the pre-steady state and steady-state.

To gain more insight into Tyr-Trp crosslink we have investigated both *r*M255I and *m*M255I variants and came across that *r*M255I has a greater catalatic and peroxidase activity than *m*M255I. However, questions remain about the sulfonium ion in the Met-Tyr bond, which alters the electronic nature of the catalytic cycle.

We have observed formation of compound II in both *r*Y229F and *m*Y229F variants which may be due to the result of its rapid accumulation and its enhanced stability compared with that in WT KatG. Further transition to compound III indicates that the KatG must cycle through compound II, involving an initial single-electron reaction of compound II.

Our *r*W107F and *m*W107F variant could not generate either compound I and/ or II consistent with previous studies due to severe disruption of the hydrogen bonding network.[260,288] The presence of compound II was not even detected by alternate peroxide (*e.g.* PAA) indicating a strong fundamental alteration in the structure, imposed by this mutation.

We have also investigated the site of radical formation by applying rapid freeze-quench EPR spectroscopy. Preliminary data that we obtained were not sufficient and may require isotopic labelling for better confirmation of the radical site. Targeting multiple variants may be another approach for the better understanding of electron transfer pathways and comprehensive confirmation of radical formation sites in KatG.

5. CHAPTER FIVE

SUMMARY

5.1. Uncovering the Catalytic Novelty of KatG by Probing its Unique Post-translational Modification

The novelty of KatG is featured among the H_2O_2-degrading enzymes in that it can utilize a single active-site to perform both catalase and peroxidase activity for the degradation of H_2O_2. Part of this distinct functionality is achieved by a novel post-translational modification, elucidation of which was the main aim of this study. We hypothesized that the KatG unique MYW adduct formation is a radical-dependent multistep-involved mechanism. In this study, we employed biochemical assays and spectroscopic techniques (stopped-flow UV-visible and EPR spectroscopies) to elucidate mechanistic insight and to help us gain a better understanding of the early catalytic steps. We also used mutagenesis to gain further insight into the role of the partial (YW) crosslink and functional changes in the absence of crosslink.

The first merit of this study is the establishment of a protocol for apo KatG expression and heme reconstitution that has overcome the difficulties impeding the observation of cross-link formation post-translationally. Moreover, this protocol is effective for generating very high yield of the active protein, expanding the possibility of using more sophisticated and material-intensive techniques like EPR and Mössbauer spectroscopy. This protocol led us to monitor the appearance of catalytically competent intermediates that lead to the formation of the MYW adduct. Based on the data collected with the reconstituted protein, we surmised that the generation of the MYW adduct results from a series of properly directed intraprotein radical transfer reactions.

Next, using stopped-flow spectroscopy, we have observed Fe^{IV}=O-like intermediate at specific time points with reconstituted WT KatG which takes part in the initiation of steady-state catalase (Fe^{III}-$O_2^{\cdot-}$-like) intermediate. These stopped flow data helped us determining the timing and appearance of heme intermediates throughout the time course of KatG reaction with H_2O_2. Early appearance of Fe^{IV}=O-like intermediate prior to Fe^{III}-$O_2^{\cdot-}$-like intermediate during steady state catalatic turnover is a rare observation for WT KatG which is suggestive occurrence of intramolecular electron transfer and protein oxidation. At this point, we hypothesized that the generation of the free radicals on either Tyr229 and or Trp107 residues and other subsequent radical species leads to the formation of the MYW adduct. To evaluate this hypothesis, we used Rapid-Freeze-Quench (RFQ) Electron Paramagnetic Resonance (EPR) experiments in parallel with optical stopped-flow kinetics to monitor the production of the catalytic MYW cofactor protein-based radicals. The 9 GHz EPR spectrum, recorded at 4 K yielded a narrow doublet signal with exchange-broadening, upon quenching the reaction at 6 ms. This is the very first attempt to capture protein-based radical intermediates with *r*WT KatG during its first encounter with H_2O_2. The early appearance of an exchange-broadened species is indicative of at least one organic radical in magnetic interaction with the heme iron and a rare observation for WT KatG when it is in the midst of active catalase turnover. Up to the present, such species have only been observed with alternative peroxides like peracetic acid or after the depletion of H_2O_2 and this Trp radical signal has been unequivocally assigned as belonging to Trp321. During active catalase turnover of *m*WT KatG with H_2O_2, spectra have been dominated by an intense narrow doublet radical signal which has been assigned to the radical derivative of the fully-formed MYW adduct (i.e., $MYW^{\bullet+}$). We surmise that an early appearance of an exchange-broadened signal may arise from a Trp which is distinct from the proximal Trp 321. We suggest Trp 107 because of its proximity to the heme iron and its H-bonded interaction with the heme iron through an intervening water molecule. Comparing the

distance with C*c*P radical site (6.81 Å[289])[2], *Mtb* KatG radical site (distance between indole-N of Trp107 and the Fe is 4.19[156] or 4.37 Å[159], depending on the crystal structure) is much closer. Therefore, it is much more convincing that the compound II like state or MYW adduct forming stage is associated with a radical formation and the probable candidate is Trp107. However, further investigation is necessary by combining the complementary information obtained on the heme electronic structure by UV-vis stopped-flow absorption spectrophotometry and the chemical nature of the radicals by RFQ EPR spectroscopy for the correct confirmation of the radical site.

5.2. Bridging the Gap: Current Study and Future directions

In this study we have employed Stopped-flow UV-visible and rapid-freeze-quench electron paramagnetic resonance spectroscopies to characterize compound I (not observed with WT), II and III. Formation of compound II is a pre-steady state for WT KatG and inactive intermediate for MYW targeting variants. Observing the progress in the series: *m*Y229F (no cross link), *m*M255I (partial crosslink YW) and *m*WT (full MYW crosslink) demonstrated an increasingly attenuated rate of compound II formation (Table 5.1). Formation of compound II becomes progressively less favored and absent entirely in *m*WT KatG, when the MYW crosslink is fully intact. Interestingly, for the reconstituted proteins (*r*WT and *r*M255I, *r*Y229F), we have observed almost similar rate of compound II formation. The rates that we have observed in our study and others, were obtained from Simulated spectra derived from global kinetic fitting of the experimental data. However, as far as the molecular mechanism is concerned, a main limitation of steady state kinetics is that the nature of the rate-limiting step in the global catalytic process cannot always be established with certainty, so that it is not always clear which step the overall rate relates to. Time-resolved techniques, *e.g.*, rapid freeze

quench or stopped-flow, allow short-lived intermediates to be trapped and examined, but they are very demanding in terms of quantity of biological material, which may be in scarce supply.

Table 5.1. Rate of compound II (Fe^{IV}=O) formation in WT[290,291], M255I[292], Y229F[290,293] and W107F[293] KatG

Protein (KatG)	**Cross-link presence**	**K_{obs} ($M^{-1}s^{-1}$)**
WT	Full MYW	$(4.8 \pm 0.4) \times 10^4$
M255I	Partial MYW	$(1.4 \pm 0.1) \times 10^5$
Y229F	No crosslink	$(5.8 \pm 0.7) \times 10^6$
W107F	No crosslink	$(7.9 \pm 0.7) \times 10^6$)

To overcome these shortcomings, mass spectrometry can be used as the readout for characterizing the kinetics of rapid reactions capturing in millisecond time resolution.[294] Detection of covalent interaction between Tyr-Trp or Met-Tyr or Met-Tyr-Trp by LC-MS/MS will provide valuable information about the molecular mechanisms of covalent intermediates leading to MYW adduct formation. Mass spectrometry (MS) measures the mass-to-charge ratio (*m/z*) of ionized analytes. Since oxidative modifications alter the chemical composition of a protein, a change is observed in the *m/z* ratio of the intact protein and of the residues where the oxidation has been occurred. Thus, MS is a powerful method for identifying the alteration of the side chain of the protein and location of the covalent modifications.

In this study, we proposed the site of protein-based radical formation based on our preliminary data obtained from RFQ-EPR spectroscopy. At the earliest reaction time (6 ms), *r*KatG produced an exchange coupled radical signal upon reacting with 333 equivalents of H_2O_2, which we proposed a contribution from the distal tryptophan (W107). Closer inspection to the crystal structure of *Mtb* KatG and the location of distal tryptophan from Fe center (4.19 Å), this residue was assessed to be a possible candidate for the respective signal. However, previous study with *m*WT KatG showed solid evidence that the exchange coupled signal was not resulted from the W107.[193] Since our experimental evidence strongly justified that the *r*KatG is structurally very different than *m*WT KatG in terms of the presence or absence of intact MYW adduct, it is reasonable to address apparent differences reported so far on the *r*KatG and *m*KatG with regard to the chemical nature of the intermediates and possible radical sites.

To justify our hypothesis, further experiments will be required employing the RFQ-EPR technique. We have seen a mixed population of radical species at different time points which can only be discerned using a combined approach of RFQ- spectroscopy with deuterium

labelling and site-directed mutagenesis. Comparison of the 4K EPR spectra of *r*WT KatG and distal-heme side variants (*e.g.*, *r*W107F) should reveal distinct differences on the spectral line shapes. Similar approach has shown previously for assigning proximal tryptophan (W321) as the radical site by comparing the line shape between WT KatG and w321F variant.[47,193] Complimentary information on the factors that may contribute to such spectral differences between the *r*W107F radical intermediate can be obtained with the other reconstituted tryptophan variants (*e.g.*, *r*W91F, *r*W412F and *r*W321F etc.). Further confirmation can be obtained by pre-deuteration of Tyr and Trp radical in reconstituted WT and variants. Previous study assigned Tyr229 residue as the radical site by monitoring the collapse of the narrow doublet signal upon deuteration of the respective residue at β-methylene position. However, to our knowledge, no such study with reconstituted proteins has been conducted to unequivocally assign the radical site.

Direct electrochemistry is another emerging technique for studying the mechanism of redox enzymes.[295] Like many other redox enzymes, KatG is too large (80 kDa) and hence, the active site of the enzyme is deeply buried in the protective protein matrix. Therefore, direct electron exchange with an electrode can only occur under exceptional conditions. The principle of direct electrochemistry can be explained by comparing the technique to the traditional enzyme activity assay. Previous study has been made significant progress towards understanding the electron transfer mechanism for various redox proteins and enzymes such as hemoglobin (Hb), horseradish peroxidase (HRP) and glucose oxidase (GOx).[296] In this study we have also investigated the redox nature of KatG protein using cyclic voltametric method. Cyclic voltammetry utilizes a triangular waveform applied between two potentials in both the forward and reverse directions, with the current measured at the working electrode during the potential scan.[297] For a reversible redox couple, E° is centered between the anodic and cathodic peak potentials.[297] The cyclic voltametric results indicated that the our enzyme is capable of

participating direct electron transfer reaction with a pair of nearly symmetrical redox peaks (Figure 5.2). The The formal redox potential, $E^{0'}$ of *a*KatG, *r*KatG and *h*KatG was determined as -0.09, -0.3 and -0.08 V (SCE, pH 7.0) respectively. This technique can further be utilized for investigating the catalytic electrochemical responses to isoniazid mediated reactions and gain more insight on antibiotic resistance of various *Mtb* strains.

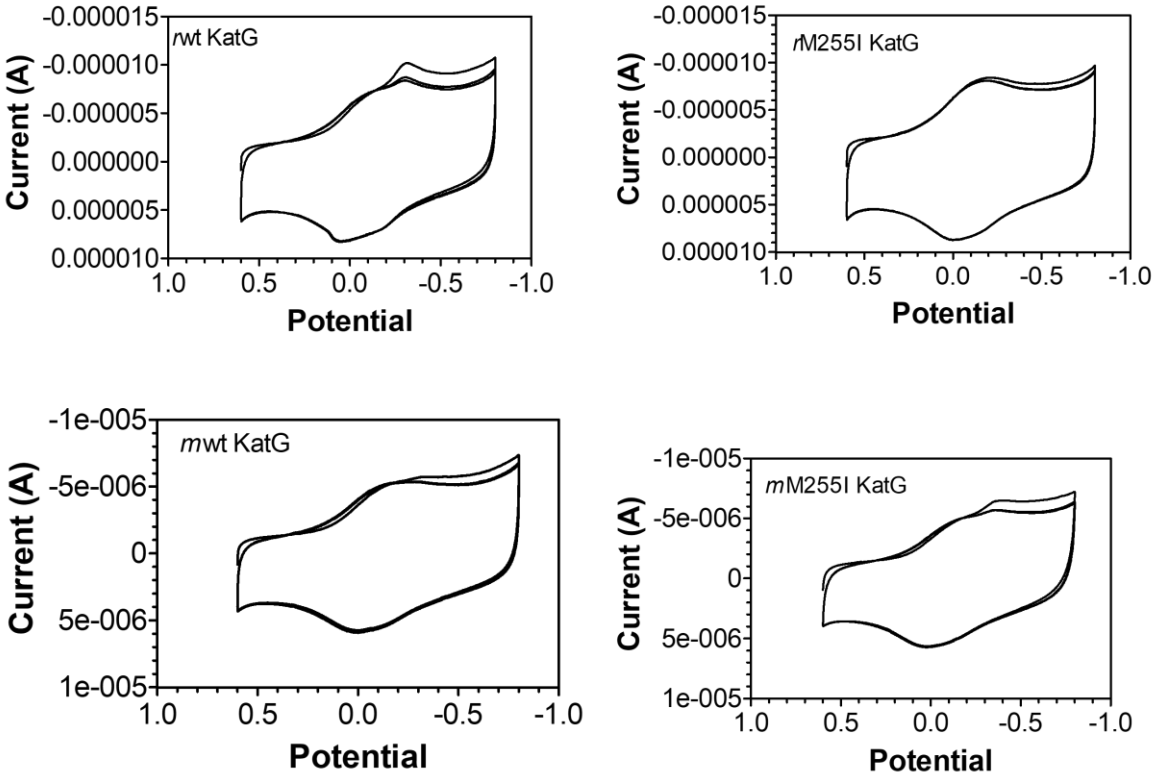

Figure 5.1. cyclic voltammogram (CV) at 100 mVS^{-1} at 25 °C, pH 7.5. Electrode choices were, Glassy carbon as working electrode, platinum wire as counter electrode and Saturated Ag/AgCl as reference electrode. Potassium phosphate buffer (pH 7.0) were purged with pure nitrogen for 20 minutes before any data recorded.

5.3. Importance of Tuberculosis Research

Tuberculosis (Tb), caused by *Mycobacterium tuberculosis* is one of the major leading causes of death worldwide, despite 90 years of vaccination and 60 years of chemotherapeutic drug invention. The bacteria usually attack the lungs, but TB bacteria can attack any part of the body such as the kidney, spine, and brain. There are two TB-related conditions exist: latent TB infection (LTBI) and TB disease. If not treated properly, TB disease can be fatal.

TB morbidity and mortality rates due to TB steadily dropped during the 20th century in the developed world, aided by better public health practices and widespread use of the *M. bovis* BCG vaccine, as well as the development of antibiotics in the 1950s. However, the numbers of new cases started increasing in the mid-1980s due to increased homelessness and poverty in the developing world and the misuse and misadministration of antibiotic delivery. In 2018, 1.7 billion people were infected by TB bacteria — roughly 23% of the world's population.[298]

Preliminary CDC data, released on World Tuberculosis (TB) Day, 2022 showed that TB disease diagnoses fell 20% in 2020 and remained 13% lower in 2021 than pre-pandemic levels.[299] These declines may be related to factors associated with the COVID-19 pandemic, including a true reduction in incidence as well as delayed or missed TB diagnoses.

Although the disease burden caused by TB is declining globally, multidrug resistant tuberculosis (MDR-TB) and extensively drug resistant TB (XDR-TB) are continuing to be a public health crisis. XDR-TB is resistant to the most-potent TB drugs such as isoniazid and rifampin, plus any fluoroquinolone and at least one of three injectable second-line drugs (*i.e.*, amikacin, kanamycin, or capreomycin).

In this context, Alleviating the global burden of TB, there is no alternative to research for discovery or improving diagnostics, therapeutics, and vaccines by developing tools and resources to advance research in understanding, preventing, diagnosing, and treating TB.

6. REFERENCES

(1) Ramazi, S.; Zahiri, J. Post-Translational Modifications in Proteins: Resources, Tools and Prediction Methods. *Database (Oxford)* **2021**, *2021*, baab012. https://doi.org/10.1093/database/baab012.

(2) Walsh, C. T.; Garneau-Tsodikova, S.; Gatto, G. J. Protein Posttranslational Modifications: The Chemistry of Proteome Diversifications. *Angew Chem Int Ed Engl* **2005**, *44* (45), 7342–7372. https://doi.org/10.1002/anie.200501023.

(3) Karve, T. M.; Cheema, A. K. Small Changes Huge Impact: The Role of Protein Posttranslational Modifications in Cellular Homeostasis and Disease. *J Amino Acids* **2011**, *2011*, 207691. https://doi.org/10.4061/2011/207691.

(4) Maclaine, N. J.; Hupp, T. R. The Regulation of P53 by Phosphorylation: A Model for How Distinct Signals Integrate into the P53 Pathway. *Aging (Albany NY)* **2009**, *1* (5), 490–502.

(5) *Biological roles of oligosaccharides: all of the theories are correct - PubMed*. https://pubmed.ncbi.nlm.nih.gov/8490246/ (accessed 2022-07-13).

(6) Chamorey, A.-L.; Magné, N.; Pivot, X.; Milano, G. Impact of Glycosylation on the Effect of Cytokines. A Special Focus on Oncology. *Eur Cytokine Netw* **2002**, *13* (2), 154–160.

(7) Foord, S. M.; Bonner, T. I.; Neubig, R. R.; Rosser, E. M.; Pin, J.-P.; Davenport, A. P.; Spedding, M.; Harmar, A. J. International Union of Pharmacology. XLVI. G Protein-Coupled Receptor List. *Pharmacol Rev* **2005**, *57* (2), 279–288. https://doi.org/10.1124/pr.57.2.5.

(8) Beazely, M. A.; Watts, V. J. Regulatory Properties of Adenylate Cyclases Type 5 and 6: A Progress Report. *European Journal of Pharmacology* **2006**, *535* (1), 1–12. https://doi.org/10.1016/j.ejphar.2006.01.054.

(9) Goulabchand, R.; Vincent, T.; Batteux, F.; Eliaou, J.-F.; Guilpain, P. Impact of Autoantibody Glycosylation in Autoimmune Diseases. *Autoimmun Rev* **2014**, *13* (7), 742–750. https://doi.org/10.1016/j.autrev.2014.02.005.

(10) Kodama, S.; Tsujimoto, M.; Tsuruoka, N.; Sugo, T.; Endo, T.; Kobata, A. Role of Sugar Chains in the In-Vitro Activity of Recombinant Human Interleukin 5. *Eur J Biochem* **1993**, *211* (3), 903–908. https://doi.org/10.1111/j.1432-1033.1993.tb17624.x.

(11) Mukherjee, S.; Keitany, G.; Li, Y.; Wang, Y.; Ball, H. L.; Goldsmith, E. J.; Orth, K. Yersinia YopJ Acetylates and Inhibits Kinase Activation by Blocking Phosphorylation. *Science* **2006**, *312* (5777), 1211–1214. https://doi.org/10.1126/science.1126867.

(12) Huang, K.-Y.; Lee, T.-Y.; Kao, H.-J.; Ma, C.-T.; Lee, C.-C.; Lin, T.-H.; Chang, W.-C.; Huang, H.-D. DbPTM in 2019: Exploring Disease Association and Cross-Talk of Post-

Translational Modifications. *Nucleic Acids Research* **2019**, *47* (D1), D298–D308. https://doi.org/10.1093/nar/gky1074.

(13) *Protein acetylation and deacetylation: An important regulatory modification in gene transcription (Review)*. https://www.spandidos-publications.com/10.3892/etm.2020.9073 (accessed 2022-07-13).

(14) Choudhary, C.; Kumar, C.; Gnad, F.; Nielsen, M. L.; Rehman, M.; Walther, T. C.; Olsen, J. V.; Mann, M. Lysine Acetylation Targets Protein Complexes and Co-Regulates Major Cellular Functions. *Science* **2009**, *325* (5942), 834–840. https://doi.org/10.1126/science.1175371.

(15) Cunin, R.; Glansdorff, N.; Piérard, A.; Stalon, V. Biosynthesis and Metabolism of Arginine in Bacteria. *Microbiol Rev* **1986**, *50* (3), 314–352. https://doi.org/10.1128/mr.50.3.314-352.1986.

(16) Bhogaraju, S.; Dikic, I. Ubiquitination without E1 and E2 Enzymes. *Nature* **2016**, *533* (7601), 43–44. https://doi.org/10.1038/nature17888.

(17) Suresh, B.; Lee, J.; Kim, H.; Ramakrishna, S. Regulation of Pluripotency and Differentiation by Deubiquitinating Enzymes. *Cell Death Differ* **2016**, *23* (8), 1257–1264. https://doi.org/10.1038/cdd.2016.53.

(18) Radivojac, P.; Vacic, V.; Haynes, C.; Cocklin, R. R.; Mohan, A.; Heyen, J. W.; Goebl, M. G.; Iakoucheva, L. M. Identification, Analysis and Prediction of Protein Ubiquitination Sites. *Proteins* **2010**, *78* (2), 365–380. https://doi.org/10.1002/prot.22555.

(19) Cheng, D.; Côté, J.; Shaaban, S.; Bedford, M. T. The Arginine Methyltransferase CARM1 Regulates the Coupling of Transcription and MRNA Processing. *Mol Cell* **2007**, *25* (1), 71–83. https://doi.org/10.1016/j.molcel.2006.11.019.

(20) Rice, J. C.; Allis, C. D. Histone Methylation versus Histone Acetylation: New Insights into Epigenetic Regulation. *Curr Opin Cell Biol* **2001**, *13* (3), 263–273. https://doi.org/10.1016/s0955-0674(00)00208-8.

(21) Cai, Z.; Yan, L.-J. Protein Oxidative Modifications: Beneficial Roles in Disease and Health. *J Biochem Pharmacol Res* **2013**, *1* (1), 15–26.

(22) Lewisch, S. A.; Levine, R. L. Determination of 2-Oxohistidine by Amino Acid Analysis. *Anal Biochem* **1995**, *231* (2), 440–446. https://doi.org/10.1006/abio.1995.9974.

(23) Giulivi, C.; Davies, K. J. A. [39] Dityrosine: A Marker for Oxidatively Modified Proteins and Selective Proteolysis. In *Methods in Enzymology*; Oxygen Radicals in Biological Systems Part C; Academic Press, 1994; Vol. 233, pp 363–371. https://doi.org/10.1016/S0076-6879(94)33042-5.

(24) G, R.; N, F.; J, M. Understanding the PK(a) of Redox Cysteines: The Key Role of Hydrogen Bonding. *Antioxidants & redox signaling* **2013**, *18* (1). https://doi.org/10.1089/ars.2012.4521.

(25) Broniowska, K. A.; Hogg, N. The Chemical Biology of S-Nitrosothiols. *Antioxid Redox Signal* **2012**, *17* (7), 969–980. https://doi.org/10.1089/ars.2012.4590.

(26) Ellis, H. R.; Poole, L. B. Roles for the Two Cysteine Residues of AhpC in Catalysis of Peroxide Reduction by Alkyl Hydroperoxide Reductase from Salmonella Typhimurium. *Biochemistry* **1997**, *36* (43), 13349–13356. https://doi.org/10.1021/bi9713658.

(27) Vogt, W. Oxidation of Methionyl Residues in Proteins: Tools, Targets, and Reversal. *Free Radical Biology and Medicine* **1995**, *18* (1), 93–105. https://doi.org/10.1016/0891-5849(94)00158-G.

(28) Kettle, A. J. Neutrophils Convert Tyrosyl Residues in Albumin to Chlorotyrosine. *FEBS Lett* **1996**, *379* (1), 103–106. https://doi.org/10.1016/0014-5793(95)01494-2.

(29) Hawkins, C. L.; Pattison, D. I.; Davies, M. J. Hypochlorite-Induced Oxidation of Amino Acids, Peptides and Proteins. *Amino Acids* **2003**, *25* (3–4), 259–274. https://doi.org/10.1007/s00726-003-0016-x.

(30) Prütz, W. A. Hypochlorous Acid Interactions with Thiols, Nucleotides, DNA, and Other Biological Substrates. *Arch Biochem Biophys* **1996**, *332* (1), 110–120. https://doi.org/10.1006/abbi.1996.0322.

(31) Winterbourn, C. C. Biological Reactivity and Biomarkers of the Neutrophil Oxidant, Hypochlorous Acid. *Toxicology* **2002**, *181–182*, 223–227. https://doi.org/10.1016/s0300-483x(02)00286-x.

(32) Berlett, B. S.; Stadtman, E. R. Protein Oxidation in Aging, Disease, and Oxidative Stress *. *Journal of Biological Chemistry* **1997**, *272* (33), 20313–20316. https://doi.org/10.1074/jbc.272.33.20313.

(33) Shacter, E. Quantification and Significance of Protein Oxidation in Biological Samples. *Drug Metabolism Reviews* **2000**, *32* (3–4), 307–326. https://doi.org/10.1081/DMR-100102336.

(34) Salsbury, F. R.; Knutson, S. T.; Poole, L. B.; Fetrow, J. S. Functional Site Profiling and Electrostatic Analysis of Cysteines Modifiable to Cysteine Sulfenic Acid. *Protein Sci* **2008**, *17* (2), 299–312. https://doi.org/10.1110/ps.073096508.

(35) Biswas, S.; Chida, A. S.; Rahman, I. Redox Modifications of Protein-Thiols: Emerging Roles in Cell Signaling. *Biochem Pharmacol* **2006**, *71* (5), 551–564. https://doi.org/10.1016/j.bcp.2005.10.044.

(36) Zhang, B.; Gu, H.; Yang, Y.; Bai, H.; Zhao, C.; Si, M.; Su, T.; Shen, X. Molecular Mechanisms of AhpC in Resistance to Oxidative Stress in Burkholderia Thailandensis. *Frontiers in Microbiology* **2019**, *10*.

(37) Gray, H. B.; Winkler, J. R. Hole Hopping through Tyrosine/Tryptophan Chains Protects Proteins from Oxidative Damage. *Proceedings of the National Academy of Sciences* **2015**, *112* (35), 10920–10925. https://doi.org/10.1073/pnas.1512704112.

(38) Aeschbach, R.; Amadoò, R.; Neukom, H. Formation of Dityrosine Cross-Links in Proteins by Oxidation of Tyrosine Residues. *Biochimica et Biophysica Acta (BBA) - Protein Structure* **1976**, *439* (2), 292–301. https://doi.org/10.1016/0005-2795(76)90064-7.

(39) Gray, H. B.; Winkler, J. R. Functional and Protective Hole Hopping in Metalloenzymes. *Chem Sci 12* (42), 13988–14003. https://doi.org/10.1039/d1sc04286f.

(40) Moosmann, B. Redox Biochemistry of the Genetic Code. *Trends in Biochemical Sciences* **2021**, *46* (2), 83–86. https://doi.org/10.1016/j.tibs.2020.10.008.

(41) Bender, A.; Hajieva, P.; Moosmann, B. Adaptive Antioxidant Methionine Accumulation in Respiratory Chain Complexes Explains the Use of a Deviant Genetic Code in Mitochondria. *Proceedings of the National Academy of Sciences* **2008**, *105* (43), 16496–16501. https://doi.org/10.1073/pnas.0802779105.

(42) Granold, M.; Hajieva, P.; Toşa, M. I.; Irimie, F.-D.; Moosmann, B. Modern Diversification of the Amino Acid Repertoire Driven by Oxygen. *Proceedings of the National Academy of Sciences* **2018**, *115* (1), 41–46. https://doi.org/10.1073/pnas.1717100115.

(43) Close, D. M. Calculated Vertical Ionization Energies of the Common α-Amino Acids in the Gas Phase and in Solution. *J. Phys. Chem. A* **2011**, *115* (13), 2900–2912. https://doi.org/10.1021/jp200503z.

(44) Minnihan, E. C.; Nocera, D. G.; Stubbe, J. Reversible, Long-Range Radical Transfer in E. Coli Class Ia Ribonucleotide Reductase. *Acc. Chem. Res.* **2013**, *46* (11), 2524–2535. https://doi.org/10.1021/ar4000407.

(45) Brettel, K.; Byrdin, M. Reaction Mechanisms of DNA Photolyase. *Curr Opin Struct Biol* **2010**, *20* (6), 693–701. https://doi.org/10.1016/j.sbi.2010.07.003.

(46) Jiang, N.; Kuznetsov, A.; Nocek, J. M.; Hoffman, B. M.; Crane, B. R.; Hu, X.; Beratan, D. N. Distance-Independent Charge Recombination Kinetics in Cytochrome *c* –Cytochrome *c* Peroxidase Complexes: Compensating Changes in the Electronic Coupling and Reorganization Energies. *J. Phys. Chem. B* **2013**, *117* (31), 9129–9141. https://doi.org/10.1021/jp401551t.

(47) Njuma, O. J.; Davis, I.; Ndontsa, E. N.; Krewall, J. R.; Liu, A.; Goodwin, D. C. Mutual Synergy between Catalase and Peroxidase Activities of the Bifunctional Enzyme KatG Is Facilitated by Electron Hole-Hopping within the Enzyme. *J. Biol. Chem.* **2017**, *292* (45), 18408–18421. https://doi.org/10.1074/jbc.M117.791202.

(48) Kathiresan, M.; English, A. M. LC-MS/MS Suggests That Hole Hopping in Cytochrome c Peroxidase Protects Its Heme from Oxidative Modification by Excess H2O2. *Chem. Sci.* **2017**, *8* (2), 1152–1162. https://doi.org/10.1039/C6SC03125K.

(49) Kathiresan, M.; English, A. M. LC-MS/MS Proteoform Profiling Exposes Cytochrome c Peroxidase Self-Oxidation in Mitochondria and Functionally Important Hole Hopping from Its Heme. *J. Am. Chem. Soc.* **2018**, *140* (38), 12033–12039. https://doi.org/10.1021/jacs.8b05966.

(50) Davidson, V. L. Generation of Protein-Derived Redox Cofactors by Posttranslational Modification. *Mol Biosyst* **2011**, *7* (1), 29–37. https://doi.org/10.1039/c005311b.

(51) Albert, A.; Dhanaraj, V.; Genschel, U.; Khan, G.; Ramjee, M. K.; Pulido, R.; Sibanda, B. L.; Delft, F. von; Witty, M.; Blundell, T. L.; Smith, A. G.; Abell, C. Crystal Structure of Aspartate Decarboxylase at 2.2 Å Resolution Provides Evidence for an Ester in Protein Self–Processing. *Nat Struct Mol Biol* **1998**, *5* (4), 289–293. https://doi.org/10.1038/nsb0498-289.

(52) Schuiki, I.; Daum, G. Phosphatidylserine Decarboxylases, Key Enzymes of Lipid Metabolism. *IUBMB Life* **2009**, *61* (2), 151–162. https://doi.org/10.1002/iub.159.

(53) Li, Q. X.; Dowhan, W. Structural Characterization of Escherichia Coli Phosphatidylserine Decarboxylase. *Journal of Biological Chemistry* **1988**, *263* (23), 11516–11522. https://doi.org/10.1016/S0021-9258(18)37988-2.

(54) Stanley, B. A.; Pegg, A. E.; Holm, I. Site of Pyruvate Formation and Processing of Mammalian S-Adenosylmethionine Decarboxylase Proenzyme. *Journal of Biological Chemistry* **1989**, *264* (35), 21073–21079. https://doi.org/10.1016/S0021-9258(19)30047-X.

(55) Gallagher, T.; Rozwarski, D. A.; Ernst, S. R.; Hackert, M. L. Refined Structure of the Pyruvoyl-Dependent Histidine Decarboxylase from Lactobacillus 30a. *Journal of Molecular Biology* **1993**, *230* (2), 516–528. https://doi.org/10.1006/jmbi.1993.1168.

(56) Davidson, V. L. Protein-Derived Cofactors Revisited: Empowering Amino Acid Residues with New Functions. *Biochemistry* **2018**, *57* (22), 3115–3125. https://doi.org/10.1021/acs.biochem.8b00123.

(57) Janes, S. M.; Mu, D.; Wemmer, D.; Smith, A. J.; Kaur, S.; Maltby, D.; Burlingame, A. L.; Klinman, J. P. A New Redox Cofactor in Eukaryotic Enzymes: 6-Hydroxydopa at the Active Site of Bovine Serum Amine Oxidase. *Science* **1990**, *248* (4958), 981–987. https://doi.org/10.1126/science.2111581.

(58) Hauge, J. G. Glucose Dehydrogenase of Bacterium Anitratum: An Enzyme with a Novel Prosthetic Group. *Journal of Biological Chemistry* **1964**, *239* (11), 3630–3639. https://doi.org/10.1016/S0021-9258(18)91183-X.

(59) Jonscher, K. R.; Chowanadisai, W.; Rucker, R. B. Pyrroloquinoline-Quinone Is More Than an Antioxidant: A Vitamin-like Accessory Factor Important in Health and Disease Prevention. *Biomolecules* **2021**, *11* (10), 1441. https://doi.org/10.3390/biom11101441.

(60) Salisbury, S. A.; Forrest, H. S.; Cruse, W. B. T.; Kennard, O. A Novel Coenzyme from Bacterial Primary Alcohol Dehydrogenases. *Nature* **1979**, *280* (5725), 843–844. https://doi.org/10.1038/280843a0.

(61) Westerling, J.; Frank, J.; Duine, J. A. The Prosthetic Group of Methanol Dehydrogenase from Hyphomicrobium X: Electron Spin Resonance Evidence for a Quinone Structure. *Biochemical and Biophysical Research Communications* **1979**, *87* (3), 719–724. https://doi.org/10.1016/0006-291X(79)92018-7.

(62) Matsuzaki, R.; Fukui, T.; Sato, H.; Ozaki, Y.; Tanizawa, K. Generation of the Topa Quinone Cofactor in Bacterial Monoamine Oxidase by Cupric Ion-Dependent Autooxidation of a Specific Tyrosyl Residue. *FEBS Lett* **1994**, *351* (3), 360–364. https://doi.org/10.1016/0014-5793(94)00884-1.

(63) Dooley, D. M.; McGuirl, M. A.; Brown, D. E.; Turowski, P. N.; McIntire, W. S.; Knowles, P. F. A Cu(I)-Semiquinone State in Substrate-Reduced Amine Oxidases. *Nature* **1991**, *349* (6306), 262–264. https://doi.org/10.1038/349262a0.

(64) Klema, V. J.; Wilmot, C. M. The Role of Protein Crystallography in Defining the Mechanisms of Biogenesis and Catalysis in Copper Amine Oxidase. *Int J Mol Sci* **2012**, *13* (5), 5375–5405. https://doi.org/10.3390/ijms13055375.

(65) Ma, Z.; Davidson, V. L. Redox Properties of a Cysteine Tryptophylquinone-Dependent Glycine Oxidase Are Distinct from Those of Tryptophylquinone-Dependent Dehydrogenases. *Biochemistry* **2019**, *58* (17), 2243–2249. https://doi.org/10.1021/acs.biochem.9b00104.

(66) Bollinger, J. A.; Brown, D. E.; Dooley, D. M. The Formation of Lysine Tyrosylquinone (LTQ) Is a Self-Processing Reaction. Expression and Characterization of a Drosophila Lysyl Oxidase. *Biochemistry* **2005**, *44* (35), 11708–11714. https://doi.org/10.1021/bi0504310.

(67) Choi, Y. H.; Matsuzaki, R.; Fukui, T.; Shimizu, E.; Yorifuji, T.; Sato, H.; Ozaki, Y.; Tanizawa, K. Copper/Topa Quinone-Containing Histamine Oxidase from Arthrobacter Globiformis. Molecular Cloning and Sequencing, Overproduction of Precursor Enzyme, and Generation of Topa Quinone Cofactor. *J Biol Chem* **1995**, *270* (9), 4712–4720. https://doi.org/10.1074/jbc.270.9.4712.

(68) Van Spanning, R. J. M.; de Boer, A. P. N.; Reijnders, W. N. M.; De Gier, J.-W. L.; Delorme, C. O.; Stouthamer, A. H.; Westerhoff, H. V.; Harms, N.; van der Oost, J. Regulation of Oxidative Phosphorylation: The Flexible Respiratory Network OfParacoccus Denitrificans. *J Bioenerg Biomembr* **1995**, *27* (5), 499–512. https://doi.org/10.1007/BF02110190.

(69) van der Palen, C. J. N. M.; Reijnders, W. N. M.; de Vries, S.; Duine, J. A.; van Spanning, R. J. M. MauE and MauD Proteins Are Essential in Methylamine Metabolism of Paracoccus Denitrificans. *Antonie van Leeuwenhoek* **1997**, *72* (3), 219–228. https://doi.org/10.1023/A:1000441925796.

(70) Wilmot, C. M.; Davidson, V. L. Uncovering Novel Biochemistry in the Mechanism of Tryptophan Tryptophylquinone Cofactor Biosynthesis. *Curr Opin Chem Biol* **2009**, *13* (4), 462–467. https://doi.org/10.1016/j.cbpa.2009.06.026.

(71) Wikström, M. Identification of the Electron Transfers in Cytochrome Oxidase That Are Coupled to Proton-Pumping. *Nature* **1989**, *338* (6218), 776–778. https://doi.org/10.1038/338776a0.

(72) Hemp, J.; Robinson, D. E.; Ganesan, K. B.; Martinez, T. J.; Kelleher, N. L.; Gennis, R. B. Evolutionary Migration of a Post-Translationally Modified Active-Site Residue in the Proton-Pumping Heme-Copper Oxygen Reductases. *Biochemistry* **2006**, *45* (51), 15405–15410. https://doi.org/10.1021/bi062026u.

(73) Das, T. K.; Pecoraro, C.; Tomson, F. L.; Gennis, R. B.; Rousseau, D. L. The Post-Translational Modification in Cytochrome c Oxidase Is Required to Establish a Functional Environment of the Catalytic Site. *Biochemistry* **1998**, *37* (41), 14471–14476. https://doi.org/10.1021/bi981500w.

(74) Pinakoulaki, E.; Pfitzner, U.; Ludwig, B.; Varotsis, C. The Role of the Cross-Link His-Tyr in the Functional Properties of the Binuclear Center in Cytochrome c Oxidase. *J Biol Chem* **2002**, *277* (16), 13563–13568. https://doi.org/10.1074/jbc.M112200200.

(75) Ito, N.; Phillips, S. E.; Stevens, C.; Ogel, Z. B.; McPherson, M. J.; Keen, J. N.; Yadav, K. D.; Knowles, P. F. Novel Thioether Bond Revealed by a 1.7 \AA Crystal Structure of Galactose Oxidase. *Nature* **1991**, *350* (6313), 87.

(76) Whittaker, M. M.; Kersten, P. J.; Cullen, D.; Whittaker, J. W. Identification of Catalytic Residues in Glyoxal Oxidase by Targeted Mutagenesis. *J Biol Chem* **1999**, *274* (51), 36226–36232. https://doi.org/10.1074/jbc.274.51.36226.

(77) McCoy, J. G.; Bailey, L. J.; Bitto, E.; Bingman, C. A.; Aceti, D. J.; Fox, B. G.; Phillips, G. N. Structure and Mechanism of Mouse Cysteine Dioxygenase. *Proc Natl Acad Sci U S A* **2006**, *103* (9), 3084–3089. https://doi.org/10.1073/pnas.0509262103.

(78) Schnell, R.; Sandalova, T.; Hellman, U.; Lindqvist, Y.; Schneider, G. Siroheme- and [Fe4-S4]-Dependent NirA from Mycobacterium Tuberculosis Is a Sulfite Reductase with a Covalent Cys-Tyr Bond in the Active Site. *J Biol Chem* **2005**, *280* (29), 27319–27328. https://doi.org/10.1074/jbc.M502560200.

(79) Polyakov, K. M.; Boyko, K. M.; Tikhonova, T. V.; Slutsky, A.; Antipov, A. N.; Zvyagilskaya, R. A.; Popov, A. N.; Bourenkov, G. P.; Lamzin, V. S.; Popov, V. O. High-Resolution Structural Analysis of a Novel Octaheme Cytochrome c Nitrite Reductase from the Haloalkaliphilic Bacterium Thioalkalivibrio Nitratireducens. *J Mol Biol* **2009**, *389* (5), 846–862. https://doi.org/10.1016/j.jmb.2009.04.037.

(80) Ye, S.; Wu, X.; Wei, L.; Tang, D.; Sun, P.; Bartlam, M.; Rao, Z. An Insight into the Mechanism of Human Cysteine Dioxygenase. Key Roles of the Thioether-Bonded Tyrosine-Cysteine Cofactor. *J Biol Chem* **2007**, *282* (5), 3391–3402. https://doi.org/10.1074/jbc.M609337200.

(81) Whittaker, J. W. Free Radical Catalysis by Galactose Oxidase. *Chem. Rev.* **2003**, *103* (6), 2347–2364. https://doi.org/10.1021/cr020425z.

(82) Forbes, D. L.; Meneely, K. M.; Chilton, A. S.; Lamb, A. L.; Ellis, H. R. 3-His Metal Coordination Site Promotes the Coupling of Oxygen Activation to Cysteine Oxidation in Cysteine Dioxygenase. *Biochemistry* **2020**, *59* (21), 2022–2031. https://doi.org/10.1021/acs.biochem.9b01085.

(83) Cuff, M. E.; Miller, K. I.; van Holde, K. E.; Hendrickson, W. A. Crystal Structure of a Functional Unit from Octopus Hemocyanin. *J Mol Biol* **1998**, *278* (4), 855–870. https://doi.org/10.1006/jmbi.1998.1647.

(84) Klabunde, T.; Eicken, C.; Sacchettini, J. C.; Krebs, B. Crystal Structure of a Plant Catechol Oxidase Containing a Dicopper Center. *Nat Struct Mol Biol* **1998**, *5* (12), 1084–1090. https://doi.org/10.1038/4193.

(85) Ismaya, W. T.; Rozeboom, H. J.; Weijn, A.; Mes, J. J.; Fusetti, F.; Wichers, H. J.; Dijkstra, B. W. Crystal Structure of *Agaricus Bisporus* Mushroom Tyrosinase: Identity of the Tetramer Subunits and Interaction with Tropolone. *Biochemistry* **2011**, *50* (24), 5477–5486. https://doi.org/10.1021/bi200395t.

(86) Nakamura, M.; Nakajima, T.; Ohba, Y.; Yamauchi, S.; Lee, B. R.; Ichishima, E. Identification of Copper Ligands in Aspergillus Oryzae Tyrosinase by Site-Directed Mutagenesis. *Biochem J* **2000**, *350 Pt 2*, 537–545.

(87) Bertrand, T.; Eady, N. A. J.; Jones, J. N.; Jesmin, null; Nagy, J. M.; Jamart-Grégoire, B.; Raven, E. L.; Brown, K. A. Crystal Structure of Mycobacterium Tuberculosis Catalase-Peroxidase. *J Biol Chem* **2004**, *279* (37), 38991–38999. https://doi.org/10.1074/jbc.M402382200.

(88) Yamada, Y.; Fujiwara, T.; Sato, T.; Igarashi, N.; Tanaka, N. The 2.0 A Crystal Structure of Catalase-Peroxidase from Haloarcula Marismortui. *Nat Struct Biol* **2002**, *9* (9), 691–695. https://doi.org/10.1038/nsb834.

(89) Donald, L. J.; Krokhin, O. V.; Duckworth, H. W.; Wiseman, B.; Deemagarn, T.; Singh, R.; Switala, J.; Carpena, X.; Fita, I.; Loewen, P. C. Characterization of the Catalase-Peroxidase KatG from Burkholderia Pseudomallei by Mass Spectrometry. *Journal of Biological Chemistry* **2003**, *278* (37), 35687–35692. https://doi.org/10.1074/jbc.M304053200.

(90) Gasselhuber, B.; Graf, M. M. H.; Jakopitsch, C.; Zamocky, M.; Nicolussi, A.; Furtmüller, P. G.; Oostenbrink, C.; Carpena, X.; Obinger, C. Interaction with the Redox Cofactor MYW and Functional Role of a Mobile Arginine in Eukaryotic Catalase-Peroxidase. *Biochemistry* **2016**, *55* (25), 3528–3541. https://doi.org/10.1021/acs.biochem.6b00436.

(91) Ghiladi, R. A.; Knudsen, G. M.; Medzihradszky, K. F.; Ortiz de Montellano, P. R. The Met-Tyr-Trp Cross-Link in Mycobacterium Tuberculosis Catalase-Peroxidase (KatG): Autocatalytic Formation and Effect on Enzyme Catalysis and Spectroscopic Properties. *J. Biol. Chem.* **2005**, *280* (24), 22651–22663. https://doi.org/10.1074/jbc.M502486200.

(92) Kudalkar, S. N.; Campbell, R. A.; Li, Y.; Varnado, C. L.; Prescott, C.; Goodwin, D. C. Enhancing the Peroxidatic Activity of KatG by Deletion Mutagenesis. *J Inorg Biochem* **2012**, *116*, 106–115. https://doi.org/10.1016/j.jinorgbio.2012.08.002.

(93) Smulevich, G.; Jakopitsch, C.; Droghetti, E.; Obinger, C. Probing the Structure and Bifunctionality of Catalase-Peroxidase (KatG). *J Inorg Biochem* **2006**, *100* (4), 568–585. https://doi.org/10.1016/j.jinorgbio.2006.01.033.

(94) Regelsberger, G.; Jakopitsch, C.; Rüker, F.; Krois, D.; Peschek, G. A.; Obinger, C. Effect of Distal Cavity Mutations on the Formation of Compound I in Catalase-Peroxidases. *Journal of Biological Chemistry* **2000**, *275* (30), 22854–22861. https://doi.org/10.1074/jbc.M002371200.

(95) Cade, C. E.; Dlouhy, A. C.; Medzihradszky, K. F.; Salas-Castillo, S. P.; Ghiladi, R. A. Isoniazid-Resistance Conferring Mutations in Mycobacterium Tuberculosis KatG: Catalase, Peroxidase, and INH-NADH Adduct Formation Activities. *Protein Sci* **2010**, *19* (3), 458–474. https://doi.org/10.1002/pro.324.

(96) Jakopitsch, C.; Auer, M.; Ivancich, A.; Rüker, F.; Furtmüller, P. G.; Obinger, C. Total Conversion of Bifunctional Catalase-Peroxidase (KatG) to Monofunctional Peroxidase by Exchange of a Conserved Distal Side Tyrosine. *J. Biol. Chem.* **2003**, *278* (22), 20185–20191. https://doi.org/10.1074/jbc.M211625200.

(97) Nguyen, G. T.; Green, E. R.; Mecsas, J. Neutrophils to the ROScue: Mechanisms of NADPH Oxidase Activation and Bacterial Resistance. *Front Cell Infect Microbiol* **2017**, *7*, 373. https://doi.org/10.3389/fcimb.2017.00373.

(98) Slauch, J. M. How Does the Oxidative Burst of Macrophages Kill Bacteria? Still an Open Question. *Mol Microbiol* **2011**, *80* (3), 580–583. https://doi.org/10.1111/j.1365-2958.2011.07612.x.

(99) Klebanoff, S. J. Myeloperoxidase: Friend and Foe. *J Leukoc Biol* **2005**, *77* (5), 598–625. https://doi.org/10.1189/jlb.1204697.

(100) Martinvalet, D.; Walch, M. Editorial: The Role of Reactive Oxygen Species in Protective Immunity. *Frontiers in Immunology* **2022**, *12*.

(101) Circu, M. L.; Aw, T. Y. Reactive Oxygen Species, Cellular Redox Systems, and Apoptosis. *Free Radical Biology and Medicine* **2010**, *48* (6), 749–762. https://doi.org/10.1016/j.freeradbiomed.2009.12.022.

(102) Montezano, A. C.; Touyz, R. M. Reactive Oxygen Species, Vascular Noxs, and Hypertension: Focus on Translational and Clinical Research. *Antioxidants & Redox Signaling* **2014**, *20* (1), 164–182. https://doi.org/10.1089/ars.2013.5302.

(103) Zhang, Y.; Du, Y.; Le, W.; Wang, K.; Kieffer, N.; Zhang, J. Redox Control of the Survival of Healthy and Diseased Cells. *Antioxidants & Redox Signaling* **2011**, *15* (11), 2867–2908. https://doi.org/10.1089/ars.2010.3685.

(104) Burgoyne, J. R.; Oka, S.; Ale-Agha, N.; Eaton, P. Hydrogen Peroxide Sensing and Signaling by Protein Kinases in the Cardiovascular System. *Antioxid Redox Signal* **2013**, *18* (9), 1042–1052. https://doi.org/10.1089/ars.2012.4817.

(105) Kregel, K. C.; Zhang, H. J. An Integrated View of Oxidative Stress in Aging: Basic Mechanisms, Functional Effects, and Pathological Considerations. *Am J Physiol Regul Integr Comp Physiol* **2007**, *292* (1), R18-36. https://doi.org/10.1152/ajpregu.00327.2006.

(106) Ezraty, B.; Gennaris, A.; Barras, F.; Collet, J.-F. Oxidative Stress, Protein Damage and Repair in Bacteria. *Nat Rev Microbiol* **2017**, *15* (7), 385–396. https://doi.org/10.1038/nrmicro.2017.26.

(107) Mylonas, C.; Kouretas, D. Lipid Peroxidation and Tissue Damage. *In Vivo* **1999**, *13* (3), 295–309.

(108) Dhalla, N. S.; Temsah, R. M.; Netticadan, T. Role of Oxidative Stress in Cardiovascular Diseases. *Journal of Hypertension* **2000**, *18* (6), 655–673.

(109) Harman, D. Aging: A Theory Based on Free Radical and Radiation Chemistry. *Journal of Gerontology* **1956**, *11* (3), 298–300. https://doi.org/10.1093/geronj/11.3.298.

(110) Nickenig, G.; Harrison, D. G. The AT(1)-Type Angiotensin Receptor in Oxidative Stress and Atherogenesis: Part I: Oxidative Stress and Atherogenesis. *Circulation* **2002**, *105* (3), 393–396. https://doi.org/10.1161/hc0302.102618.

(111) Zalba, G.; San José, G.; Moreno, M. U.; Fortuño, M. A.; Fortuño, A.; Beaumont, F. J.; Díez, J. Oxidative Stress in Arterial Hypertension: Role of NAD(P)H Oxidase. *Hypertension* **2001**, *38* (6), 1395–1399. https://doi.org/10.1161/hy1201.099611.

(112) Johnson, L. A.; Hug, L. A. Distribution of Reactive Oxygen Species Defense Mechanisms across Domain Bacteria. *Free Radical Biology and Medicine* **2019**, *140*, 93–102. https://doi.org/10.1016/j.freeradbiomed.2019.03.032.

(113) Sareila, O.; Kelkka, T.; Pizzolla, A.; Hultqvist, M.; Holmdahl, R. NOX2 Complex-Derived ROS as Immune Regulators. *Antioxid Redox Signal* **2011**, *15* (8), 2197–2208. https://doi.org/10.1089/ars.2010.3635.

(114) Armstrong, J. A.; Hart, P. D. Response of Cultured Macrophages to Mycobacterium Tuberculosis, with Observations on Fusion of Lysosomes with Phagosomes. *J Exp Med* **1971**, *134* (3 Pt 1), 713–740. https://doi.org/10.1084/jem.134.3.713.

(115) Dannenberg, A. M.; Rook, G. A. W. Pathogenesis of Pulmonary Tuberculosis: An Interplay of Tissue-Damaging and Macrophage-Activating Immune Responses-Dual Mechanisms That Control Bacillary Multiplication. In *Tuberculosis*; Bloom, B. R., Ed.; ASM Press: Washington, DC, USA, 2014; pp 459–483. https://doi.org/10.1128/9781555818357.ch27.

(116) Chen, L.; Xie, Q. W.; Nathan, C. Alkyl Hydroperoxide Reductase Subunit C (AhpC) Protects Bacterial and Human Cells against Reactive Nitrogen Intermediates. *Mol Cell* **1998**, *1* (6), 795–805. https://doi.org/10.1016/s1097-2765(00)80079-9.

(117) Cooper, A. M.; Segal, B. H.; Frank, A. A.; Holland, S. M.; Orme, I. M. Transient Loss of Resistance to Pulmonary Tuberculosis in P47phox−/− Mice. *Infect Immun* **2000**, *68* (3), 1231–1234.

(118) Fazal, N. Influence of Mycobacterium Tuberculosis Catalase Gene (KatG) Expression on Nitric Oxide Production and the Intracellular Growth of Transfected Mycobacterium Smegmatis Strains within Murine Macrophages. *Biochem Mol Biol Int* **1997**, *42* (1), 135–142. https://doi.org/10.1080/15216549700202511.

(119) Heym, B.; Stavropoulos, E.; Honoré, N.; Domenech, P.; Saint-Joanis, B.; Wilson, T. M.; Collins, D. M.; Colston, M. J.; Cole, S. T. Effects of Overexpression of the Alkyl Hydroperoxide Reductase AhpC on the Virulence and Isoniazid Resistance of Mycobacterium Tuberculosis. *Infect Immun* **1997**, *65* (4), 1395–1401. https://doi.org/10.1128/iai.65.4.1395-1401.1997.

(120) Hillas, P. J.; del Alba, F. S.; Oyarzabal, J.; Wilks, A.; Ortiz De Montellano, P. R. The AhpC and AhpD Antioxidant Defense System of Mycobacterium Tuberculosis. *J Biol Chem* **2000**, *275* (25), 18801–18809. https://doi.org/10.1074/jbc.M001001200.

(121) Heym, B.; Zhang, Y.; Poulet, S.; Young, D.; Cole, S. T. Characterization of the KatG Gene Encoding a Catalase-Peroxidase Required for the Isoniazid Susceptibility of Mycobacterium Tuberculosis. *J Bacteriol* **1993**, *175* (13), 4255–4259. https://doi.org/10.1128/jb.175.13.4255-4259.1993.

(122) Piddington, D. L.; Fang, F. C.; Laessig, T.; Cooper, A. M.; Orme, I. M.; Buchmeier, N. A. Cu,Zn Superoxide Dismutase of Mycobacterium Tuberculosis Contributes to Survival in Activated Macrophages That Are Generating an Oxidative Burst. *Infect Immun* **2001**, *69* (8), 4980–4987. https://doi.org/10.1128/IAI.69.8.4980-4987.2001.

(123) Johnsson, K.; Froland, W. A.; Schultz, P. G. Overexpression, Purification, and Characterization of the Catalase-Peroxidase KatG from Mycobacterium Tuberculosis*. *Journal of Biological Chemistry* **1997**, *272* (5), 2834–2840. https://doi.org/10.1074/jbc.272.5.2834.

(124) Paul, B. D.; Snyder, S. H. The Unusual Amino Acid L-Ergothioneine Is a Physiologic Cytoprotectant. *Cell Death Differ* **2010**, *17* (7), 1134–1140. https://doi.org/10.1038/cdd.2009.163.

(125) Jackett, P. S.; Aber, V. R.; Lowrie, D. B. Virulence and Resistance to Superoxide, Low PH and Hydrogen Peroxide among Strains of Mycobacterium Tuberculosis. *Journal of General Microbiology* **1978**, *104* (1), 37–45. https://doi.org/10.1099/00221287-104-1-37.

(126) Nair, C. N.; Mackay-Scollay, E. M.; Ramachandran, K.; Selkon, J. B.; Tripathy, S. P.; Mitchison, D. A.; Dickinson, J. M. Virulence in the Guinea-Pig and Susceptibility to

Hydrogen Peroxide of Isoniazid-Sensitive Tubercle Bacilli from South Indian Patients. *Tubercle* **1964**, *45*, 345–353. https://doi.org/10.1016/s0041-3879(64)80048-9.

(127) Sherman, D. R.; Mdluli, K.; Hickey, M. J.; Arain, T. M.; Morris, S. L.; Barry, C. E.; Stover, C. K. Compensatory AhpC Gene Expression in Isoniazid-Resistant Mycobacterium Tuberculosis. *Science* **1996**, *272* (5268), 1641–1643. https://doi.org/10.1126/science.272.5268.1641.

(128) Leto, T. L.; Morand, S.; Hurt, D.; Ueyama, T. Targeting and Regulation of Reactive Oxygen Species Generation by Nox Family NADPH Oxidases. *Antioxid Redox Signal* **2009**, *11* (10), 2607–2619. https://doi.org/10.1089/ars.2009.2637.

(129) McCaffrey, R. L.; Allen, L.-A. H. Francisella Tularensis LVS Evades Killing by Human Neutrophils via Inhibition of the Respiratory Burst and Phagosome Escape. *J Leukoc Biol* **2006**, *80* (6), 1224–1230. https://doi.org/10.1189/jlb.0406287.

(130) Siemsen, D. W.; Kirpotina, L. N.; Jutila, M. A.; Quinn, M. T. Inhibition of the Human Neutrophil NADPH Oxidase by Coxiella Burnetii. *Microbes Infect* **2009**, *11* (6–7), 671–679. https://doi.org/10.1016/j.micinf.2009.04.005.

(131) Harada, T.; Miyake, M.; Imai, Y. Evasion of Legionella Pneumophila from the Bactericidal System by Reactive Oxygen Species (ROS) in Macrophages. *Microbiol Immunol* **2007**, *51* (12), 1161–1170. https://doi.org/10.1111/j.1348-0421.2007.tb04011.x.

(132) Bylund, J.; Burgess, L.-A.; Cescutti, P.; Ernst, R. K.; Speert, D. P. Exopolysaccharides from Burkholderia Cenocepacia Inhibit Neutrophil Chemotaxis and Scavenge Reactive Oxygen Species. *J Biol Chem* **2006**, *281* (5), 2526–2532. https://doi.org/10.1074/jbc.m510692200.

(133) Criss, A. K.; Seifert, H. S. Neisseria Gonorrhoeae Suppresses the Oxidative Burst of Human Polymorphonuclear Leukocytes. *Cell Microbiol* **2008**, *10* (11), 2257–2270. https://doi.org/10.1111/j.1462-5822.2008.01205.x.

(134) Wellington, M.; Dolan, K.; Krysan, D. J. Live Candida Albicans Suppresses Production of Reactive Oxygen Species in Phagocytes. *Infect Immun* **2009**, *77* (1), 405–413. https://doi.org/10.1128/IAI.00860-08.

(135) Orciuolo, E.; Stanzani, M.; Canestraro, M.; Galimberti, S.; Carulli, G.; Lewis, R.; Petrini, M.; Komanduri, K. V. Effects *of Aspergillus Fumigatus* Gliotoxin and Methylprednisolone on Human Neutrophils: Implications for the Pathogenesis of Invasive Aspergillosis. *Journal of Leukocyte Biology* **2007**, *82* (4), 839–848. https://doi.org/10.1189/jlb.0207090.

(136) Manca, C.; Paul, S.; Barry, C. E.; Freedman, V. H.; Kaplan, G. Mycobacterium Tuberculosis Catalase and Peroxidase Activities and Resistance to Oxidative Killing in Human Monocytes in Vitro. *Infect Immun* **1999**, *67* (1), 74–79. https://doi.org/10.1128/IAI.67.1.74-79.1999.

(137) Johnsson, K.; Schultz, P. G. Mechanistic Studies of the Oxidation of Isoniazid by the Catalase Peroxidase from Mycobacterium Tuberculosis. *J. Am. Chem. Soc.* **1994**, *116* (16), 7425–7426. https://doi.org/10.1021/ja00095a063.

(138) Johnsson, K.; King, D. S.; Schultz, P. G. Studies on the Mechanism of Action of Isoniazid and Ethionamide in the Chemotherapy of Tuberculosis. *J. Am. Chem. Soc.* **1995**, *117* (17), 5009–5010. https://doi.org/10.1021/ja00122a038.

(139) Timmins, G. S.; Deretic, V. Mechanisms of Action of Isoniazid. *Mol Microbiol* **2006**, *62* (5), 1220–1227. https://doi.org/10.1111/j.1365-2958.2006.05467.x.

(140) Rozwarski, D. A.; Grant, G. A.; Barton, D. H.; Jacobs, W. R.; Sacchettini, J. C. Modification of the NADH of the Isoniazid Target (InhA) from Mycobacterium Tuberculosis. *Science* **1998**, *279* (5347), 98–102. https://doi.org/10.1126/science.279.5347.98.

(141) Lempens, P.; Meehan, C. J.; Vandelannoote, K.; Fissette, K.; de Rijk, P.; Van Deun, A.; Rigouts, L.; de Jong, B. C. Isoniazid Resistance Levels of Mycobacterium Tuberculosis Can Largely Be Predicted by High-Confidence Resistance-Conferring Mutations. *Sci Rep* **2018**, *8*, 3246. https://doi.org/10.1038/s41598-018-21378-x.

(142) Srinivasan, V.; Ha, V. T. N.; Vinh, D. N.; Thai, P. V. K.; Ha, D. T. M.; Lan, N. H.; Hai, H. T.; Walker, T. M.; Thu, D. D. A.; Dunstan, S. J.; Thwaites, G. E.; Ashton, P. M.; Caws, M.; Thuong, N. T. T. Sources of Multidrug Resistance in Patients With Previous Isoniazid-Resistant Tuberculosis Identified Using Whole Genome Sequencing: A Longitudinal Cohort Study. *Clin Infect Dis* **2020**, *71* (10), e532–e539. https://doi.org/10.1093/cid/ciaa254.

(143) Musser, J. M. Antimicrobial Agent Resistance in Mycobacteria: Molecular Genetic Insights. *Clin Microbiol Rev* **1995**, *8* (4), 496–514. https://doi.org/10.1128/CMR.8.4.496.

(144) Pym, A. S.; Saint-Joanis, B.; Cole, S. T. Effect of KatG Mutations on the Virulence of Mycobacterium Tuberculosis and the Implication for Transmission in Humans. *Infect Immun* **2002**, *70* (9), 4955–4960. https://doi.org/10.1128/IAI.70.9.4955-4960.2002.

(145) Abe, C.; Kobayashi, I.; Mitarai, S.; Wada, M.; Kawabe, Y.; Takashima, T.; Suzuki, K.; Sng, L.-H.; Wang, S.; Htay, H. H.; Ogata, H. Biological and Molecular Characteristics of Mycobacterium Tuberculosis Clinical Isolates with Low-Level Resistance to Isoniazid in Japan. *J Clin Microbiol* **2008**, *46* (7), 2263–2268. https://doi.org/10.1128/JCM.00561-08.

(146) Master, S.; Zahrt, T. C.; Song, J.; Deretic, V. Mapping of Mycobacterium Tuberculosis KatG Promoters and Their Differential Expression in Infected Macrophages. *Journal of Bacteriology* **2001**, *183* (13), 4033–4039. https://doi.org/10.1128/JB.183.13.4033-4039.2001.

(147) Zámocký, M.; Furtmüller, P. G.; Obinger, C. Evolution of Structure and Function of Class I Peroxidases. *Arch. Biochem. Biophys.* **2010**, *500* (1), 45–57. https://doi.org/10.1016/j.abb.2010.03.024.

(148) Zámocký, M.; Gasselhuber, B.; Furtmüller, P. G.; Obinger, C. Molecular Evolution of Hydrogen Peroxide Degrading Enzymes. *Arch Biochem Biophys* **2012**, *525* (2), 131–144. https://doi.org/10.1016/j.abb.2012.01.017.

(149) Zámocký, M.; Regelsberger, G.; Jakopitsch, C.; Obinger, C. The Molecular Peculiarities of Catalase-Peroxidases. *FEBS Letters* **2001**, *492* (3), 177–182. https://doi.org/10.1016/S0014-5793(01)02237-2.

(150) Kudalkar, S. N.; Njuma, O. J.; Li, Y.; Muldowney, M.; Fuanta, N. R.; Goodwin, D. C. A Role for Catalase-Peroxidase Large Loop 2 Revealed by Deletion Mutagenesis: Control of Active Site Water and Ferric Enzyme Reactivity. *Biochemistry* **2015**, *54* (8), 1648–1662. https://doi.org/10.1021/bi501221a.

(151) Welinder, K. G. Superfamily of Plant, Fungal and Bacterial Peroxidases. *Current Opinion in Structural Biology* **1992**, *2* (3), 388–393. https://doi.org/10.1016/0959-440X(92)90230-5.

(152) Duroux, L.; Welinder, K. G. The Peroxidase Gene Family in Plants: A Phylogenetic Overview. *J Mol Evol* **2003**, *57* (4), 397–407. https://doi.org/10.1007/s00239-003-2489-3.

(153) Baker, R. D.; Cook, C. O.; Goodwin, D. C. Catalase−Peroxidase Active Site Restructuring by a Distant and "Inactive" Domain. *Biochemistry* **2006**, *45* (23), 7113–7121. https://doi.org/10.1021/bi052392y.

(154) Baker, R. D.; Cook, C. O.; Goodwin, D. C. Properties of Catalase–Peroxidase Lacking Its C-Terminal Domain. *Biochemical and Biophysical Research Communications* **2004**, *320* (3), 833–839. https://doi.org/10.1016/j.bbrc.2004.06.026.

(155) Murthy, M. R.; Reid, T. J.; Sicignano, A.; Tanaka, N.; Rossmann, M. G. Structure of Beef Liver Catalase. *J Mol Biol* **1981**, *152* (2), 465–499. https://doi.org/10.1016/0022-2836(81)90254-0.

(156) Bertrand, T.; Eady, N. A. J.; Jones, J. N.; Jesmin; Nagy, J. M.; Jamart-Grégoire, B.; Raven, E. L.; Brown, K. A. Crystal Structure of Mycobacterium Tuberculosis Catalase-Peroxidase *. *Journal of Biological Chemistry* **2004**, *279* (37), 38991–38999. https://doi.org/10.1074/jbc.M402382200.

(157) Hillar, A.; Peters, B.; Pauls, R.; Loboda, A.; Zhang, H.; Mauk, A. G.; Loewen, P. C. Modulation of the Activities of Catalase-Peroxidase HPI of Escherichia Coli by Site-Directed Mutagenesis. *Biochemistry* **2000**, *39* (19), 5868–5875. https://doi.org/10.1021/bi0000059.

(158) Zhao, X.; Hersleth, H.-P.; Zhu, J.; Andersson, K. K.; Magliozzo, R. S. Access Channel Residues Ser315 and Asp137 in Mycobacterium Tuberculosis Catalase-Peroxidase (KatG) Control Peroxidatic Activation of the pro-Drug Isoniazid. *Chem Commun (Camb)* **2013**, *49* (99), 11650–11652. https://doi.org/10.1039/c3cc47022a.

(159) Zhao, X.; Yu, H.; Yu, S.; Wang, F.; Sacchettini, J. C.; Magliozzo, R. S. Hydrogen Peroxide-Mediated Isoniazid Activation Catalyzed by Mycobacterium Tuberculosis

Catalase-Peroxidase (KatG) and Its S315T Mutant. *Biochemistry* **2006**, *45* (13), 4131–4140. https://doi.org/10.1021/bi051967o.

(160) Singh, R.; Wiseman, B.; Deemagarn, T.; Jha, V.; Switala, J.; Loewen, P. C. Comparative Study of Catalase-Peroxidases (KatGs). *Arch. Biochem. Biophys.* **2008**, *471* (2), 207–214. https://doi.org/10.1016/j.abb.2007.12.008.

(161) Njuma, O. J.; Ndontsa, E. N.; Goodwin, D. C. Catalase in Peroxidase Clothing: Interdependent Cooperation of Two Cofactors in the Catalytic Versatility of KatG. *Archives of Biochemistry and Biophysics* **2014**, *544*, 27–39. https://doi.org/10.1016/j.abb.2013.11.007.

(162) Carpena, X.; Loprasert, S.; Mongkolsuk, S.; Switala, J.; Loewen, P. C.; Fita, I. Catalase-Peroxidase KatG of Burkholderia Pseudomallei at 1.7Å Resolution. *Journal of Molecular Biology* **2003**, *327* (2), 475–489. https://doi.org/10.1016/S0022-2836(03)00122-0.

(163) Wada, K.; Tada, T.; Nakamura, Y.; Kinoshita, T.; Tamoi, M.; Shigeoka, S.; Nishimura, K. Crystallization and Preliminary X-Ray Diffraction Studies of Catalase-Peroxidase from Synechococcus PCC 7942. *Acta Crystallogr D Biol Crystallogr* **2002**, *58* (Pt 1), 157–159. https://doi.org/10.1107/s0907444901017735.

(164) Jakopitsch, C.; Kolarich, D.; Petutschnig, G.; Furtmüller, P. G.; Obinger, C. Distal Side Tryptophan, Tyrosine and Methionine in Catalase–Peroxidases Are Covalently Linked in Solution. *FEBS Letters* **2003**, *552* (2), 135–140. https://doi.org/10.1016/S0014-5793(03)00901-3.

(165) Ghiladi, R. A.; Medzihradszky, K. F.; Ortiz de Montellano, P. R. Role of the Met-Tyr-Trp Cross-Link in Mycobacterium Tuberculosis Catalase-Peroxidase (KatG) as Revealed by KatG(M255I). *Biochemistry* **2005**, *44* (46), 15093–15105. https://doi.org/10.1021/bi051463q.

(166) Carpena, X.; Wiseman, B.; Deemagarn, T.; Herguedas, B.; Ivancich, A.; Singh, R.; Loewen, P. C.; Fita, I. Roles for Arg426 and Trp111 in the Modulation of NADH Oxidase Activity of the Catalase-Peroxidase KatG from Burkholderia Pseudomallei Inferred from PH-Induced Structural Changes,. *Biochemistry* **2006**, *45* (16), 5171–5179. https://doi.org/10.1021/bi060017f.

(167) Carpena, X.; Wiseman, B.; Deemagarn, T.; Singh, R.; Switala, J.; Ivancich, A.; Fita, I.; Loewen, P. C. A Molecular Switch and Electronic Circuit Modulate Catalase Activity in Catalase-Peroxidases. *EMBO reports* **2005**, *6* (12), 1156–1162. https://doi.org/10.1038/sj.embor.7400550.

(168) Vidossich, P.; Alfonso-Prieto, M.; Carpena, X.; Loewen, P. C.; Fita, I.; Rovira, C. Versatility of the Electronic Structure of Compound I in Catalase-Peroxidases. *J. Am. Chem. Soc.* **2007**, *129* (44), 13436–13446. https://doi.org/10.1021/ja072245i.

(169) Carpena, X.; Loprasert, S.; Mongkolsuk, S.; Switala, J.; Loewen, P. C.; Fita, I. Catalase-Peroxidase KatG of Burkholderia Pseudomallei at 1.7A Resolution. *J. Mol. Biol.* **2003**, *327* (2), 475–489. https://doi.org/10.1016/s0022-2836(03)00122-0.

(170) Jakopitsch, C.; Vlasits, J.; Wiseman, B.; Loewen, P. C.; Obinger, C. Redox Intermediates in the Catalase Cycle of Catalase-Peroxidases from Synechocystis PCC 6803, Burkholderia Pseudomallei, and Mycobacterium Tuberculosis. *Biochemistry* **2007**, *46* (5), 1183–1193. https://doi.org/10.1021/bi062266+.

(171) Zhao, X.; Suarez, J.; Khajo, A.; Yu, S.; Metlitsky, L.; Magliozzo, R. S. A Radical on the Met-Tyr-Trp Modification Required for Catalase Activity in Catalase-Peroxidase Is Established by Isotopic Labeling and Site-Directed Mutagenesis. *J. Am. Chem. Soc.* **2010**, *132* (24), 8268–8269. https://doi.org/10.1021/ja103311e.

(172) Vlasits, J.; Jakopitsch, C.; Bernroitner, M.; Zamocky, M.; Furtmüller, P. G.; Obinger, C. Mechanisms of Catalase Activity of Heme Peroxidases. *Arch Biochem Biophys* **2010**, *500* (1), 74–81. https://doi.org/10.1016/j.abb.2010.04.018.

(173) Zhao, X.; Khajo, A.; Jarrett, S.; Suarez, J.; Levitsky, Y.; Burger, R. M.; Jarzecki, A. A.; Magliozzo, R. S. Specific Function of the Met-Tyr-Trp Adduct Radical and Residues Arg-418 and Asp-137 in the Atypical Catalase Reaction of Catalase-Peroxidase KatG. *J. Biol. Chem.* **2012**, *287* (44), 37057–37065. https://doi.org/10.1074/jbc.M112.401208.

(174) Yu, S.; Girotto, S.; Zhao, X.; Magliozzo, R. S. Rapid Formation of Compound II and a Tyrosyl Radical in the Y229F Mutant of Mycobacterium Tuberculosis Catalase-Peroxidase Disrupts Catalase but Not Peroxidase Function. *J. Biol. Chem.* **2003**, *278* (45), 44121–44127. https://doi.org/10.1074/jbc.M304757200.

(175) Zhang, Y.; Yao, P.; Cai, X.; Xu, H.; Zhang, X.; Jiang, J. Density Functional Theory Study of the Inner Hydrogen Atom Transfer in Metal-Free Porphyrins: Meso-Substitutional Effects. *J Mol Graph Model* **2007**, *26* (1), 319–326. https://doi.org/10.1016/j.jmgm.2006.12.008.

(176) Suarez, J.; Ranguelova, K.; Jarzecki, A. A.; Manzerova, J.; Krymov, V.; Zhao, X.; Yu, S.; Metlitsky, L.; Gerfen, G. J.; Magliozzo, R. S. An Oxyferrous Heme/Protein-Based Radical Intermediate Is Catalytically Competent in the Catalase Reaction of Mycobacterium Tuberculosis Catalase-Peroxidase (KatG). *J Biol Chem* **2009**, *284* (11), 7017–7029. https://doi.org/10.1074/jbc.M808106200.

(177) *Analysis of heme structural heterogeneity in Mycobacterium tuberculosis catalase-peroxidase (KatG). - Abstract - Europe PMC*. https://europepmc.org/article/MED/12506108 (accessed 2020-05-04).

(178) Martin, S. R.; Schilstra, M. J. Rapid Mixing Kinetic Techniques. *Methods Mol Biol* **2013**, *1008*, 119–138. https://doi.org/10.1007/978-1-62703-398-5_5.

(179) Zheng, X.; Bi, C.; Li, Z.; Podariu, M.; Hage, D. S. ANALYTICAL METHODS FOR KINETIC STUDIES OF BIOLOGICAL INTERACTIONS: A REVIEW. *J Pharm Biomed Anal* **2015**, *113*, 163–180. https://doi.org/10.1016/j.jpba.2015.01.042.

(180) Roder, H.; Maki, K.; Cheng, H. Early Events in Protein Folding Explored by Rapid Mixing Methods. *Chem Rev* **2006**, *106* (5), 1836–1861. https://doi.org/10.1021/cr040430y.

(181) Youngman, K. M.; Spencer, D. B.; Brems, D. N.; DeFelippis, M. R. Kinetic Analysis of the Folding of Human Growth Hormone. Influence of Disulfide Bonds. *J Biol Chem* **1995**, *270* (34), 19816–19822. https://doi.org/10.1074/jbc.270.34.19816.

(182) Wang, Z.; Watt, W.; Brooks, N. A.; Harris, M. S.; Urban, J.; Boatman, D.; McMillan, M.; Kahn, M.; Heinrikson, R. L.; Finzel, B. C.; Wittwer, A. J.; Blinn, J.; Kamtekar, S.; Tomasselli, A. G. Kinetic and Structural Characterization of Caspase-3 and Caspase-8 Inhibition by a Novel Class of Irreversible Inhibitors. *Biochimica et Biophysica Acta (BBA) - Proteins and Proteomics* **2010**, *1804* (9), 1817–1831. https://doi.org/10.1016/j.bbapap.2010.05.007.

(183) Isin, E. M.; Guengerich, F. P. Kinetics and Thermodynamics of Ligand Binding by Cytochrome P450 3A4. *J Biol Chem* **2006**, *281* (14), 9127–9136. https://doi.org/10.1074/jbc.M511375200.

(184) Adams, A.; Guss, J. M.; Collyer, C. A.; Denny, W. A.; Prakash, A. S.; Wakelin, L. P. Acridinecarboxamide Topoisomerase Poisons: Structural and Kinetic Studies of the DNA Complexes of 5-Substituted 9-Amino-(N-(2-Dimethylamino)Ethyl)Acridine-4-Carboxamides. *Mol Pharmacol* **2000**, *58* (3), 649–658. https://doi.org/10.1124/mol.58.3.649.

(185) Gomez-Hens, A.; Perez-Bendito, D. The Stopped-Flow Technique in Analytical Chemistry. *Analytica Chimica Acta* **1991**, *242*, 147–177. https://doi.org/10.1016/0003-2670(91)87060-K.

(186) Chouchane, S.; Lippai, I.; Magliozzo, R. S. Catalase-Peroxidase (Mycobacterium Tuberculosis KatG) Catalysis and Isoniazid Activation. *Biochemistry* **2000**, *39* (32), 9975–9983. https://doi.org/10.1021/bi0005815.

(187) Jakopitsch, C.; Wanasinghe, A.; Jantschko, W.; Furtmüller, P.; Obinger, C. Kinetics of Interconversion of Ferrous Enzymes, Compound II and Compound III, of Wild-Type Synechocystis Catalase-Peroxidase and Y249F. *The Journal of biological chemistry* **2005**, *280*, 9037–9042. https://doi.org/10.1074/jbc.M413317200.

(188) Goodwin, D. C.; Hertwig, K. M. Peroxidase-Catalyzed Oxidation of Capsaicinoids: Steady-State and Transient-State Kinetic Studies. *Archives of biochemistry and biophysics* **2003**, *417* (1), 18–26.

(189) Palmer, G. The Electron Paramagnetic Resonance of Metalloproteins. *Biochem Soc Trans* **1985**, *13* (3), 548–560. https://doi.org/10.1042/bst0130548.

(190) Bracci, M.; Bruzzese, P. C.; Famulari, A.; Fioco, D.; Guidetti, A.; Liao, Y.-K.; Podvorica, L.; Rezayi, S. F.; Serra, Ii.; Thangavel, K.; Murphy, D. M. Paramagnetic Species in Catalysis Research: A Unified Approach towards (the Role of EPR in) Heterogeneous, Homogeneous and Enzyme Catalysis. In *Electron Paramagnetic Resonance*; 2020; pp 1–46. https://doi.org/10.1039/9781839162534-00001.

(191) Miller, M. A.; Vitello, L.; Erman, J. E. Regulation of Interprotein Electron Transfer by Trp 191 of Cytochrome c Peroxidase. *Biochemistry* **1995**, *34* (37), 12048–12058. https://doi.org/10.1021/bi00037a048.

(192) Rutter, R.; Valentine, M.; Hendrich, M. P.; Hager, L. P.; Debrunner, P. G. Chemical Nature of the Porphyrin .Pi. Cation Radical in Horseradish Peroxidase Compound I. *Biochemistry* **1983**, *22* (20), 4769–4774. https://doi.org/10.1021/bi00289a024.

(193) Singh, R.; Switala, J.; Loewen, P. C.; Ivancich, A. Two [Fe(IV)=O Trp*] Intermediates in M. Tuberculosis Catalase-Peroxidase Discriminated by Multifrequency (9-285 GHz) EPR Spectroscopy: Reactivity toward Isoniazid. *J Am Chem Soc* **2007**, *129* (51), 15954–15963. https://doi.org/10.1021/ja075108u.

(194) Jeschke, G. EPR Techniques for Studying Radical Enzymes. *Biochim Biophys Acta* **2005**, *1707* (1), 91–102. https://doi.org/10.1016/j.bbabio.2004.02.012.

(195) Ivancich, A.; Jakopitsch, C.; Auer, M.; Un, S.; Obinger, C. Protein-Based Radicals in the Catalase-Peroxidase of Synechocystis PCC6803: A Multifrequency EPR Investigation of Wild-Type and Variants on the Environment of the Heme Active Site. *J. Am. Chem. Soc.* **2003**, *125* (46), 14093–14102. https://doi.org/10.1021/ja035582+.

(196) Gerfen, G. J.; Bellew, B. F.; Griffin, R. G.; Singel, D. J.; Ekberg, C. A.; Whittaker, J. W. High-Frequency Electron Paramagnetic Resonance Spectroscopy of the Apogalactose Oxidase Radical. *J. Phys. Chem.* **1996**, *100* (41), 16739–16748. https://doi.org/10.1021/jp960709l.

(197) Kaupp, M.; Remenyi, C.; Vaara, J.; Malkina, O. L.; Malkin, V. G. Density Functional Calculations of Electronic G-Tensors for Semiquinone Radical Anions. The Role of Hydrogen Bonding and Substituent Effects. *J. Am. Chem. Soc.* **2002**, *124* (11), 2709–2722. https://doi.org/10.1021/ja0162764.

(198) Singh, R.; Geetanjali, null; Chauhan, S. M. S. Electron Transfer in Natural and Unnatural Flavoporphyrins. *Bioorg Chem* **2004**, *32* (3), 140–169. https://doi.org/10.1016/j.bioorg.2003.11.003.

(199) Berglund, G. I.; Carlsson, G. H.; Smith, A. T.; Szöke, H.; Henriksen, A.; Hajdu, J. The Catalytic Pathway of Horseradish Peroxidase at High Resolution. *Nature* **2002**, *417* (6887), 463–468. https://doi.org/10.1038/417463a.

(200) Della Pia, E. A.; Elliott, M.; Jones, D. D.; Macdonald, J. E. Orientation-Dependent Electron Transport in a Single Redox Protein. *ACS Nano* **2012**, *6* (1), 355–361. https://doi.org/10.1021/nn2036818.

(201) Finkel, T. Oxidant Signals and Oxidative Stress. *Curr Opin Cell Biol* **2003**, *15* (2), 247–254. https://doi.org/10.1016/s0955-0674(03)00002-4.

(202) Guiseppi-Elie, A.; Lei, C.; Baughman, R. H. Direct Electron Transfer of Glucose Oxidase on Carbon Nanotubes. *Nanotechnology* **2002**, *13* (5), 559–564. https://doi.org/10.1088/0957-4484/13/5/303.

(203) Monteiro, H. P.; Stern, A. Redox Modulation of Tyrosine Phosphorylation-Dependent Signal Transduction Pathways. *Free Radic Biol Med* **1996**, *21* (3), 323–333. https://doi.org/10.1016/0891-5849(96)00051-2.

(204) Nakamura, H.; Nakamura, K.; Yodoi, J. Redox Regulation of Cellular Activation. *Annu Rev Immunol* **1997**, *15*, 351–369. https://doi.org/10.1146/annurev.immunol.15.1.351.

(205) Moser, C. C.; Keske, J. M.; Warncke, K.; Farid, R. S.; Dutton, P. L. Nature of Biological Electron Transfer. *Nature* **1992**, *355* (6363), 796–802. https://doi.org/10.1038/355796a0.

(206) Singh, R.; Wiseman, B.; Deemagarn, T.; Jha, V.; Switala, J.; Loewen, P. C. Comparative Study of Catalase-Peroxidases (KatGs). *Arch Biochem Biophys* **2008**, *471* (2), 207–214. https://doi.org/10.1016/j.abb.2007.12.008.

(207) Branchaud, B. P. Heme Peroxidases By H. Brian Dunford (University of Alberta). Wiley-VCH, John Wiley and Sons: New York. 1999. Xi + 507 Pp. $195.00. ISBN 0-471-24244-6. *J. Am. Chem. Soc.* **2000**, *122* (30), 7434–7434. https://doi.org/10.1021/ja995730p.

(208) Moore, R. L.; Powell, L. J.; Goodwin, D. C. The Kinetic Properties Producing the Perfunctory PH Profiles of Catalase-Peroxidases. *Biochim. Biophys. Acta* **2008**, *1784* (6), 900–907. https://doi.org/10.1016/j.bbapap.2008.03.008.

(209) Ghisla, S.; Thorpe, C. Acyl-CoA Dehydrogenases. A Mechanistic Overview. *Eur J Biochem* **2004**, *271* (3), 494–508. https://doi.org/10.1046/j.1432-1033.2003.03946.x.

(210) Fitzpatrick, P. F. Oxidation of Amines by Flavoproteins. *Arch Biochem Biophys* **2010**, *493* (1), 13–25. https://doi.org/10.1016/j.abb.2009.07.019.

(211) Vrielink, A.; Ghisla, S. Cholesterol Oxidase: Biochemistry and Structural Features. *FEBS J* **2009**, *276* (23), 6826–6843. https://doi.org/10.1111/j.1742-4658.2009.07377.x.

(212) Ellis, H. R. The FMN-Dependent Two-Component Monooxygenase Systems. *Arch Biochem Biophys* **2010**, *497* (1–2), 1–12. https://doi.org/10.1016/j.abb.2010.02.007.

(213) Anderson, J. L. R.; Chapman, S. K. Molecular Mechanisms of Enzyme-Catalysed Halogenation. *Mol. BioSyst.* **2006**, *2* (8), 350–357. https://doi.org/10.1039/B607813C.

(214) Blasiak, L. C.; Drennan, C. L. Structural Perspective on Enzymatic Halogenation. *Acc Chem Res* **2009**, *42* (1), 147–155. https://doi.org/10.1021/ar800088r.

(215) Fejzagić, A. V.; Gebauer, J.; Huwa, N.; Classen, T. Halogenating Enzymes for Active Agent Synthesis: First Steps Are Done and Many Have to Follow. *Molecules* **2019**, *24* (21), 4008. https://doi.org/10.3390/molecules24214008.

(216) Mowat, C. G.; Gazur, B.; Campbell, L. P.; Chapman, S. K. Flavin-Containing Heme Enzymes. *Archives of Biochemistry and Biophysics* **2010**, *493* (1), 37–52. https://doi.org/10.1016/j.abb.2009.10.005.

(217) Otvos, J. D.; Krum, D. P.; Masters, B. S. Localization of the Free Radical on the Flavin Mononucleotide of the Air-Stable Semiquinone State of NADPH-Cytochrome P-450

Reductase Using 31P NMR Spectroscopy. *Biochemistry* **1986**, *25* (22), 7220–7228. https://doi.org/10.1021/bi00370a068.

(218) Williams, C. H.; Kamin, H. Microsomal Triphosphopyridine Nucleotide-Cytochrome c Reductase of Liver. *J Biol Chem* **1962**, *237*, 587–595.

(219) Lu, A. Y.; Junk, K. W.; Coon, M. J. Resolution of the Cytochrome P-450-Containing Omega-Hydroxylation System of Liver Microsomes into Three Components. *J Biol Chem* **1969**, *244* (13), 3714–3721.

(220) Horecker, B. L. Triphosphopyridine Nucleotidecytochrome c Reductase in Liver. *Journal of Biological Chemistry* **1950**, *183* (2), 593–605. https://doi.org/10.1016/S0021-9258(19)51185-1.

(221) Schacter, B. A.; Nelson, E. B.; Marver, H. S.; Masters, B. S. Immunochemical Evidence for an Association of Heme Oxygenase with the Microsomal Electron Transport System. *J Biol Chem* **1972**, *247* (11), 3601–3607.

(222) Z, I.; R, I.; Dl, C. Evidence for a New Physiological Role of Hepatic NADPH:Ferricytochrome (P-450) Oxidoreductase. Direct Electron Input to the Microsomal Fatty Acid Chain Elongation System. *The Journal of biological chemistry* **1981**, *256* (19).

(223) Sato, H.; Hayashi, T.; Ando, T.; Hisaeda, Y.; Ueno, T.; Watanabe, Y. Hybridization of Modified-Heme Reconstitution and Distal Histidine Mutation to Functionalize Sperm Whale Myoglobin. *J. Am. Chem. Soc.* **2004**, *126* (2), 436–437. https://doi.org/10.1021/ja038798k.

(224) Hayashi, T.; Hitomi, Y.; Ando, T.; Mizutani, T.; Hisaeda, Y.; Kitagawa, S.; Ogoshi, H. Peroxidase Activity of Myoglobin Is Enhanced by Chemical Mutation of Heme-Propionates. *J. Am. Chem. Soc.* **1999**, *121* (34), 7747–7750. https://doi.org/10.1021/ja9841005.

(225) Fruk, L.; Kuo, C.-H.; Torres, E.; Niemeyer, C. M. Apoenzyme Reconstitution as a Chemical Tool for Structural Enzymology and Biotechnology. *Angewandte Chemie International Edition* **2009**, *48* (9), 1550–1574. https://doi.org/10.1002/anie.200803098.

(226) Teale, F. W. Cleavage of the Haem-Protein Link by Acid Methylethylketone. *Biochim Biophys Acta* **1959**, *35*, 543. https://doi.org/10.1016/0006-3002(59)90407-x.

(227) Wagner, G. C.; Gunsalus, I. C.; Wang, M. Y.; Hoffman, B. M. Cobalt-Substituted Cytochrome P-450cam. *Journal of Biological Chemistry* **1981**, *256* (12), 6266–6273. https://doi.org/10.1016/S0021-9258(19)69158-1.

(228) Chien, S.-C.; Shoji, O.; Morimoto, Y.; Watanabe, Y. Use of Apomyoglobin to Gently Remove Heme from a H 2 O 2 -Dependent Cytochrome P450 and Allow Its Reconstitution. *New Journal of Chemistry* **2017**, *41* (1), 302–307. https://doi.org/10.1039/C6NJ02882A.

(229) Dalton, D. A.; Diaz del Castillo, L.; Kahn, M. L.; Joyner, S. L.; Chatfield, J. M. Heterologous Expression and Characterization of Soybean Cytosolic Ascorbate Peroxidase. *Arch Biochem Biophys* **1996**, *328* (1), 1–8. https://doi.org/10.1006/abbi.1996.0135.

(230) Metcalfe, C. L.; Daltrop, O.; Ferguson, S. J.; Raven, E. L. Tuning the Formation of a Covalent Haem–Protein Link by Selection of Reductive or Oxidative Conditions as Exemplified by Ascorbate Peroxidase. *Biochem J* **2007**, *408* (Pt 3), 355–361. https://doi.org/10.1042/BJ20071041.

(231) Sudhamsu, J.; Kabir, M.; Airola, M. V.; Patel, B. A.; Yeh, S.-R.; Rousseau, D. L.; Crane, B. R. Co-Expression of Ferrochelatase Allows for Complete Heme Incorporation into Recombinant Proteins Produced in E. Coli. *Protein Expr Purif* **2010**, *73* (1), 78–82. https://doi.org/10.1016/j.pep.2010.03.010.

(232) Varnado, C. L.; Goodwin, D. C. System for the Expression of Recombinant Hemoproteins in Escherichia Coli. *Protein Expr Purif* **2004**, *35* (1), 76–83. https://doi.org/10.1016/j.pep.2003.12.001.

(233) Weickert, M. J.; Pagratis, M.; Curry, S. R.; Blackmore, R. Stabilization of Apoglobin by Low Temperature Increases Yield of Soluble Recombinant Hemoglobin in Escherichia Coli. *Appl Environ Microbiol* **1997**, *63* (11), 4313–4320. https://doi.org/10.1128/aem.63.11.4313-4320.1997.

(234) Jung, Y.; Kwak, J.; Lee, Y. High-Level Production of Heme-Containing Holoproteins in Escherichia Coli. *Appl Microbiol Biotechnol* **2001**, *55* (2), 187–191. https://doi.org/10.1007/s002530000502.

(235) Nishimoto, M.; Clark, J. E.; Masters, B. S. Cytochrome P450 4A4: Expression in Escherichia Coli, Purification, and Characterization of Catalytic Properties. *Biochemistry* **1993**, *32* (34), 8863–8870. https://doi.org/10.1021/bi00085a018.

(236) Sinha, N.; Ferguson, S. J. An Escherichia Coli Ccm (Cytochrome c Maturation) Deletion Strain Substantially Expresses Hydrogenobacter Thermophilus Cytochrome C552 in the Cytoplasm: Availability of Haem Influences Cytochrome C552 Maturation. *FEMS Microbiology Letters* **1998**, *161* (1), 1–6. https://doi.org/10.1111/j.1574-6968.1998.tb12921.x.

(237) Ag, T.; Sm, P. Haem Iron-Transport System in Enterohaemorrhagic Escherichia Coli O157:H7. *Molecular microbiology* **1997**, *23* (4). https://doi.org/10.1046/j.1365-2958.1997.2641628.x.

(238) Yamada, Y.; Fujiwara, T.; Sato, T.; Igarashi, N.; Tanaka, N. The 2.0 A Crystal Structure of Catalase-Peroxidase from Haloarcula Marismortui. *Nat Struct Biol* **2002**, *9* (9), 691–695. https://doi.org/10.1038/nsb834.

(239) Zámocký, M.; García-Fernández, Q.; Gasselhuber, B.; Jakopitsch, C.; Furtmüller, P. G.; Loewen, P. C.; Fita, I.; Obinger, C.; Carpena, X. High Conformational Stability of Secreted Eukaryotic Catalase-Peroxidases: Answers from First Crystal Structure and

Unfolding Studies. *J Biol Chem* **2012**, *287* (38), 32254–32262. https://doi.org/10.1074/jbc.M112.384271.

(240) Carpena, X.; Melik-Adamyan, W.; Loewen, P. C.; Fita, I. Structure of the C-Terminal Domain of the Catalase-Peroxidase KatG from Escherichia Coli. *Acta Crystallogr D Biol Crystallogr* **2004**, *60* (Pt 10), 1824–1832. https://doi.org/10.1107/S0907444904020621.

(241) Zamocky, M.; Furtmüller, P. G.; Bellei, M.; Battistuzzi, G.; Stadlmann, J.; Vlasits, J.; Obinger, C. Intracellular Catalase/Peroxidase from the Phytopathogenic Rice Blast Fungus Magnaporthe Grisea: Expression Analysis and Biochemical Characterization of the Recombinant Protein. *Biochem J* **2009**, *418* (2), 443–451. https://doi.org/10.1042/BJ20081478.

(242) Heering, H. A.; Indiani, C.; Regelsberger, G.; Jakopitsch, C.; Obinger, C.; Smulevich, G. New Insights into the Heme Cavity Structure of Catalase-Peroxidase: A Spectroscopic Approach to the Recombinant Synechocystis Enzyme and Selected Distal Cavity Mutants. *Biochemistry* **2002**, *41* (29), 9237–9247. https://doi.org/10.1021/bi025740u.

(243) Jakopitsch, C.; Ivancich, A.; Schmuckenschlager, F.; Wanasinghe, A.; Pöltl, G.; Furtmüller, P. G.; Rüker, F.; Obinger, C. Influence of the Unusual Covalent Adduct on the Kinetics and Formation of Radical Intermediates in Synechocystis Catalase Peroxidase: A STOPPED-FLOW AND EPR CHARACTERIZATION OF THE MET275, TYR249, AND ARG439 VARIANTS *. *Journal of Biological Chemistry* **2004**, *279* (44), 46082–46095. https://doi.org/10.1074/jbc.M408399200.

(244) Suarez, J.; Ranguelova, K.; Jarzecki, A. A.; Manzerova, J.; Krymov, V.; Zhao, X.; Yu, S.; Metlitsky, L.; Gerfen, G. J.; Magliozzo, R. S. An Oxyferrous Heme/Protein-Based Radical Intermediate Is Catalytically Competent in the Catalase Reaction of Mycobacterium Tuberculosis Catalase-Peroxidase (KatG). *J. Biol. Chem.* **2009**, *284* (11), 7017–7029. https://doi.org/10.1074/jbc.M808106200.

(245) Ndontsa, E. N.; Moore, R. L.; Goodwin, D. C. Stimulation of KatG Catalase Activity by Peroxidatic Electron Donors. *Arch Biochem Biophys* **2012**, *525* (2), 215–222. https://doi.org/10.1016/j.abb.2012.06.003.

(246) Barr, I.; Guo, F. Pyridine Hemochromagen Assay for Determining the Concentration of Heme in Purified Protein Solutions. *Bio Protoc* **2015**, *5* (18), e1594.

(247) Nelson, D. P.; Kiesow, L. A. Enthalpy of Decomposition of Hydrogen Peroxide by Catalase at 25 Degrees C (with Molar Extinction Coefficients of H 2 O 2 Solutions in the UV). *Anal Biochem* **1972**, *49* (2), 474–478. https://doi.org/10.1016/0003-2697(72)90451-4.

(248) Jakopitsch, C.; Obinger, C.; Un, S.; Ivancich, A. Identification of Trp106 as the Tryptophanyl Radical Intermediate in Synechocystis PCC6803 Catalase-Peroxidase by Multifrequency Electron Paramagnetic Resonance Spectroscopy. *J Inorg Biochem* **2006**, *100* (5–6), 1091–1099. https://doi.org/10.1016/j.jinorgbio.2006.02.009.

(249) Gundinger, T.; Spadiut, O. A Comparative Approach to Recombinantly Produce the Plant Enzyme Horseradish Peroxidase in Escherichia Coli. *J Biotechnol* **2017**, *248*, 15–24. https://doi.org/10.1016/j.jbiotec.2017.03.003.

(250) Nicholls, P.; Fita, I.; Loewen, P. C. Enzymology and Structure of Catalases. In *Advances in Inorganic Chemistry*; Elsevier, 2000; Vol. 51, pp 51–106. https://doi.org/10.1016/S0898-8838(00)51001-0.

(251) Kapetanaki, S. M.; Chouchane, S.; Yu, S.; Zhao, X.; Magliozzo, R. S.; Schelvis, J. P. M. Mycobacterium Tuberculosis KatG(S315T) Catalase-Peroxidase Retains All Active Site Properties for Proper Catalytic Function. *Biochemistry* **2005**, *44* (1), 243–252. https://doi.org/10.1021/bi048097f.

(252) Assessment, U. E. N. C. for E. *Handbook of metalloproteins*. https://hero.epa.gov/hero/index.cfm/reference/details/reference_id/673541 (accessed 2021-06-14).

(253) Woodard, S. I.; Dailey, H. A. Regulation of Heme Biosynthesis in Escherichia Coli. *Arch Biochem Biophys* **1995**, *316* (1), 110–115. https://doi.org/10.1006/abbi.1995.1016.

(254) Ghiladi, R. A.; Knudsen, G. M.; Medzihradszky, K. F.; Ortiz de Montellano, P. R. The Met-Tyr-Trp Cross-Link in Mycobacterium Tuberculosis Catalase-Peroxidase (KatG): Autocatalytic Formation and Effect on Enzyme Catalysis and Spectroscopic Properties. *J Biol Chem* **2005**, *280* (24), 22651–22663. https://doi.org/10.1074/jbc.M502486200.

(255) Dixon, S. J.; Stockwell, B. R. The Role of Iron and Reactive Oxygen Species in Cell Death. *Nature Chemical Biology* **2014**, *10* (1), 9–17. https://doi.org/10.1038/nchembio.1416.

(256) Delogu, G.; Sali, M.; Fadda, G. The Biology of Mycobacterium Tuberculosis Infection. *Mediterr J Hematol Infect Dis* **2013**, *5* (1). https://doi.org/10.4084/MJHID.2013.070.

(257) Welinder, K. G. Superfamily of Plant, Fungal and Bacterial Peroxidases. *Current Opinion in Structural Biology* **1992**, *2* (3), 388–393. https://doi.org/10.1016/0959-440X(92)90230-5.

(258) Ortiz de Montellano, P. R. Catalytic Sites of Hemoprotein Peroxidases. *Annual Review of Pharmacology and Toxicology* **1992**, *32* (1), 89–107. https://doi.org/10.1146/annurev.pa.32.040192.000513.

(259) Finzel, B. C.; Poulos, T. L.; Kraut, J. Crystal Structure of Yeast Cytochrome c Peroxidase Refined at 1.7-A Resolution. *J Biol Chem* **1984**, *259* (21), 13027–13036.

(260) Zhao, X.; Yu, S.; Ranguelova, K.; Suarez, J.; Metlitsky, L.; Schelvis, J. P. M.; Magliozzo, R. S. Role of the Oxyferrous Heme Intermediate and Distal Side Adduct Radical in the Catalase Activity of Mycobacterium Tuberculosis KatG Revealed by the W107F Mutant. *J Biol Chem* **2009**, *284* (11), 7030–7037. https://doi.org/10.1074/jbc.M808107200.

(261) Cl, Q.; Iv, P.; M, H.-M.; Al, O.; Md, B. Sites of Reactive Oxygen Species Generation by Mitochondria Oxidizing Different Substrates. *Redox biology* **2013**, *1* (1). https://doi.org/10.1016/j.redox.2013.04.005.

(262) Harvey, P. J.; Palmer, J. M. Oxidation of Phenolic Compounds by Ligninase. *Journal of Biotechnology* **1990**, *13* (2), 169–179. https://doi.org/10.1016/0168-1656(90)90102-H.

(263) Zamocky, M.; Furtmüller, P. G.; Obinger, C. Evolution of Catalases from Bacteria to Humans. *Antioxid Redox Signal* **2008**, *10* (9), 1527–1548. https://doi.org/10.1089/ars.2008.2046.

(264) Yoshikawa, S.; Shinzawa-Itoh, K.; Nakashima, R.; Yaono, R.; Yamashita, E.; Inoue, N.; Yao, M.; Fei, M. J.; Libeu, C. P.; Mizushima, T.; Yamaguchi, H.; Tomizaki, T.; Tsukihara, T. Redox-Coupled Crystal Structural Changes in Bovine Heart Cytochrome c Oxidase. *Science* **1998**, *280* (5370), 1723–1729. https://doi.org/10.1126/science.280.5370.1723.

(265) Buse, G.; Soulimane, T.; Dewor, M.; Meyer, H. E.; Blüggel, M. Evidence for a Copper-Coordinated Histidine-Tyrosine Cross-Link in the Active Site of Cytochrome Oxidase. *Protein Sci* **1999**, *8* (5), 985–990.

(266) Ito, N.; Phillips, S. E.; Yadav, K. D.; Knowles, P. F. Crystal Structure of a Free Radical Enzyme, Galactose Oxidase. *J Mol Biol* **1994**, *238* (5), 794–814. https://doi.org/10.1006/jmbi.1994.1335.

(267) Kamachi, S.; Hirabayashi, K.; Tamoi, M.; Shigeoka, S.; Tada, T.; Wada, K. The Crystal Structure of Isoniazid-Bound KatG Catalase-Peroxidase from Synechococcus Elongatus PCC7942. *FEBS J* **2015**, *282* (1), 54–64. https://doi.org/10.1111/febs.13102.

(268) Varnado, C. L.; Goodwin, D. C. System for the Expression of Recombinant Hemoproteins in Escherichia Coli. *Protein Expr Purif* **2004**, *35* (1), 76–83. https://doi.org/10.1016/j.pep.2003.12.001.

(269) Moore, S. D.; Prevelige, P. E. A P22 Scaffold Protein Mutation Increases the Robustness of Head Assembly in the Presence of Excess Portal Protein. *J Virol* **2002**, *76* (20), 10245–10255. https://doi.org/10.1128/JVI.76.20.10245-10255.2002.

(270) Barr, I.; Guo, F. Pyridine Hemochromagen Assay for Determining the Concentration of Heme in Purified Protein Solutions. *Bio Protoc* **2015**, *5* (18).

(271) Wood, E. Molecular Cloning. A Laboratory Manual. *Biochemical Education* **1983**, *11* (2), 82. https://doi.org/10.1016/0307-4412(83)90068-7.

(272) Liu, A.; Pötsch, S.; Davydov, A.; Barra, A. L.; Rubin, H.; Gräslund, A. The Tyrosyl Free Radical of Recombinant Ribonucleotide Reductase from Mycobacterium Tuberculosis Is Located in a Rigid Hydrophobic Pocket. *Biochemistry* **1998**, *37* (46), 16369–16377. https://doi.org/10.1021/bi981471p.

(273) Wengenack, N. L.; Lopes, H.; Kennedy, M. J.; Tavares, P.; Pereira, A. S.; Moura, I.; Moura, J. J. G.; Rusnak, F. Redox Potential Measurements of the Mycobacterium Tuberculosis Heme Protein KatG and the Isoniazid-Resistant Enzyme KatG(S315T): Insights into Isoniazid Activation. *Biochemistry* **2000**, *39* (37), 11508–11513. https://doi.org/10.1021/bi001239v.

(274) *Comparison of Isoniazid Oxidation Catalyzed by Bacterial Catalase–Peroxidases and Horseradish Peroxidase - ScienceDirect*. https://www.sciencedirect.com/science/article/pii/S0003986185700653 (accessed 2022-06-03).

(275) Chouchane, S.; Girotto, S.; Kapetanaki, S.; Schelvis, J. P. M.; Yu, S.; Magliozzo, R. S. Analysis of Heme Structural Heterogeneity in Mycobacterium Tuberculosis Catalase-Peroxidase (KatG). *Journal of Biological Chemistry* **2003**, *278* (10), 8154–8162. https://doi.org/10.1074/jbc.M208256200.

(276) Regelsberger, G.; Jakopitsch, C.; Furtmüller, P. G.; Rueker, F.; Switala, J.; Loewen, P. C.; Obinger, C. The Role of Distal Tryptophan in the Bifunctional Activity of Catalase-Peroxidases. *Biochem Soc Trans* **2001**, *29* (Pt 2), 99–105. https://doi.org/10.1042/0300-5127:0290099.

(277) Singh, R.; Switala, J.; Loewen, P. C.; Ivancich, A. Two [Fe(IV)O Trp•] Intermediates in M. Tuberculosis Catalase-Peroxidase Discriminated by Multifrequency (9−285 GHz) EPR Spectroscopy: Reactivity toward Isoniazid. *J. Am. Chem. Soc.* **2007**, *129* (51), 15954–15963. https://doi.org/10.1021/ja075108u.

(278) *Distinct Role of Specific Tryptophans in Facilitating Electron Transfer or as [Fe(IV)=O Trp•] Intermediates in the Peroxidase Reaction of Bulkholderia pseudomallei Catalase-Peroxidase: A Multifrequency EPR Spectroscopy Investigation | Journal of the American Chemical Society*. https://pubs.acs.org/doi/full/10.1021/ja901402v (accessed 2022-06-21).

(279) Claiborne, A.; Fridovich, I. Purification of the O-Dianisidine Peroxidase from Escherichia Coli B. Physicochemical Characterization and Analysis of Its Dual Catalatic and Peroxidatic Activities. *Journal of Biological Chemistry* **1979**, *254* (10), 4245–4252. https://doi.org/10.1016/S0021-9258(18)50722-5.

(280) Ma, Z.; Strickland, K. T.; Cherne, M. D.; Sehanobish, E.; Rohde, K. H.; Self, W. T.; Davidson, V. L. The Rv2633c Protein of Mycobacterium Tuberculosis Is a Non-Heme Di-Iron Catalase with a Possible Role in Defenses against Oxidative Stress. *Journal of Biological Chemistry* **2018**, *293* (5), 1590–1595. https://doi.org/10.1074/jbc.RA117.000421.

(281) *Catalase-peroxidases (KatG) Exhibit NADH Oxidase Activity* | Elsevier Enhanced Reader*. https://doi.org/10.1074/jbc.M406374200.

(282) Bank, R. P. D. *RCSB PDB - 2CCA: Crystal structure of the catalase-peroxidase (KatG) and S315T mutant from Mycobacterium tuberculosis*. https://www.rcsb.org/structure/2cca (accessed 2022-11-08).

(283) Santoni, E.; Jakopitsch, C.; Obinger, C.; Smulevich, G. Manipulating the Covalent Link between Distal Side Tryptophan, Tyrosine, and Methionine in Catalase-Peroxidases: An Electronic Absorption and Resonance Raman Study. *Biopolymers* **2004**, *74* (1–2), 46–50. https://doi.org/10.1002/bip.20041.

(284) Yu, S.; Girotto, S.; Zhao, X.; Magliozzo, R. S. Rapid Formation of Compound II and a Tyrosyl Radical in the Y229F Mutant of Mycobacterium Tuberculosis Catalase-Peroxidase Disrupts Catalase but Not Peroxidase Function. *J Biol Chem* **2003**, *278* (45), 44121–44127. https://doi.org/10.1074/jbc.M304757200.

(285) Chouchane, S.; Girotto, S.; Yu, S.; Magliozzo, R. S. Identification and Characterization of Tyrosyl Radical Formation in Mycobacterium TuberculosisCatalase-Peroxidase (KatG) *. *Journal of Biological Chemistry* **2002**, *277* (45), 42633–42638. https://doi.org/10.1074/jbc.M207916200.

(286) Nakajima, R.; Yamazaki, I. The Mechanism of Oxyperoxidase Formation from Ferryl Peroxidase and Hydrogen Peroxide. *J. Biol. Chem.* **1987**, *262* (6), 2576–2581.

(287) Goodwin, D. C.; Grover, T. A.; Aust, S. D. Roles of Efficient Substrates in Enhancement of Peroxidase-Catalyzed Oxidations. *Biochemistry* **1997**, *36* (1), 139–147. https://doi.org/10.1021/bi961465y.

(288) Jakopitsch, C.; Droghetti, E.; Schmuckenschlager, F.; Furtmüller, P. G.; Smulevich, G.; Obinger, C. Role of the Main Access Channel of Catalase-Peroxidase in Catalysis. *J Biol Chem* **2005**, *280* (51), 42411–42422. https://doi.org/10.1074/jbc.m508009200.

(289) Bonagura, C. A.; Bhaskar, B.; Shimizu, H.; Li, H.; Sundaramoorthy, M.; McRee, D. E.; Goodin, D. B.; Poulos, T. L. High-Resolution Crystal Structures and Spectroscopy of Native and Compound I Cytochrome c Peroxidase. *Biochemistry* **2003**, *42* (19), 5600–5608. https://doi.org/10.1021/bi034058c.

(290) Singh, R.; Wiseman, B.; Deemagarn, T.; Donald, L. J.; Duckworth, H. W.; Carpena, X.; Fita, I.; Loewen, P. C. Catalase-Peroxidases (KatG) Exhibit NADH Oxidase Activity. *J Biol Chem* **2004**, *279* (41), 43098–43106. https://doi.org/10.1074/jbc.M406374200.

(291) Yu, S.; Chouchane, S.; Magliozzo, R. S. Characterization of the W321F Mutant of Mycobacterium Tuberculosis Catalase–Peroxidase KatG. *Protein Sci* **2002**, *11* (1), 58–64.

(292) Jakopitsch, C.; Wanasinghe, A.; Jantschko, W.; Furtmüller, P. G.; Obinger, C. Kinetics of Interconversion of Ferrous Enzymes, Compound II and Compound III, of Wild-Type Synechocystis Catalase-Peroxidase and Y249F: Proposal for the Catalatic Mechanism. *J Biol Chem* **2005**, *280* (10), 9037–9042. https://doi.org/10.1074/jbc.M413317200.

(293) Svistunenko, D. A.; Cooper, C. E. A New Method of Identifying the Site of Tyrosyl Radicals in Proteins. *Biophys J* **2004**, *87* (1), 582–595. https://doi.org/10.1529/biophysj.104.041046.

(294) Lee, J. K. Fast Reaction Kinetics with Time-Resolved Mass Spectrometry. *Nat Methods* **2015**, *12* (5), 387–387. https://doi.org/10.1038/nmeth.3382.

(295) Léger, C.; Bertrand, P. Direct Electrochemistry of Redox Enzymes as a Tool for Mechanistic Studies. *Chem. Rev.* **2008**, *108* (7), 2379–2438. https://doi.org/10.1021/cr0680742.

(296) Yin, Y.; Lü, Y.; Wu, P.; Cai, C. Direct Electrochemistry of Redox Proteins and Enzymes Promoted by Carbon Nanotubes. *Sensors (Basel)* **2005**, *5* (4), 220–234.

(297) Kissinger, P. T.; Heineman, W. R. Cyclic Voltammetry. *J. Chem. Educ.* **1983**, *60* (9), 702. https://doi.org/10.1021/ed060p702.

(298) World Health Organization. *Global Tuberculosis Report 2020*; World Health Organization: Geneva, 2020.

(299) Althomsons, S. P.; Winglee, K.; Heilig, C. M.; Talarico, S.; Silk, B.; Wortham, J.; Hill, A. N.; Navin, T. R. Using Machine Learning Techniques and National Tuberculosis Surveillance Data to Predict Excess Growth in Genotyped Tuberculosis Clusters. *Am J Epidemiol* **2022**, kwac117. https://doi.org/10.1093/aje/kwac117.